Bubble dynamics and regime transitions in two-phase flow





Victoria Ellen Pereira

Mansfield College

University of Oxford

A thesis submitted for the degree of

Doctor of Philosophy

Trinity 2019

Abstract

Two-phase flows comprise the concurrent flow of two fluids in different physical states. In this thesis we are are concerned with the flow of liquid and gas mixtures through a vertical pipe. Two-phase pipe-flows are categorised into *flow regimes* which describe the macroscopic geometries of the two fluids. Mathematical models are typically developed for specific flow regimes, and this leads to the study of the transition domain between regimes.

The underlying industrial motivation for the analysis of two-phase flows arises from oil wells. In Part I of this thesis we study a two-fluid model for vertical upwelling flow, and explicitly account for the exsolution of the dissolved gas as the pressure decreases along the well. We find that the application of Henry's law for the dissolved gas concentration predicts a rapid transition to a foam, which is unexpected and non-intuitive. In order to study ways in which this rapid transition could be avoided, we examine rate-limiting non-equilibrium dynamics by incorporating nucleation and bubble growth dynamics in the two-phase model.

In Part II of this thesis we address the question of how to model the bubbly-to-slug flow regime transition. We develop a master equation to describe the evolution of bubble size and shape in a two-phase flow. The approach is based on the derivation of the Boltzmann equation which is generalised to allow for the description of coalescence and fragmentation. The model provides the foundation for further study of the mechanism of regime transition.

Acknowledgements

The first piece of advice that Andrew Fowler gave me was to embrace my Harry Potter predicament and reincarnate. I am eternally grateful to Andrew, without whom this thesis would not have materialised. I feel extremely lucky to have been the recipient of his patient supervision and exceptional generosity with his time, teaching and advice. Thank you for encouraging me to ask big questions, and for inspiring me to try to answer them. Thank you also for the myriad of adventures; may this be just the beginning.

I would like to thank Ian Griffiths for his incredible support and morale-boosting humour; and Chris Farmer, for the countless and insightful discussions over the last few years.

I am indebted to my wonderful support system of friends and family. I am hugely grateful to Michael McPhail, who has been there for me through all the highs and lows (and there were many). Jason Hendry, thank you for the inspiring conservations and endless laughter. Svenison Jaeschke, thank you for your calm enthusiasm and dependable friendship. Thank you to Jack, Dylan, Ellie and Holly for being an ever present force of reassurance and solidarity from afar.

Andrew Brent Linden, your support and encouragement throughout this whole saga has been monumental, thank you.

Thank you also to the EPSRC and PDS for their financial support, and to Colin, Chris and the InFoMM family for this opportunity.

Contents

1 Introduction **1**

1.1 Geology of hydrocarbon reservoirs 2

1.1.1 Locating reservoirs 2

1.1.2 Reservoir fluid properties 3

1.2 Hydrocarbon extraction 6

1.2.1 Oil well domain 6

1.2.2 Recovery process 8

1.3 Industrial modelling of oil wells 9

1.3.1 Oil well performance 10

1.3.2 Oil well models 11

1.4 Two-phase flow 12

1.4.1 Two-phase flow regimes 12

1.5 Overview 13

2 Modelling two-phase flow **15**

2.1 Introduction 15

2.2 Averaging methods 16

2.2.1 Jump conditions 20

2.3 Closure framework 21

2.3.1 Volume fraction condition 22

2.3.2 Equations of state 22

2.3.3 Pressure difference 22

2.3.4 Stresses 23

2.3.5 Interfacial momentum 24

2.3.6 Heat fluxes 26

2.3.7 Interfacial energy 26

2.4 Homogeneous models 27

2.5 Drift-flux models 29

2.6 Two-fluid models 30

2.6.1 One-dimensional two-fluid model 32
2.6.2 Characteristics of the one-dimensional model 37
2.7 Flow regimes 38
2.7.1 Flow regime maps 39
2.7.2 Modelling of flow regime transitions 40
2.8 Summary 40

I Modelling the two-phase flow in oil wells 43

3 Homogeneous model 45
3.1 Introduction 45
3.2 Two-fluid model including exsolution dynamics 46
3.2.1 Boundary conditions 49
3.2.2 Nondimensionalisation and scaling 50
3.3 Incompressible–incompressible system 55
3.3.1 Characteristics 56
3.3.2 The case $\delta \ll 1$, $c_0 \sim O(1)$ 57
3.3.3 The case $c_0 \sim \delta \ll 1$ 59
3.4 Incompressible–compressible system 62
3.4.1 Characteristics 62
3.4.2 The case $\delta \ll 1$, $c_0 \sim O(1)$ 63
3.4.3 The case $c_0 \sim \delta \ll 1$ 64
3.5 Summary 66

4 Non-equilibrium dynamics 69
4.1 Introduction 69
4.2 Diffusion of dissolved gas 73
4.3 Nucleating bubbles 75
4.3.1 $\gamma \gg 1$ 78
4.3.2 $\gamma \ll 1$ 78
4.3.3 $\gamma \sim O(1)$ 79
4.4 Summary 82

II Modelling the bubbly-to-slug flow regime transition 85

5 Nucleation, growth and coalescence in one dimension 87
5.1 Introduction 87

5.2 Problem set up . . . 90
5.3 Discrete formulation . . . 92
5.3.1 Holes . . . 93
5.3.2 Bubbles . . . 93
5.3.3 Numerical solution to the discrete formulation . . . 94
5.4 Continuous limit . . . 97
5.4.1 Holes . . . 97
5.4.2 Bubbles . . . 98
5.5 Dimensionless model . . . 99
5.5.1 Holes . . . 99
5.5.2 Bubbles . . . 100
5.5.3 Continuum model for the infinite domain . . . 100
5.6 Conservation of volume . . . 101
5.6.1 Conservation in the finite domain . . . 101
5.6.1.1 Amended boundary condition . . . 102
5.6.1.2 Amended rate of coalescence . . . 103
5.6.2 Conservation in the infinite domain . . . 104
5.7 Finite domain solution . . . 105
5.8 The limit $\mathcal{L} \gg 1$ . . . 107
5.8.1 Solution for the hole size distribution . . . 107
5.8.2 Solution to the bubble size distribution . . . 109
5.9 Summary . . . 110

6 Coalescence and fragmentation in higher dimensions 113
6.1 Introduction . . . 113
6.2 Single bubble characterisation . . . 114
6.3 Bubble evolution . . . 116
6.3.1 Volume conservation . . . 116
6.3.2 Model equations . . . 117
6.4 Bubble interactions . . . 119
6.4.1 Coalescence . . . 119
6.4.2 Fragmentation . . . 120
6.4.3 Wall effects . . . 121
6.5 Stochastic simulation . . . 122
6.5.1 Results . . . 123
6.6 Summary . . . 128

7 Two-phase flow regime transition **131**
7.1 Introduction . . . 131
7.2 Boltzmann equation . . . 132
7.2.1 Collision criteria . . . 132
7.2.2 Collision sink . . . 133
7.2.3 Collision source term . . . 135
7.3 Modelling the bubble distribution . . . 136
7.3.1 Bubble shape . . . 138
7.3.2 Formulating the master equation . . . 139
7.4 Coalescence . . . 140
7.4.1 Coalescence criteria . . . 140
7.4.2 Criteria for the coalesced bubble . . . 141
7.4.3 Coalescence terms . . . 143
7.5 Fragmentation . . . 148
7.5.1 Fragmentation criteria . . . 148
7.5.2 Criteria for the daughter bubbles . . . 149
7.5.3 Fragmentation terms . . . 149
7.6 The master equation for a bubble distribution . . . 150
7.7 Conserved quantities . . . 151
7.7.1 Conservation of volume . . . 151
7.7.2 Conservation of momentum . . . 152
7.7.3 Conservation of energy . . . 153
7.8 Summary . . . 154

8 Conclusions **159**
8.1 Part I . . . 159
8.2 Part II . . . 161

Appendices **163**

A Comparison between discrete and continuum models **163**

References **166**

List of Figures

1.1 PVT diagrams governing the phase composition in a reservoir. 5
1.2 Schematic of a completed oil well. 7
1.3 Schematic of the production system viewed as a network of components. 9
1.4 IPR and VFP curves describing well performance. 11
1.5 Schematics of flow-regimes for two-phase liquid–gas vertical pipe-flow. 13

2.1 Schematic indicating the two-dimensional normal to the cross-section $\mathbf{n}'$ and the length $\delta n'$. 33
2.2 Schematic for the calculation of the integral in (2.80). 33
2.3 Schematic of a flow regime map. 39

3.1 Oil well domain with boundary conditions. 50
3.2 The relationship between gas volume fraction and pressure in an oil well. 60
3.3 Analytical steady-state solutions for the incompressible–incompressible system. 61
3.4 Analytical steady-state solutions for the incompressible–compressible system. 65

4.1 Gibbs free energy as a function of radius. 71
4.2 Schematic of a nucleated gas bubble on a solid wall. 71
4.3 Steady state solutions for the number of bubbles as a function of surface area. 80
4.4 Steady state solutions for the gas volume fraction and number density of bubbles for varying values of γ. 81
4.5 The exit volume fraction as a function of γ. 81

5.1 Schematic of a section of the one-dimensional domain of bubbles and holes. 89
5.2 Schematic of the discretised one-dimensional circle domain. 91
5.3 Results from the Monte Carlo simulation of nucleation and growth dynamics. 92

5.4 Comparison between the Monte Carlo simulation and discrete formulation of growth dynamics. 95
5.5 Convergence of discrete formulation to the Monte Carlo simulation for varying N. 96
5.6 Relationship between the size domain discretisation and the limit of the discrete formulation. 96
5.7 Numerical solution to the finite domain system for varying values of domain length. 106

6.1 Varying bubble shapes described by the finite-dimensional surface function. 116
6.2 Varying bubble shapes described by the finite-dimensional surface function. 117
6.3 Schematic of a single bubble in a one-dimensional domain defined by (X, η, ξ). 117
6.4 Contour plot for bubble volume. 118
6.5 Schematic of coalescence in (X, η, ξ) configuration space. 120
6.6 Schematic of fragmentation in (X, η, ξ) configuration space. 121
6.7 Performance of averaging process. 124
6.8 Scalability of the system visualised through the volume probability density function. 125
6.9 Scalability of the system visualised through histograms. 125
6.10 Evolving number of bubbles for different initial numbers of bubbles. . 126
6.11 Histogram results for different initial numbers of bubbles. 126
6.12 Evolving number of bubbles for different total volumes of bubbles. . . 127
6.13 Histogram results for different total volumes of bubbles. 128

7.1 Colliding particles. 132
7.2 Schematic of the collisional configuration space between particles. . . 134
7.3 Bubble shape and volume as a function of ξ and η. 138
7.4 Coalescence of bubbles. 140
7.5 Schematic for the evolution of bubbles with horizontal compression only. 143
7.6 Coalescence and fragmentation on the $V(\xi, \eta)$ domain. 145
7.7 Vertical and horizontal fragmentation of bubbles. 148
7.8 Schematic of bubbly and slug flow regimes as probability density functions of volume. 155
7.9 Schematic of a bifurcation diagram in bubble volume–energy space. . 156

I Convergence of continuous formulation to discrete formulation for the volume fractions of holes and bubbles. 165

List of Tables

1.1 Molar composition of various reservoir fluids. 4

2.1 Averaged variables in the one-dimensional two-fluid model. 35

3.1 Dimensional parameters for the homogeneous model. 53
3.2 Dimensionless parameters for the homogeneous model. 54

6.1 List of parameters used in the simulation. 123

Chapter 1

Introduction

This chapter introduces the underlying motivation for this thesis from the oil and gas industry. We will provide the problem statement and context, and conclude with a brief overview of the subsequent chapters outlining the basic structure of the thesis.

Two-phase flow is the simultaneous flow of two fluids in different physical states. These systems are ubiquitous in nature. Examples include geological systems (e.g. volcanoes) and biological systems (e.g. blood flow). Moreover, there are wide-ranging industrial applications, examples of which range from food manufacturing to oil and gas production. This thesis is concerned with two-phase flow through oil wells.

The oil and gas industry use wells to extract liquid and gaseous hydrocarbons from underground stores. The highly combustible nature of hydrocarbons is utilised in many applications including heating systems, transportation fuels and in generating electricity. Aside from energy resources, hydrocarbons are used in construction and in the manufacture of plastics, cosmetics and numerous other industrial products. Their extensive applications make hydrocarbons a valuable resource.

Our motivation to study the flow in oil wells is driven by the industry partner Petrotechnical Data Systems (PDS) — a technical company who develop software for the oil and gas industry. PDS are interested in a deeper understanding of the fluid dynamics throughout the extraction process; this is required to advise optimisation of the end production.

In this chapter we will introduce the physical and geological setting of oil wells, and review the methods used to analyse them.

1.1 Geology of hydrocarbon reservoirs

Hydrocarbons are derived from the remains of organic matter deposited in sedimentary basins. These chemical compounds are primarily made up of hydrogen (H) and carbon (C) atoms. The general chemical formula for a hydrocarbon comprising n carbon atoms is C_nH_{2n+2}. The transformation from organic matter to hydrocarbons takes place over millions of years, and transformation rates depend on the type of organic matter and the thermal history of the area. The process can be considered in three phases; diagenesis, catagenesis and metagenesis.

Diagenesis is the process of initial compaction of organic matter under increasing heat and pressure (temperatures up to 50°C); the end result of which is solid organic matter, known as *kerogen*, held within sedimentary rocks [Hantschel and Kauerauf, 2009]. Kerogen comprises organic matter for which there is no one specific chemical formula. The 'type' of kerogen is identified through concentrations of carbon, hydrogen, oxygen, nitrogen and sulphur, and this is used to predict the potential for hydrocarbon production [Allen and Allen, 2013].

As compaction of the rock continues, and the temperature and pressure increase, the chemical bonds in kerogen are broken down. This occurs at temperatures between 50 to 150°C, and typically at 1 to 3 km underground [Hantschel and Kauerauf, 2009]. This irreversible process is called catagenesis, and the resulting materials are gaseous, liquid and solid hydrocarbons [Allen and Allen, 2013]. The final stage of hydrocarbon formation is metagenesis which involves further bond breakage and occurs at temperatures above 150°C (distinguishing this process from the earlier bond breakage in catagenesis) forming lighter gases (e.g. methane).

Hydrocarbons in gaseous and liquid form are larger in volume than solid kerogen. The hydrocarbons therefore migrate through pores in the rock, driven by high pressures from below, until they escape to the surface or until they are trapped by an impermeable rock layer above. The porous rock stores holding trapped hydrocarbons are called *reservoirs*, and are typically found several kilometres below the Earth's surface [Iske and Randen, 2006].

1.1.1 Locating reservoirs

Finding a reservoir is straightforward enough in cases where the hydrocarbons have escaped to the surface. However, the high demand for oil and gas means that these reservoirs have been mainly exploited already. There is therefore interest in locating oil and gas reservoirs by examining geological subsurface structure. Geological and basin models are used to understand the geological processes that govern the evo-

lution of subsurface rock formations over long time scales [Iske and Randen, 2006]. The models aim to capture the complex processes in reservoir formation: deposition, pressure-driven compaction, heat analysis, petroleum production and migration [Hantschel and Kauerauf, 2009]. These processes are used to predict the whereabouts and size of reservoirs, and to predict the types of hydrocarbons that might be present.

Basin and geological models look at the development of reservoirs. The existing subsurface structure of the Earth may be analysed through seismic imaging. Exploration seismology is the study of the propagation of elastic waves through the Earth's structure. Its aim is to develop a reflectivity distribution that enables prediction of the subsurface structure [Schuster, 2010]. Structural features include the type of rock and presence of hydrocarbon reservoirs. Exploration seismology begins with a source on the Earth's surface that sends seismic waves created by an explosion through the Earth's layers. These waves reflect off interfaces in the rock, scatter and bend back towards the surface, and the waves received back at the source position are recorded. This process is repeated for varying source locations. The recordings are used to solve an inverse problem for the wave equation [Iske and Randen, 2006]. The result is a visualisation of the subsurface geometry, and an indication of the existence and location of reservoirs. Once located, the properties of the fluid held within the porous reservoir rock are tested and analysed to gauge viability of production.

1.1.2 Reservoir fluid properties

A reservoir holds hydrocarbons and water in multiphase mixtures. A *phase* is a physically homogeneous region of fluid that is separated by a defined boundary to other phases. Typically we think of possible phases to include gas, liquid and solid. However, researchers in the oil industry consider hydrocarbon reservoirs to comprise three phases: aqueous, oleic and gaseous. We will, for now, follow this description of three phases. The two liquid phases (aqueous and oleic) are treated as distinct due to their immiscibility. Each of the phases is made up of several distinct *components*. Chen [2007] defines a component to be a single chemical species.

The aqueous phase contains water trapped in the rock pores, and this is often called *formation water*. The components of the aqueous phase are water (H_2O), sodium chloride (NaCl) and dissolved oxygen (O_2). It is typically assumed that H_2O is insoluble in hydrocarbons, implying that H_2O is found only in the aqueous phase [Hantschel and Kauerauf, 2009]. Consequently, there is no assumed mass transfer between the aqueous phase and the oleic or gaseous phases. We note that it is reasonable to take the aqueous phase as incompressible with a constant density.

The oleic phase consists of hydrocarbons in liquid form; and the gaseous phase is

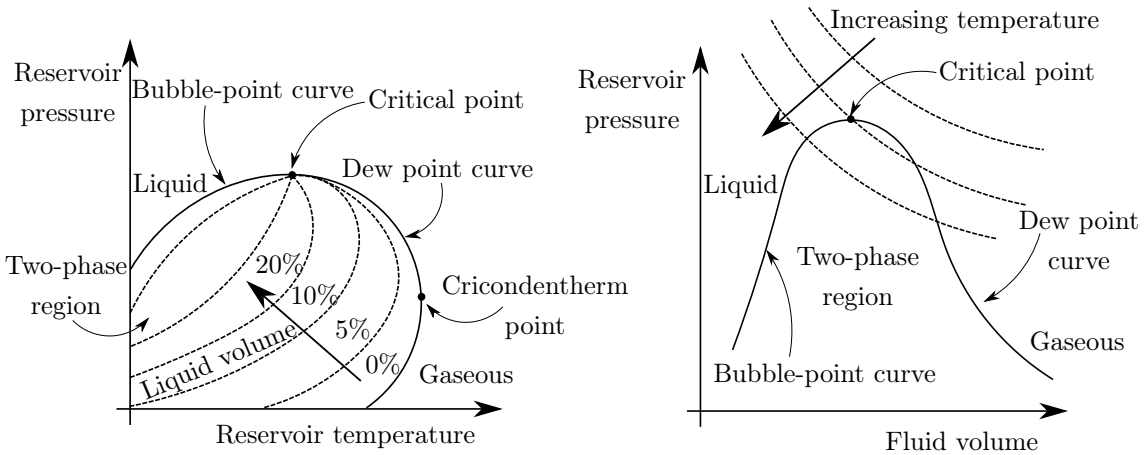
comprised of gaseous hydrocarbons. The phase composition (i.e. which hydrocarbons are present) in a particular reservoir depends on the temperatures and pressures present in the hydrocarbon formation. We detail the chemical composition of four reservoir fluids: dry gas, wet gas, volatile oil and black oil in table 1.1. Dry gas is natural gas that does not produce any sort of liquid oil during the extraction process (e.g. by condensation); wet gas is natural gas that does produce some liquid oil. Volatile oils are liquid hydrocarbons that are brown in colour; and black oils comprise heavier chemical compounds and black viscous liquids [Riaza, 2005].

Component	Reservoir fluid			
	Dry gas	Wet gas	Volatile oil	Black oil
Carbon dioxide (CO_2)	3.70	0.00	1.19	0.09
Nitrogen (N_2)	0.30	0.00	0.51	2.09
Hydrogen sulfide (H_2S)	0.00	0.00	0.00	1.89
Methane (C_1H_4)	96.00	82.28	45.21	29.18
Ethane (C_2H_6)	0.00	9.52	7.09	13.60
Propane (C_3H_8)	0.00	4.64	4.61	9.20
Isobutane (iC_4H_{10})	0.00	0.64	1.69	0.95
n-butane (nC_4H_{10})	0.00	0.96	2.81	4.30
Isopentane (iC_5H_{12})	0.00	0.35	1.55	1.38
n-pentane (nC_5H_{12})	0.00	0.29	2.01	2.60
Hexane (C_6H_{14})	0.00	0.29	4.42	4.32
Heptane plus fraction ($C_{7+}H_{16+}$)	0.00	1.01	28.91	30.40

Table 1.1: Molar composition of various reservoir fluids presented as mole fraction measured as percentage, adapted from Riaza [2005]. The hydrocarbon components have the chemical formula C_nH_{2n+2} for n carbon atoms and $(2n + 2)$ hydrogen atoms.

A given reservoir may contain hydrocarbons in both liquid and gaseous forms; or only a single hydrocarbon phase. Mass transfer between the phases is driven by changing pressure and temperature. The oil and gas industry rely on experimentally derived pressure-volume-temperature (PVT) diagrams to visualise this relationship; see figure 1.1. In a pressure-temperature (PT) diagram, the liquid volume curves identify the conditions at which oil and gas coexist in a saturated reservoir; see figure 1.1a. Below the *cricondentherm point* (T_c, p_c), for temperatures $T < T_c$ and pressures $p < p_c$, liquid and gaseous hydrocarbons coexist. The cricondentherm point indicates the highest temperature at which this is possible. Above the cricondentherm point ($T < T_c$ and $p > p_c$), there is a *dew point* curve which corresponds to the conditions at

which the gas begins to dissolve into the oil. An important feature is the *bubble-point* curve which represents the conditions at which gas begins to be released from the oil. Above the bubble-point curve the reservoir fluid is completely liquid. For a given temperature, as the pressure is reduced below the bubble point, gas will exsolve and liquid and gaseous hydrocarbons coexist. We can use pressure-volume (PV) diagrams, which describe the phase composition for varying temperatures in an analogous way; see figure 1.1b. Hereinafter, we will use the terminology 'water' for the aqueous phase, 'oil' for the liquid hydrocarbons and 'gas' for the gaseous hydrocarbons.



(a) PT diagram **(b)** PV diagram

Figure 1.1: PVT diagrams governing the phase composition in a reservoir.

The thermodynamic properties of the reservoir fluid are modelled by equations of state which prescribe the relationship between the pressure and temperature with volume. A commonly used equation of state for a hypothetical 'ideal' gas is the *ideal gas law*,

$$p_g = \frac{RT_g}{V_g}, \tag{1.1}$$

where p_g is the gas pressure, T_g is the temperature of the gas, V_g is gas molar volume and R is the ideal gas constant [Al-Safran and Brill, 2017]. The ideal gas law (1.1) may equivalently be expressed in terms of gas density ρ_g and molar weight m_g; $p_g = \rho_g RT_g/m_g$. The gas is assumed ideal in the sense that the intermolecular forces are negligible. To account for the compressibility in an equation of state for a 'real' gas, the *real gas law* is

$$p_g = \frac{ZRT_g}{V_g}, \tag{1.2}$$

where the gas compressibility factor Z represents the distinction between a real and

an ideal gas,

$$Z = \frac{V_{real}}{V_{ideal}}; \tag{1.3}$$

here V_{real} and V_{ideal} are the volumes of the real and ideal gases, respectively [Al-Safran and Brill, 2017]. The ideal gas law (1.1) is recovered for $Z = 1$. In practice, values for Z are dependent on the pressure and temperature. There are many other forms of equation of state. Another common choice is the Van der Waals equation which improves the ideal gas law by including intermolecular forces, and improves the real gas law as it does not include the uncertain Z factor; Van der Waals equation is

$$p_g = \frac{RT_g}{V_g - b} - \frac{a}{V_g^2}, \tag{1.4}$$

where a is the intermolecular attraction and b is a measure of the volume of the molecules [Hantschel and Kauerauf, 2009]. PVT diagrams (such as those shown in figure 1.1) are developed using these thermodynamic laws together with empirical data from laboratory testing. Note that the PVT diagrams contain information regarding the phase behaviour, not the components.

1.2 Hydrocarbon extraction

Once the existence and fluid properties of a reservoir are deemed lucrative with sufficient certainty, the extraction process can begin. The basic system comprises the reservoir and numerous deep wells connecting the reservoir to the surface through which the reservoir fluid is extracted. Once on the surface, the fluid travels through a network of pipes to post-processing plants, where the hydrocarbons are separated and stored for their various uses. Here, we introduce the oil well domain, and the various recovery processes used in extraction.

1.2.1 Oil well domain

Oil wells are drilled in stages. First a large hole is drilled, around 10 m long, and a metal casing is introduced and supported with a cement filling; see figure 1.2. A smaller hole is then drilled further down and supported by casing and cement in the same way. This process is repeated until the desired depth is achieved. A production tube is then inserted through the middle of the well surrounded by a supporting annular fluid. The repeated casing and cement aims to avoid unmanaged flow from the reservoir. Furthermore, the structure supports the inner production tubing as the flow is at high temperature and pressure. The *well head* is at the top of the well,

and consists of a size restricting *choke* and several control valves that regulate the pressure and consequently the flow from the well.

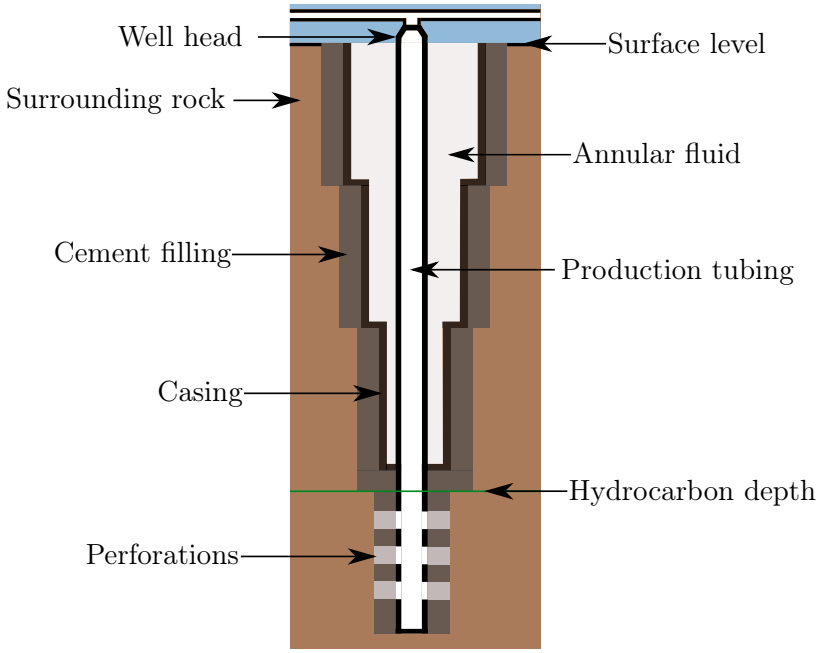


Figure 1.2: Schematic of a completed oil well.

Once a well has been drilled, to allow fluid to flow in and out of it, the tubing is perforated in several places in what is called *well completion* [Iske and Randen, 2006]. The perforation is typically achieved by using a gun to shoot holes through the tubing. Inevitably, the completion will effect the structure of the *near well bore* domain, which will already have been altered by the initial drilling.

We note that wells can be drilled at any angle. Vertical wells are drilled to cover the depth from surface to reservoir. At reservoir depth wells are often drilled at various angles including horizontally, to optimise the reach of the well. Wells are drilled for one of three purposes; exploration, production or injection, and the desired purpose and understanding of the subsurface geology advises the location of drilling. Exploratory wells are drilled to confirm the location of hydrocarbons through sampling. Reservoir fluid is extracted up to the surface through production wells, and these are therefore positioned to optimise the upwell flow, for example in the deeper parts of the reservoir. Injection wells pump fluids (gas or liquid) into the reservoir to encourage flow towards production wells.

1.2.2 Recovery process

Once the well has been completed, production can begin. Initially, the pressure in the reservoir will be significantly higher than the pressure in the oil well. This pressure difference drives the reservoir fluid into the oil well and up to the surface. This initial upward flow of hydrocarbons through the well is called *natural lift*, and is considered to be part of the *primary recovery* process. Over time, due to production, the reservoir pressure will decrease and the pressure gradient will reach hydrostatic equilibrium which results in reduced flow into the well. The flow can be encouraged by means of *artificial lift* systems which aim to increase the local energy in the well [Golan and Whitson, 1991]. The two main methods of artificial lift in a well are pumping and gas lift. Examples of pumping systems are beam pumps ('nodding donkeys') and downhole pumps. Gas lift systems are introduced through the annular fluid around the production well. In such systems gas is injected near the bottom of the pump, thereby reducing the density of the fluid. Both lift mechanisms aim to increase the rate of production by controlling the pressure in the production wells.

Primary recovery relies on the energy in the reservoir and production wells only. However, when the reservoir pressure decreases so much that production rates can not be maintained through primary recovery alone, *secondary recovery* methods are used to increase the reservoir pressure [Muggeridge et al., 2014]. This is achieved through gas or water injection into the reservoir, known as gas-flooding or water-flooding through injection wells. Both methods aim to increase the reservoir pressure to its initial levels and keep it there. Another practical use is that the flooding may displace oil inside the reservoir and encourage flow towards the producing wells.

Primary and secondary recovery only extract around 30% of hydrocarbons from reservoirs. There is therefore a need for *tertiary recovery*, also known as *enhanced oil recovery (EOR)*. These methods aim to increase the mobility of the oil by changing the properties of reservoir fluids. EOR techniques can be classified in three main groups: thermal, chemical and miscible flooding [Muggeridge et al., 2014; Terry, 2001]. An example of thermal EOR is steam injection. Such methods seek to improve mobility through reducing the viscosity of heavy oils. In chemical EOR, compounds are added to the injected fluids to alter the viscosity of the oil, so that it is similar to the viscosity of the injected fluid. Miscible flooding injects a fluid that is miscible with oil, the idea of which is to reduce the interfacial tension between the injected fluid and the reservoir fluid, thereby effectively washing out the trapped oil.

1.3 Industrial modelling of oil wells

It is important to note that at almost every stage in the recovery process, through from predicting the reservoir location to drilling and maintaining the oil wells to the resultant production, there is an issue of uncertainty. As such, the oil and gas industry relies heavily on mathematical modelling of the processes.

As introduced above in Section 1.1.2, reservoir fluid is made up of mixtures of water and hydrocarbons in either gaseous or liquid form, depending on the thermodynamic properties of the reservoir. The flow through the production system is therefore inherently multiphase. This adds the complication of interfacial effects between the multiple fluids. Furthermore, there is clearly a two way coupling between the flow in the reservoir and the flow in the wells, and for a single reservoir there will be multiple wells, both injection and production. The production system therefore becomes very complicated to analyse very quickly. Consequently, industrial models are based on *nodal analysis*, which break down the large system into components connected at nodes [Dale, 1991]; see figure 1.3.

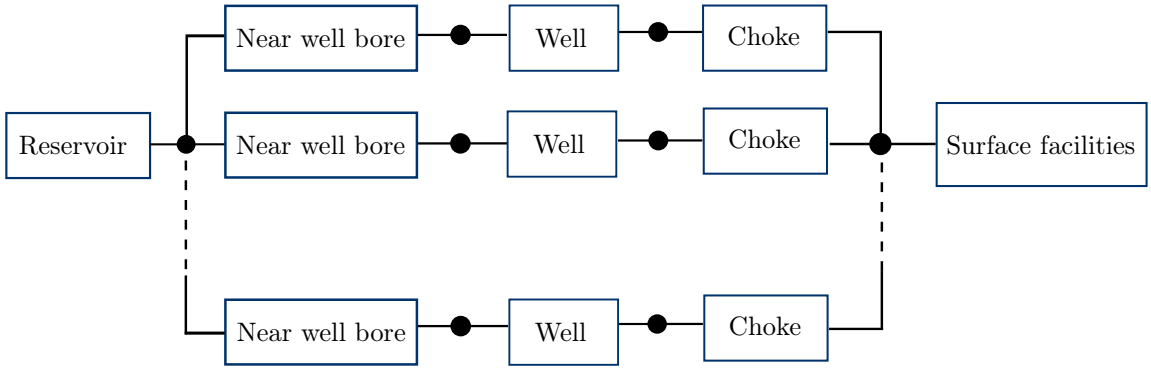


Figure 1.3: Schematic of the production system viewed as a network of components.

Models of the reservoir predict the flow through a large porous domain, often kilometres in diameter. These supply boundary conditions to the near-well-bore domain, which is the linking component between the reservoir and the wells. Near-well-bore models analyse the porous flow in a radial domain localised around the well. The near-well-bore model feeds into the well model, which can be considered as a multiphase pipe-flow. The top of the well links to the choke which is a restricted flow system connecting the subsurface to the surface facilities. The focus of this thesis is on the dynamics of upwelling multiphase flow in the oil well domain.

1.3.1 Oil well performance

Steady state oil well performance is assessed using nodal analysis by comparing the inflow performance relationship (IPR) with the vertical flow performance (VFP). In this instance, the node is the bottom of the well that connects the reservoir to the well. At every node, the flow in is assumed to equal the flow out. At the bottom of the well, the inflow is given by the IPR and the outflow by the VFP. The VFP is therefore also known as the outflow performance relationship (OPR), the tubing head performance (TFP) and the tubing performance curve (TPC).

Consider first the IPR; the flow through the porous reservoir rock is modelled with Darcy's law, so that the flow rate into the well from the reservoir q_{res} is given by

$$q_{res} = k_r(p_{res} - p_{wb}), \tag{1.5}$$

where k_r is a constant related to the permeability of the reservoir rock, p_{res} is the reservoir pressure and p_{wb} is the pressure at the bottom of the well. The IPR therefore corresponds to the *reservoir capability* and can be maintained through secondary and tertiary recovery processes.

Now for the VFP; we assume a Poiseuille-type flow for the flow in the well, so that the flow rate is proportional to the pressure gradient [Batchelor, 1967]. We write the flow rate in the well q_w as

$$q_w = k_w(p_{wb} - p_{ch}), \tag{1.6}$$

where k_w is a constant and p_{ch} is the pressure at the choke. The VFP corresponds to the *well capability* and can be modified by making changes in the well structure, such as including artificial lift systems in the primary recovery.

At the bottom of the well the flow rate q_{wb} must be equal to that for the inflow and the outflow so we have $q_{wb} = q_w = q_{res}$. Plotting the IPR and VFP shows the point at which the two curves meet and the flow rate is balanced; this point is called the *operating point* of the well; see figure 1.4.

If the curves do not intersect, it is assumed that the system cannot be operated to produce hydrocarbons. The objective of these plots is to relate the well and reservoir performance. They allow engineers to understand when and how it is necessary to consider measures to maintain or optimise the well deliverability. Graphically, optimising the well deliverability corresponds to shifting the intersection of the two curves to the bottom right corner of the performance curve; that is to maximise the flow rate whilst minimising the pressure under given reservoir and surface constraints.

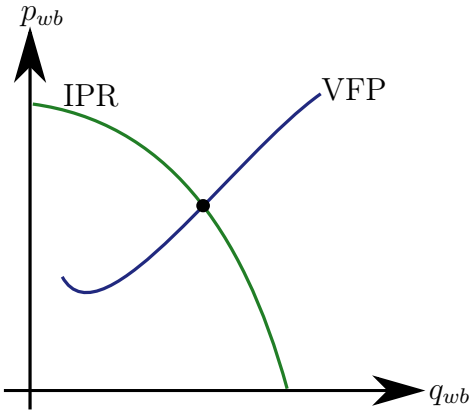


Figure 1.4: IPR and VFP curves describing well performance.

1.3.2 Oil well models

The IPR curve is predicted from reservoir models, whilst the VFP curve is informed by well models. The term 'well model' covers a variety of modelling methods used to understand the multiphase flow through the well. Modelling techniques include empirical models constructed from data and physics-based methods. These methods are distinguished by how the derivation depends on fundamental laws of physics, and also whether they are steady in time or transient.

In the past, the common practice in the industry was to use empirical models known as *correlations*, such as those by Poettman and Carpenter [1952], Hagedorn and Brown [1965], Duns Jr and Ros [1963] and Beggs and Brill [1973]. These steady state models are constructed from data collected from a particular well or artificial set up. They are commonly used to determine VFP curves in order to determine the operating point of the well. If the well system is held constant in time, steady state models can advise how to optimise the steady production through the analysis of the well performance (VFP and IPR) curves. However, applicability of these models is greatly limited as the results are reliable only for the specific system from which the data were collected. Accuracy can also be a problem, as these models are not governed by the laws of physics but are fitted to experimental data, the validity of which may be questionable.

In recent years, there has been a move towards 'physics-based' modelling of oil wells [Shippen and Bailey, 2012]; but in practice, it is common for a combination of empirical and physics-based methods to be used. The shift away from empirical models to physics-based approaches is thanks in part to the greater simulation capabilities of modern computers.

For the majority of the lifetime of the well, the dynamics are assumed to be at

steady state, and thus steady state models like those derived by Taitel and Dukler [1976], Ansari et al. [1990] and Cazarez-Candia and Vásquez-Cruz [2005] are utilised. Transient models, such as those by Livescu et al. [2010] and Bendiksen et al. [1991], are used in the initial start up of the well and when changes are being made to the system, for example the introduction of an artificial lift system.

The fluid in the well is composed of water, oil and gas. These can be treated as three separate fluids in a 'three-phase' flow model such as that by Livescu et al. [2010] and Cazarez et al. [2010]. However, the physical properties of oil and water are much closer to each other than they are to those of gas, and so treating the oil and water as a single liquid phase is a reasonable simplification. In this thesis, we therefore consider a two-phase liquid–gas flow.

1.4 Two-phase flow

We reserve the main discussion of two-phase flow for Chapter 2. However, we note that there are many examples of two-phase flows in nature and in everyday systems that are analogous to oil wells. In an oil well, as the pressure decreases, dissolved gaseous hydrocarbons come out of solution. We highlight the analogy of such a two-phase flow with that in boilers and volcanoes. In boiling systems, the flow is heated to boiling point by an external wall temperature. This causes nucleation of gas bubbles as steam is produced. A gaseous phase is also released in a volcano due to exsolution from the liquid magma [Fowler and Robinson, 2018].

1.4.1 Two-phase flow regimes

A clear distinction between two-phase and single phase flow is the presence of interfaces separating the phases. The dynamics of single phase flows are influenced by the structural geometry of the environment and the type of flow; for example, laminar or turbulent. Two-phase mixtures are more complex, as the flow of each fluid is affected by the presence of the other fluid. Brennen [2005] defines a two-way coupling between the *geometry of the flow* and the flow of the different phases. These particular geometries govern the distribution of the components in two-phase mixtures, and are known as *flow regimes* or *flow patterns*. Flow regimes describe the macroscopic flow, and are distinguished and best understood through visualisation.

The two-phase liquid–gas flow in vertical pipes can be categorised into five distinct flow regimes; bubbly, slug, churn, annular and mist flow, as shown in figure 1.5. A system in one regime can undergo a transition into another regime; for example,

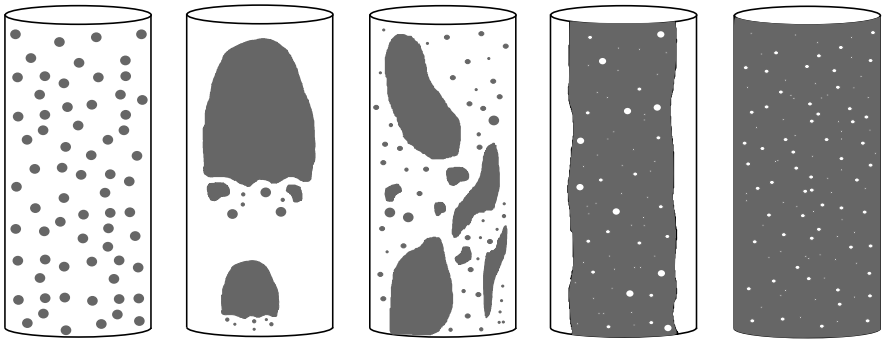


Figure 1.5: Schematics of flow-regimes for two-phase liquid–gas vertical pipe-flow. Gas is shown in grey, and the white depicts the liquid phase.

increasing the gas flow rate in a bubbly flow drives a transition to slug flow. The dynamics driving transitions between the flow regimes are not well understood, but a common hypothesis is that an instability of a flow regime results in a transition [Fowler, 2011].

It is understood that in an oil well the two-phase flow can occur in any flow regime. In particular, as the dissolved gas exsolves, a bubbly-to-slug transition is likely to occur. The sudden impact of a heavy liquid slug in the oil well structure can be damaging, and controls to avoid the bubbly-to-slug flow transition are beneficial.

1.5 Overview

The work in this thesis is focused on two-phase liquid–gas flow through vertical pipes. In Chapter 2, we review modelling approaches for two-phase flow. In the subsequent chapters, the work can be considered in two largely self-contained parts. First, in Part I, comprising Chapters 3 and 4, we examine the flow through an oil well. In Chapter 3, we present a mathematical model of the two-phase liquid and gas mixtures driven upwards through an oil well due to a pressure gradient, and explicitly account for the exsolution of the dissolved gas as the pressure decreases along the well. We find that the application of Henry's law for the dissolved gas concentration predicts a rapid transition to a foam, which runs counter-to-intuition. In order to study ways in which this rapid transition could be avoided, we examine rate limiting non-equilibrium dynamics by incorporating nucleation and bubble growth dynamics in a two-phase model in Chapter 4.

When examining two-phase pipe flow one cannot avoid the issue of flow regime transitions, the dynamics of which are not well understood. In Chapter 2, we discuss

the current methods used for studying flow regime transitions, and outline the scope for novel ideas in this area. This motivates the second part of this thesis; in Chapters 5, 6 and 7, which make up Part II, we turn our attention to the big question of how to model the bubbly-to-slug flow regime transition. We aim to derive a kinetic-theory-based model of evolving bubble distributions to address this question.

The key processes governing the bubbly-to-slug regime transition are bubble coalescence (the merging of multiple bubbles) and bubble fragmentation (the splitting up of a single bubble). In Chapter 5, we consider a simple model that is similar, in some respects, to the model of bubbles that we seek. To this end, we study one-dimensional nucleation, growth and coalescence of bubbles in a liquid domain. We derive the governing equations from first principles, and analyse the resulting model in a finite domain and in the limit of an infinite domain. We establish the criteria necessary for ensuring that the appropriate conservation laws hold.

It is clear that the shape of individual bubbles is important in coalescence and fragmentation. In Chapter 6 we therefore consider how to include higher dimensions in a model formulation for bubble evolution. More specifically, we define a shape variable that tracks the evolution of the bubble shape. We incorporate this into a simulation of a system of bubbles, and examine the resulting distribution of bubble volumes.

Finally, in Chapter 7, we build on ideas developed in Chapters 5 and 6 to derive a master equation which describes the evolution for the shapes, sizes and positions of a bubble population. We adapt the ideas used in the derivation of the Boltzmann equation applied to stochastic processes, and present the appropriate derivation for the master equation that accounts for fragmentation and coalescence of bubbles. This provides the foundation for the study of the bubble dynamics in the bubbly-to-slug flow regime transition.

Chapter 2

Modelling two-phase flow

This chapter provides the relevant literature review for general two-phase flow modelling. We discuss the averaging techniques used for continuum modelling of two-phase flows, and outline the three classical modelling approaches; homogeneous, drift-flux and two-fluid. Discussion will be presented for the necessary closure framework comprising equations of state and extensive constitutive closure laws. This initial review of two-phase models leads us to consider the identification of flow regimes, and in particular the transition between them.

2.1 Introduction

There has been substantial research into the mathematical modelling of two-phase flows [Brennen, 2005; Shoham, 2006; Drew and Passman, 2006; Ishii and Hibiki, 2010; Al-Safran and Brill, 2017]. One of the largest difficulties in two-phase modelling is the existence of numerous distinct single-phase regions bound by evolving interfaces (think of gas bubbles moving in a liquid), the positions of which are unknown. Capturing all this detail on the microscopic level is highly complicated and, as such, there is a need for *averaging*. Appropriate averaging of the local flow properties describes the macroscopic flow. Drew and Lahey [1979] note that this averaging filters unnecessary details of flow. However, the lost information comes at the cost of under-determined equations that require constitutive relations for closure [Aldridge and Fowler, 1996].

In this chapter, we will discuss the averaging methods used for two-phase flows in Section 2.2, and introduce the general governing equations for two-phase flow together with the necessary closure framework in Section 2.3. There are three typical modelling approaches derived from the general governing equations, which we discuss

in Sections 2.4–2.6. It is important to note that the models discussed are developed for individual flow regimes and as the flow evolves from one regime to another, the system undergoes a *transition*. We will talk about the definition and identification of a regime, the dependence on regimes in the modelling and how one may model the transition between regimes in Section 2.7.

2.2 Averaging methods

The governing equations for two-phase flow models are derived from conservation of mass, momentum and energy. The general conservation equation for an arbitrary conserved quantity ψ is

$$\frac{\partial}{\partial t}(\rho\psi) + \boldsymbol{\nabla} \cdot (\rho\psi\mathbf{v}) = -\boldsymbol{\nabla} \cdot \mathbf{J} + \rho f, \tag{2.1}$$

where ρ is the density, $\mathbf{v}$ the velocity, $\mathbf{J}$ the flux and f a source term. We need to account for the conserved quantities for each phase separated by interfaces; the exact location of these interfaces is uncertain [Drew and Passman, 2006]. Averaging is used to smooth the local microscopic field over spatial or temporal regions. Aldridge and Fowler [1996] note that averaging relies on the underlying assumption that there exists an intermediate averaging scale that is larger than the microscopic scale, in order to smooth local variations, but smaller than the overall macroscopic scale of interest.

We consider ensemble averaging methods for an exact microscopic function $h(\mathbf{x}, t)$ defined on the domain $\mathbf{x} \in \mathbb{R}^3$ at time $t \in \mathbb{R}$ and denote the associated averaged quantity with angled brackets. *Ensemble averaging* is defined as the average over the set of all possible states of the system; where the ensemble is the set of possible realisations. Drew [1982] introduced the following ensemble averages:

$$\langle h(\mathbf{x}, t)\rangle = \frac{1}{N}\sum_{n=1}^{N} h_n(\mathbf{x}, t), \tag{2.2a}$$

$$\langle h(\mathbf{x}, t)\rangle = \int_{\Omega} h(\mathbf{x}, t; \omega)\, \mathrm{d}\mu(\omega), \tag{2.2b}$$

where $h_n(\mathbf{x}, t)$ and $h(\mathbf{x}, t; \omega)$ denote a single realisation of the quantity $h(\mathbf{x}, t)$, N denotes the number of possible realisations, Ω denotes the set of all possible realisations, ω is a specific realisation and $\mathrm{d}\mu(\omega)$ is a probability measure of realising ω. In our application of liquid–gas mixtures, we will assume ensemble averaging in order to average over the different interfacial configurations of the two phases.

Averaging processes satisfy Reynolds' rules:

$$\langle h + g \rangle = \langle h \rangle + \langle g \rangle, \tag{2.3a}$$

$$\langle \langle h \rangle g \rangle = \langle h \rangle \langle g \rangle, \tag{2.3b}$$

$$\langle c \rangle = c, \tag{2.3c}$$

where h and g are exact microscopic fields, and c is a constant. Averaging processes are further assumed to satisfy Leibniz's rule and Gauss's rule which are, respectively,

$$\left\langle \frac{\partial h}{\partial t} \right\rangle = \frac{\partial}{\partial t} \langle h \rangle, \tag{2.4}$$

$$\left\langle \frac{\partial h}{\partial x_i} \right\rangle = \frac{\partial}{\partial x_i} \langle h \rangle. \tag{2.5}$$

Whilst time and volume averages are commonly used, they fail to satisfy (2.3b) so are in fact not valid averages and will not be discussed here.

To isolate each phase, we require an indicator function $X_k(\mathbf{x}, t)$ for the k^{th} phase, defined to be

$$X_k(\mathbf{x}, t) = \begin{cases} 1, & \text{if } \mathbf{x} \text{ is in phase } k \text{ at time } t, \\ 0, & \text{otherwise.} \end{cases} \tag{2.6}$$

In this thesis we consider two phases, liquid and gas, denoted by the subscripts $k = l,\ g$ respectively. Drew [1982] notes that the function X_k should be considered as a *generalised function*, also known as a *distribution*. This approach enables differentiation of X_k and consequently we can write down a conservation equation for X_k:

$$\frac{\partial X_k}{\partial t} + \mathbf{v}_i \cdot \boldsymbol{\nabla} X_k = 0, \tag{2.7}$$

where $\mathbf{v}_i$ is the velocity of the interface. Multiplying (2.1) by X_k gives

$$X_k \left[\frac{\partial}{\partial t}(\rho\psi) + \boldsymbol{\nabla} \cdot (\rho\psi\mathbf{v}) \right] = -X_k \boldsymbol{\nabla} \cdot \mathbf{J} + X_k \rho f. \tag{2.8}$$

Note that from (2.7) we have

$$X_k \frac{\partial}{\partial t}(\rho\psi) = \frac{\partial}{\partial t}(X_k \rho\psi) + \rho_{ki}\psi_{ki}\mathbf{v}_i \cdot \boldsymbol{\nabla} X_k, \tag{2.9a}$$

$$X_k \boldsymbol{\nabla} \cdot (\rho\psi\mathbf{v}) = \boldsymbol{\nabla} \cdot (X_k \rho\psi\mathbf{v}) - \rho_{ki}\psi_{ki}\mathbf{v}_{ki} \cdot \boldsymbol{\nabla} X_k, \tag{2.9b}$$

where the subscript ki denotes the variables on the k^{th}-phase-side of the interface between phases. We note that (2.9b) comes from (2.7) and is a consequence of

treating X_k as a distribution function. Using (2.9) in (2.8) and averaging yields the averaged conservation equation for the conserved quantity ψ:

$$\frac{\partial}{\partial t}\langle X_k\rho\psi\rangle + \boldsymbol{\nabla}\cdot\langle X_k\rho\psi\mathbf{v}\rangle = -\boldsymbol{\nabla}\cdot\langle X_k\mathbf{J}\rangle + \langle X_k\rho f\rangle + \langle(\rho_{ki}\psi_{ki}(\mathbf{v}_{ki}-\mathbf{v}_i)+\mathbf{J}_{ki})\cdot\boldsymbol{\nabla}X_k\rangle. \tag{2.10}$$

For mass conservation $\psi = 1$, $\mathbf{J} = 0$, $f = 0$ so the averaged equation is

$$\frac{\partial}{\partial t}\langle X_k\rho\rangle + \boldsymbol{\nabla}\cdot\langle X_k\rho\mathbf{v}\rangle = \langle\rho_{ki}(\mathbf{v}_{ki}-\mathbf{v}_i)\cdot\boldsymbol{\nabla}X_k\rangle. \tag{2.11}$$

Similarly for momentum conservation $\psi = \mathbf{v}$, $\mathbf{J} = -\mathbf{T}$, $f = \mathbf{g}$, where $\mathbf{T}$ is the stress tensor and $\mathbf{g}$ denotes acceleration due to gravity. Note that the stress tensor $\mathbf{T}$ is

$$\mathbf{T} = -p\mathbf{I} + \boldsymbol{\tau}, \tag{2.12}$$

where p is pressure, $\mathbf{I}$ is the identity matrix and $\boldsymbol{\tau}$ is the shear stress tensor. From (2.10), the averaged momentum conservation equation is

$$\frac{\partial}{\partial t}\langle X_k\rho\mathbf{v}\rangle+\boldsymbol{\nabla}\cdot\langle X_k\rho\mathbf{v}\mathbf{v}\rangle = \boldsymbol{\nabla}\cdot\langle X_k\mathbf{T}\rangle+\langle X_k\rho\mathbf{g}\rangle+\langle(\rho_{ki}\mathbf{v}_{ki}(\mathbf{v}_{ki}-\mathbf{v}_i)-\mathbf{T}_{ki})\cdot\boldsymbol{\nabla}X_k\rangle. \tag{2.13}$$

For energy conservation, we have $\psi = e$, $\mathbf{J} = \mathbf{q}$, $\rho f = \mathbf{T}\colon\boldsymbol{\nabla}\mathbf{v}$, where e denotes the internal energy and $\mathbf{q}$ is the heat flux. The averaged equation of conservation of internal energy is therefore given by

$$\begin{aligned}\frac{\partial}{\partial t}\langle X_k\rho e\rangle + \boldsymbol{\nabla}\cdot\langle X_k\rho e\mathbf{v}\rangle = &-\nabla\cdot\langle X_k\mathbf{q}\rangle + \langle X_k\mathbf{T}\colon\boldsymbol{\nabla}\mathbf{v}\rangle \\ &+\langle(\rho_{ki}e_{ki}(\mathbf{v}_{ki}-\mathbf{v}_i)+\mathbf{q}_{ki})\cdot\boldsymbol{\nabla}X_k\rangle.\end{aligned} \tag{2.14}$$

In (2.11), (2.13) and (2.14) we have terms that account for interfacial quantities. Drew [1982] introduces the following notation for these interfacial terms,

$$\Gamma_k = \langle\rho_{ki}(\mathbf{v}_{ki}-\mathbf{v}_i)\cdot\boldsymbol{\nabla}X_k\rangle, \tag{2.15a}$$

$$\tilde{\mathbf{v}}_{ki} = \frac{\langle\rho_{ki}\mathbf{v}_{ki}(\mathbf{v}_{ki}-\mathbf{v}_i)\cdot\boldsymbol{\nabla}X_k\rangle}{\langle\rho_{ki}(\mathbf{v}_{ki}-\mathbf{v}_i)\cdot\boldsymbol{\nabla}X_k\rangle}, \tag{2.15b}$$

$$\mathbf{M}_k = \langle-\mathbf{T}_{ki}\cdot\boldsymbol{\nabla}X_k\rangle. \tag{2.15c}$$

Note that Γ_k is the mass transfer between phases. The interfacial momentum source in (2.13) separates into the diffusive flux $\mathbf{M}_k$ and the convective flux $\tilde{\mathbf{v}}_{ki}\Gamma_k$. In an analogous way, we denote the interfacial terms in the energy equation (2.14) as

$$\tilde{e}_{ki} = \frac{\langle\rho_{ki}e_{ki}(\mathbf{v}_{ki}-\mathbf{v}_i)\cdot\boldsymbol{\nabla}X_k\rangle}{\langle\rho_{ki}(\mathbf{v}_{ki}-\mathbf{v}_i)\cdot\boldsymbol{\nabla}X_k\rangle}, \tag{2.16a}$$

$$\tilde{q}_{ki} = \langle\mathbf{q}_{ki}\cdot\boldsymbol{\nabla}X_k\rangle, \tag{2.16b}$$

where $\tilde{e}_{ki}$ is the interfacial internal energy source and $\tilde{q}_{ki}$ is the interfacial heat transfer.

A key variable in modelling two-phase flow is the *volume fraction* of each phase defined as the average of the indicator function:

$$\alpha_k = \langle X_k \rangle. \tag{2.17}$$

There exist two different averaged quantities: volume averaged and mass averaged denoted $\hat{\psi}$ and $\overline{\psi}$ respectively. These are defined by:

$$\hat{\psi}_k = \frac{\langle X_k \psi \rangle}{\alpha_k}, \tag{2.18a}$$

$$\overline{\psi}_k = \frac{\langle X_k \rho \psi \rangle}{\hat{\rho}_k \alpha_k}. \tag{2.18b}$$

Using the notation introduced above in (2.11), (2.13) and (2.14) we arrive at the averaged conservation equations for the k^{th} phase:

$$\frac{\partial}{\partial t}(\alpha_k \hat{\rho}_k) + \boldsymbol{\nabla} \cdot (\alpha_k \hat{\rho}_k \overline{\mathbf{v}}_k) = \Gamma_k, \tag{2.19a}$$

$$\frac{\partial}{\partial t}(\alpha_k \hat{\rho}_k \overline{\mathbf{v}}_k) + \boldsymbol{\nabla} \cdot (\alpha_k \hat{\rho}_k \overline{\mathbf{v}}_k \overline{\mathbf{v}}_k) = \boldsymbol{\nabla} \cdot [\alpha_k (\hat{\mathbf{T}}_k + \mathbf{T}'_k)] + \alpha_k \hat{\rho}_k \mathbf{g} + \tilde{\mathbf{v}}_{ki} \Gamma_k + \mathbf{M}_k, \tag{2.19b}$$

$$\frac{\partial}{\partial t}(\alpha_k \hat{\rho}_k \overline{e}_k) + \boldsymbol{\nabla} \cdot (\alpha_k \hat{\rho}_k \overline{e}_k \overline{\mathbf{v}}_k) = -\nabla \cdot [\alpha_k (\hat{\mathbf{q}}_k + \mathbf{q}'_k)] + \alpha_k \phi_k + \tilde{e}_{ki} \Gamma_k + \tilde{q}_{ki}, \tag{2.19c}$$

where $\mathbf{T}'_k$ is a Reynolds stress defined by [Fowler, 2011]

$$\langle X_k \rho \mathbf{v}\mathbf{v} \rangle = \alpha_k \hat{\rho}_k \overline{\mathbf{v}}_k \overline{\mathbf{v}}_k - \alpha_k \mathbf{T}'_k, \tag{2.20}$$

and $\mathbf{q}'_k$ is the turbulent heat transfer defined by

$$\langle X_k \rho e \mathbf{v} \rangle = \alpha_k \hat{\rho}_k \overline{e}_k \overline{\mathbf{v}}_k + \alpha_k \mathbf{q}'_k. \tag{2.21}$$

We have also introduced a viscous dissipation term in the energy conservation equation (2.19c) defined as

$$\phi_k = \frac{\langle X_k \mathbf{T} \colon \boldsymbol{\nabla} \mathbf{v} \rangle}{\alpha_k}. \tag{2.22}$$

It is common to rewrite the energy equation (2.19c) in terms of enthalpy $h = e + p/\rho$. The averaged enthalpy for each phase is

$$\overline{h}_k = \overline{e}_k + \frac{\hat{p}_k}{\hat{\rho}_k}. \tag{2.23}$$

Using this in (2.19c) the enthalpy conservation equation is

$$\begin{aligned} \frac{\partial}{\partial t}(\alpha_k \hat{\rho}_k \overline{h}_k) + \boldsymbol{\nabla} \cdot (\alpha_k \hat{\rho}_k \overline{h}_k \overline{\mathbf{v}}_k) = \alpha_k \left(\frac{\partial \hat{p}_k}{\partial t} + \overline{\mathbf{v}}_k \cdot \boldsymbol{\nabla} \hat{p}_k \right) - \nabla \cdot [\alpha_k (\hat{\mathbf{q}}_k + \tilde{\mathbf{q}}'_k)] \\ + \alpha_k \tilde{\phi}_k + \tilde{h}_{ki} \Gamma_k + \tilde{q}_{ki}, \end{aligned} \tag{2.24}$$

where the turbulent heat transfer $\tilde{\mathbf{q}}'_k$ can now be defined in terms of the enthalpy:

$$\langle X_k \rho h \mathbf{v} \rangle = \alpha_k \hat{\rho}_k \overline{h}_k \overline{\mathbf{v}}_k + \alpha_k \tilde{\mathbf{q}}'_k, \tag{2.25}$$

and using (2.12), the viscous dissipation is written in terms of the shear stress τ:

$$\tilde{\phi}_k = \frac{\langle X_k \tau \colon \boldsymbol{\nabla} \mathbf{v} \rangle}{\alpha_k}. \tag{2.26}$$

The interfacial enthalpy term $\tilde{h}_{ki}$, in an analogous way to the interfacial energy term (2.16a), is

$$\tilde{h}_{ki} = \frac{\langle \rho_{ki} h_{ki} (\mathbf{v}_{ki} - \mathbf{v}_i) \cdot \boldsymbol{\nabla} X_k \rangle}{\langle \rho_{ki} (\mathbf{v}_{ki} - \mathbf{v}_i) \cdot \boldsymbol{\nabla} X_k \rangle}. \tag{2.27}$$

The averaged conservation equations (2.19c) for mass, momentum and energy in terms of enthalpy for the k^{th} phase therefore become

$$\frac{\partial}{\partial t}(\alpha_k \hat{\rho}_k) + \boldsymbol{\nabla} \cdot (\alpha_k \hat{\rho}_k \overline{\mathbf{v}}_k) = \Gamma_k, \tag{2.28a}$$

$$\frac{\partial}{\partial t}(\alpha_k \hat{\rho}_k \overline{\mathbf{v}}_k) + \boldsymbol{\nabla} \cdot (\alpha_k \hat{\rho}_k \overline{\mathbf{v}}_k \overline{\mathbf{v}}_k) = \boldsymbol{\nabla} \cdot [\alpha_k (\hat{\mathbf{T}}_k + \mathbf{T}'_k)] + \alpha_k \hat{\rho}_k \mathbf{g} + \tilde{\mathbf{v}}_{ki} \Gamma_k + \mathbf{M}_k, \tag{2.28b}$$

$$\frac{\partial}{\partial t}(\alpha_k \hat{\rho}_k \overline{h}_k) + \boldsymbol{\nabla} \cdot (\alpha_k \hat{\rho}_k \overline{h}_k \overline{\mathbf{v}}_k) = \alpha_k \left(\frac{\partial \hat{p}_k}{\partial t} + \overline{\mathbf{v}}_k \cdot \boldsymbol{\nabla} \hat{p}_k \right) - \nabla \cdot [\alpha_k (\hat{\mathbf{q}}_k + \tilde{\mathbf{q}}'_k)] + \alpha_k \tilde{\phi}_k + \tilde{h}_{ki} \Gamma_k + \tilde{q}_{ki}. \tag{2.28c}$$

The system of equations (2.28) for $k = l,\, g$ governs conservation within each phase. Mass, momentum and energy must also be conserved between the phases, and as such we need to consider jump conditions [Drew and Passman, 2006].

2.2.1 Jump conditions

We can see from (2.10) that the interfacial terms for the conserved quantity ψ, with flux $\mathbf{J}$, are of the form

$$\langle [\rho_{ki} \psi_{ki} (\mathbf{v}_{ki} - \mathbf{v}_i) + \mathbf{J}_{ki}] \cdot \boldsymbol{\nabla} X_k \rangle = 0. \tag{2.29}$$

Thus using the definition of Γ_k in (2.15a), it is clear that to ensure that no mass is created or lost at the interface (i.e. conservation of mass between the phases) we require the following interfacial jump condition

$$\sum_{k=l,\,g} \Gamma_k = 0. \tag{2.30}$$

Similarly, from the definitions of $\tilde{\mathbf{v}}_{ki}$ and $\mathbf{M}_k$ in (2.15b) and (2.15c) respectively, the conservation of interfacial momentum is

$$\sum_{k=l,\,g} (\tilde{\mathbf{v}}_{ki} \Gamma_k + \mathbf{M}_k) = \mathbf{M}_m, \tag{2.31}$$

where $\mathbf{M}_m$ is the momentum source due to changes of the interfaces.

The energy equation, however, requires different treatment. We need to consider the total energy $\psi = \frac{1}{2}v^2 + e$ with $\mathbf{J} = -\mathbf{T}\cdot\mathbf{v} + \mathbf{q}$, so the corresponding interfacial terms from (2.29) are

$$\left\langle \left[\rho_{ki}\left(\tfrac{1}{2}v_{ki}^2 + e_{ki}\right)(\mathbf{v}_{ki} - \mathbf{v}_i) - \mathbf{T}_{ki}\cdot\mathbf{v}_{ki} + \mathbf{q}_{ki}\right]\cdot\boldsymbol{\nabla}X_k\right\rangle = 0, \tag{2.32}$$

with speed $v_{ki} = \sqrt{\mathbf{v}_{ki}\cdot\mathbf{v}_{ki}}$ contributing to kinetic energy. The jump condition for the total energy is therefore

$$\sum_{k=l,\,g}\left[\Gamma_k\left(\tilde{e}_{ki} + \tfrac{1}{2}(v_{ki}^e)^2\right) + \tilde{q}_{ki} + W_k\right] = E_m, \tag{2.33}$$

where the interfacial kinetic energy source and interfacial work done are, respectively, defined by

$$(v_{ki}^e)^2 = \frac{\langle\rho_{ki}v_{ki}^2(\mathbf{v}_{ki} - \mathbf{v}_i)\cdot\boldsymbol{\nabla}X_k\rangle}{\langle\rho_{ki}(\mathbf{v}_{ki} - \mathbf{v}_i)\cdot\boldsymbol{\nabla}X_k\rangle}, \tag{2.34a}$$

$$W_k = -\langle\mathbf{T}_{ki}\cdot\mathbf{v}_{ki}\cdot\boldsymbol{\nabla}X_k\rangle, \tag{2.34b}$$

where the total energy source due to the evolving interfaces is E_m. When working with enthalpy, we replace $\tilde{e}_{ki}$ with $\tilde{h}_{ki}$ in (2.33).

2.3 Closure framework

The conservation equations (2.28a)–(2.28c) together with the jump conditions (2.30)–(2.33) give an under-determined system with more unknowns than equations. For two phases, (2.28) and (2.30)–(2.33) constitute nine equations for the unknowns: $\{\alpha_k,\ \hat{\rho}_k,\ \overline{\mathbf{v}}_k,\ \hat{p}_k,\ \overline{h}_k,\ \Gamma_k,\ \mathbf{T}_k,\ \mathbf{T}'_k,\ \tilde{\mathbf{v}}_{ki},\ \mathbf{M}_k,\ \hat{\mathbf{q}}_k,\ \tilde{\mathbf{q}}'_k,\ \tilde{\phi}_k,\ \tilde{h}_{ki},\ \tilde{q}_{ki},\ v_{ki}^e,\ W_k\}$ with $k = l,\ g$. The system must therefore be supplemented with additional equations through assumed constitutive relations and equations of state. Initial and boundary conditions are also required for closure. There is a large literature attempting to determine these closure laws [Drew and Wood, 1985; Brennen, 2005; Shoham, 2006; Ishii and Hibiki, 2010; Al-Safran and Brill, 2017; Drew, 1982; Drew and Lahey, 1979; Ishii and Mishima, 1984; Hibiki and Ishii, 2000]. In this section we will work through the necessary closure framework to conclude a system of twelve equations for twelve key variables $\{\alpha_k,\ \hat{\rho}_k,\ \overline{\mathbf{v}}_k,\ \hat{p}_k,\ \overline{h}_k,\ \Gamma_k\}$ with $k = l,\ g$.

2.3.1 Volume fraction condition

A trivial additional equation arises from the fact that the volume fractions must sum to unity:

$$\alpha_g + \alpha_l = 1. \tag{2.35}$$

This relates to the total space being occupied by one of the two phases only.

2.3.2 Equations of state

The densities are assumed to satisfy equations of state. The liquid phase is generally assumed to be incompressible, and thus $\hat{\rho}_l$ is an assumed known constant. The gaseous phase is taken to satisfy some prescribed gas law. As mentioned earlier in Chapter 1, the *ideal gas law* is

$$\hat{\rho}_g = \frac{m_g \hat{p}_g}{R\overline{T}_g}, \tag{2.36}$$

where m_g is the molecular mass of the gas, R is the universal gas constant and $\overline{T}_g$ is the gas temperature (this is analogous to (1.1)). We note that this does not introduce new variables to the system as the average temperature of the k^{th} phase, $\overline{T}_k$ is related to enthalpy by

$$\mathrm{d}\overline{h}_k = c_{pk}\,\mathrm{d}\overline{T}_k, \tag{2.37}$$

where c_{pk} is the specific heat capacity at constant pressure [Fowler, 2011].

The ideal gas law is derived from the assumption that the gas molecules have zero volume and any attractive or repulsive intermolecular forces are negligible. However, these assumptions break down at high pressures where the gas molecules are packed more closely together and their volume becomes important [Al-Safran and Brill, 2017]. To model 'real' gases at reservoir conditions, empirical corrections to the gas law are made to give the *real gas law* (as given in (1.2)):

$$\hat{\rho}_g = \frac{m_g \hat{p}_g}{ZR\overline{T}_g}, \tag{2.38}$$

where Z is the gas deviation factor or the gas compressibility factor, and is found through experimental evidence.

2.3.3 Pressure difference

Typically one assumes a relationship between the pressures. If the interface between phases is considered to have zero mass then the pressure difference across the interface must balance the effective pressure due to surface tension [Batchelor, 1967]:

$$\hat{p}_g - \hat{p}_l = 2\gamma\kappa, \tag{2.39}$$

where γ is surface tension and κ is the average mean curvature of the surface. These parameters are not easily accessible, particularly when the interfacial surface is evolving and γ and κ become variables of the system. To avoid this complication, we prescribe a constitutive law for the pressure difference.

The simplest approach is to assume $\hat{p}_g = \hat{p}_l$. This however can result in an ill-posed problem. Alternatively, Stuhmiller [1977] examines inviscid flow around a spherical gas bubble in a continuous liquid domain to derive the following pressure difference:

$$\hat{p}_g - \hat{p}_l = -H\hat{\rho}_l|\overline{\mathbf{v}}_g - \overline{\mathbf{v}}_l|^2, \tag{2.40}$$

where H is a constant. For spherical bubbles $H = \frac{1}{4}$ [Pauchon and Banerjee, 1986], and for simplicity, in what is already becoming a complex system of equations, we will assume $H = \frac{1}{4}$ hereinafter. We will examine the effect of (2.40) on the well-posedness of the model equations in Section 2.6.2.

2.3.4 Stresses

We require constitutive equations for the stress tensor $\hat{\mathbf{T}}_k$ and Reynolds stress tensor $\mathbf{T}'_k$ in the momentum equation (2.28b). Recall that for each phase the stress tensor (2.12) is given in terms of the pressure $\hat{p}_k$ and shear stress tensor $\hat{\boldsymbol{\tau}}_k$:

$$\hat{\mathbf{T}}_k = -\hat{p}_k\mathbf{I} + \hat{\boldsymbol{\tau}}_k. \tag{2.41}$$

The shear stress tensor is given by [Batchelor, 1967]

$$\hat{\boldsymbol{\tau}}_k = 2\mu_k\boldsymbol{\epsilon}_k, \tag{2.42}$$

where μ_k is viscosity and

$$\boldsymbol{\epsilon}_k = \frac{1}{2}\left(\boldsymbol{\nabla}\overline{\mathbf{v}}_k + \boldsymbol{\nabla}\overline{\mathbf{v}}_k^T\right). \tag{2.43}$$

The shear stress corresponds to the internal forces between neighbouring fluid particles. It is therefore reasonable to assume that in a gaseous phase the shear stress is negligible: $\hat{\boldsymbol{\tau}}_g = 0$.

The Reynolds stress accounts for the turbulent fluctuations in the velocity. The complex effect of turbulence in fluid flow is not a main focus for this thesis; we will therefore skip the detailed discussion of turbulence and assume a simple closure equation for the Reynolds stress. Fowler [2011] provides an analogy to (2.42) with:

$$\mathbf{T}'_k = 2\mu_k^T\boldsymbol{\epsilon}_k, \tag{2.44}$$

where μ_k^T is the eddy viscosity. In pipe flow, the eddy viscosity is taken to be

$$\mu_k^T = d\hat{\rho}_k\epsilon_k^T\overline{v}_k, \tag{2.45}$$

where d is the pipe diameter, ϵ_k^T is a constant and $\overline{v}_k$ is the average velocity.

2.3.5 Interfacial momentum

If we assume the rate of mass transfer Γ_k to be either known or given for a particular system, then prescribing the interfacial momentum source due to the convective flux $\tilde{\mathbf{v}}_{ki}\Gamma_k$ reduces to prescribing a constitutive equation for $\tilde{\mathbf{v}}_{ki}$. The simplest approach would be to assume $\tilde{\mathbf{v}}_{ki} = \overline{\mathbf{v}}_k$. Drew and Wood [1985] provide a more comprehensive definition:

$$\tilde{\mathbf{v}}_{ki} = \overline{\mathbf{v}}_i + \frac{\Gamma_k \nabla \alpha_k}{C_v \hat{\rho}_k |\nabla \alpha_k|^2}, \tag{2.46}$$

where C_v is a constant and $\overline{\mathbf{v}}_i$ is the averaged interfacial velocity. For the particular system where the gaseous phase is dispersed in the continuous liquid phase $\overline{\mathbf{v}}_i$ is given by

$$\overline{\mathbf{v}}_i = \overline{\mathbf{v}}_g + \eta(\overline{\mathbf{v}}_l - \overline{\mathbf{v}}_g), \tag{2.47}$$

where η is a constant. If we assume that the interface between phases moves with the dispersed gaseous phase, Drew and Wood [1985] prescribe $\eta = 0$; to the best of our knowledge this has not been experimentally validated.

The interfacial momentum source due to the diffusive flux is written as

$$\mathbf{M}_k = \hat{p}_{ki} \boldsymbol{\nabla} \alpha_k + \mathbf{M}_k^+, \tag{2.48}$$

where $\hat{p}_{ki}$ is the interfacial pressure and $\mathbf{M}_k^+$ is the additional interfacial momentum source accounting for any drag or virtual mass forces. Drew and Passman [2006] define $\hat{p}_{ki}$ as a function of the specific interfacial area a_i,

$$\hat{p}_{ki} = \frac{\langle p \mathbf{n}_k \cdot \boldsymbol{\nabla} X_k \rangle}{a_i}, \tag{2.49}$$

where $\mathbf{n}_k$ is the outward pointing unit normal to the interface surrounding the k^{th} phase. We seek constitutive laws for $\mathbf{M}_k^+$ and $\hat{p}_{ki}$.

Interfacial pressure

The interfacial pressure $\hat{p}_{ki}$ can be prescribed through considering the interfacial structure. In a two-phase liquid–gas system where the gas is the dispersed phase (e.g. bubbly flow) Drew and Lahey [1979] note that it is unlikely for there to be a large pressure difference $\hat{p}_g - \hat{p}_{gi}$ in the small region of gas. Therefore the assumption $\hat{p}_{gi} = \hat{p}_g$ is reasonable. For the continuous liquid phase, the pressure difference $\hat{p}_l - \hat{p}_{li}$ will change with growing or shrinking gas bubbles. The Rayleigh–Plesset equation gives the interfacial pressure difference in terms of the bubble radius, r_b:

$$\hat{p}_{li} = \hat{p}_l + \hat{\rho}_l \left[r_b \frac{\mathrm{d}^2 r_b}{\mathrm{d}t^2} + \frac{3}{2} \left(\frac{\mathrm{d}r_b}{\mathrm{d}t} \right)^2 \right] + \frac{\mu_l}{r_b} \frac{\mathrm{d}r_b}{\mathrm{d}t}. \tag{2.50}$$

This does however increase the complexity of the equations, as it introduces the bubble radius variable. We therefore make the simplifying assumption that $\hat{p}_{ki} = \hat{p}_k$ for both the gaseous and liquid phases.

Interfacial force

The interfacial momentum source $\mathbf{M}_k^+$ is the sum of the associated force densities

$$\mathbf{M}_k^+ = \sum F_n, \tag{2.51}$$

where F_n denotes the various force densities, including drag forces F_D, virtual-mass forces F_{vm} and lift forces F_L. The drag force accounts for the resistance between phases and is given in terms of a dimensionless drag coefficient C_D which is dependent on the particular flow regime. Where the gaseous phase is dispersed in the continuous liquid phase, Ishii and Mishima [1984] give

$$F_D = \frac{1}{2}\frac{A_b}{V_b} C_D \alpha_g \hat{\rho}_l (\overline{\mathbf{v}}_g - \overline{\mathbf{v}}_l)|\overline{\mathbf{v}}_g - \overline{\mathbf{v}}_l|, \tag{2.52}$$

where A_b and V_b are the typical area and volume of the dispersed bubbles. If we assume spherical bubbles then $A_b/V_b = 3/r_b$, and (2.52) becomes

$$F_D = \frac{3}{2}\frac{C_D \alpha_g \hat{\rho}_l}{r_b} (\overline{\mathbf{v}}_g - \overline{\mathbf{v}}_l)|\overline{\mathbf{v}}_g - \overline{\mathbf{v}}_l|. \tag{2.53}$$

The drag force, as given above, is appropriate for turbulent flow at high Reynolds numbers. For low Reynolds numbers, at the scale of the bubbles, one can assume a linear relationship with the relative velocities [Drew and Passman, 2006].

There are various versions of the drag force in the literature. For high Reynolds numbers Drew and Passman [2006] use the definition in (2.53) with $\frac{3}{8}$ in place of $\frac{3}{2}$. However, this is not a major concern, as the difference in the prefactors can be accounted for through the specification of C_D. In this thesis we will assume the drag force to take the form given in (2.53).

The virtual-mass force corresponds to the inertia introduced to the system due to each phase accelerating through the other [Batchelor, 1967]; this force is given by [Drew, 1982]

$$F_{vm} = \frac{1}{2}\alpha_g \hat{\rho}_l \left[\left(\frac{\partial \overline{\mathbf{v}}_l}{\partial t} + \overline{\mathbf{v}}_l \cdot \boldsymbol{\nabla} \overline{\mathbf{v}}_l \right) - \left(\frac{\partial \overline{\mathbf{v}}_g}{\partial t} + \overline{\mathbf{v}}_g \cdot \boldsymbol{\nabla} \overline{\mathbf{v}}_g \right) \right]. \tag{2.54}$$

The lift force is the resistance force acting transverse to the flow, Drew and Passman [2006] gives the following form for the flow of spherical gas bubbles in a continuous liquid phase:

$$F_L = -C_L \alpha_g \rho_l (\overline{\mathbf{v}}_l - \overline{\mathbf{v}}_g) \times (\boldsymbol{\nabla} \times \overline{\mathbf{v}}_l), \tag{2.55}$$

where C_L is the lift coefficient.

Commonly, in the two-phase flow literature, one can find mention of an *interfacial stress* term in the momentum equations. However we believe the drag force between the phases captures the necessary dynamics associated with such an interfacial stress. We note that whilst there are other relevant forces (e.g. lift and Basset forces) we will, in this thesis, consider only drag and virtual-mass forces.

2.3.6 Heat fluxes

We need to prescribe constitutive laws for the heat flux $\hat{\mathbf{q}}_k$ and turbulent heat flux $\mathbf{q}'_k$ in (2.28c). For $\hat{\mathbf{q}}_k$ we average Fourier's law to get [Drew and Wood, 1985]

$$\hat{\mathbf{q}}_k = -k_k \boldsymbol{\nabla} \overline{T}_k, \tag{2.56}$$

where k_k is the thermal conductivity of the fluid. We can assume a similar form for the turbulent heat flux $\mathbf{q}'_k$:

$$\mathbf{q}'_k = -k_k^T \boldsymbol{\nabla} \overline{T}_k, \tag{2.57}$$

where k_k^T is now the turbulent energy transport coefficient.

2.3.7 Interfacial energy

The interfacial energy source comprises the interfacial internal energy source $\tilde{e}_{ki}\Gamma_k$ and the interfacial heat transfer $\tilde{q}_{ki}$. For the interfacial energy, the simplest approach is to assume $\tilde{e}_{ki} = \overline{e}_k$. Similarly when working with enthalpy we take $\tilde{h}_{ki} = \overline{h}_k$.

For the interfacial heat transfer, we can assume Newton's law of cooling which provides a dependence on the temperature gradient between the bulk liquid and the interface [Bird et al., 2014]:

$$\tilde{q}_{ki} = \beta_{ki}(T_i - \overline{T}_k), \tag{2.58}$$

where β_{ki} is a constant. We make the simplifying assumption that $T_i \approx \overline{T}_l \approx \overline{T_g}$, which is appropriate where β_{ki} is large. Consequently $\tilde{q}_{ki}$ is assumed negligible.

A simple assumption for interfacial kinetic energy source (2.34a) can be given in terms of $\tilde{\mathbf{v}}_{ki}$ in (2.46):

$$v_{ki}^e = \sqrt{\tilde{\mathbf{v}}_{ki} \cdot \tilde{\mathbf{v}}_{ki}}. \tag{2.59}$$

For the viscous dissipation (2.26), we assume an approximate constitutive equation advised by the definition of the averaged viscous dissipation:

$$\phi_k = \hat{\boldsymbol{\tau}}_k : \boldsymbol{\nabla} \overline{\mathbf{v}}_k. \tag{2.60}$$

Finally the interfacial work W_k (2.34b) is typically neglected but for completeness we present the constitutive form appropriate for hard spheres in a liquid as given by Drew and Passman [2006]. It is clear that applying this to bubbles in a liquid would be a simplifying assumption. The interfacial work for the liquid is given by

$$W_l = \frac{1}{2}\alpha_g \hat{\rho}_l (\overline{\mathbf{v}}_l - \overline{\mathbf{v}}_g) \cdot \left[\frac{\partial \overline{\mathbf{v}}_l}{\partial t} + (\overline{\mathbf{v}}_l \cdot \boldsymbol{\nabla}) \overline{\mathbf{v}}_l - \frac{\partial \overline{\mathbf{v}}_g}{\partial t} \right], \tag{2.61}$$

and we additionally assume negligible interfacial work for the gas bubbles: $W_g = 0$. Whilst it is not a focus of this thesis, we do note that (2.61) appears to be missing an advective term on the right-hand side.

Applying the closure framework discussed in this section reduces the system to twelve equations: (2.28a)–(2.28c) with $k = l,\, g$ give six conservation equations; three jump conditions (2.30)–(2.33); two equations for state for $\hat{\rho}_l$ and $\hat{\rho}_g$ and the volume fraction condition (2.35). These twelve equations are solved for the twelve variables: $\{\alpha_k,\, \hat{\rho}_k,\, \overline{\mathbf{v}}_k,\, \hat{p}_k,\, \overline{h}_k,\, \Gamma_k\}$. We have shown that all other terms can be written in terms of these variables.

There are many complexities in modelling two-phase flows. As we have seen, capturing the full physics of the interacting phases yields a large and complicated system of equations. Various modelling techniques have been developed to reduce these complexities. Due to the differences in their underlying assumptions, the different methods are better suited to particular flows. We now discuss the three main modelling approaches: homogeneous, drift-flux and two-fluid models. Hereinafter, we will drop the overline and hat notation for the averaged quantities.

2.4 Homogeneous models

Homogeneous models treat the two-phase fluid mixture as a single 'pseudo-fluid' which is then modelled using well established single-phase fluid dynamics [Aldridge and Fowler, 1996]. Summation of each conservation law (2.28a)–(2.28c) for $k = l,\, g$, and applying the relevant jump conditions (2.30)–(2.33), yields the following system of equations for the single fluid:

$$\frac{\partial \rho_m}{\partial t} + \boldsymbol{\nabla} \cdot (\rho_m \mathbf{v}_m) = 0, \tag{2.62a}$$

$$\frac{\partial}{\partial t}(\rho_m \mathbf{v}_m) + \boldsymbol{\nabla} \cdot (\rho_m \mathbf{v}_m \mathbf{v}_m) = -\boldsymbol{\nabla} \cdot \mathbf{T}_m + \rho_m \mathbf{g} + \mathbf{M}_m, \tag{2.62b}$$

$$\frac{\partial}{\partial t}(\rho_m h_m) + \boldsymbol{\nabla} \cdot (\rho_m \mathbf{v}_m h_m) = -\nabla \cdot \mathbf{q}_m + \left(\frac{\partial p_m}{\partial t} + \mathbf{v}_m \cdot \boldsymbol{\nabla} p_m \right) + \Phi_m + E_m + W_m, \tag{2.62c}$$

where ρ_m is the mixture density defined by the weighted sum of the liquid and gas densities:

$$\rho_m = \alpha_g \rho_g + \alpha_l \rho_l, \tag{2.63}$$

the mixture velocity $\mathbf{v}_m$ is

$$\mathbf{v}_m = \frac{\alpha_g \rho_g \mathbf{v}_g + \alpha_l \rho_l \mathbf{v}_l}{\rho_m}, \tag{2.64}$$

the mixture enthalpy h_m is

$$h_m = \frac{\alpha_g \rho_g h_g + \alpha_l \rho_l h_l}{\rho_m}, \tag{2.65}$$

and the mixture pressure p_m is

$$p_m = \alpha_g p_g + \alpha_l p_l. \tag{2.66}$$

We have also introduced the mixture stress tensor $\mathbf{T}_m$ in (2.62b) defined by

$$\mathbf{T}_m = \alpha_l(\mathbf{T}_l + \mathbf{T}'_l) + \alpha_g(\mathbf{T}_g + \mathbf{T}'_g) - (\alpha_l \rho_l \tilde{\mathbf{v}}_l \tilde{\mathbf{v}}_l + \alpha_g \rho_g \tilde{\mathbf{v}}_g \tilde{\mathbf{v}}_g), \tag{2.67}$$

where $\tilde{\mathbf{v}}_k = (\mathbf{v}_k - \mathbf{v}_m)$; and the mixture heat flux $\mathbf{q}_m$ in (2.62c) which is given by

$$\mathbf{q}_m = \alpha_l(\mathbf{q}_l + \mathbf{q}'_l) + \alpha_g(\mathbf{q}_g + \mathbf{q}'_g) - \left(\alpha_l \rho_l \tilde{h}_l \tilde{\mathbf{v}}_l + \alpha_g \rho_g \tilde{h}_g \tilde{\mathbf{v}}_g\right), \tag{2.68}$$

where $\tilde{h}_k = (h_k - h_m)$.

The viscous dissipation in the mixture Φ_m in (2.62c) is

$$\Phi_m = \alpha_l \Phi_l + \alpha_g \Phi_g, \tag{2.69}$$

and the total work done W_m is

$$\begin{aligned} W_m \;= W_l + W_g + \Bigg[& p_l \left(\frac{\partial \alpha_l}{\partial t} + \mathbf{v}_m \cdot \nabla \alpha_l \right) + p_g \left(\frac{\partial \alpha_g}{\partial t} + \mathbf{v}_m \cdot \nabla \alpha_g \right) + \\ & \alpha_l \tilde{\mathbf{v}}_l \cdot \nabla p_l + \alpha_g \tilde{\mathbf{v}}_g \cdot \nabla p_g \Bigg]. \end{aligned} \tag{2.70}$$

Finally E_m is the total energy source which arises from the jump condition (2.33).

The unknown variables in the three equations (2.62a)–(2.62c) are $\{\rho_m,\ \mathbf{v}_m,\ p_m,\ h_m,\ \mathbf{T}_m,\ \mathbf{q}_m,\ \Phi_m,\ E_m,\ W_m\}$. Further equations are therefore required to complete the model. An equation of state for the density of the fluid ρ_m (e.g. (2.36)), and constitutive equations for the stress tensor $\mathbf{T}_m$ (e.g. (2.41)) and heat flux $\mathbf{q}_m$ (e.g. (2.56)) can be assumed. For simplicity the viscous dissipation Φ_m, energy source E_m and work W_m are typically neglected, thus leaving three unknown variables $\{\mathbf{v}_m, p_m, h_m\}$ for the three governing equations (2.62a)–(2.62c).

Cazarez-Candia and Vásquez-Cruz [2005] used a homogeneous model to study transient one-dimensional two-phase liquid–gas flow in oil wells. The system of equations was closed using an empirically derived correlation for the mixture density given as a function of pressure. This approach has also been used by Turcotte et al. [1990] to model volcanic eruptions for a single magma–vapour mixture fluid. Fowler [1978] used the homogeneous modelling approach for water–vapour flows in heat exchangers.

Homogeneous models are the simplest of the modelling approaches. The simplification comes at the cost of failure to capture interfacial interactions or the individual behaviour of the distinct phases. The assumption of an averaged fluid travelling at a single velocity neglects the slippage between the phases. Therefore this modelling approach is best suited to two-phase mixtures where the individual phases have inherently strongly coupled flows [Aldridge and Fowler, 1996]. The analytical tractability of this simplified model is a clear advantage. Furthermore, with more complex models, uncertain closure laws for the interactions between phases are required. Al-Safran and Brill [2017] suggest that this method is a good reference case to compare with more sophisticated models.

2.5 Drift-flux models

Drift-flux modelling treats the two-phase fluid as a single fluid mixture whilst capturing interfacial dynamics through modelling the relative motion of the gas to the mixture [Brennen, 2005; Ishii and Hibiki, 2010]. This approach was first introduced by Wallis [1969] and Zuber and Findlay [1965]. The density, velocity and enthalpy of the mixture fluid are given by (2.63)–(2.65).

A key variable in this modelling approach is the drift velocity of each phase which is the velocity of the phase relative to that of the mixture denoted $\mathbf{v}_{dk}$ which is defined in terms of the volumetric flux $\mathbf{j}_m$:

$$\mathbf{j}_m = \alpha_g \mathbf{v}_g + \alpha_l \mathbf{v}_l. \tag{2.71}$$

The drift velocity of the gas is defined by Brennen [2005] as

$$\mathbf{v}_{dg} = \mathbf{v}_g - \mathbf{j}_m = (1 - \alpha_g)(\mathbf{v}_g - \mathbf{v}_l). \tag{2.72}$$

The four governing equations are conservation of mass for the mixture fluid and the

gas phase, and conservation of momentum and energy for the mixture fluid:

$$\frac{\partial}{\partial t}(\alpha_g \rho_g) + \boldsymbol{\nabla} \cdot (\alpha_g \rho_g \mathbf{v}_m) = \Gamma_g - \boldsymbol{\nabla} \cdot \left(\frac{\alpha_g \rho_g \rho_l}{\rho_m} \mathbf{v}_{dg} \right), \tag{2.73a}$$

$$\frac{\partial \rho_m}{\partial t} + \boldsymbol{\nabla} \cdot (\rho_m \mathbf{v}_m) = 0, \tag{2.73b}$$

$$\frac{\partial}{\partial t}(\rho_m \mathbf{v}_m) + \boldsymbol{\nabla} \cdot (\rho_m \mathbf{v}_m \mathbf{v}_m) = -\boldsymbol{\nabla} \cdot \mathbf{T}_m + \rho_m \mathbf{g} + \mathbf{M}_m, \tag{2.73c}$$

$$\frac{\partial}{\partial t}(\rho_m h_m) + \boldsymbol{\nabla} \cdot (\rho_m \mathbf{v}_m h_m) = -\nabla \cdot \mathbf{q}_m + \left(\frac{\partial p_m}{\partial t} + \mathbf{v}_m \cdot \boldsymbol{\nabla} p_m \right) + \Phi_m + E_m + W_m, \tag{2.73d}$$

where the mixture stress tensor $\mathbf{T}_m$, heat flux $\mathbf{q}_m$, viscous dissipation Φ_m and work W_m are given by (2.67)–(2.70). Recall that Γ_g is the rate of mass transfer from the liquid to the gas phase. As before, the terms $\mathbf{M}_m$ and E_m govern the rates of interfacial momentum and energy transfer.

The drift flux approach reduces the six conservation equations (three for each of the two phases) to four. The generalised conservation equations (2.28a)–(2.28c) are reduced by one momentum and one energy equation. The model is closed with equations of state for the densities ρ_g and ρ_l; the volume fraction condition (2.35); an assumption for the form of the drift velocity $\mathbf{v}_{dg}$; an equation relating $\mathbf{v}_{dg}$ and $\mathbf{v}_m$; and constitutive relations for Γ_g, $\mathbf{M}_m$, E_m [Aldridge and Fowler, 1996]. Using the definitions of the mixture variables (2.63)–(2.65) the problem can be reduced to four variables $\{\alpha_g, \mathbf{v}_m, p_m, h_m\}$ and four equations (2.73a)–(2.73d).

Drift flux models capture more detail than homogeneous models (2.62a)–(2.62c) but still simplify the full system of equations (2.28a)–(2.28c). The simplicity of the drift-flux approach relies on the assumption that the relative motion can be prescribed constitutively. Ishii and Hibiki [2010] argued that drift-flux models do not capture the important interactions between the phases. This approach is best suited to flows consisting of closely coupled phases, i.e. dispersed flow regimes.

For the oil well domain, the drift-flux approach is detailed in Shoham [2006] and Al-Safran and Brill [2017]. Livescu et al. [2010] utilised the drift-flux approach for a one-dimensional, transient, three-phase oil, water and gas flow through an oil well.

2.6 Two-fluid models

In a two-fluid model each phase is treated as a separate fluid. Model equations are derived from the conservation of mass, momentum and energy for each phase. The governing equations are exactly (2.28a)–(2.28c); dropping the hat and overline

notation, the system is

$$\frac{\partial}{\partial t}(\alpha_k\rho_k) + \boldsymbol{\nabla}\cdot(\alpha_k\rho_k\mathbf{v}_k) = \Gamma_k, \tag{2.74a}$$

$$\frac{\partial}{\partial t}(\alpha_k\rho_k\mathbf{v}_k) + \boldsymbol{\nabla}\cdot(\alpha_k\rho_k\mathbf{v}_k\mathbf{v}_k) = \boldsymbol{\nabla}\cdot[\alpha_k(\mathbf{T}_k + \mathbf{T}'_k)] + \alpha_k\rho_k\mathbf{g} + \tilde{\mathbf{v}}_{ki}\Gamma_k + \mathbf{M}_k, \tag{2.74b}$$

$$\begin{aligned}\frac{\partial}{\partial t}(\alpha_k\rho_k h_k) + \boldsymbol{\nabla}\cdot(\alpha_k\rho_k h_k\mathbf{v}_k) = \alpha_k\left(\frac{\partial p_k}{\partial t} + \mathbf{v}_k\cdot\boldsymbol{\nabla}p_k\right) - \nabla\cdot[\alpha_k(\mathbf{q}_k + \tilde{\mathbf{q}}'_k)] \\ + \alpha_k\tilde{\phi}_k + \tilde{h}_{ki}\Gamma_k + \tilde{q}_{ki}.\end{aligned} \tag{2.74c}$$

As discussed in Section 2.3, numerous constitutive relations, equations of state and jump conditions are assumed to close the system of equations. This method is the most detailed modelling approach as it explicitly models the dynamics within each phase and also accounts for the interaction between the phases.

Several authors have used this detailed approach to model oil wells. Shoham [2006], Al-Safran and Brill [2017] and Jerez-Carrizales et al. [2014] used the general two-fluid model for two-phase liquid–gas flow in oil wells by assuming a single liquid phase comprised of water and oil. The complexity of the model is reduced by simplifying the dynamics considered; for example Jerez-Carrizales et al. [2014] neglect shear stress effects.

Cazarez et al. [2010] extended the two-fluid modelling approach to introduce a three-fluid model for the bubbly flow of oil, water and gas in a well, assuming a single pressure for all three phases. Results presented by Cazarez et al. [2010] suggested that the interfacial stress (which we interpret as the interfacial drag force) between the phases had an important influence on the flow dynamics. Bendiksen et al. [1991] used the two-fluid method to model the conservation of a gas phase, a bulk liquid phase and a droplet field together with constitutive relations for the densities and temperatures of each phase in the development of the underlying model in OLGA. OLGA is the industry leading oil well software and was developed by Schlumberger [2016].

Two-fluid models have opposing problems to the homogeneous models. They capture all the possible detail and include all the interactions between phases. However, because these models are so comprehensive, the system of equations require an extensive closure framework (as is evident in Section 2.3). It is important to note that where the interaction terms are inaccurately modelled, the two-fluid approach has little advantage over the simpler drift-flux modelling. This complexity is unnecessary for strongly coupled phases (e.g. bubbly flow) that behave comparably, but this level of detail is necessary for systems where the phases are weakly coupled (e.g. annular) [Brennen, 2005].

2.6.1 One-dimensional two-fluid model

In pipe flow (as is appropriate for oil well flow), the three-dimensional equations (2.28a)–(2.28c) are averaged over a cross-sectional slice of the pipe to provide a one-dimensional system of equations. We will consider the one-dimensional reduction for the two-fluid model (2.74a)–(2.74c) as this is the basis for the work in Chapter 3. Recall that we have already assumed an ensemble average to write down the model equations (2.74a)–(2.74c). We now add another layer of averaging through a cross-sectional average of the ensemble-averaged quantity $h(\mathbf{x}, t)$ and follow the analysis by Drew and Wood [1985].

It is reasonable to assume a constant diameter for an oil well, but for completeness we will present equations for a varying cross-sectional area $A(z)$ where z is the spatial coordinate along the pipe axis. The cross-sectional average is defined to be

$$\langle h(\mathbf{x}, t) \rangle = \frac{1}{A(z)} \iint_{A(z)} h(\mathbf{x}, t) \, \mathrm{d}A. \tag{2.75}$$

To apply this averaging to (2.74a)–(2.74c) we note the following:

$$\left\langle \frac{\partial h}{\partial t} \right\rangle = \frac{\partial}{\partial t} \langle h \rangle , \tag{2.76a}$$

$$\langle \boldsymbol{\nabla} h \rangle = \left\langle \frac{\partial h}{\partial x} \right\rangle \mathbf{e}_x + \left\langle \frac{\partial h}{\partial y} \right\rangle \mathbf{e}_y + \left\langle \frac{\partial h}{\partial z} \right\rangle \mathbf{e}_z. \tag{2.76b}$$

Applying the divergence theorem to the first two terms on the right-hand side of (2.76b) we find that

$$\langle \boldsymbol{\nabla} h \rangle = \frac{1}{A} \int_C \mathbf{n}' h \, \mathrm{d}l + \left\langle \frac{\partial h}{\partial z} \right\rangle \mathbf{e}_z, \tag{2.77}$$

where we have introduced the two-dimensional unit normal $\mathbf{n}'$ orthogonal to $\mathbf{e}_z$, and $C = C(z)$ is the cross-sectional perimeter.
Consider the partial derivative of the cross-sectional average:

$$\begin{aligned} \frac{\partial}{\partial z} \langle h \rangle &= \frac{\partial}{\partial z} \left[\frac{1}{A(z)} \iint_{A(z)} h \, \mathrm{d}A \right] \\ &= -\frac{1}{A^2} \frac{\partial A}{\partial z} \iint_{A(z)} h \, \mathrm{d}A + \frac{1}{A} \iint_{A(z)} \frac{\partial h}{\partial z} \, \mathrm{d}A + \frac{1}{A} \int_C \frac{\delta n'}{\delta z} h \, \mathrm{d}l, \end{aligned} \tag{2.78}$$

where $\delta n'$ is the length of the segment along the normal $\mathbf{n}'$ to the cross-section, as indicated in figure 2.1. To see this note that for a change in cross-sectional area $\mathrm{d}A$ (see figure 2.1) we have

$$\delta \, \mathrm{d}A = \delta n' \, \mathrm{d}l. \tag{2.79}$$

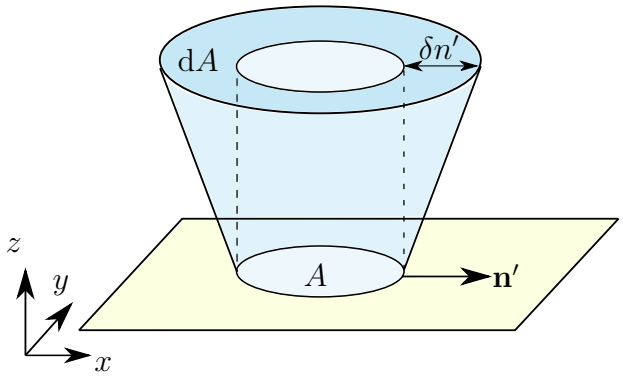
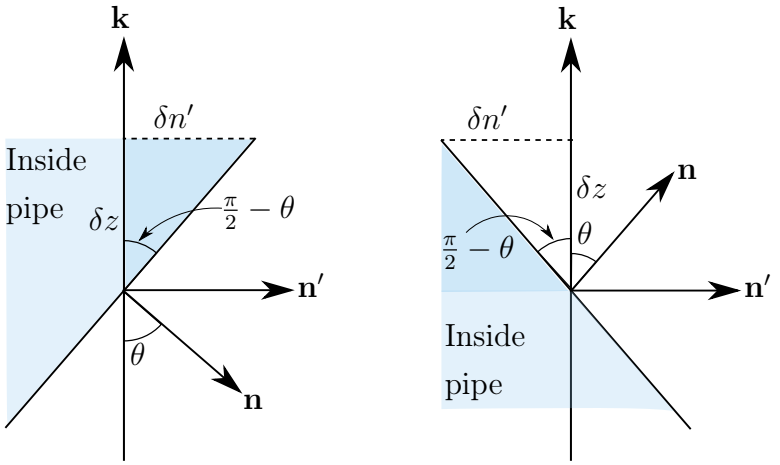


Figure 2.1: Schematic indicating the two-dimensional normal to the cross-section $\mathbf{n}'$ and the length $\delta n'$.



(a) Increasing $A(z)$. **(b)** Decreasing $A(z)$.

Figure 2.2: Schematic for the calculation of the integral in (2.80) for an increasing and decreasing cross-sectional area $A(z)$ where $\mathbf{k}$ is the vector in the direction of the z-axis, $\mathbf{n}$ is the unit normal to the pipe and $\mathbf{n}'$ is the two-dimensional unit normal.

Integration gives

$$\begin{aligned} \iint_A \delta \, \mathrm{d}A &= \int_C \delta n' \, \mathrm{d}l \\ \Rightarrow \iint_A \frac{\delta}{\delta z} \, \mathrm{d}A &= \int_C \frac{\delta n'}{\delta z} \, \mathrm{d}l. \end{aligned} \tag{2.80}$$

From figure 2.2 we can see that

$$\frac{\delta n'}{\delta z} = -\frac{\mathbf{n} \cdot \mathbf{k}}{\sqrt{1 - (\mathbf{n} \cdot \mathbf{k})^2}}, \tag{2.81}$$

where $\mathbf{k}$ is the unit vector in the direction of the z-axis and $\mathbf{n}$ is the unit normal to

the pipe. Figure 2.2 shows that (2.81) holds for both an increasing and decreasing area.

Using (2.81) the partial derivative of the average (2.78) becomes

$$\frac{\partial}{\partial z}\langle h\rangle = -\frac{1}{A^2}\frac{\partial A}{\partial z}\iint_{A(z)} h(\mathbf{x},t)\,\mathrm{d}A + \frac{1}{A}\iint_{A(z)}\frac{\partial h}{\partial z}\,\mathrm{d}A - \frac{1}{A}\int_C \frac{\mathbf{n}\cdot\mathbf{k}}{\sqrt{1-(\mathbf{n}\cdot\mathbf{k})^2}} h\,\mathrm{d}l. \tag{2.82}$$

Using the definition of the cross-sectional average (2.75) and rearranging for $\langle \partial h/\partial z\rangle$ we find

$$\left\langle \frac{\partial h}{\partial z}\right\rangle = \frac{\partial}{\partial z}\langle h\rangle + \frac{1}{A}\frac{\partial A}{\partial z}\langle h\rangle + \frac{1}{A}\int_C \frac{\mathbf{n}\cdot\mathbf{k}}{\sqrt{1-(\mathbf{n}\cdot\mathbf{k})^2}} h\,\mathrm{d}l. \tag{2.83}$$

Note the following identity [Drew and Wood, 1985]:

$$\mathbf{n}' + \frac{\mathbf{n}\cdot\mathbf{k}}{\sqrt{1-(\mathbf{n}\cdot\mathbf{k})^2}}\mathbf{e}_z = \frac{\mathbf{n}}{\mathbf{n}\cdot\mathbf{n}'}. \tag{2.84}$$

Using (2.83) and (2.84) in (2.77) gives

$$\langle \boldsymbol{\nabla} h\rangle = \frac{1}{A}\frac{\partial}{\partial z}\left(A\,\langle h\rangle\,\right)\mathbf{e}_z + \frac{1}{A}\int_C \frac{\mathbf{n}}{\mathbf{n}\cdot\mathbf{n}'} h\,\mathrm{d}l. \tag{2.85}$$

Applying the cross-sectional average (2.75) to the mass conservation equations (2.74a) and utilising (2.76a) and (2.85) we get

$$\frac{\partial}{\partial t}\langle \alpha_k\rho_k\rangle + \frac{1}{A}\frac{\partial}{\partial z}\left(A\langle \alpha_k\rho_k\mathbf{v}_k\rangle\right)\cdot\mathbf{e}_z = \langle \Gamma_k\rangle. \tag{2.86}$$

Similarly the axial component of the momentum conservation equation (2.74b) becomes

$$\begin{aligned}\frac{\partial}{\partial t}\langle \alpha_k\rho_k\mathbf{v}_k\rangle\cdot\mathbf{e}_z + \frac{1}{A}\frac{\partial}{\partial z}\left(A\langle \alpha_k\rho_k\mathbf{v}_k\mathbf{v}_k\rangle\right):\mathbf{e}_z\mathbf{e}_z &= \frac{1}{A}\frac{\partial}{\partial z}\left[A\langle \alpha_k(\mathbf{T}_k+\mathbf{T}_k')\rangle\right]:\mathbf{e}_z\mathbf{e}_z \\ &+ \langle \alpha_k\rho_k\rangle\mathbf{g}\cdot\mathbf{e}_z + \langle \tilde{\mathbf{v}}_{ki}\Gamma_k\rangle\cdot\mathbf{e}_z + \langle \mathbf{M}_k\rangle\cdot\mathbf{e}_z + \frac{1}{A}\int_C \alpha_k\frac{\mathbf{T}_k:\mathbf{n}\mathbf{e}_z}{\mathbf{n}\cdot\mathbf{n}'}\,\mathrm{d}l.\end{aligned} \tag{2.87}$$

Finally the cross-sectionally averaged enthalpy equation (2.74c) is

$$\begin{aligned}\frac{\partial}{\partial t}\langle \alpha_k\rho_k h_k\rangle + \frac{1}{A}\frac{\partial}{\partial z}\left(A\langle \alpha_k\rho_k h_k\mathbf{v}_k\rangle\right)\cdot\mathbf{e}_z &= \left\langle \alpha_k\left(\frac{\partial p_k}{\partial t} + \mathbf{v}_k\cdot\boldsymbol{\nabla}p_k\right)\right\rangle \\ &- \frac{1}{A}\frac{\partial}{\partial z}\left[A\,\langle \alpha_k(\mathbf{q}_k+\tilde{\mathbf{q}}_k')\rangle\right]\cdot\mathbf{e}_z + \langle \alpha_k\tilde{\phi}_k\rangle + \langle \tilde{h}_{ki}\Gamma_k\rangle + \langle \tilde{q}_{ki}\rangle \\ &- \frac{1}{A}\int_C \alpha_k\frac{\mathbf{q}_k\cdot\mathbf{n}}{\mathbf{n}\cdot\mathbf{n}'}\,\mathrm{d}l,\end{aligned} \tag{2.88}$$

where we have followed Drew and Wood [1985] by assuming

$$(\alpha_k\rho_k\psi_k\mathbf{v}_k)\cdot\mathbf{n} = 0, \quad (\alpha_k\mathbf{T}_k')\cdot\mathbf{n} = 0, \quad (\alpha_k\tilde{\mathbf{q}}_k')\cdot\mathbf{n} = 0, \tag{2.89}$$

for $\psi_k = 1$, $\mathbf{v}_k$ and h_k for mass, momentum and enthalpy respectively.

One-dimensional averaged variable		Definition
Volume fraction	$\overline{\alpha}_k$	$\langle \alpha_k \rangle$
Density	$\overline{\rho}_k$	$\dfrac{\langle \alpha_k \rho_k \rangle}{\overline{\alpha}_k}$
Axial velocity	$\overline{v}_k$	$\dfrac{\langle \alpha_k \rho_k \mathbf{v}_k \rangle \cdot \mathbf{e}_z}{\overline{\alpha}_k \overline{\rho}_k}$
Pressure	$\overline{p}_k$	$\dfrac{\langle \alpha_k p_k \rangle}{\overline{\alpha}_k}$
Enthalpy	$\overline{h}_k$	$\dfrac{\langle \alpha_k \rho_k h_k \rangle}{\overline{\alpha}_k \overline{\rho}_k}$
Mass transfer rate	$\overline{\Gamma}_k$	$\langle \Gamma_k \rangle$
Stress	$\overline{\mathcal{T}}_k$	$\dfrac{\langle \alpha_k \mathbf{T}_k \rangle : \mathbf{e}_z \mathbf{e}_z}{\overline{\alpha}_k}$
Reynolds stress	$\overline{\mathcal{T}}'_k$	$\dfrac{\langle \alpha_k \mathbf{T}'_k \rangle : \mathbf{e}_z \mathbf{e}_z}{\overline{\alpha}_k}$
Wall stress	$\overline{\tau}_{kw}$	$\dfrac{D}{4} \dfrac{1}{A} \displaystyle\int_C \alpha_k \dfrac{\mathbf{T}_k : \mathbf{n} \mathbf{e}_z}{\mathbf{n} \cdot \mathbf{n}'} \, \mathrm{d}l$
Heat flux	$\overline{q}_k$	$\dfrac{\langle \alpha_k \mathbf{q}_k \rangle \cdot \mathbf{e}_z}{\overline{\alpha}_k}$
Turbulent heat transfer	$\overline{q}'_k$	$\dfrac{\langle \alpha_k \tilde{\mathbf{q}}'_k \rangle \cdot \mathbf{e}_z}{\overline{\alpha}_k}$
Wall heat transfer	$\overline{q}_{kw}$	$\dfrac{A}{\xi_h} \dfrac{1}{A} \displaystyle\int_C \alpha_k \dfrac{\mathbf{T}_k : \mathbf{n} \mathbf{e}_z}{\mathbf{n} \cdot \mathbf{n}'} \, \mathrm{d}l$
Interfacial velocity	$\overline{v}_{ki}$	$\dfrac{\langle \tilde{\mathbf{v}}_{ki} \Gamma_k \rangle \cdot \mathbf{e}_z}{\overline{\Gamma}_k}$
Interfacial enthalpy	$\overline{h}_{ki}$	$\dfrac{\langle \tilde{h}_{ki} \Gamma_k \rangle}{\overline{\Gamma}_k}$
Interfacial force density	$\overline{M}_k$	$\langle \mathbf{M}_k \rangle \cdot \mathbf{e}_z$
Interfacial heat transfer	$\overline{q}_{ki}$	$\langle \tilde{q}_{ki} \rangle$
Dissipation	$\overline{\phi}_k$	$\dfrac{\langle \alpha_k \tilde{\phi}_k \rangle}{\overline{\alpha}_k}$

Table 2.1: Averaged variables in the one-dimensional two-fluid model where the hydraulic (wetted) perimeter is $D = 4A/C$ and the heated perimeter is ξ_h.

We define the one-dimensional variables in table 2.1 using the overline notation (not to be confused with the mass averaged notation in (2.18b)). We introduce the hydraulic (wetted) perimeter $D = 4A/C$ and heated perimeter ξ_h. The one-dimensional two-fluid model (2.86)–(2.88) is:

$$\frac{\partial}{\partial t}(\overline{\alpha}_k\overline{\rho}_k) + \frac{\partial}{\partial z}(\overline{\alpha}_k\overline{\rho}_k\overline{v}_k) = \overline{\Gamma}_k, \tag{2.90a}$$

$$\frac{\partial}{\partial t}(\overline{\alpha}_k\overline{\rho}_k\overline{v}_k) + \frac{\partial}{\partial z}(\overline{\alpha}_k\overline{\rho}_k\overline{v}_k^2) = \frac{\partial}{\partial z}\left[\overline{\alpha}_k\left(\overline{\mathcal{T}}_k + \overline{\mathcal{T}}'_k\right)\right] + \overline{\alpha}_k\overline{\rho}_k g + \overline{v}_{ki}\overline{\Gamma}_k + \overline{M}_k + \frac{4}{D}\overline{\tau}_{kw}, \tag{2.90b}$$

$$\frac{\partial}{\partial t}(\overline{\alpha}_k\overline{\rho}_k\overline{h}_k) + \frac{\partial}{\partial z}(\overline{\alpha}_k\overline{\rho}_k\overline{h}_k\overline{v}_k) = \overline{\alpha}_k\left(\frac{\partial\overline{p}_k}{\partial t} + \overline{v}_k\frac{\partial\overline{p}_k}{\partial z}\right) - \frac{\partial}{\partial z}[\overline{\alpha}_k\left(\overline{q}_k + \overline{q}'_k\right)] + P_k + \overline{\alpha}_k\overline{\phi}_k + \overline{h}_{ki}\overline{\Gamma}_k + \overline{q}_{ki} + \frac{\xi_h}{A}\overline{q}_{kw}, \tag{2.90c}$$

where P_k is defined via

$$\left\langle \alpha_k\left(\frac{\partial p_k}{\partial t} + \mathbf{v}_k\cdot\boldsymbol{\nabla}p_k\right)\right\rangle = \overline{\alpha}_k\left(\frac{\partial\overline{p}_k}{\partial t} + \overline{v}_k\cdot\frac{\partial\overline{p}_k}{\partial z}\right) + P_k. \tag{2.91}$$

We have introduced the following new variables: wall stress $\overline{\tau}_{kw}$, wall heat flux $\overline{q}_{kw}$ and P_k, as defined above, which all require further constitutive equations. It is not trivial to prescribe expressions for P_k which capture the difference between the average of the function and the function of the average. We will, in this thesis, assume P_k to be negligible.

For the wall stress, empirical evidence suggests the following form [Drew and Wood, 1985; Fowler, 2011]:

$$\overline{\tau}_{kw} = f_k\overline{\rho}_k\overline{v}_k|\overline{v}_k|, \tag{2.92}$$

where f_k is the wall friction factor, which in practice is an empirically derived parameter dependent on the particular flow regime.

For the wall heat flux one may assume Newton's law of cooling (analogous to the interfacial heat transfer (2.58)), which gives the wall heat flux proportional to the difference in temperature between the liquid and the wall: $\overline{q}_{kw} = \beta_{kw}(\overline{T}_k - \overline{T}_w)$, where β_{kw} is a constant, $\overline{T}_k$ is the averaged temperature of the k^{th} phase and $\overline{T}_w$ is the wall temperature. If β_{kw} is large, then it is reasonable to assume $\overline{T}_k \approx \overline{T}_w$. An alternative constitutive form for the wall heat flux mirrors the wall stress in (2.92): $\overline{q}_{kw} = f_k\overline{\rho}_k\overline{v}_k\overline{h}_k$. In terms of temperature (using (2.37)) this is

$$\overline{q}_{kw} = f_k c_{pk}\overline{\rho}_k\overline{v}_k\overline{T}_k. \tag{2.93}$$

2.6.2 Characteristics of the one-dimensional model

The simplest two-phase system we can consider is the isothermal flow of two incompressible fluids (with ρ_g and ρ_l constant) along a one-dimensional domain of length L: $z \in [0, L]$ with the inflow and outflow at $z = 0$ and $z = L$ respectively. We assume that there is no mass transfer, and a single pressure: $p_g = p_l = p$. Neglecting shear stress, turbulent stress, gravitational acceleration, wall stress and assuming the interfacial momentum term $M_k = p_k \, \partial\alpha_k/\partial z$, the corresponding system of equations from (2.90a)–(2.90c) (dropping the overline notation) becomes

$$\frac{\partial \alpha}{\partial t} + \frac{\partial}{\partial z}(\alpha v) = 0, \tag{2.94a}$$

$$-\frac{\partial \alpha}{\partial t} + \frac{\partial}{\partial z}((1-\alpha)u) = 0, \tag{2.94b}$$

$$\rho_g \left(\frac{\partial v}{\partial t} + v \frac{\partial v}{\partial z} \right) = -\frac{\partial p}{\partial z}, \tag{2.94c}$$

$$\rho_l \left(\frac{\partial u}{\partial t} + u \frac{\partial u}{\partial z} \right) = -\frac{\partial p}{\partial z}, \tag{2.94d}$$

where $\alpha = \alpha_g$ is the gas volume fraction and we have used condition (2.35) to write $\alpha_l = 1 - \alpha$. Moreover we have denoted the gas and liquid velocities by v and u respectively. To study the associated characteristics we write (2.94) in matrix form as

$$\mathbf{A}\frac{\partial \mathbf{\Psi}}{\partial t} + \mathbf{B}\frac{\partial \mathbf{\Psi}}{\partial z} = \mathbf{0}, \tag{2.95}$$

where $\mathbf{\Psi} = (\alpha, v, u, p)^T$. The characteristics of the system are computed by solving $\det(\mathbf{B} - \lambda\mathbf{A}) = 0$ for λ, where $\mathrm{d}z/\mathrm{d}t = \lambda$ gives the slopes of the characteristics. Writing (2.94) in the form (2.95) and solving for the characteristics, we find the system has complex characteristics of the form $\lambda_{1,2} = 0$ and

$$\lambda_{3,4} = \lambda_{\mathbb{R}} \pm i\lambda_{\mathbb{I}}, \tag{2.96}$$

where

$$\lambda_{\mathbb{R}} = \frac{(1-\alpha)\rho_g v + \alpha\rho_l u}{(1-\alpha)\rho_g v^2 + \alpha\rho_l u^2}, \quad \text{and} \quad \lambda_{\mathbb{I}} = \frac{\sqrt{(u-v)^2\alpha(1-\alpha)\rho_g\rho_l}}{(1-\alpha)\rho_g v^2 + \alpha\rho_l u^2}. \tag{2.97}$$

Complex characteristics indicate an elliptic problem which requires prescription of boundary conditions at both ends of the time domain. Thus the system of equations (2.94) is ill-posed. Note that the ellipticity is independent of including algebraic interfacial momentum source terms.

If we now consider the pressure as derived by Stuhmiller [1977] and given in (2.40), the equations (2.94) become:

$$\frac{\partial \alpha}{\partial t} + \frac{\partial}{\partial z}(\alpha v) = 0, \tag{2.98a}$$

$$-\frac{\partial \alpha}{\partial t} + \frac{\partial}{\partial z}((1-\alpha)u) = 0, \tag{2.98b}$$

$$\rho_g \left(\frac{\partial v}{\partial t} + v\frac{\partial v}{\partial z} \right) = -\frac{\partial p_g}{\partial z}, \tag{2.98c}$$

$$\rho_l \left(\frac{\partial u}{\partial t} + u\frac{\partial u}{\partial z} \right) = -\frac{\partial p_l}{\partial z}, \tag{2.98d}$$

$$p_g - p_l = -H\rho_l (v-u)^2. \tag{2.98e}$$

Writing the above as in (2.95), we find the associated characteristics to be $\hat{\lambda}_{1,2} = 0$, and

$$\hat{\lambda}_{3,4} = \hat{\lambda}_A \pm \hat{\lambda}_B, \tag{2.99}$$

where

$$\begin{aligned} \hat{\lambda}_A &= \frac{(1-\alpha)\rho_g v + (H(u-v)+u\alpha)\rho_l}{(1-\alpha)\rho_g v^2 + \alpha\rho_l u^2}, \quad \text{and} \\ \hat{\lambda}_B &= \frac{\sqrt{\rho_l (u-v)^2 \left[H(2(1-\alpha)\alpha + H)\rho_l - (1+2H)(1-\alpha)\alpha\rho_g \right]}}{(1-\alpha)\rho_g v^2 + \alpha\rho_l u^2}. \end{aligned} \tag{2.100}$$

These characteristics are real and distinct if $H(2(1-\alpha)\alpha+H)\rho_l > (1+2H)(1-\alpha)\alpha\rho_g$. Introducing $\delta = \rho_g/\rho_l$ for the density ratio and using $H = \frac{1}{4}$, then this is equivalent to

$$(1-\alpha)\alpha \left(\frac{1}{2} - \frac{3}{2}\delta \right) + \frac{1}{16} > 0. \tag{2.101}$$

It is clear that $0 \leq \alpha \leq 1$ and furthermore it is reasonable to assume the density ratio to be such that $\delta \ll 1$, so we find that the pressure relation as proposed by Stuhmiller [1977] yields a well-posed hyperbolic system of equations. This shows how important the choice of constitutive laws can be in formulating a two-phase flow model.

2.7 Flow regimes

In reviewing the closure framework in Section 2.3 we saw that the dependence of a model on the particular flow regime is captured by the parameters supplied to the system; for example the drag coefficient in (2.53) and the wall friction factor in (2.92). In practice these parameters are difficult to specify, thus they themselves are modelled with constitutive relations, typically through an empirically derived function specific to the flow regime [Al-Safran and Brill, 2017].

It is understood that when a flow regime becomes unstable, the flow enters another regime. At this transition, the modelling requires the constitutive laws to change. While two-phase systems are well studied within flow regimes, there has been little research into how flow regimes transition from one to another.

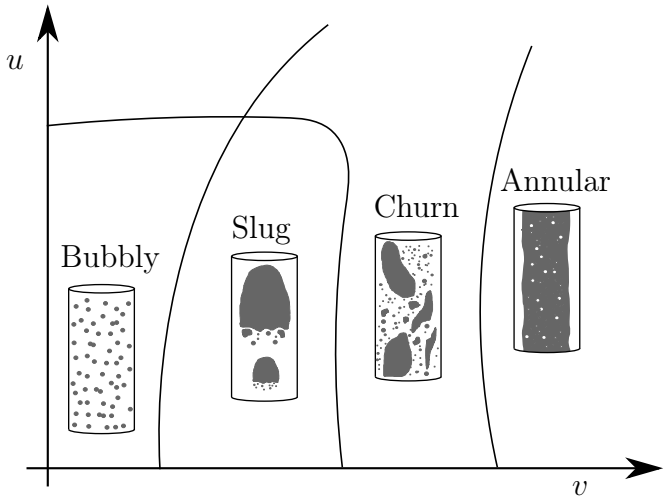


Figure 2.3: Schematic of a flow regime map for the two-phase liquid–gas flow regimes dependent on gas and liquid velocities denoted v, u respectively.

2.7.1 Flow regime maps

Flow regimes are typically identified through visualisations from experiments. For a particular pipe geometry, the relationship between the flow regime and the flow variables is presented in a *flow regime map* [Brennen, 2005]; see figure 2.3. The lines on the maps indicate a regime transition. A regime map can be developed based on purely observational findings, like that by Beggs and Brill [1973]. Maps can also be derived from theory such as that by Taitel and Dukler [1976], which was based on a flow-chart assessing the physical system.

Where visualisation of the system is not possible, flow regimes are identified using these maps or empirically derived transition criteria [Wang et al., 2012]. However, flow regime maps vary with pipe inclination, pipe diameter and other structural parameters, which means that a single generalised regime map is not realisable. Moreover, employing empirical methods for systems other than that for which the map or correlation was developed raises questions of reliability. There is even doubt concerning the use of a map to indicate transitions in the specific system for which the map was constructed. Brennen [2005] goes so far as to describe the flow regime boundaries on

the maps to be nothing more than "poorly defined transition zones". This motivates mathematical modelling of the two-phase flow regime transitions.

2.7.2 Modelling of flow regime transitions

The literature concerning mathematical modelling of flow regime transitions is quite sparse in comparison to the rest of the two-phase flow literature. The transition between each pair of regimes needs to be treated separately. For example, the transition from bubbly to slug flow will have different dynamics to that governing the transition from churn to annular flow. Algebraic criteria for pairwise flow regime transitions based on the system variables have been independently developed by Taitel et al. [1980] and Mishima and Ishii [1984]. Their results enabled the prediction of system-dependent flow regime maps. However, the corresponding steady state transition criteria assume that transitions occur instantaneously, and fail to capture the dynamic behaviour of the transitions.

The main difficulty in modelling transitions lies in the prescription of interfacial interaction terms. This has motivated the study of particle distributions where bubbles are treated as particles. One can then look to kinetic theory and the Boltzmann equation to model the evolution of bubbles through a liquid domain. Kinetic theory has been used to model the bubbly-to-slug regime transition (see for example Navarro-Valenti et al. [1991]; Kalkach-Navarro et al. [1994]; Hibiki and Ishii [2000]). We believe that there is scope to build on previous work to further examine the transition period. Studies have thus far considered the *point of transition*. However, there is a time period and spatial domain in which the transition occurs. Mathematical modelling of such dynamics would provide novel insight into the evolution of flow regimes. We provide further detail concerning the previous studies in Chapter 7, where we derive a master equation for an evolving shape distribution of bubbles.

2.8 Summary

In this chapter we have presented a detailed derivation for the averaged conservation equations of mass, momentum and energy for a two-phase flow in Section 2.2. The literature pertaining to the modelling of two-phase flows and the relevant closure framework is vast, and this was discussed in Section 2.3. We note that there is a choice of what equations of state and constitutive relations one can assume; the choice is typically dependent on the particular application. We have been guided by an assumed initial bubbly flow.

There are three main methods of modelling two-phase flows; homogeneous, drift-flux and two-fluid. We derived each of these in turn from our generalised averaged conservation equations, and discussed the advantages and disadvantages of the different approaches. In Chapter 3, we will consider a two-fluid model for the upwelling flow through an oil well. It is reasonable to assume a one-dimensional domain for the oil well, and so we discussed additional averaging to derive a one-dimensional two-fluid model in Section 2.6.1. We analysed the characteristics of the simplest such one-dimensional model by neglecting much of the physics, and found the simplest model to be ill-posed. In fact the ill-posedness of two-fluid models is well-known and there has been plentiful debate surrounding the relation between this ill-posedness and the stability of the system of equations (see Drew [1982]; Ramshaw and Trapp [1978]; Dinh et al. [2003]; Jones and Prosperetti [1985]; Lyczkowski et al. [1978]; Stewart [1979]). For the purposes of this thesis, we conclude this review chapter by highlighting the importance of choosing suitable closure relations relevant to the physics and also guided by the stability and well-posedness of the resulting model.

In discussing the general modelling approach for two-phase flow the importance of flow regimes becomes evident. We have briefly introduced the basic identification of flow regimes through flow regime maps. There is plenty of scope to examine the domain of transition further, and as mentioned in Chapter 1, this observation motivates the work in Part II of this thesis.

We now focus our attention on Part I, namely the modelling of two-phase flow through oil wells which specifically accounts for the exsolution of the dissolved gas.

Part I

Modelling the two-phase flow in oil wells

Chapter 3

Homogeneous model

In this chapter we derive an isothermal homogeneous model (with a single velocity and pressure) for two-phase flows. We study the model for two systems of two-phase liquid–gas flow: incompressible–incompressible and incompressible–compressible. In both cases, we find that the application of Henry's law for the dissolved gas concentration predicts an unexpected rapid transition to a foam.

3.1 Introduction

Oil wells contain two-phase liquid and gas mixtures driven upwards due to a pressure gradient. At the high pressures in the reservoir, gaseous hydrocarbon components may be dissolved in the liquid phase. As the fluid mixture travels up the well the pressure decreases, allowing for the exsolution of the dissolved gaseous components. There is a pressure p_b, known as the *bubble-point pressure*, at which gas is first released from the liquid [Economides, 2013; Guo et al., 2011]. For pressures above the bubble-point, only liquid is present, and there is no free gas in the reservoir. At pressures below the bubble-point, gas and liquid phases co-exist.

In Section 3.2 we derive the mathematical model for the exsolving two-phase flow in an oil well producing under natural lift. We consider a system with a liquid inflow at the bottom of the well where $p > p_b$. Exsolution is assumed to first occur at a point along the well where $p = p_b$. We consider parameter ranges for the oil viscosity and density appropriate for a light oil, such as that produced in the Ekofisk oil field in the North Sea [Van Den Bark and Thomas, 1981].

The oil in the liquid phase is only slightly compressible; we therefore make the simplifying assumption that the density and viscosity of the oil, and consequently

the liquid phase, remains constant throughout the domain. The gaseous phase is clearly compressible and we will examine the effect of compressibility of the gas. We do this by studying both the incompressible–incompressible and incompressible–compressible liquid–gas systems in Sections 3.3 and 3.4 respectively. We will show that the inclusion of compressibility for the gas phase does not significantly affect the results. Moreover, in both systems, we find that the application of Henry's law for the dissolved gas concentration predicts a rapid transition to a foam, which is unexpected.

This chapter is motivated by recent work by Fowler and Robinson [2018] for the exsolving flow in volcanic conduits — we will follow their model derivation for the oil-well application. As discussed in Chapters 1 and 2, there is plentiful research concerning the modelling of multiphase flow in oil wells. To our knowledge, previous models of oil wells account for exsolution through mass transfer between the phases, but do not account for conservation of the dissolved gas phase. We adapt the two-fluid modelling approach, as presented in Section 2.6, to explicitly include the exsolution dynamics.

3.2 Two-fluid model including exsolution dynamics

In this section we introduce a two-fluid model for the exsolving upwelling flow in an oil well of length L and diameter d. For an oil well we assume a one-dimensional domain as the production tubing is long and thin: the length is of the order of kilometres, and the diameter is typically 10 cm. We describe the one-dimensional flow by the spatial coordinate along the pipe axis z: $z = 0$ is the bottom of the pipe and $z = L$ is the top.

The governing equations are derived from conservation of mass for the liquid, gas, and dissolved gas, and conservation of momentum and energy for the liquid and gas phases. Conservation of mass for the two phases is given by

$$(\alpha\rho_g)_t + (\alpha\rho_g v)_z = \Gamma, \tag{3.1a}$$

$$[(1-\alpha)\rho_l]_t + [(1-\alpha)\rho_l u]_z = -\Gamma, \tag{3.1b}$$

(see (2.90a) in Chapter 2) where we have used subscripts t and z to denote partial derivatives with respect to time and the spatial coordinate z; α is the gas volume fraction, ρ_g is the gas density, ρ_l is the liquid density, v is the velocity of the gas phase, u is the liquid velocity and Γ is the rate of exsolution.

We assume the density of the liquid phase to be the average of the oil and water densities; $\rho_l = \frac{1}{2}(\rho_w + \rho_o)$ where ρ_w and ρ_o are the densities of water and oil respec-

tively. Note that this assumes equal amounts of water and oil in the liquid phase. We will take the liquid phase as incompressible with a constant density ρ_l. This implicitly assumes that the exsolution of dissolved gas has a negligible effect on the density of the liquid phase.

Moreover, we will assume the real gas law (2.38) for an equation of state for the density of the gas,

$$\rho_g = \frac{p_g m_g}{ZRT_g}, \tag{3.2}$$

where p_g is the gas pressure, m_g is the molecular mass of the gas, R is the universal gas constant, T_g is the temperature of the gas and Z is the gas compressibility factor [Al-Safran and Brill, 2017].

Conservation of mass for the solute component gives

$$[(1-\alpha)\rho_l c + \alpha\rho_g]_t + [(1-\alpha)\rho_l cu + \alpha\rho_g v]_z = 0, \tag{3.3}$$

where c is concentration of dissolved gas defined as a mass fraction. We can use (3.1a) to rewrite this as

$$[(1-\alpha)\rho_l c]_t + [(1-\alpha)\rho_l cu]_z = -\Gamma. \tag{3.4}$$

Recall that the gas exsolution only begins at $p_l = p_b$, where p_l is the liquid pressure; until then $\alpha = 0$, $c = c_0$ and $\Gamma = 0$. So (3.1a) and (3.4) become relevant only in the region $p_l \leq p_b$.

The momentum-conservation equations (see (2.90b) in Chapter 2) for the liquid and gas phases are

$$(\alpha\rho_g v)_t + (\alpha\rho_g v^2)_z = -(\alpha p_g)_z - \alpha\rho_g g + M_g, \tag{3.5a}$$

$$[(1-\alpha)\rho_l u]_t + [(1-\alpha)\rho_l u^2]_z = -[(1-\alpha)p_l]_z - \frac{4}{d}\tau_l^w - (1-\alpha)\rho_l g + M_l, \tag{3.5b}$$

where g is the acceleration due to gravity, τ_l^w is the resistance due to wall shear stress for the liquid phase, and M_g, M_l are the rates of interfacial momentum transfer. Note that for both phases we have neglected the shear and Reynolds stresses and the interfacial convective flux. Furthermore, we have assumed the wall stress of the gas to be negligible, as we expect the gas phase to initially appear as bubbles dispersed in the liquid phase. This assumption may need to be altered if α becomes too large causing a bubbly-to-slug flow regime transition. The liquid wall stress is given (assuming $u > 0$) by

$$\tau_l^w = f_l \rho_l u^2, \tag{3.6}$$

where f_l is the friction factor (see (2.92) in Chapter 2). We assume the pressure difference (2.40) given by Stuhmiller [1977].

The interfacial-momentum transfer terms account for the interfacial pressure, and the drag and virtual-mass forces:

$$M_g = p_{gi}\alpha_z + \frac{3}{8}\frac{C_D\alpha\rho_l}{r_b}(v-u)|v-u| + \frac{1}{2}\alpha\rho_l\left[(u_t+uu_z)-(v_t+vv_z)\right], \tag{3.7a}$$

$$M_l = -p_{li}\alpha_z - \frac{3}{8}\frac{C_D\alpha\rho_l}{r_b}(v-u)|v-u| - \frac{1}{2}\alpha\rho_l\left[(u_t+uu_z)-(v_t+vv_z)\right], \tag{3.7b}$$

where p_{li}, p_{gi} are interfacial pressures, C_D is the drag coefficient and r_b is the typical bubble radius (see (2.48) in Chapter 2).

As discussed in Section 2.3.5, $p_{gi} = p_g$ is a reasonable assumption to make. The liquid interfacial preessure, however, is better modelled through an additional constitutive law such as $p_{li} = p_l + H\rho_l|v-u|^2$ (analogous to (2.40)). This is because as bubbles of gas move through the liquid, they will develop an average pressure that is distinct to the liquid pressure. In this chapter, we will however make the simplifying assumption that $p_{li} = p_l$. Using this in (3.7), and including the definition for the wall stress in (3.6) in (3.5) the momentum-conservation equations becomes

$$\begin{aligned}(\alpha\rho_g v)_t + (\alpha\rho_g v^2)_z = {}& -\alpha p_{gz} - g\alpha\rho_g + \frac{3}{8}\frac{C_D\alpha\rho_l}{r_b}|v-u|(v-u)\\ &+ \frac{1}{2}\alpha\rho_l\left[(u_t+uu_z)-(v_t+vv_z)\right],\end{aligned} \tag{3.8a}$$

$$\begin{aligned}[(1-\alpha)\rho_l u]_t + [(1-\alpha)\rho_l u^2]_z = {}& -(1-\alpha)p_{lz} - \frac{4f_l\rho_l u^2}{d} - g(1-\alpha)\rho_l\\ &- \frac{3}{8}\frac{C_D\alpha\rho_l}{r_b}|v-u|(v-u) - \frac{1}{2}\alpha\rho_l\left[(u_t+uu_z)-(v_t+vv_z)\right].\end{aligned} \tag{3.8b}$$

For the energy equations, we sum the two conservation equations (see (2.90c) in Chapter 2) to get

$$\begin{aligned}\rho_g c_{pg}\alpha\left(T_t+vT_z\right) + \rho_l c_{pl}(1-\alpha)\left(T_t+uT_z\right) = {}& \alpha\left[(p_g)_t + v(p_g)_z\right]\\ &+ (1-\alpha)\left[(p_l)_t + u(p_l)_z\right] + \left[(1-\alpha)k_l T_z\right]_z - \frac{4f_l\rho_l c_{pl}uT}{d},\end{aligned} \tag{3.9}$$

where c_{pk} is the specific heat capacity and we have employed the enthalpy–temperature relation (2.37) assuming a single temperature; $T = T_g = T_l$, which is based on the assumption that the interfacial transfer coefficients (β_{ki} in (2.58)) are large. Note that we have neglected the conductive heat flux and the wall heat flux of the gaseous phase, and the turbulent heat flux and viscous dissipation for both phases. We used (2.56) to write the heat flux for the liquid as $q_l = -k_l T_z$, where k_l is the thermal conductivity of the liquid phase. For the wall heat flux in the liquid phase we used (2.93) and assumed that the heated perimeter is equal to the hydraulic perimeter:

$q_{lw} = 4f_l\rho_l c_{pl} uT/d$. Finally we assumed $h_{ki} = h_k$ and then used (3.1) to enable cancellation of the interfacial enthalpy term in summation.

It is well understood through Henry's law that the concentration of dissolved gas is dependent on the pressure in the system; $c = Kp_l^\nu$, where K is a function of temperature T and ν is an empirically calculated constant. We assume K to be constant, which is appropriate for an isothermal flow. A commonly used correlation for oil developed by Vazquez and Beggs [1977] gives $\nu \approx 1$. The equilibrium between the dissolved gas concentration and the liquid pressure is therefore assumed to be:

$$c = Kp_l. \tag{3.10}$$

Recall that the pressure at which the dissolved gas starts to come out of solution is known as the bubble-point pressure p_b. Thus at this pressure the concentration of dissolved gas is saturated and we have: $c_0 = Kp_b$, where c_0 is the initial concentration of dissolved gas. If we assume the values for p_b and c_0 to be known, we can calculate the value of the parameter K.

Henry's law (3.10) states that the amount of dissolved gas decreases with the pressure in the well; thus as the pressure drops more gas comes out of solution. In reality, the growth of bubbles occurs through diffusion of the dissolved gas phase to the bubble surface; this may be a rate-limiting mechanism for gas exsolution, and we will examine this further in Chapter 4.

The conservation equations (3.1), (3.4), (3.8), (3.9) together with closure laws (2.40) for the pressure difference, (3.2) for the gas density and (3.10) giving Henry's law, are to be solved for the unknowns α, c, ρ_g, v, u, p_g, p_l, T, Γ. We need to supply inflow boundary conditions at the bottom of the well.

3.2.1 Boundary conditions

We consider a system with an inflow of liquid and an initial concentration c_0 of dissolved gas at the base $z = 0$. The inlet pressure, velocity and temperature are respectively denoted by p_{in}, $U(t)$ and T_{in}; thus the inlet boundary conditions are

$$p_l = p_{in}, \quad \alpha = 0, \quad c = c_0, \quad u = U(t), \quad T = T_{in} \ \text{ at } \ z = 0. \tag{3.11}$$

We prescribe the inflow velocity by consideration of the reservoir domain in which the producing well can effectively be considered as a point sink. Flow into the well is assumed to be as a spherically radial flow through a porous medium, driven by the pressure difference $(p_{res} - p_{in})$ between the far-field reservoir pressure p_{res} and that at the bottom of the well. This causes an approximate pressure field

$$p_l \sim p_{res} - \frac{d(p_{res} - p_{in})}{2r}, \tag{3.12}$$

(the quantity $d/2$ is the pipe radius and also the effective radius of the spherical sink for the reservoir flow), and thus a volume flux $2\pi k(p_{res} - p_{in})d/\mu$, where k is permeability and μ is liquid viscosity. Equating this to the volume flux in the well gives the prescription for the inlet velocity,

$$U(t) = \frac{8k(p_{res} - p_{in})}{\mu d}. \tag{3.13}$$

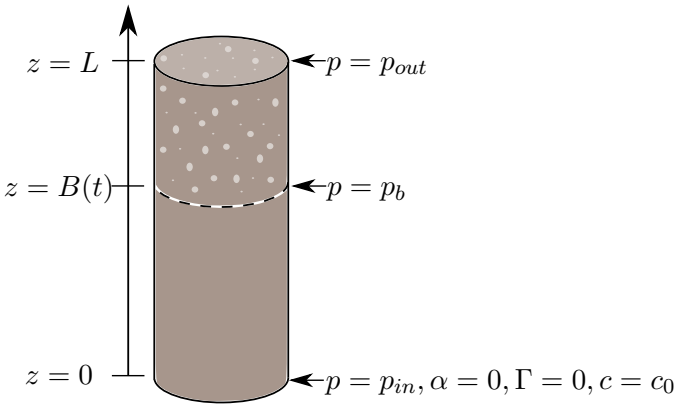


Figure 3.1: Oil well domain with boundary conditions.

Gas starts to come out of solution when the pressure reaches the bubble-point pressure p_b, whose location is denoted $z = B(t)$. The domain is thus split into a single-phase liquid domain in $0 \le z \le B(t)$ and a two-phase domain in $B(t) \le z \le L$; see figure 3.1. On the bubble-point boundary, the boundary conditions are

$$p_l = p_b, \quad \alpha = 0, \quad c = c_0, \quad u = U(t) \ \text{ at } \ z = B(t), \tag{3.14}$$

the last being a consequence of the incompressibility of the liquid.

Finally, at the exit, we prescribe the pressure; this is known as the 'choke' pressure, and is used to control the flow in the well:

$$p_l = p_g = p_{out} \ \text{ at } \ z = L. \tag{3.15}$$

We need this additional boundary condition for the pressure because the inflow pressure p_{in} is actually unknown, and appears as part of the solution to the model.

3.2.2 Nondimensionalisation and scaling

To nondimensionalise the model equations we introduce the following scalings:

$$\begin{gathered} z \sim L, \quad t \sim \frac{L}{U_0}, \quad v, u, U \sim U_0 = \frac{8kp_{res}}{\mu d}, \quad c \sim c_0, \quad \Gamma \sim \frac{\rho_l U_0}{L}, \\ p_l, p_g \sim \rho_l g L, \quad \rho_g \sim \rho_g^0 = \frac{\rho_l g L\, M_g}{ZR\Delta T}, \quad T - T_w \sim \Delta T, \end{gathered} \tag{3.16}$$

where U_0, c_0, ρ_g^0 are typical velocity (from (3.13)), dissolved gas concentration and gas density (from (3.2)) scales, respectively. T_w is the temperature of the wall and ΔT is the temperature difference between the top and bottom of the well, which we assume to be due to the crustal rock temperature. Thus $\Delta T = GL/k_R$, where G is the geothermal heat flux through continental crust and k_R is the rock thermal conductivity. Moreover, we suppose

$$p_{res} = \rho_c g L, \tag{3.17}$$

where ρ_c is the density of crustal rock. From (3.16) the dimensionless domain becomes $0 \leq z \leq 1$, with $z = b(t)$, defined via $B = Lb$, denoting the location of the bubble-point pressure.

Using the scalings in (3.16), conservation of mass (3.1) and (3.4), and momentum (3.8) yield

$$\delta\left[(\alpha\rho_g)_t + (\alpha\rho_g v)_z\right] = \Gamma, \tag{3.18a}$$

$$(1-\alpha)_t + ((1-\alpha)u)_z = -\Gamma, \tag{3.18b}$$

$$\left[(1-\alpha)c\right]_t + \left[(1-\alpha)uc\right]_z = -\frac{1}{c_0}\Gamma, \tag{3.18c}$$

$$\begin{aligned} F^2\delta\left[(\alpha\rho_g v)_t + (\alpha\rho_g v^2)_z\right] &= -\alpha p_{gz} - \delta\alpha - \kappa_D\alpha|v-u|(v-u) \\ &\quad + \frac{1}{2}F^2\left[(u_t + uu_z) - (v_t + vv_z)\right], \end{aligned} \tag{3.18d}$$

$$\begin{aligned} F^2\left[((1-\alpha)u)_t + ((1-\alpha)u^2)_z\right] &= -(1-\alpha)p_{lz} - \kappa_w u^2 - (1-\alpha) \\ &\quad + \kappa_D\alpha|v-u|(v-u) - \frac{1}{2}F^2\left[(u_t + uu_z) - (v_t + vv_z)\right], \end{aligned} \tag{3.18e}$$

with dimensionless closure laws from (3.2), (2.40) and (3.10):

$$\rho_g = \frac{p_g}{T}, \tag{3.19a}$$

$$p_g - p_l = -HF^2(v-u)^2, \tag{3.19b}$$

$$c = \frac{p_l}{\Pi}. \tag{3.19c}$$

We have introduced the following dimensionless parameters:

$$\delta = \frac{\rho_g^0}{\rho_l}, \quad F = \frac{U_0}{\sqrt{gL}}, \quad \kappa_D = \frac{3C_D}{8}\frac{U_0^2}{gr_b}, \quad \kappa_w = \frac{4f_l U_0^2}{gd}, \quad \Pi = \frac{p_b}{\rho_l g L}. \tag{3.20}$$

Note that the parameter Π, defined above, is the dimensionless bubble-point pressure. For exsolution in the well we require that the bubble-point pressure is less than the

reservoir pressure, i. e. $\Pi < p_R$ where $p_R = p_{res}/\rho_l g L$ is the dimensionless reservoir pressure.

The dimensionless energy equation is

$$\delta\gamma\rho_g\alpha\left(T_t + vT_z\right) + (1-\alpha)\left(T_t + uT_z\right) = \sigma\left[(1-\alpha)T_z\right]_z + \beta\left[\alpha\left((p_g)_t + v(p_g)_z\right) + (1-\alpha)\left((p_l)_t + u(p_l)_z\right)\right] - \frac{4}{\mathrm{Pe}_T}u(T - \hat{T}_w), \tag{3.21}$$

where

$$\gamma = \frac{c_{pg}}{c_{pl}}, \quad \beta = \frac{Lg}{c_{pl}\Delta T}, \quad \sigma = \frac{k_l}{c_{pl}\rho_l U_0 L}, \quad \mathrm{Pe}_T = \frac{U_0 d^2}{\kappa_T L}, \quad \hat{T}_w = \frac{T_w}{\Delta T}. \tag{3.22}$$

The reduced Péclet number Pe_T is defined in terms of the eddy thermal diffusivity $\kappa_T = f_l U_0 d$, which is also used to define the thermal conductivity in a turbulent flow: $k_l = \rho_l c_{pl}\kappa_T$ [Fowler, 2011].

The boundary conditions (3.11), (3.14) and (3.15) become

$$p_l = p_0, \quad \alpha = 0, \quad c = 1, \quad u = U(t) = 1 - \delta_c p_0, \quad T = \hat{T}_{in} \quad \text{at} \quad z = 0, \tag{3.23a}$$

$$p_l = \Pi, \quad \alpha = 0, \quad c = 1, \quad u = U(t) \quad \text{at} \quad z = b(t), \tag{3.23b}$$

$$p_l = p_g = p_1 \quad \text{at} \quad z = 1, \tag{3.23c}$$

where

$$\delta_c = \frac{\rho_l}{\rho_c}, \quad p_0 = \frac{p_{in}}{\rho_l g L}, \quad p_1 = \frac{p_{out}}{\rho_l g L}, \quad \hat{T}_{in} = \frac{T_{in}}{\Delta T}. \tag{3.24}$$

The model parameters are given in table 3.1 and are used to compute the dimensionless parameters in table 3.2. We first note that using these parameters in (3.21) suggests that the convective and advective terms in the energy equation are negligibly small, and the adiabatic term in β is quite small. Importantly, the wall heat flux term scaled by $4/\mathrm{Pe}_T$ is large. We interpret this as the temperature in the well rapidly adjusting to the wall temperature. It is therefore sensible to consider an isothermal flow with a constant temperature T.

Moreover, using H and F from tables 3.1 and 3.2 in (3.19b) suggests that it is reasonable to take $p_g \approx p_l$, and denote the single pressure as p. Table 3.2 also gives $\delta, F, \kappa_w \ll 1$; thus if we neglect terms of $O(F^2)$ and $O(\delta)$ in (3.18d)–(3.18e) and assume the single pressure we get

$$\alpha p_z = -\kappa_D \alpha |v-u|(v-u), \tag{3.25a}$$

$$(1-\alpha)p_z = -(1-\alpha) + \kappa_D \alpha |v-u|(v-u). \tag{3.25b}$$

Summation of the two equations above shows the pressure gradient to be dependent on gravitational deceleration:

$$p_z = -(1-\alpha). \tag{3.26}$$

Parameter	Value	Source
d	0.1 m	Govier and Aziz [2008]
L	10^3 m	Govier and Aziz [2008]
C_D	$O(1)$	Ishii and Mishima [1984]
f_l	0.005	Wallis [1969]
k	10^{-12}–10^{-15} m^2	Chen [2007]
H	0.25 kg m^{-3}	Pauchon and Banerjee [1986]
p_{res}	28 MPa	$(= \rho_c g L)$
U_0	0.2 m s^{-1}	$(= 8kp_{res}/\mu d$, using $k = 10^{-13}$ m$^2)$
μ	$10^{-4} - 10^{-3}$ Pa s	Chen [2007]
ρ_g^0	1.14 kg m^{-3}	Shoham [2006]
ρ_w	10^3 kg m^{-3}	Livescu et al. [2010]
ρ_o	$\leq 0.92 \times 10^3$ kg m^{-3}	Meyer and Attanasi [2003]
ρ_l	0.96×10^3 kg m^{-3}	$(= \frac{1}{2}(\rho_w + \rho_o))$
ρ_c	2.8×10^3 kg m^{-3}	Christensen and Mooney [1995]
c_{pg}	10^3 J kg^{-1} K^{-1}	Guo et al. [2014]
c_{pl}	10^3 J kg^{-1} K^{-1}	Guo et al. [2014]
κ_T	10^{-4} m^2 s^{-1}	$(= f_l U_0 d)$
k_l	96 W m^{-1} K^{-1}	$(= \rho_l c_{pl} \kappa_T)$
G	65 mW m^{-2}	Davies [2013]
k_R	2.5 Wm^{-1} K^{-1}	Fowler [1990]
ΔT	26 K	$(= GL/k_R)$

Table 3.1: Parameters and typical values. The drag coefficient C_D is a decreasing function of the particle Reynolds number $\mathrm{Re}_p = r_b U_0 \rho_l / \mu$. In this chapter, we assume the parameter values for a light oil with viscosity $\mu = 10^{-3}$ Pa s, density $\rho_l = 0.96 \times 10^3$ kg m^{-3}.

Using this in (3.25a) we find

$$v - u = \sqrt{\frac{(1-\alpha)}{\kappa_D}}. \tag{3.27}$$

If $\kappa_D \gg 1$, which is the case for sufficiently small bubbles, then $v \approx u$ is appropriate. Note that, as discussed previously in Section 2.3.5, we could have assumed a linear drag with respect to the relative velocity. We see from (3.27) that this would have resulted in the same conclusion that for κ_D sufficiently large it is reasonable to take $v \approx u$.

Parameter	Value
δ	1.2×10^{-3}
F	2×10^{-3}
δ_c	0.34
κ_D	$(1.5 \times 10^{-3})\, C_D/[r_b]$
κ_w	0.8×10^{-3}
γ	1
β	0.38
σ	0.5×10^{-6}
Pe_T	0.02
p_R	2.97
Π	$< p_R$

Table 3.2: Dimensionless parameters and their approximate values using table 3.1. $[r_b]$ is the numerical value of r_b in centimetres.

We define a homogeneous model to be one in which a single velocity is assumed for both phases. The reduced model (where we keep the $O(\delta)$ conservation of mass for the gaseous phase) that we consider is therefore given by

$$\delta\left[(\rho_g\alpha)_t + (\rho_g\alpha u)_z\right] = \Gamma, \tag{3.28a}$$

$$(1-\alpha)_t + \left[(1-\alpha)u\right]_z = -\Gamma, \tag{3.28b}$$

$$\left[(1-\alpha)c\right]_t + \left[(1-\alpha)cu\right]_z = -\frac{1}{c_0}\Gamma, \tag{3.28c}$$

$$p_z = -(1-\alpha), \tag{3.28d}$$

$$\rho_g = p, \tag{3.28e}$$

$$c = \frac{p}{\Pi}, \tag{3.28f}$$

where we have rescaled the gas density by $\rho_g^0 = \rho_l g L\, m_g/ZRT$ with constant temperature T to get (3.28e). The boundary conditions are now

$$p = p_0, \quad \alpha = 0, \quad c = 1, \quad u = U(t) = 1 - \delta_c p_0, \ \text{ at } \ z = 0, \tag{3.29a}$$

$$p = \Pi, \quad \alpha = 0, \quad c = 1, \quad u = U(t) \ \text{ at } \ z = b(t), \tag{3.29b}$$

$$p = p_1 \ \text{ at } \ z = 1. \tag{3.29c}$$

In this chapter we will study two systems; one in which we ignore the effects of compressibility and assume the gas density to be constant in an incompressible–incompressible two-phase flow in Section 3.3; and a second where we account for

compressibility and repeat the analysis for a compressible–incompressible flow in Section 3.4.

As indicated in table 3.1, there is a large range of possible parameter choices across the different kinds of oil and gases; this holds true on the scale of a single oil field. Ghorbani et al. [2019] supplied data for the following quantities for 127 oil and gas production wells in the Reshadat oil field in Iran: oil viscosity $\mu_o = 3.8 - 4.3 \times 10^{-3}$ Pa s; oil density $\rho_o = 0.9 - 0.94 \times 10^3$ kg m^{-3}; reservoir pressure $p_{res} = 17 - 26$ MPa; bubble-point pressure $p_b = 14 - 18$ MPa; well-head pressure $p_{out} = 2 - 6$ MPa; and the gas–liquid ratio $GLR = 7 - 137$. The gas–liquid ratio is the dimensionless ratio, by volume, of produced gas to produced liquid (oil and water) and is given at *standard conditions*, that is at atmospheric pressure $p_{atm} = 0.1$ MPa and temperature 288 K.

The GLR can be used to derive a mass fraction for the gas phase. For 1 m^3 of liquid, we have GLR m^3 of gas. Converting this into mass measurements we find that ρ_l kg of liquid corresponds to $(\rho_g^0\, GLR)$ kg of gas. Assuming $\rho_g^0 = 1$ kg m^{-3} at standard conditions then, using the range $GLR = 7 - 137$, the mass of the gas lies in the range $\overline{m}_g = 7 - 137$ kg. Similarly, using ρ_l from table 3.1, we calculate the mass of the liquid phase to be $\overline{m}_l = 0.96 \times 10^3$ kg. If we assume all the gas to be initially dissolved in the liquid phase, we can derive a range for the initial dissolved gas concentration to be $c_0 \approx 0.007 - 0.14$. For this particular oil field it is therefore appropriate to assume $c_0 \ll 1$, however there are fields producing predominantly gaseous hydrocarbons for which $c_0 \sim O(1)$. We therefore study the system (3.28) in two limits: $\delta \ll 1$, $c_0 \sim O(1)$ and $\delta \sim c_0 \ll 1$.

3.3 Incompressible–incompressible system

If we assume constant densities in both phases then we can take $\rho_g = 1$ in place of (3.28e). Thus our incompressible–incompressible system is:

$$\delta\left[\alpha_t + (\alpha u)_z\right] = \Gamma, \tag{3.30a}$$

$$(1-\alpha)_t + ((1-\alpha)u)_z = -\Gamma, \tag{3.30b}$$

$$[(1-\alpha)c]_t + [(1-\alpha)cu]_z = -\frac{1}{c_0}\Gamma \tag{3.30c}$$

$$p_z = -(1-\alpha), \tag{3.30d}$$

$$c = \frac{p}{\Pi}. \tag{3.30e}$$

We will examine the characteristics of (3.30) and seek solutions in two limits: $\delta \ll 1$, $c_0 \sim O(1)$ and $\delta \sim c_0 \ll 1$.

3.3.1 Characteristics

In (3.30) we have five equations for the five unknowns α, u, p, Γ, c, but we only have derivatives of α, u, p, so to analyse the characteristics we must rearrange the equations as a system of three equations. We do this by using (3.30a) for Γ and (3.30e) for c in (3.30b) and (3.30c). The resulting system of equations can be represented by

$$\mathbf{A}\boldsymbol{\psi}_t + \mathbf{B}\boldsymbol{\psi}_z = \mathbf{c}, \tag{3.31}$$

where $\boldsymbol{\psi} = (\alpha, u, p)^T$ with

$$\begin{aligned}
\mathbf{A} &= \begin{bmatrix} (1-\delta) & 0 & 0 \\ -\left(p - \frac{\delta\Pi}{c_0}\right) & 0 & (1-\alpha) \\ 0 & 0 & 0 \end{bmatrix}, \quad \mathbf{c} = \begin{bmatrix} 0 \\ 0 \\ -(1-\alpha) \end{bmatrix}, \\
\mathbf{B} &= \begin{bmatrix} (1-\delta)u & -(1-\alpha+\delta\alpha) & 0 \\ -u\left(p - \frac{\delta\Pi}{c_0}\right) & \left(\frac{\delta\Pi}{c_0}\alpha + (1-\alpha)p\right) & (1-\alpha)u \\ 0 & 0 & 1 \end{bmatrix}.
\end{aligned} \tag{3.32}$$

The characteristics slopes are computed by solving

$$\det(\mathbf{B} - \lambda\mathbf{A}) = 0, \tag{3.33}$$

which, using (3.32), gives

$$(u-\lambda)\left[(1-\delta)\left(\frac{\delta\Pi}{c_0}\alpha + (1-\alpha)p\right) - ((1-\alpha+\delta\alpha)\left(p - \frac{\delta\Pi}{c_0}\right)\right] = 0. \tag{3.34}$$

The polynomial (3.34) has a single root $\lambda = u$. We have 'lost' two characteristics; the system of three equations only has one characteristic speed. This lost information is due to previously neglecting the $O(F^2)$ terms in the momentum equations (3.18d)–(3.18e) in the derivation of (3.30d). In principle we have lost the terms $\epsilon(u_t + uu_z)$, for constant $\epsilon > 0$, in (3.30d). For demonstration purposes we consider only the inclusion of an ϵu_t term in the left-hand side of (3.30d); the matrix $\mathbf{A}$ in (3.32) then becomes

$$\mathbf{A}' = \begin{bmatrix} (1-\delta) & 0 & 0 \\ -\left(p - \frac{\delta\Pi}{c_0}\right) & 0 & (1-\alpha) \\ 0 & \epsilon & 0 \end{bmatrix}. \tag{3.35}$$

Solving (3.33) with $\mathbf{A}'$ replacing $\mathbf{A}$ yields the characteristic polynomial:

$$(u-\lambda)\left[\epsilon\lambda(u-\lambda)(1-\delta)(1-\alpha) + \left(p - \frac{\delta\Pi}{c_0}\right)\right] = 0, \tag{3.36}$$

which solves to give the characteristic speed we already had ($\lambda_1 = u$) and two further solutions:

$$\lambda_{2,3} = \frac{1}{2}\left[u \pm \left(u^2 + \frac{4\delta\left(\frac{\Pi}{c_0} - p\right)}{\epsilon(1-\delta)(1-\alpha)}\right)^{1/2}\right]. \tag{3.37}$$

As we take $\epsilon \to 0$, (3.37) shows $\lambda_{2,3} \to \pm\infty$ corresponding to infinite wave speeds. Thus we see that by neglecting the $F^2 u_t$ term in (3.18) we introduce infinite speed of information translation through the system. This analysis shows that (3.30) is a hyperbolic system of equations.

3.3.2 The case $\delta \ll 1$, $c_0 \sim O(1)$

To solve (3.30), we consider the domain in two regions; the single-phase region $0 \leq z \leq b(t)$ and the two-phase region $b(t) \leq z \leq 1$. In the single-phase region we have $\alpha = 0$, $c = 1$ and $\Gamma = 0$. Recall that Henry's law in (3.30e) does not become relevant until $p \leq \Pi$. (3.30b) then implies $u = U(t)$ and (3.30d) gives a linear pressure drop:

$$p = p_0 - z. \tag{3.38}$$

Since $z = b(t)$ is defined by the bubble-point pressure $p = \Pi$, we have

$$b(t) = p_0 - \Pi. \tag{3.39}$$

In the two-phase region $b(t) \leq z \leq 1$, we still have $\Gamma \approx 0$ from (3.30a). Using this together with (3.30b) and (3.30e) in (3.30c) gives

$$(1-\alpha)\left(p_t + u p_z\right) = 0, \tag{3.40}$$

which implies that above $z = b$, either $\alpha = 1$ or the pressure stays constant. But from (3.30d) we have

$$p_z = -(1-\alpha). \tag{3.41}$$

The two equations (3.40) and (3.41) demand that $\alpha = 1$ and $p = \Pi$, which means that above $z = b(t)$ the pressure stays constant, and the fluid is (almost) all gas. The resulting discontinuity in α at $z = b(t)$ implies that the limit $\delta \ll 1$ is singular, and there is a thin transition layer where α changes rapidly.

To study the transition layer near $b(t)$ we define

$$z = b(t) + \delta Z. \tag{3.42}$$

The governing equations become

$$\delta\left[\alpha_t - \frac{\dot{b}}{\delta}\alpha_Z + \frac{1}{\delta}(\alpha u)_Z\right] = \Gamma, \tag{3.43a}$$

$$-\alpha_t + \frac{\dot{b}}{\delta}\alpha_Z + \frac{1}{\delta}[(1-\alpha)u]_Z = -\Gamma, \tag{3.43b}$$

$$(1-\alpha)\left(p_t - \frac{\dot{b}}{\delta}p_Z + \frac{u}{\delta}p_Z\right) = \Gamma\left(p - \frac{\Pi}{c_0}\right), \tag{3.43c}$$

$$\frac{1}{\delta}p_Z = -(1-\alpha), \tag{3.43d}$$

where $\dot{b}$ denotes the time derivative of $b(t)$ and we have used Henry's law (3.30e) to write the concentration c in terms of the pressure. The boundary conditions at the bubble-point boundary are

$$p = \Pi, \quad \alpha = 0, \quad u = U(t), \quad \text{at} \quad Z = 0. \tag{3.44}$$

Letting $\delta \to 0$, we see that (3.43d) gives $p = \Pi$. We can also solve for Γ by substituting (3.43d) into (3.43c) to get

$$\Gamma = \frac{c_0(1-\alpha)^2(u-\dot{b})}{\Pi\,(1-c_0)}. \tag{3.45}$$

We can then solve the first two equations (with $\delta \to 0$) to find the velocity

$$u(Z,t) = \dot{b} - (\dot{b} - U(t))\sqrt{1 + \frac{2Zc_0}{\Pi(1-c_0)}}, \tag{3.46}$$

and the gas volume fraction:

$$\alpha(Z,t) = 1 - \frac{1}{\sqrt{1 + \dfrac{2Zc_0}{\Pi(1-c_0)}}}. \tag{3.47}$$

The model predicts that at the bubble-point the flow converts almost instantaneously from a pure liquid to a highly gaseous foam, or else to a misty flow. The physical reason for this is that for any significant pressure below the bubble-point pressure, the equilibrium equation for the dissolved gas concentration indicates that a significant fraction of gas has been exsolved, and simple expansion necessitates that it must fill almost all the available volume.

This is contradictory to the oil-well literature which suggests that the oil domain supports gradual transitions between two-phase flow regimes [Shoham, 2006; Al-Safran and Brill, 2017] and that a significant liquid oil fraction exists at the outlet. The only way this can be consistent with the present homogeneous model is if the

outlet pressure $p_{out} \approx p_b$ ($p_1 \approx \Pi$ in dimensionless variables), but there is no reason that this should be the case, and it is generally not; for example, values quoted by Golan and Whitson [1991] for well No. B-11 in the Ekofisk oil field are $p_{res} = 50$ MPa, $p_b = 36$ MPa and $p_{out} = 29$ MPa.

It is possible that this conclusion is a result of the simplification to equal phase velocities, which is due to the assumption that $\kappa_D \gg 1$ (see (3.27)), which requires sufficiently small bubbles (see table 3.2). As α grows, it is natural to suppose that this assumption breaks down, either through bubble growth or through regime transition, and that a two-fluid model with different velocities ($u \neq v$) becomes relevant. However, this would not alter the conclusion of a rapid transition to a foam or mist, which is due to the fact that since $\delta \ll 1$ in (3.30a), then $\Gamma \ll 1$, so that (3.30c) again implies $p \approx$ constant, which requires $\alpha \approx 1$. We therefore keep the homogeneous model, but consider a different parameter regime, specifically that in which the initial concentration of dissolved gas is small; $c_0 \sim \delta \ll 1$. It can be seen from (3.47) that this is likely to spread out the exsolution region.

3.3.3 The case $c_0 \sim \delta \ll 1$

Let us suppose that $\delta/c_0 = \lambda \sim O(1)$. We rescale $\Gamma = \delta\bar{\Gamma}$ (and then subsequently drop the overbar) and assume $\delta \ll 1$, so that the equations (3.30a)–(3.30d) take the approximate form

$$\alpha_t + (\alpha u)_z = \Gamma, \tag{3.48a}$$

$$(1-\alpha)_t + [(1-\alpha)u]_z = 0, \tag{3.48b}$$

$$[(1-\alpha)c]_t + [(1-\alpha)cu]_z = -\lambda\Gamma, \tag{3.48c}$$

$$p_z = -(1-\alpha), \tag{3.48d}$$

$$c = \frac{p}{\Pi}. \tag{3.48e}$$

In the liquid region $0 \leq z \leq b(t)$ we solve (3.48a)–(3.48d) with $c = 1$. The results are the same as those derived above in Section 3.3.2:

$$p = p_0 - z, \quad \alpha = 0, \quad u = U(t), \quad b(t) = p_0 - \Pi. \tag{3.49}$$

For the two-phase region $b(t) \leq z \leq 1$ (3.48e) applies, and we utilise an observation by Fowler and Robinson [2018] that if two quantities ϕ and ψ satisfy

$$\phi_t + (\phi u)_z = 0, \tag{3.50a}$$

$$\psi_t + (\psi u)_z = 0, \tag{3.50b}$$

then

$$\left(\frac{\phi}{\psi}\right)_t + u\left(\frac{\phi}{\psi}\right)_z = 0. \tag{3.51}$$

If we apply the above observation to the equation (λ(3.48a)+(3.48c)) and (3.48b), we find that $(c + \lambda\alpha/(1-\alpha))$ is advected with the flow. Using the fact that at $z = b(t)$, $\alpha = 0$ and $c = 1$, this conserved quantity is in fact equal to one. Using (3.48e), we can write an expression for α in terms of p:

$$\alpha = \frac{1 - \dfrac{p}{\Pi}}{1 + \lambda - \dfrac{p}{\Pi}}. \tag{3.52}$$

The gas volume fraction increases as the pressure decreases (see figure 3.2), but now importantly α is bounded above by $1/(1+\lambda)$.

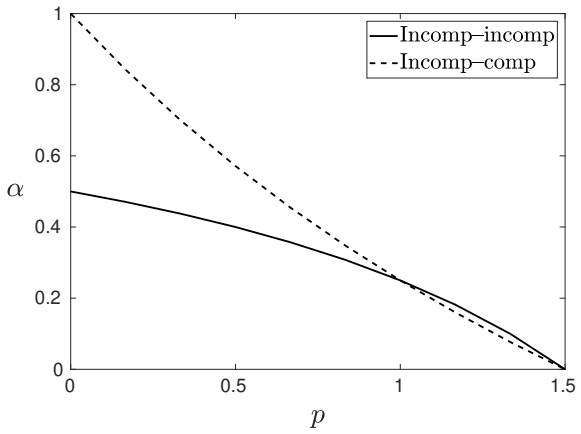


Figure 3.2: The relationship between gas volume fraction and dimensionless pressure for the incompressible–incompressible system (3.52) and the incompressible–compressible system (3.67) with $\Pi = 1.5$ and $\lambda = 1$.

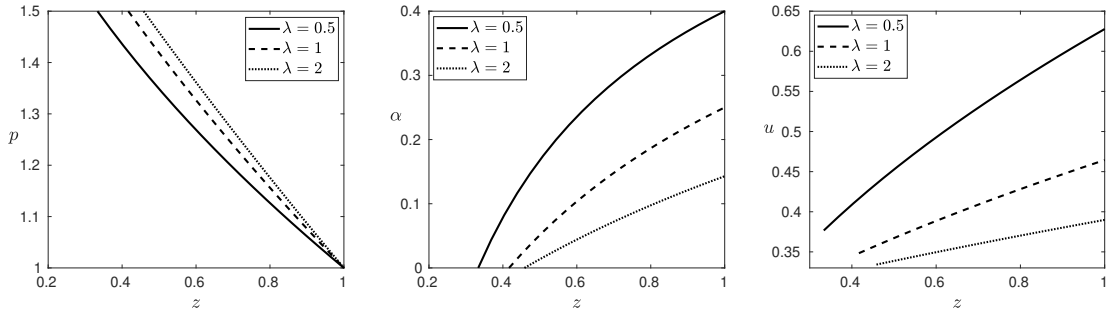
We solve the pressure-drop equation (3.48d) using (3.52) to obtain

$$p = \Pi(1+\lambda) - \sqrt{\lambda^2\Pi^2 + 2\lambda\Pi(z-b)}. \tag{3.53}$$

In writing (3.53), we have selected the negative square root, as this corresponds to a profile in which the pressure decreases with height.

The velocity profile can be found by using (3.52) and (3.53) in (3.48b) with the appropriate boundary conditions at $z = b(t)$, and the result of this is

$$u = \dot{b} + \left(U(t) - \dot{b}\right)\left[\frac{2(z-b) + \lambda\Pi}{\lambda\Pi}\right]^{1/2}. \tag{3.54}$$



(a) $p(z)$. **(b)** $\alpha(z)$. **(c)** $u(z)$.

Figure 3.3: Analytical steady-state solutions to (3.48a)–(3.48e) using parameters from tables 3.1 and 3.2. For illustration purposes, we choose $\Pi = 1.5$, $p_1 = 1$. Varying the value of λ gives different p_0 from (3.55) which in turns changes $b(t)$ from (3.39).

Applying the boundary condition for the pressure p_1 at $z = 1$ in (3.53), with the definition of $b(t)$ from (3.39), we obtain

$$p_0 = (1 + p_1) - \frac{(p_1 - \Pi)^2}{2\lambda\Pi}, \tag{3.55}$$

and this determines the inlet velocity, since from (3.29a), $U = 1 - \delta_c p_0$. Note that in (3.55), as Π and λ are constants, the inlet pressure is a function of the outflow pressure p_1. Namely, if p_1 is kept constant, then p_0 is also fixed.

The steady-state analytical solutions α (3.52), p (3.53) and u (3.54) are shown in figure 3.3. We used the parameters given in tables 3.1 and 3.2, and examined the effect of changing the parameter λ which corresponds to changing the inflow pressure p_0 from (3.55) and consequently the value for b.

Increasing λ resulted in a shorter two-phase domain i.e. increased b (see figure 3.3) which suggests that for lower initial gas concentrations, the pressure gradient from the inlet pressure to the bubble-point pressure is increased. The exit pressure p_1 is a boundary condition in the system, so changing λ has an effect on the length of the two-phase domain, but not the exit pressure. Thus the pressure drop will be the same but over a different length domain; see figure 3.3a. The exit volume fraction however depends on λ from (3.52), so different amounts of gas are released over the changing domain lengths, namely more gas comes out of solution for decreasing λ (i.e. increasing c_0); see figure 3.3b. We also see that the velocity increases for decreasing λ, so the velocity is higher when there is more exsolved gas in the system; see figure 3.3c.

This analysis shows that by assuming that the initial amount of dissolved gas is small and comparable to the density ratio, we can essentially stretch out the two-phase flow region. This parameter limit is appropriate for oil wells in producing fields

such as Reshadat in Iran, discussed in Section 3.2.2.

We now consider how realistic it is to assume the two-phase flow in an oil well to be incompressible–incompressible. The liquid phase comprises water and oil. It is reasonable to assume water to be incompressible, and as oil is only slightly compressible, we conclude it reasonable to treat the liquid phase as approximately incompressible. The gaseous phase, however, is evidently compressible. We therefore now repeat the same analysis for an incompressible–compressible two-phase mixture.

3.4 Incompressible–compressible system

We use the equation of state for ρ_g (3.28e) in the mass conservation equation (3.28a), then we can write (3.28) as:

$$\delta\left[(p\alpha)_t + (p\alpha u)_z\right] = \Gamma, \tag{3.56a}$$

$$(1-\alpha)_t + \left[(1-\alpha)u\right]_z = -\Gamma, \tag{3.56b}$$

$$\left[(1-\alpha)c\right]_t + \left[(1-\alpha)cu\right]_z = -\frac{1}{c_0}\Gamma, \tag{3.56c}$$

$$p_z = -(1-\alpha), \tag{3.56d}$$

$$c = \frac{p}{\Pi}. \tag{3.56e}$$

3.4.1 Characteristics

We can write (3.56) in the form (3.31) with

$$\mathbf{A} = \begin{bmatrix} 1-\delta p & 0 & -\delta\alpha \\ p\left(1-\frac{\delta\Pi}{c_0}\right) & 0 & -\left((1-\alpha)+\frac{\delta\Pi}{c_0}\alpha\right) \\ 0 & 0 & 0 \end{bmatrix}, \quad \mathbf{c} = \begin{bmatrix} 0 \\ 0 \\ -(1-\alpha) \end{bmatrix},$$

$$\mathbf{B} = \begin{bmatrix} u(1-\delta p) & -((1-\alpha)+\delta\alpha p) & -\delta\alpha u \\ pu\left(1-\frac{\delta\Pi}{c_0}\right) & -\left((1-\alpha)p+\frac{\delta\Pi}{c_0}\alpha p\right) & -\left((1-\alpha)u+\frac{\delta\Pi}{c_0}\alpha u\right) \\ 0 & 0 & 1 \end{bmatrix}. \tag{3.57}$$

The characteristic speeds are given by solving (3.33) which gives

$$(u-\lambda)\left[((1-\alpha)+\delta\alpha p)\left(1-\frac{\delta\Pi}{c_0}\right)p - (1-\delta p)p\left((1-\alpha)+\frac{\delta\Pi}{c_0}\alpha\right)\right] = 0. \tag{3.58}$$

As in the incompressible–incompressible case this has only one characteristic speed ($\lambda = u$) for a system of three equations. The discussion presented in Section 3.3.1

also applies here, and so we consider the same equations (3.56) with an additional ϵu_t term on the left hand side in (3.56d). This alters the matrix $\mathbf{A}$ to be

$$\mathbf{A}' = \begin{bmatrix} 1-\delta p & 0 & -\delta\alpha \\ p\left(1-\frac{\delta\Pi}{c_0}\right) & 0 & -\left((1-\alpha)+\frac{\delta\Pi}{c_0}\alpha\right) \\ 0 & \epsilon & 0 \end{bmatrix}. \tag{3.59}$$

The resultant polynomial from (3.33) with $\mathbf{B}$ in (3.57) and $\mathbf{A}'$ as above is

$$(u-\lambda)\left(f_3 - \epsilon\lambda f_2 - \epsilon\lambda^2 f_1\right) = 0, \tag{3.60}$$

with $f_1 = \delta\alpha p(1-\delta\Pi/c_0)$, $f_2 = [(1-\delta p)(1-\alpha+\alpha\delta\Pi/c_0) - u\delta\alpha p(1-\delta\Pi/c_0)]$ and $f_3 = \delta p(p-\Pi/c_0)$. Solving (3.60) gives $\lambda_1 = u$ again, and two further solutions:

$$\lambda_{2,3} = -\frac{f_2}{2f_1} \pm \frac{1}{2f_1}\left(f_2^2 + \frac{4f_1 f_3}{\epsilon}\right)^{1/2}, \tag{3.61}$$

thus $\lambda_{2,3} \to \pm\infty$ when we take $\epsilon \to 0$. As in the incompressible–incompressible case this corresponds to infinite wave speeds, and we thus retain a hyperbolic system. We will now study solutions of the homogeneous model in the same parameter limits $\delta \ll 1$, $c_0 \sim O(1)$ and $c_0 \sim \delta \ll 1$.

3.4.2 The case $\delta \ll 1$, $c_0 \sim O(1)$

In the single-phase domain $0 \le z \le b(t)$ the equations are (3.56a)–(3.56d) without Henry's law in (3.56e), and the analysis is the same as the incompressible–incompressible case. We have $\alpha = 0$, $c = 1$, $u = U(t)$ and $p = p_0 - z$ from (3.56d). We also find that $b(t) = p_0 - \Pi$ as in (3.39).

In the two-phase region $b(t) \le z \le 1$, the dissolved gas mass-conservation (3.56b) and momentum-conservation (3.56c) equations give the same conclusion as the incompressible–incompressible case; which is that above $z = b(t)$ we must have $\alpha = 1$ and $p = \Pi$ constant (see discussion following (3.41)). The outer solutions in both cases are exactly the same, and we will again have a transition layer at $z = b(t)$. In the domain $z = b(t) + \delta Z$ we can rewrite (3.56a)–(3.56e) as:

$$\delta\left[(p\alpha)_t - \frac{\dot{b}}{\delta}(\alpha p)_Z + \frac{1}{\delta}(p\alpha u)_Z\right] = \Gamma, \tag{3.62a}$$

$$-\alpha_t + \frac{\dot{b}}{\delta}\alpha_Z + \frac{1}{\delta}((1-\alpha)u)_Z = -\Gamma, \tag{3.62b}$$

$$(1-\alpha)\left[p_t - \frac{\dot{b}}{\delta}p_Z + \frac{u}{\delta}p_Z\right] = \Gamma\left(p - \frac{\Pi}{c_0}\right), \tag{3.62c}$$

$$\frac{1}{\delta}p_Z = -(1-\alpha), \tag{3.62d}$$

with boundary conditions (3.44) at $Z = 0$. For $\delta \to 0$ we have constant pressure $p = \Pi$ from (3.62d). The rate of exsolution is given by rearranging (3.62c) to derive the same analytical form as the incompressible–incompressible model for the rate function Γ in (3.45). Summing (3.62a) and (3.62b) and taking $p = \Pi$ and $\delta \to 0$ we find

$$u_Z = \frac{\Gamma}{\Pi}. \tag{3.63}$$

Rearranging (3.63) for Γ and substituting it into (3.45) we are able to find an analytical form for the velocity:

$$u(Z,t) = \dot{b} - (\dot{b} - U(t))\sqrt{1 + \frac{2Zc_0}{\Pi^2(1-c_0)}}, \tag{3.64}$$

which in turn gives an expression for the gas volume fraction

$$\alpha(Z,t) = 1 - \frac{1}{\sqrt{1 + \dfrac{2Zc_0}{\Pi^2(1-c_0)}}}. \tag{3.65}$$

Besides an additional factor of Π that comes from the compressible equation of state in (3.28e), the expressions for the velocity and gas volume fraction above are exactly the same as those in the incompressible–incompressible system in (3.46) and (3.47), and thus the model conclusions are also identical. We now examine the compressible–incompressible system with $\delta/c_0 \sim O(1)$.

3.4.3 The case $c_0 \sim \delta \ll 1$

If we assume a small initial concentration of dissolved gas such that $\delta/c_0 \sim O(1)$, and introduce $\lambda = \delta/c_0$ then we can follow the same analysis presented above in Section 3.3.3. We rescale $\Gamma = \delta\overline{\Gamma}$ and, dropping the overbar notation, the system (3.28) becomes

$$(p\alpha)_t + (p\alpha u)_z = \Gamma, \tag{3.66a}$$

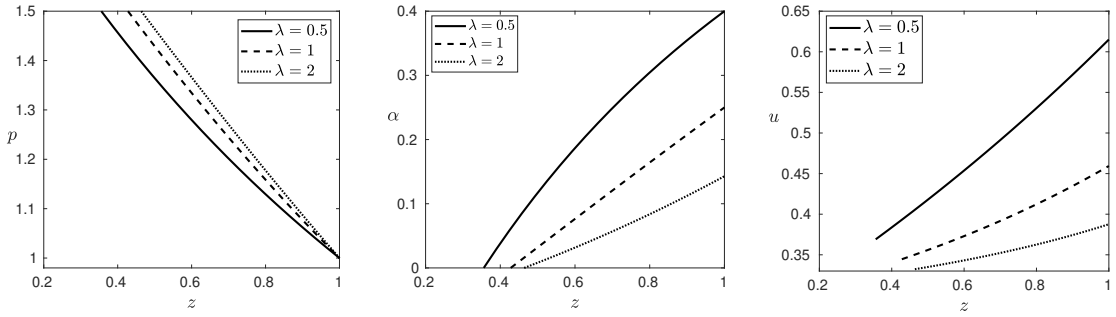
$$(1-\alpha)_t + ((1-\alpha)u)_z = 0, \tag{3.66b}$$

$$((1-\alpha)c)_t + ((1-\alpha)cu)_z = -\lambda\Gamma, \tag{3.66c}$$

$$p_z = -(1-\alpha), \tag{3.66d}$$

$$c = \frac{p}{\Pi}. \tag{3.66e}$$

In the single-phase region $0 \le z \le b(t)$ we solve (3.66a)–(3.66d) with $c = 1$, $\alpha = 0$ and $\Gamma = 0$ to again find $p = p_0 - z$, $u = U(t)$ and $b = p_0 - \Pi$.



(a) $p(z)$. **(b)** $\alpha(z)$. **(c)** $u(z)$.

Figure 3.4: Analytical steady-state solutions to (3.66) using parameters from tables 3.1 and 3.2. For illustration purposes, we choose $\Pi = 1.5$, $p_1 = 1$. Varying the value of c_0 gives different p_0 from (3.69) which in turn changes $b(t)$ from (3.39).

In the two-phase region $b(t) \leq z \leq 1$, we find that applying (3.50)–(3.51) to (3.66b) and (λ(3.66a)+(3.66c)) gives $(c + \lambda p\alpha/(1-\alpha))$ as a conserved quantity. The boundary condition (3.29b) at $z = b(t)$ gives this conserved quantity to be equal to one. Then using (3.66e) we derive the following relationship between the gas volume fraction and the pressure:

$$\alpha = \frac{1 - \dfrac{p}{\Pi}}{1 + \lambda p - \dfrac{p}{\Pi}}. \tag{3.67}$$

This relationship is shown in figure 3.2. In both the incompressible–incompressible system and the compressible–incompressible, the volume fraction is a decreasing function of pressure. However the decrease in the compressible–incompressible case is steeper than the incompressible–incompressible case.

Substituting (3.67) into (3.66d), we derive the following implicit form for pressure:

$$\ln\left(\frac{p}{\Pi}\right) + \left(\lambda - \frac{1}{\Pi}\right)(p - \Pi) + \lambda(z - b) = 0. \tag{3.68}$$

Finally, to close the system of equations we need to solve for the unknown inflow pressure p_0. We do this by applying the exit boundary condition $p = p_1$ at $z = 1$ in (3.68), and then using the relation $b(t) = p_1 - \Pi$ to isolate p_0:

$$p_0 = 1 + \Pi + \frac{1}{\lambda}\left[\ln\left(\frac{p_1}{\Pi}\right) + \left(\lambda - \frac{1}{\Pi}\right)(p_1 - \Pi)\right]. \tag{3.69}$$

We present the analytical solutions for the pressure, volume fraction and velocity in figure 3.4, where we use (3.68) for the pressure to calculate the velocity from (3.66b), and the volume fraction from (3.67). The results for the incompressible–compressible

system are analogous to those for the incompressible–incompressible system in figure 3.3.

The analysis in this section shows that including compressibility has negligible effect on the end conclusions for this model; in both parameter limits $\delta \ll 1$, $c_0 \sim O(1)$ and $c_0 \sim \delta \ll 1$ the conclusions for the incompressible–compressible system are, in fact, analogous to the incompressible–incompressible system studied in Section 3.3.

3.5 Summary

In this chapter we formulated a homogeneous model for the upwelling two-phase flow in oil wells. Previous oil-well models do not consider conservation of mass for the gas dissolved in the liquid phase as well as the gas that is a distinct phase itself. The novelty in the model derived in this chapter is that there are three mass conservation equations; one each for the liquid phase, the total gas phase and the dissolved gas in the liquid. The theory behind the model was motivated by noting the similarity between upwelling flow in oil wells and volcanic eruptions, and we were motivated by recent work by Fowler and Robinson [2018].

The simple model of two incompressible fluids produced an unexpected rapid change from liquid to a highly gaseous fluid at the bubble-point pressure. We found that if the gas-to-liquid density ratio δ is small, the model is singularly perturbed. By examining the boundary layer at the bubble-point pressure boundary, we derived analytical solutions to the model equations. A predominantly gaseous outflow is unexpected as the oil literature commonly describes two-phase producing wells. To our knowledge, no previous model has observed the dramatic change from liquid to highly gaseous mixtures at the bubble-point.

In order to find a more realistic solution in which the transition zone is elongated, so that a two-phase mixture is produced at the outlet, we can suppose the initial amount of dissolved gas c_0 to be proportional to the density ratio δ.

We repeated the analysis in both parameter regions for a system comprising an incompressible liquid phase and a compressible gaseous phase. The conclusions of the model were equivalent to the simpler incompressible–incompressible system. Thus we can conclude that the inclusion of compressibility for the gaseous phase does not significantly affect the results.

Reservoir fluids are complex, and there is significant variability of parameter values for a given oil field (see discussion in Section 3.2.2). Thus, although there may be some oil wells where $c_0 \sim \delta \ll 1$ is a reasonable assumption to make, this constraint will not generally be satisfied. We therefore need to consider additional rate-limiting dynam-

ics. This motivates the work in Chapter 4 examining appropriate non-equilibrium dynamics.

Chapter 4

Non-equilibrium dynamics

In this chapter we study ways in which the rapid transition observed in Chapter 3 might be avoided; we examine rate-limiting non-equilibrium dynamics by incorporating nucleation and bubble growth dynamics in the two-phase model.

4.1 Introduction

In Chapter 3 we found that using Henry's law (3.10) for equilibrium between the concentration of dissolved gas and the bulk pressure resulted in an unexpectedly rapid transition from a liquid to a highly gaseous foam. However, it is understood that oil wells produce two-phase flow with intermediate volume fractions of the gaseous phase. Thus we need to consider rate-limiting mechanisms for the exsolution of gas. The results from Chapter 3 suggest that the system may not be in equilibrium; in which case Henry's law is not an appropriate assumption. In this chapter we examine two ways in which the system will not be in equilibrium; the first is non-equilibrium bubble growth due to the diffusion of dissolved gas. The second is the problem of bubble nucleation in the first place.

Nucleation occurs when a bubble of gas forms from a solution. In the oil well mixture, at pressures above the bubble-point pressure, the liquid is *supersaturated*: the concentration of dissolved gas is higher than the equilibrium concentration. When the pressure drops below the bubble-point, the dissolved gas is able to come out of solution and finite radius bubbles are nucleated which then grow due to the diffusion of the gas in solution. The process of nucleation is classified as either *homogeneous* or *heterogeneous*. In both cases nucleation is governed by Gibbs free energy; there exists a free-energy barrier which opposes nucleation and must be overcome for the nucle-

ation to be successful [Hargraves, 2014]. The free energy change due to nucleation of a single bubble is

$$\Delta G = \frac{V}{V_m}\Delta G_c + \sum A\gamma, \tag{4.1}$$

where V and A are the volume and surface area of the nucleated bubble, V_m is the molar volume of the gas, ΔG_c is the bulk free energy change (per mole) and γ is the surface energy. The summation is over any new surfaces introduced. We assume $\Delta G_c < 0$ which is energetically favourable. We will briefly introduce the two classifications of nucleation and discuss how they compare.

Homogeneous nucleation assumes that bubbles initially form spontaneously within the liquid, so any bubbles formed are surrounded by liquid. If we suppose a spherical bubble of radius r spontaneously forms then we have $A = 4\pi r^2$, $V = \frac{4}{3}\pi r^3$, so the free energy change for homogeneous nucleation ΔG_O from (4.1) becomes

$$\Delta G_O = \frac{4\pi}{3}\frac{\Delta G_c}{V_m}r^3 + 4\pi\gamma r^2. \tag{4.2}$$

The relationship between ΔG_O and r is shown in figure 4.1. We see that there exists a critical radius r_c (associated with the maximum):

$$r_c = \frac{-2\gamma V_m}{\Delta G_c}. \tag{4.3}$$

The growth of bubbles nucleated with radius $r > r_c$ reduces the energy ΔG_O, thus these bubbles are energetically favourable and will survive. Bubbles nucleated with $r < r_c$ will dissolve and not survive. Thus there is a critical radius and corresponding energy barrier $\Delta G_O(r_c)$ that must be met for viable nucleation.

Heterogeneous nucleation occurs at nucleation sites, e.g. impurities in the liquid or the wall boundary. This type of nucleation is what typically happens in reality. In homogeneous nucleation volume is spontaneously introduced into the system; in heterogeneous nucleation, however, the emphasis is on the surface energies [Duley et al., 2017]. For example, when a monolayer of gas molecules is formed on a nucleation site, two new surfaces are introduced, and one is removed. The free energy change for heterogeneous nucleation ΔG_E from (4.1) is

$$\Delta G_E = \frac{V}{V_m}\Delta G_c + A_{GL}\gamma_{GL} + A_{GS}(\gamma_{GS} - \gamma_{LS}), \tag{4.4}$$

where A_{GL} and A_{GS} are, respectively, the gas–liquid and gas–solid surface areas, and γ_{GL}, γ_{GS} and γ_{LS} are the gas–liquid, gas–solid and liquid–solid surface energies; see figure 4.2.

The last term on the right of (4.4) arises because we are replacing a portion of the liquid–solid interface with a gas–solid interface. We might assume the nucleated

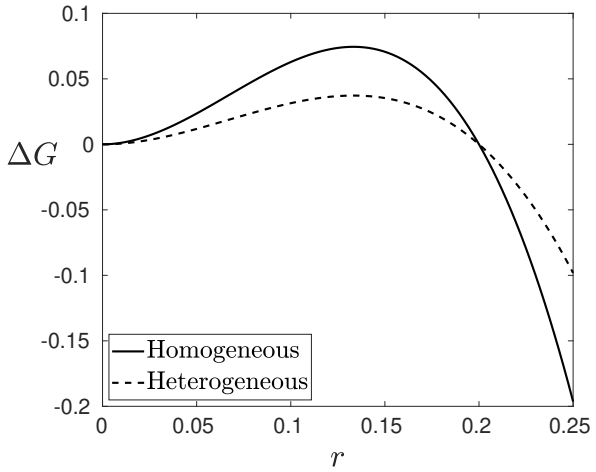


Figure 4.1: Gibbs free energy as a function of radius for homogeneous and heterogeneous nucleation given by (4.2) and (4.4) respectively, with $\gamma = 1$ kJ mol^{-1} mm^{-2}, $V_m = 0.1$ mm^{-3}, $\Delta G_c = 0.5$ kJ mol^{-1}, $\theta = \pi/2$.

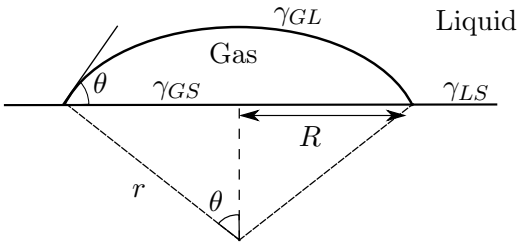


Figure 4.2: Schematic of a nucleated gas bubble on a solid wall.

bubble forms a spherical cap with contact angle θ, and let r be the radius of the sphere that would complete the cap. The area and volume of the spherical bubble cap are $A_{GL} = 2\pi r^2(1-\cos\theta)$ and $V = \frac{\pi}{3}r^3(2+\cos\theta)(1-\cos\theta)^2$. The area of the gas–solid interface is simply a circle given by $A_{GS} = \pi r^2 \sin^2\theta$. So (4.4) becomes

$$\Delta G_E = \frac{\pi}{3}r^3(2+\cos\theta)(1-\cos\theta)^2\frac{\Delta G_c}{V_m} + 2\pi r^2(1-\cos\theta)\gamma_{GL} + \pi r^2\sin^2\theta(\gamma_{GS}-\gamma_{LS}). \tag{4.5}$$

We can derive the relationship between ΔG_E in (4.5) and the homogeneous energy barrier ΔG_O in (4.2). We do so with the help of Young's equation: $\gamma_{GS} - \gamma_{LS} = -\gamma_{GL}\cos\theta$. Using this in (4.5), we can write ΔG_E as

$$\Delta G_E = \left(\frac{4\pi}{3}\frac{\Delta G_c}{V_m}r^3 + 4\pi\gamma_{GL}r^2\right)\left[\frac{1}{4}(2+\cos\theta)(1-\cos\theta)^2\right]. \tag{4.6}$$

This is shown in figure 4.1 together with the homogeneous free energy change ΔG_O. From (4.2) and (4.6) we see that, for $f(\theta) = \frac{1}{4}(2+\cos\theta)(1-\cos\theta)^2$, $\Delta G_E = f(\theta)\Delta G_O$;

so the critical radius for bubble survival is the same for homogeneous and heterogeneous. Note that $f(\theta) \in [0, 1)$, so for the same critical radius the energy barrier is less for heterogeneous: $\Delta G_E(r_c) < \Delta G_O(r_c)$. Therefore we see that heterogeneous nucleation is more likely to be realised than homogeneous which reinforces our expectation that heterogeneous nucleation is the predominant process.

However, the existence of a contact angle and Young's equation requires the macroscopic flow to be in thermodynamic equilibrium. We are concerned with the initial nucleation of the bubble where gas molecules are landing on the surface, this is evidently time dependent and the system is therefore not in equilibrium. Moreover, as the molecules land on the surface they form a monolayer of molecules which provides the foundation of nucleation. Therefore it does not make sense to talk about a contact angle, and we need to consider $\theta \to 0$.

As such, we re-examine the form of the heterogeneous energy barrier (4.5), and take $\theta \to 0$. To do this, we re-write it in terms of the planar bubble radius $R = r \sin\theta$; see figure 4.2. This gives

$$\begin{aligned} \Delta G_E &= \frac{\pi}{1+\cos\theta}\Bigg[\frac{(1-\cos\theta)(2+\cos\theta)}{\sin\theta}\frac{\Delta G_c}{3V_m}R^3 \\ &\qquad +2R^2\left(\gamma_{GL}+\tfrac{1}{2}(1+\cos\theta)(\gamma_{GS}-\gamma_{LS})\right)\Bigg]. \end{aligned} \tag{4.7}$$

For $\theta \to 0$, we see that $\Delta G_E \to \pi R^2(\gamma_{GL}+\gamma_{GS}-\gamma_{LS})$. So, for nucleation, we require $\Delta\gamma = (\gamma_{GL}+\gamma_{GS}-\gamma_{LS}) > 0$.

Including the nucleation and bubble growth kinetics in the homogeneous two-phase model presented in Chapter 3 should be rate limiting for the exsolution of gas. Recall that the model was applied to a one-dimensional oil-well domain with a liquid inflow i.e. the inflow pressure was taken to be greater than the bubble-point pressure $p_{in} > p_b$. The pressure reached bubble-point at $z = b(t)$ indicating a two-phase flow in the domain $b(t) \leq z \leq L$. The model was analysed for both incompressible–incompressible and compressible–incompressible mixtures; the results were found to be analogous. We introduce non-equilibrium dynamics by adapting the homogeneous model presented in Chapter 3. It is reasonable to assume the study of non-equilibrium dynamics for the incompressible–incompressible case, as the equations are simpler and the findings in Chapter 3 suggest that the results would still hold in the compressible–incompressible case.

We therefore seek to add non-equilibrium dynamics to the dimensionless system (3.30) with boundary conditions (3.29). We first neglect nucleation dynamics and

suppose that a fixed number of bubbles appear at the boundary $z = b(t)$ and examine the growth of the bubbles. Following that we will analyse the nucleation kinetics of bubble formation.

4.2 Diffusion of dissolved gas

The simplest rate-limiting process to include is the diffusive growth of bubbles. We therefore suppose, for now, that at $z = b(t)$ some fixed number of small bubbles appear and then grow due to diffusion of dissolved gas from the liquid to the bubble interface. We seek a relevant diffusive time scale where bubble growth is important.

Let N be the number density, by volume, of bubbles. If the typical distance between the bubbles is L_b, then we have $N = 1/L_b^3$. If r_b is the bubble radius and we assume spherical bubbles then the volume of each bubble V_b is

$$V_b = \frac{4\pi r_b^3}{3}. \tag{4.8}$$

Note that

$$\alpha = NV_b = \frac{4\pi r_b^3}{3L_b^3}. \tag{4.9}$$

To compare the time scale of diffusive growth to that of the large scale flow we assume that $L_b \gg r_b$, which enables us to consider the diffusive growth of a single bubble independently of the rest of the bubbles. Thus we write down the diffusion equation in a spherical domain centred at a bubble:

$$\bar{c}_t = D\nabla^2\bar{c}, \tag{4.10a}$$

$$\bar{c} = c_{\text{sat}} \quad \text{at} \quad r = r_b, \tag{4.10b}$$

$$\bar{c} \to c \quad \text{as} \quad r \to \infty, \tag{4.10c}$$

where $\bar{c}$ is the concentration of dissolved gas, D is the diffusion coefficient, c_{sat} is the saturated concentration and c is the far-field supersaturated concentration (the same c we considered in our models in Chapter 3).

The time scale of the large-scale flow, from (3.16) and table 3.1, is $t_f = L/U_0 \sim 0.5 \times 10^4$ s. Scaling (4.10a) with typical bubble radius r_0 ($r \sim r_0$) gives the diffusive time scale to be $t_d = r_0^2/D$. To gauge the size of the diffusive time scale we consider the molecular diffusion coefficient for propane at reservoir conditions: $D \sim 10^{-9}$ m^2 s [Tharanivasan et al., 2006]. If we consider small bubbles (which is reasonable, at least initially) with $r_0 = 0.1$ mm, then $t_d \sim 10$ s, so we may reasonably take $t_d \ll t_f$. This analysis is already suggesting that the diffusive time scale is not significant.

To see how the diffusive growth time scale relates to the number density of bubbles N in the system we take $t_d \ll t_f$ in (4.10a) which implies $\nabla^2 \bar{c} = 0$. Solving this using the boundary conditions (4.10b) and (4.10c) yields

$$\bar{c} = c + \frac{(c_{\text{sat}} - c) r_b}{r}. \tag{4.11}$$

The diffusive flux of gas across the bubble boundary provides the following constitutive equation for bubble growth [Lifshitz and Slyozov, 1961]:

$$\begin{aligned} \rho_g \left[(r_b)_t + u(r_b)_z \right] &= -\rho_l D c_r|_{r=r_b} && \text{(4.12a)} \\ &= \frac{\rho_l D}{r_b} \left(c - c_{\text{sat}} \right), && \text{(4.12b)} \end{aligned}$$

where, as in Chapter 3, we use subscripts t and z to denote the associated partial differentiation. The bubbles will therefore stop growing when equilibrium at $c = c_{\text{sat}}$ is reached. We can rewrite the equation for the growth of the bubble radius (4.12) in terms of α using (4.9) and assuming the number density N is fixed; this gives

$$\rho_g \left(\alpha_t + u\alpha_z \right) = (4\pi N)^{2/3} (3\alpha)^{1/3} \rho_l D \left(c - c_{\text{sat}} \right). \tag{4.13}$$

Note that the saturated concentration is reached at equilibrium, and is therefore proportional to the pressure as in Henry's law, $c_{\text{sat}} = Kp$ in dimensional form. (4.13) therefore replaces the Henry's law equilibrium in which the right hand side is zero.

Recall that we are considering an isothermal two-phase incompressible – incompressible model with a single pressure and a single velocity. The dimensional system of equations accounting for diffusive growth is derived from (3.1), (3.4), (3.8) and (4.13):

$$(\alpha\rho_g)_t + (\alpha\rho_g u)_z = \Gamma, \tag{4.14a}$$

$$[(1-\alpha)\rho_l]_t + [(1-\alpha)\rho_l u]_z = -\Gamma, \tag{4.14b}$$

$$[(1-\alpha)\rho_l c]_t + [(1-\alpha)\rho_l c u]_z = -\Gamma, \tag{4.14c}$$

$$\begin{aligned} [((1-\alpha)\rho_l + \alpha\rho_g)u]_t + [((1-\alpha)\rho_l + \alpha\rho_g)u^2]_z &= -p_z - \frac{4 f_l \rho_l u^2}{d} \\ &\quad - g((1-\alpha)\rho_l + \alpha\rho_g), \end{aligned} \tag{4.14d}$$

$$\rho_g \left(\alpha_t + u\alpha_z \right) = (4\pi N)^{2/3} (3\alpha)^{1/3} \rho_l D \left(c - c_{\text{sat}} \right). \tag{4.14e}$$

We make (4.14) dimensionless utilising the scalings in (3.16). Using the dimensionless parameters as given in (3.20) and parameter values from tables 3.1 and 3.2,

we re-produce the dimensionless system (3.30) with Henry's law (3.30e) replaced by the scaled version of (4.14e):

$$\frac{t_g}{t_f}\left[\alpha_t + u\alpha_z\right] = (48\pi^2\alpha)^{1/3}\left(c - \frac{p}{\Pi}\right), \tag{4.15}$$

where t_g is the associated bubble-growth time scale, which can be expressed in terms of the interbubble distance L_b, the diffusion coefficient D and the initial dissolved gas concentration c_0:

$$t_g = \frac{\rho_g}{\rho_l D c_0 N^{2/3}} = \frac{\rho_g}{\rho_l}\frac{L_b^2}{D c_0}. \tag{4.16}$$

From (4.15), we see that our earlier assumption in Chapter 3 of equilibrium through Henry's law is essentially equivalent to $t_g \ll (48\pi^2)^{1/3} t_f$. Note that t_g depends on the number of bubbles, and thus the assumption of equilibrium solubility essentially rests on the number of bubbles that are nucleated. In particular, $t_g \ll (48\pi^2)^{1/3} t_f$ is equivalent to

$$N \gg N^* \equiv \frac{1}{4\pi\sqrt{3}}\left(\frac{\rho_g}{\rho_l}\frac{U_0}{L D c_0}\right)^{3/2}, \tag{4.17}$$

where N^* is the critical minimum number of bubbles in the system for the diffusive growth time scale to be assumed negligible. With the molecular diffusivity $D \approx 10^{-9}$ m^2 s^{-1} introduced above, together with the parameter values in table 3.1 and the assumption that $c_0 = 0.2$, we find that (4.17) gives $N^* = 1.9 \times 10^3$ m^{-3}. Our earlier conclusion that diffusion is not by itself rate limiting is found to be reasonable when a large number of bubbles appear at $z = b(t)$. We now turn to the issue of nucleation.

4.3 Nucleating bubbles

Consider a population of bubbles whose number density is a function of their size. For convenience we choose the size variable to be the bubble surface area $s = 4\pi r_b^2$, and denote the bubble number density as $n(s, z, t)$. The number density of bubbles per unit volume with surface area in the range $(s, s + \mathrm{d}s)$ is $n(s, z, t)\,\mathrm{d}s$. The number density of bubbles per unit volume is thus given by

$$N(z, t) = \int_0^\infty n \,\mathrm{d}s. \tag{4.18}$$

The gas volume fraction is given by the following integral:

$$\alpha = \int_0^\infty V_b\, n \,\mathrm{d}s. \tag{4.19}$$

Using (4.8), we can write the volume V_b in terms of the surface area s via $V_b = s^{3/2}/(6\sqrt{\pi})$. Thus the gas volume fraction (4.19) becomes

$$\alpha = \frac{1}{6\sqrt{\pi}} \int_0^\infty s^{3/2} n \, \mathrm{d}s. \tag{4.20}$$

Conservation of the bubble size distribution is given by

$$n_t + (nu)_z + (nv)_s = 0, \tag{4.21}$$

where v is the bubble growth rate. Writing the diffusive growth (4.12) in terms of s, we find the bubble growth rate to be given by

$$v = \frac{8\pi D \rho_l}{\rho_g} \left(c - c_{\mathrm{sat}}\right). \tag{4.22}$$

We can presume $n \to 0$ as $s \to \infty$; we also prescribe a boundary condition at $s = 0$: $n|_{s=0} = n_0$. Using the definition of number density N given in (4.18) and integrating (4.21) yields

$$N_t + (Nu)_z = \left[\frac{8\pi D \rho_l}{\rho_g} \left(c - c_{\mathrm{sat}}\right)\right] n_0. \tag{4.23}$$

If we assume that the rate of nucleation is proportional to the supersaturation of dissolved gas (which we now assume to be out of equilibrium, i.e. $c > c_{\mathrm{sat}}$), then we can write

$$N_t + (Nu)_z = k_N (c - c_{\mathrm{sat}}), \tag{4.24}$$

where k_N is a prescribed rate constant with units of $\mathrm{m}^{-3}\ \mathrm{s}^{-1}$. Using this in (4.23) provides the boundary condition for n:

$$n = n_0 = \frac{k_N}{8\pi D} \frac{\rho_g}{\rho_l} \quad \text{at} \quad s = 0. \tag{4.25}$$

Multiplying (4.21) by $s^{3/2}/(6\sqrt{\pi})$ and integrating gives an equation for the gas volume fraction:

$$\alpha_t + (\alpha u)_z = 2\sqrt{\pi} D \left(c - c_{\mathrm{sat}}\right) \frac{\rho_l}{\rho_g} \int_0^\infty s^{1/2} n \, \mathrm{d}s. \tag{4.26}$$

The dimensionless homogeneous model (3.30) we derived earlier in Chapter 3 is now modified by the bubble density (4.21) and the gas volume fraction (4.26). The boundary conditions are also as in (3.29) but now with additional conditions for n. The model is made dimensionless as earlier in (3.16) with the modification for the scaling of Γ. In Chapter 3 we scaled the mass transfer by $\Gamma \sim \rho_l U_0 / L$ and the density ratio δ appeared in the gas mass conservation equation. However, in this chapter, we have in fact re-derived a gas mass conservation equation (4.26) that incorporates

nucleation and growth of bubbles. Thus to examine the non-equilibrium dynamics further we now scale the mass transfer by $\Gamma \sim \rho_g U_0/L$ so that δ instead appears in the liquid mass conservation equation. We are considering an incompressible–incompressible system with ρ_g constant. We introduce the additional scaling for (4.21):

$$n \sim n_0 = \frac{k_N}{8\pi D}\frac{\rho_g}{\rho_l}, \quad s \sim \left(\frac{6\sqrt{\pi}}{n_0}\right)^{2/5}; \tag{4.27}$$

we thus obtain the dimensionless model

$$\alpha_t + (\alpha u)_z = \Gamma, \tag{4.28a}$$

$$(1-\alpha)_t + [(1-\alpha)u]_z = -\delta\Gamma, \tag{4.28b}$$

$$[(1-\alpha)c]_t + [(1-\alpha)cu]_z = -\frac{\delta}{c_0}\Gamma, \tag{4.28c}$$

$$F^2[(1-\alpha)+\delta\alpha]\,[u_t + uu_z] = -p_z - \kappa_w u^2 - [(1-\alpha)+\delta\alpha], \tag{4.28d}$$

$$\Gamma = \gamma\left(c - \frac{p}{\Pi}\right)\int_0^\infty s^{1/2} n \,\mathrm{d}s, \tag{4.28e}$$

$$n_t + (nu)_z + \frac{2\gamma}{3}\left(c - \frac{p}{\Pi}\right) n_s = 0, \tag{4.28f}$$

where the parameters are those defined in (3.20), and we have introduced the dimensionless parameter

$$\gamma = \frac{2Lc_0}{U_0}\left(\frac{27}{8}\frac{\rho_l^3}{\rho_g^3}\pi^2 k_N^2 D^3\right)^{1/5}, \tag{4.29}$$

which involves the nucleation rate constant k_N, diffusive growth D and flow time scale $t_f = L/U_0$. The scaled version of (4.20) is:

$$\alpha = \int_0^\infty s^{3/2} n \,\mathrm{d}s, \tag{4.30}$$

which together with (4.28f) gives (4.28e). The boundary conditions for these equations are

$$\alpha = 0, \quad c = 1, \quad p = p_0, \quad u = U(t) = 1 - \delta_c p_0 \ \text{ at } \ z = 0, \tag{4.31a}$$

$$\alpha = 0, \quad c = 1, \quad p = \Pi, \quad n = 0 \ \text{ at } \ z = b(t), \tag{4.31b}$$

$$p = p_1 \ \text{ at } \ z = 1, \tag{4.31c}$$

$$n = 1 \ \text{ at } \ s = 0. \tag{4.31d}$$

In the single-phase region $0 \le z \le b(t)$ our earlier results still hold: $\alpha = 0$, $\Gamma = 0$, $c = 1$, $u = U(t)$ and $p = p_0 - z$. We also find that $b(t) = p_0 - \Pi$ as in (3.39). We therefore analyse the two-phase region $b(t) \le z \le 1$. Again we take $F^2, \kappa_w, \delta \ll c_0 \sim 1$, and consider different parameter limits for γ.

4.3.1 $\gamma \gg 1$

From the definition (4.29) large $\gamma \gg 1$ corresponds to a large nucleation rate k_N and diffusive growth. If we take $\gamma \gg 1$ and neglect other small terms, from (4.28) the equations to solve become:

$$\alpha_t + (\alpha u)_z = \gamma \left(c - \frac{p}{\Pi}\right) \int_0^\infty s^{1/2} n \, \mathrm{d}s, \tag{4.32a}$$

$$(1-\alpha)_t + ((1-\alpha)u)_z = 0, \tag{4.32b}$$

$$((1-\alpha)c)_t + ((1-\alpha)cu)_z = 0, \tag{4.32c}$$

$$p_z = -(1-\alpha), \tag{4.32d}$$

$$n_t + (nu)_z + \frac{2\gamma}{3}\left(c - \frac{p}{\Pi}\right) n_s = 0. \tag{4.32e}$$

Using (3.50) and (3.51) we see that (4.32b) and (4.32c) imply that $c = 1$ is advected with the flow. Moreover, (4.32a) gives $c = p/\Pi$, so the dissolved concentration is at equilibrium, and we have again that $p = \Pi$. From (4.32d) this implies $\alpha = 1$, which in (4.32b) gives $u = U(t)$. The model conclusions are exactly the same as in Section 3.3.2; above the bubble-point pressure at $z = b(t)$ the mixture is mostly gas. This is an intuitive finding for $\gamma \gg 1$ as high rates of nucleation and diffusive growth will drive a rapid transition to a highly gaseous mixture.

4.3.2 $\gamma \ll 1$

If we consider small $\gamma \ll 1$, i.e. small nucleation rate and slow diffusive growth, then the model equations (4.28) are approximately

$$\alpha_t + (\alpha u)_z = 0, \tag{4.33a}$$

$$(1-\alpha)_t + ((1-\alpha)u)_z = 0, \tag{4.33b}$$

$$((1-\alpha)c)_t + ((1-\alpha)cu)_z = 0, \tag{4.33c}$$

$$p_z = -(1-\alpha), \tag{4.33d}$$

$$n_t + (nu)_z = 0. \tag{4.33e}$$

If we sum (4.33a) and (4.33b) we get $u = U(t)$. Again, (4.33b) and (4.33c) imply that $c = 1$ is advected with the flow. We also have a constant gas volume fraction $\alpha = 0$ being advected with the flow, from (4.33a). Using this in (4.33d) gives a linearly decreasing pressure $p = \Pi - z$. The model solutions are again trivial, but the conclusion for small γ is that the gas volume fraction remains small throughout the pipe.

An item of interest is how the bubble number density behaves. Solving the equation for n indicates that $n = 1$ at $s = 0$ from (4.31d), but (4.31b) gives $n = 0$ for $s > 0$. The discontinuity is resolved by a boundary layer when $s \sim \gamma$, as can be seen from (4.28f).

4.3.3 $\gamma \sim O(1)$

For large $\gamma \gg 1$ we have mostly gas at the top of the well, and for small $\gamma \ll 1$ we have mostly liquid. We now consider the case $\gamma \sim O(1)$, where in the $\delta \ll c_0 \sim 1$ limit, the system of equations (4.28) become approximately

$$\alpha_t + (\alpha u)_z = \Gamma = \gamma \left(c - \frac{p}{\Pi}\right) \int_0^\infty s^{1/2} n \, \mathrm{d}s, \tag{4.34a}$$

$$(1-\alpha)_t + ((1-\alpha)u)_z = 0, \tag{4.34b}$$

$$((1-\alpha)c)_t + ((1-\alpha)cu)_z = 0, \tag{4.34c}$$

$$p_z = -(1-\alpha), \tag{4.34d}$$

$$n_t + (nu)_z + \frac{2\gamma}{3}\left(c - \frac{p}{\Pi}\right) n_s = 0. \tag{4.34e}$$

Note that (4.34b) and (4.34c) again imply that $c = 1$ is advected with the flow. From (4.34a) and (4.34b), $u_z = \Gamma$. Further, we can integrate (4.34d) to obtain p as

$$p = \Pi - \int_b^z [1 - \alpha(y,t)] \, \mathrm{d}y, \tag{4.35}$$

and thus, using (4.35) in (4.34a), we have

$$\Gamma = u_z = \frac{\gamma}{\Pi} \int_b^z (1-\alpha) \, \mathrm{d}y \int_0^\infty s^{1/2} n \, \mathrm{d}s. \tag{4.36}$$

The equation for n (4.34e) can be written as

$$n_t + u n_z + \frac{2\gamma}{3}\left(1 - \frac{p}{\Pi}\right) n_s = -u_z n, \tag{4.37}$$

together with boundary conditions

$$n = 1 \text{ on } s = 0, \tag{4.38a}$$

$$n = 0 \text{ on } z = b(t). \tag{4.38b}$$

There is also an initial condition for n at $t = 0$. Using the definition of α (given in (4.30)) in (4.36), the equation (4.37) becomes an equation in terms of $n(z, s, t)$ alone.

Note that $b(t)$ and p_0 (and thus $U(t)$) in the boundary conditions (4.31a)–(4.31b) are not known. Applying $p = p_1$ at $z = 1$ in (4.35) provides an equation for $b(t)$, and then p_0 is determined from $p_0 - \Pi = b$.

To solve the steady state version of (4.37) numerically we applied a change of variables $\hat{z} = \frac{z-b}{1-b}$ to remove b from the integral limits in (4.35) and (4.36). The solution domain is consequently $\hat{z} \in [0, 1]$. We then used an implicit-explicit finite difference scheme for $n(z, s)$ and a shooting method for the unknown b minimising the error using (4.35). The numerical solution of the number of bubbles n as a function of s is shown in figure 4.3 for distinct points along the domain. We see that initially, we have lots of small bubbles, but as we move up the well, the bubbles grow in size. However, it is clear that there are consistently more smaller bubbles, which is due to bubbles continuously nucleating with small surface area.

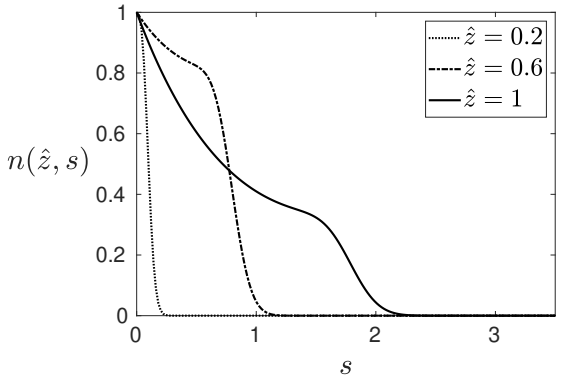
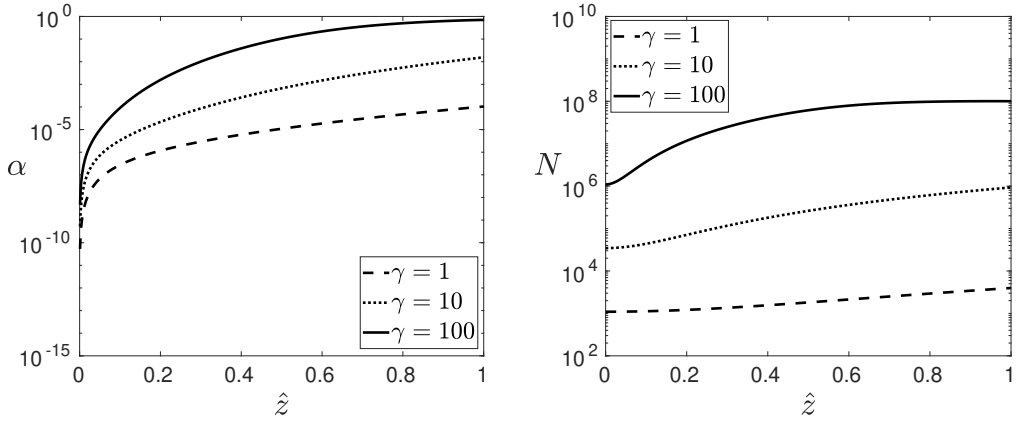


Figure 4.3: Steady state solutions for number of bubbles n as a function of surface area s for varying points in the domain $\hat{z} = 0.2$, 0.6, 1, with parameters from tables 3.1 and 3.2, and $\Pi = 1.5$, $p_1 = 1$. Results are shown for $\gamma = 100$ and $k_N = 1.3 \times 10^5$ m^{-3} s^{-1}. The numerical discretisation parameters are $\Delta z = 0.001$ and $\Delta s = 0.05$.

The number density of bubbles N and gas volume fraction α can be calculated from n using (4.18) and (4.30) respectively. We present the numerical solutions, using parameters from tables 3.1 and 3.2, in figure 4.4 for different values of γ.

For large γ, the results predict a larger volume fraction α, and a higher number of bubbles N. The gas volume fraction profiles in figure 4.4a support the conclusion from Section 4.3.1: increasing γ corresponds to increased gas in the pipe. We can investigate this further by looking at the gas volume fraction at the top of the pipe as a function of γ. The model predicts an increasing exit volume fraction which tends to $\alpha = 0.9$; see figure 4.5. It is clear that the value that the exit volume fraction tends to is dependent on the choice of parameters, namely the exit pressure p_1.

The number density of bubbles per unit volume is given by N. We rescale the numerical solutions according to (3.16) to plot the dimensional number density N in figure 4.4b. We see that for larger γ we have more bubbles. These results suggest that for larger γ there are lots of small bubbles in the pipe corresponding to a foam-like



(a) $\alpha(\hat{z})$ **(b)** $N(\hat{z})$

Figure 4.4: Steady state solutions for the gas volume fraction α and number density of bubbles N (m^{-3}) for varying values of γ with parameters from tables 3.1 and 3.2, and $\Pi = 1.5$, $p_1 = 1$. Results are shown for $\gamma = 1,\ 10,\ 100$ and $k_N = 1.3, 409.1, 1.3 \times 10^5\ \mathrm{m}^{-3}\ \mathrm{s}^{-1}$ respectively. The numerical discretisation parameters are $\Delta z = 0.001$ and $\Delta s = 0.05$.

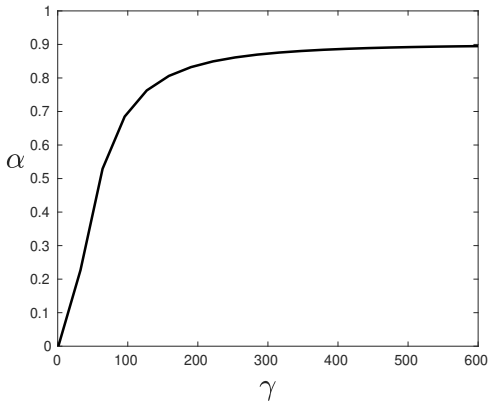


Figure 4.5: The exit volume fraction $\alpha(z = 1)$ as a function of γ with parameters from tables 3.1 and 3.2, and $\Pi = 1.5$, $p_1 = 1$, $\Delta z = 0.001$ and $\Delta s = 0.05$.

mixture.

We conclude that the addition of non-equilibrium dynamics to the two-phase flow equations is suitably rate-limiting, and the results predict a two-phase flow in which the gas volume fraction increases over the length of the tube, with an increasing outflow volume fraction for increasing γ.

4.4 Summary

In this chapter, we considered the effects of non-equilibrium dynamics. Firstly, Henry's law was modified to allow for supersaturation of the dissolved gas phase: this made little difference to the solution, as diffusion through the liquid was found to be rapid. Secondly, a model for nucleation and bubble growth was formulated, and the solutions were found to depend critically on the nucleation rate; if this is sufficiently low, then exsolution is significantly diminished.

More precisely, it was found that gas formation is suppressed ($\alpha < 1$ at the outlet) if a dimensionless parameter γ given by (4.29) is less than a critical value $\gamma_c \approx 70$ which corresponds to the value where $\alpha = 0.5$ in figure 4.5. Rewriting this in terms of the nucleation rate constant k_N using (4.29), we find that a two-phase mixture at the outlet requires

$$k_N > k_c = \frac{1}{\pi}\left(\frac{2\rho_g}{3D\rho_l}\right)^{3/2}\left(\frac{\gamma_c U_0}{2Lc_0}\right)^{5/2}. \tag{4.39}$$

Using the values $D = 10^{-9}$ m^2 s^{-1}, $U_0 = 0.2$ m s^{-1}, $L = 10^3$ m, $\rho_g = 1.14$ kg m^{-3}, $\rho_l = 0.96 \times 10^3$ kg m^{-3} and $c_0 = 0.2$, this gives $k_c \approx 5.3 \times 10^4$ m^{-3} s^{-1}, or equivalently $k_c \approx 5.3 \times 10^{-2}$ cm^{-3} s^{-1}. Unfortunately, little is known about the nucleation characteristics of the flows in oil wells, and access to empirical data to validate these values is limited. To relate this nucleation rate to a unit length of pipe we observe that 1 m^3 of pipe can be written as a length h of pipe through: $\pi d^2 h/4$ m^3. Equating this to 1 m^3 we find that $h = 127$ m. So in one unit length of pipe, we have $k_c/127 \approx 418$ nucleation sites per second.

In the homogeneous model examined in Chapters 3 and 4 we considered governing equations relevant for a bubbly flow characterised by a sufficiently small gas volume fraction. However, as the bubbles nucleate and grow, additional bubble dynamics including coalescence and break-up will occur. When the gas volume fraction is sufficiently large, the flow will undergo a regime transition from bubbly to slug flow. In slug flow, dynamics which we have so far neglected (including the slip between phases) become important. However, the main conclusions of the model remain unchanged for a system at thermodynamic equilibrium, as the prediction of a rapid increase in gas volume fraction is driven by the decompression of the gas and the prescribed relationship between pressure and dissolved gas concentration in Henry's law (3.28e).

The results of this part of the thesis suggest it is important to include nucleation and growth kinetics when modelling upwelling flow in oil wells. To our knowledge, this approach is not used in commercial oil-well models. Such models rely heavily on empirically derived correlations between unknown parameters and variables. The

work presented in this chapter, together with the work in Chapter 3, provides a more deterministic approach.

Part II

Modelling the bubbly-to-slug flow regime transition

Chapter 5

Nucleation, growth and coalescence in one dimension

In this chapter we consider one-dimensional bubble dynamics. We re-derive a model of nucleation and growth that was first introduced by Ben-Naim and Krapivsky [1996]. We compare the model predictions to a Monte Carlo simulation of the system, and study the model in the continuum limit.

5.1 Introduction

In two-phase pipe flow, the flow of each fluid is affected by the presence of the other fluid. The geometry of the interfaces separating the two phases gives rise to distinct *flow regimes*, which describe the macroscopic flow. The two-phase liquid–gas flow in vertical pipes can be categorised into five distinct flow regimes: bubbly, slug, churn, annular and mist flow; see figure 1.5 in Chapter 1.

It is understood that when a flow regime becomes unstable, the flow *transitions* into another regime. Such a transition is associated with changes in the microscale geometry of the flow. The aim of this part of the thesis is to model the bubbly-to-slug flow regime transition. The governing processes of this transition include the coalescence and fragmentation of bubbles in a turbulent pipe-flow. We therefore consider the statistical behaviour of bubble populations, where the variable of interest is a bubble distribution function, as a function of size and shape.

In order to understand how to model a system of bubbles in a liquid pipe-flow, we spend this chapter looking at a simple model that is similar in some respect to the kinetic-theory-based model we seek. This is followed by further preliminary work

in Chapter 6 that examines the appropriate configuration space for a more detailed kinetic-theory-based model of an evolving bubble distribution, which will be discussed in Chapter 7.

Ben-Naim and Krapivsky [1996] introduce a model of two populations (islands and holes) in a one-dimensional domain, and account for nucleation and growth dynamics of the island population. In this chapter, we apply this approach to populations of bubbles and inter-bubble liquid holes in a pipe-flow. A one-dimensional domain is reasonable if we consider taking cross-sectional slices of the pipe along the vertical axis, then we have distributions of bubbles and inter-bubble liquid holes which are functions of (horizontal) length. In this chapter, we study the nucleation and growth of the bubble population (note that we do not account for fragmentation dynamics).

Analogous nucleation and growth dynamics occur in many different systems, including crystallisation [Levi and Kotrla, 1997; Teran et al., 2010] and granular compaction [Caglioti et al., 1997; Ben-Naim et al., 1998], as well as in biological and ecological systems including protein absorption [Ramsden, 1995] and DNA replication [Herrick et al., 2002]. In these systems, where the nucleation occurs randomly over time, the dynamics are typically modelled using *random sequential absorption (RSA)* models [Evans, 1993]. These are lattice models for which each point in the lattice is either vacant or occupied by some particle. In RSA models, particles are absorbed at randomly allocated sites, and typically once a particle has been absorbed at a particular site, the state of the site is changed irreversibly from empty to filled. In the simplest systems, no overlap, diffusion or desorption of the absorbed particles is considered [Evans, 1993; Tarjus et al., 1990]. A well-known RSA system is the *random car parking problem* [Krapivsky, 1992].

We employ a lattice model for a bubble and liquid system by considering a one-dimensional lattice domain for which every point on the domain is either a bubble or a liquid hole. Bubbles therefore correspond to occupied sites and liquid holes to vacant sites. We define holes to be the existing space between two bubbles. We nucleate bubbles randomly with probability p at each time step and consider deterministic growth in each direction along the line with growth rate v; see figure 5.1. We will not formulate our system as an RSA model, but we do look to the literature to gain some understanding of the methods used and concerns that may arise in similar nucleation and growth models.

An early study of an RSA system is the packing of particles of volume v_0 in a finite volume v_{tot} by Widom [1966]. In the one-dimensional system, a line of length L is divided into M intervals each of length l, where M is an integer. At each time

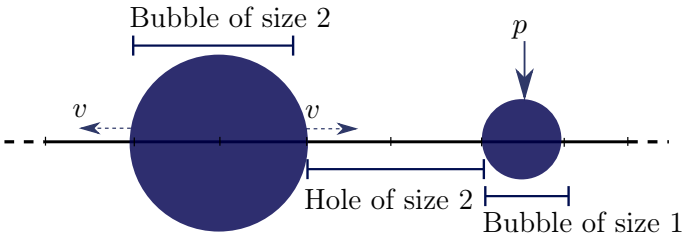


Figure 5.1: Schematic of a section of the one-dimensional domain of bubbles and holes; B_i denotes bubbles of size i; analogous notation for holes H_i. Holes are defined to be the space between two bubbles. Existing bubbles grow deterministically with rate v, and bubbles of size one are nucleated with probability p.

step, a particle is added at a randomly allocated available interval. In finite time, the system may reach a *jammed state*; one for which there is no available room for another particle to be added. It is possible for the system to become jammed before complete coverage is achieved. In fact, for the one-dimensional system, the jamming volume fraction $\alpha \approx 0.75$, where the volume fraction is defined as $\alpha = Nv_0/v_{tot}$ for N particles [Evans, 1993]. Total coverage, i.e. $\alpha = 1$, is only achievable in the particular scenarios where either $v_0 = nl$ where n is an integer and $n|M$, or $v_0 = l/m$ where m is an integer.

There have been various extensions of the basic RSA model including reversibility through desorption [Tarjus et al., 1990], this is relevant to systems in which proteins may absorb and desorb from a surface. Further extensions to RSA include growth of the particles [Evans, 1993; Rodgers and Filipe, 1997]; diffusive growth occurs where a particle is randomly allocated a filled site, and then diffuses along the filled sites and is absorbed at the first available empty site it reaches. This was observed in and motivated by experiments of gas absorption on a metal surface [Bradley et al., 1997]. Ben-Naim and Krapivsky [1996] developed the idea of growth further yet and considered continuous nucleation of bubbles with deterministic growth in an infinite domain.

In the framework of islands and holes developed by Ben-Naim and Krapivsky [1996], we consider bubbles to be nucleated with zero length randomly in space at rate $\gamma(t)$ and to grow deterministically by one spatial step at every time step. The model equations, as given by Ben-Naim and Krapivsky [1996], for the evolution of the hole size density $f(x,t)$ and bubble size density $g(x,t)$ are:

$$f_t - f_x = -\gamma x f + 2\gamma \int_x^\infty f(y,t)\,\mathrm{d}y, \tag{5.1a}$$

$$g_t + g_x = \frac{f(0,t)}{n_f^2}\left[\int_0^x g(y,t)g(x-y,t)\,\mathrm{d}y - 2n_f g\right] + \gamma\alpha_f\delta(x), \tag{5.1b}$$

where we denote partial differentiation with respect to x and t by the corresponding subscripts, and

$$\alpha_f = \int_0^\infty xf \, \mathrm{d}x, \quad n_f = \int_0^\infty f \, \mathrm{d}x. \tag{5.2}$$

In this chapter we will use this system as a basis to derive a mathematical model for bubble nucleation, growth and coalescence. Note that (5.1) and (5.2) model the infinite domain; in our case, however, we are interested in a finite domain (in pipe flow the bubbles cannot grow bigger than the diameter of the pipe) and so we will derive the analogous equations for a discrete lattice corresponding to a cross-sectional slice of pipe. From the discrete formulation, we will derive the analogous continuous equations in a finite domain. We will show how we recover the system (5.1)–(5.2) in the limit that our domain becomes infinite.

Ben-Naim and Krapivsky [1996] apply the following initial condition to close the model (5.1)–(5.2):

$$\int_0^\infty f \, \mathrm{d}x = 0, \quad \int_0^\infty xf \, \mathrm{d}x = 1. \tag{5.3}$$

The first of these suggests there are no holes initially present; the second however suggests the domain is filled by the hole population only. We wish to better understand the initial conditions, and see how they emerge when considering a finite domain.

We will set up the system on a finite one-dimensional domain of length L and validate results from a discrete model of the one-dimensional growth and coalescence dynamics against a Monte Carlo simulation. We then derive the corresponding continuum model, and examine the results of the model with a finite domain and in the limit of an infinite domain.

5.2 Problem set up

We consider a discrete lattice of N (where N is an integer) equally spaced points arranged on a circle as this precludes dealing with end effects; see figure 5.2. The points are a distance Δx apart, and the total length of the circle is thus $L = N\Delta x$. The system is evolved through discrete time steps Δt and, after N_t time steps, the total length of the time domain is $T = N_t \Delta t$. For every j^{th} time step $j\Delta t$ for some integer $j \in [0, N_t]$, bubbles are nucleated in unoccupied sites with probability p^j and pre-existing bubbles grow by one spatial step Δx in both directions. Whilst one may take a time-dependent probability p^j, in this chapter we will assume a constant probability $p = p^j$. We denote the number of bubbles of size i at time step j to be B_i^j, and the number of holes (or spaces between bubbles) of size i at time step j to be H_i^j, where $i = 1, \ldots, N$.

For the initial condition, we would ideally start with all sites empty, in which case $B_i^0 = 0$ and thus $H_i^0 = 0$. However, recall that we define a hole to exist between two bubbles — so the system in which there are no bubbles is not defined. We therefore start with a single bubble of size one, and in that case

$$\begin{aligned} H_{N-1}^0 = 1, \quad H_i^0 = 0 \quad \text{for } i \neq N-1, \\ B_1^0 = 1, \quad B_i^0 = 0 \quad \text{for } i \neq 1. \end{aligned} \tag{5.4}$$

The total numbers of holes and bubbles at time j are, respectively,

$$N_h^j = \sum_{i=1}^{N} H_i^j, \quad N_b^j = \sum_{i=1}^{N} B_i^j. \tag{5.5}$$

We note that $N_h^j = N_b^j$: we start with one hole and one bubble, following which, for every bubble we nucleate, we split an existing hole into two, thereby adding one bubble and one hole to the system. Similarly when two bubbles coalesce we lose a hole, thereby losing both a bubble and a hole. Note that our system will terminate when a single bubble fills the domain, at which point $N_h^j = 0$ and $N_b^j = 1$. Thus the number of holes is equal to the number of bubbles only while $N_h^j > 1$.

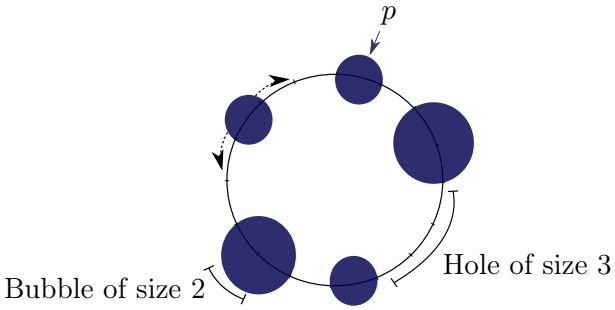


Figure 5.2: Schematic of the discretised one-dimensional circle domain; bubbles nucleate with probability p and grow by Δx in both directions at every time step.

The total amount of space unoccupied by bubbles (i.e. occupied by holes) is $\sum_{i=1}^{N} iH_i^j$, and thus the fraction of unoccupied space is

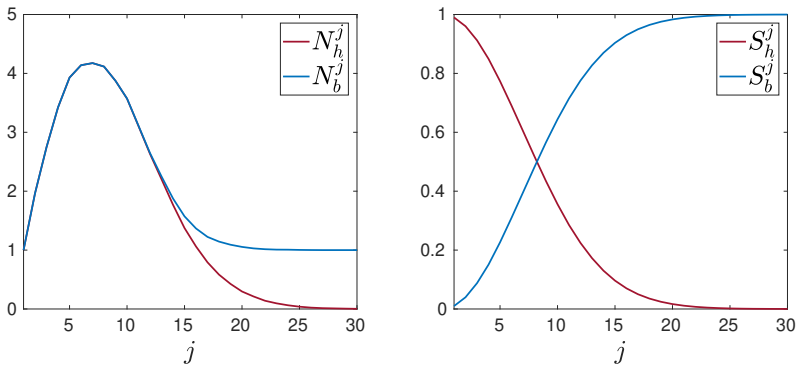
$$S_h^j = \frac{1}{N} \sum_{i=1}^{N} iH_i^j. \tag{5.6}$$

Similarly, the fraction of space occupied by bubbles is

$$S_b^j = \frac{1}{N} \sum_{i=1}^{N} iB_i^j. \tag{5.7}$$

We will refer to these as volume fractions, as the generalisation to three dimensions is clear. The volume fractions must sum to unity: $S_h^j + S_b^j = 1$ for all time steps j.

We use a Monte Carlo simulation to average over many realisations of this system. At each time step, we grow pre-existing bubbles by $2\Delta x$ and then, with probability p, we nucleate in the holes. Note that in the simulations, growth of pre-existing bubbles occurs before nucleation. The results from 10^3 runs, $N = 10^2$ spatial steps, $N_t = 30$ time steps and $p = 10^{-2}$ are shown in figure 5.3. The total number of holes N_h^j and bubbles N_b^j are equal, as expected, until the system equilibrates with a single bubble filling the domain with no holes remaining; see figure 5.3a. The volume fractions, in figure 5.3b, tell a similar story in that we start with $S_b^0 = \Delta x$ and $S_h^0 = 1 - \Delta x$, and then the bubble volume fraction increases at the same rate as the hole volume fraction decreases. This corresponds to the bubbles filling the domain with $S_b^{N_t} = 1$ and $S_h^{N_t} = 0$. Thus for every time step j we have $S_h^j + S_b^j = 1$ as expected.



(a) Number of holes/bubbles (5.5). **(b)** Volume fractions (5.6)–(5.7).

Figure 5.3: Monte Carlo results for the nucleation and growth dynamics with initial conditions (5.4) for 10^3 runs, $N = 10^2$ and $N_t = 30$ time steps with $p = 1/N$.

5.3 Discrete formulation

In deriving a model for this system we could consider a single population; this approach was used for modelling the random car-parking problem [Krapivsky, 1992]. We consider modelling the holes only. From the size distribution of holes we can derive the volume fraction and total number of bubbles from the conservation-of-volume condition that $S_h^j = 1 - S_b^j$ and the observation that $N_h^j = N_b^j$ (provided $N_h^j > 1$). However, from this we would not be able to analyse the resulting bubble size distribution, which is vital for our end goal of modelling the bubbly-to-slug flow regime transition. Thus we must also model the bubbles.

5.3.1 Holes

For the evolution of the hole density, we prescribe every hole to shrink by $2\Delta x$ after every time step Δt. Moreover, we account for the increase and loss of holes due to nucleation. The difference equation for the number density of holes of size i is:

$$H_i^{j+1} = H_{i+2}^j - ipH_{i+2}^j + 2p\sum_{k=i+1}^{N-2} H_{k+2}^j. \tag{5.8}$$

The three terms on the right-hand side signify bubble growth (thus hole contraction), hole loss by nucleation, and hole creation due to nucleation within larger holes; there is a factor of two because a hole of size $(k+2)$ shrinks to a hole of size k, and there are then two ways to form a hole of size i within this.

From the initial condition (5.4) we have $H_N^0 = 0$, and from (5.8) the holes are continuously shrinking, so we actually have

$$H_N^j = 0 \quad \text{for all} \quad j. \tag{5.9}$$

5.3.2 Bubbles

For the bubble density, each bubble is assumed to grow by $2\Delta x$ at every step, and there are growth and loss terms due to nucleation and coalescence. Mathematically, this corresponds to

$$B_i^{j+1} = B_{i-2}^j - 2(p_1^a + p_2^a)B_{i-2}^j + p_1\sum_{k=1}^{i-4} B_k^j B_{i-k-3}^j + p_2\sum_{k=1}^{i-5} B_k^j B_{i-k-4}^j. \tag{5.10}$$

The four terms on the right-hand side represent the following processes: bubble growth; the loss of bubbles due to coalescence with other bubbles as a result of growth in a hole of size one or two; growth due to coalescence of two smaller bubbles with a hole of size one between them; the same, but for a hole of size two. In (5.10) p_1^a and p_2^a are the probabilities that any hole is of size one or two; p_1 and p_2 are the probabilities that a specific hole on either side of a bubble of size i is of size one or two. These probabilities are given by

$$p_1^a = \frac{H_1^j}{N_h}, \quad p_2^a = \frac{H_2^j}{N_h}, \quad p_1 = \frac{H_1^j}{N_h^2}, \quad p_2 = \frac{H_2^j}{N_h^2}. \tag{5.11}$$

Note that (5.10) holds for $i > 2$. Bubbles of size one are the result of nucleation, similarly bubbles of size two only appear when two bubbles simultaneously nucleate next to each other, and thus coalescence occurs instantly. The number of bubbles

of size one, B_1^j, therefore corresponds to the nucleation rate of bubbles. We need to supply this nucleation rate to introduce bubbles into the system; this is given by

$$B_1^{j+1} = p \sum_{i=5}^{N} (i-4) H_i^j; \tag{5.12}$$

this is because holes of length i at time step j become of length $i-2$ at $j+1$ before any bubbles are nucleated, so that $\sum_{i\geq 3}(i-2)H_i^j$ is the total available space for nucleation. For the nucleation of a distinct bubble of size one this nucleation needs to occur at an interior point of the hole (i.e. not at an end point), otherwise the nucleation will result in instantaneous coalescence with the neighbouring bubble. Thus the available space for nucleation of a stand-alone bubble is $\sum_{i\geq 5}(i-4)H_i^j$. Similarly, note that a bubble of size two, B_2^j, will only exist as the result of the simultaneous nucleation of two neighbouring bubbles in a hole of size $i \geq 6$:

$$B_2^{j+1} = p^2 \sum_{i=6}^{N} (i-5) H_i^j. \tag{5.13}$$

Note that (5.10) is amended as follows for bubbles of size N:

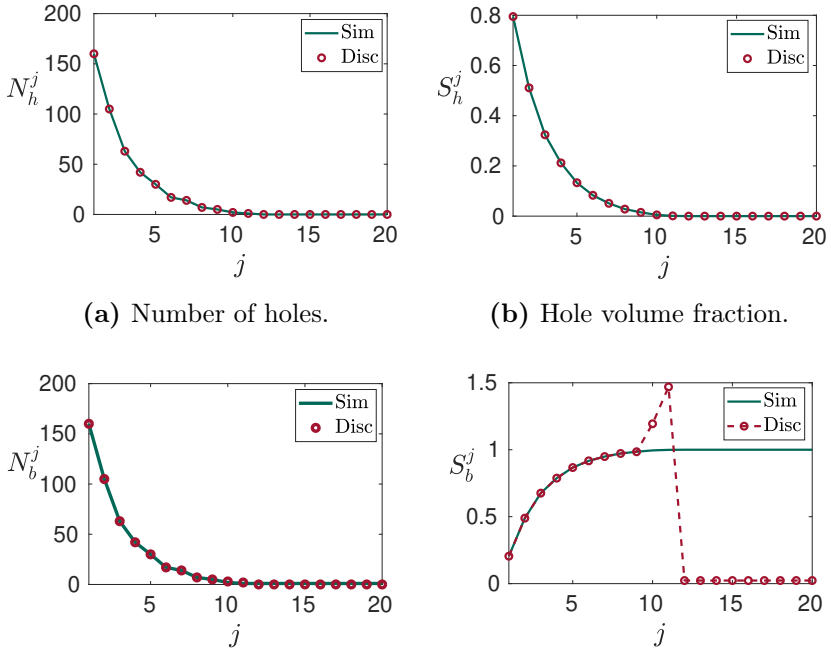
$$B_N^{j+1} = B_N^j + B_{N-1}^j + B_{N-2}^j + p_1 \sum_{k=1}^{N-4} B_k^j B_{i-k-3}^j + p_2 \sum_{k=1}^{N-5} B_k^j B_{i-k-4}^j, \tag{5.14}$$

as bubbles cannot grow larger than the size of the domain.

5.3.3 Numerical solution to the discrete formulation

We can compare the results from Monte Carlo simulations with the discrete difference formula for H_i^j in (5.8) and B_i^j in (5.10). We take the simplest problem by setting $p = 0$ which corresponds to zero nucleation rate, and is therefore a deterministic system. As we are not introducing further bubbles into the system we change our initial conditions from (5.4) to a random distribution of bubbles at $j = 0$ with $S_h^0 = 0.8$. The only dynamics are then growth and coalescence of bubbles.

We simulate the deterministic system with $N = 10^3$ for the size domain discretisation and $N_t = 20$ time steps; see figure 5.4. There is good agreement between the simulation and the discrete results for the hole size distribution in figures 5.4a and 5.4b. For the bubble size distribution however, there is only agreement for the first few time steps. Whilst the discrete formulation captures the decrease in total number of bubbles (see figure 5.4c), it predicts an unphysical increase in bubble volume fraction to above unity; see figure 5.4d.



(a) Number of holes. **(b)** Hole volume fraction.

(c) Number of bubbles. **(d)** Bubble volume fraction.

Figure 5.4: Comparison between the Monte Carlo simulation and discrete formulation of growth dynamics for N_h^j, S_h^j, N_b^j, S_b^j with $N = 10^3$, $N_t = 20$, $p = 0$.

We hypothesise that this mismatch is due to the coalescence terms in the discrete formulation — we have neglected the possible situation where multiple coalescence occurs, e.g. where three or more bubbles simultaneously coalesce. In fact, when coalescence of three bubbles is possible, the model over-accounts for coalescence of two bubbles, and introduces overlapping bubbles. This is supported by noting that the agreement between the simulation and discrete formulation improves by taking larger N; see figure 5.5. Increasing N lessens the probability of multiple coalescence.

If we define $\hat{t}$ as the time at which the discrete formulation fails to match the Monte Carlo simulation, we can examine how $\hat{t}$ changes with N. Formally we define $\hat{t}$ to be

$$\hat{t} = \min j\Delta t \quad \text{such that} \quad \|(S_b^j)^{SIM} - (S_b^j)^{DISC}\|_\infty \geq \epsilon, \tag{5.15}$$

where ϵ is some error tolerance, and $(S_b^j)^{SIM}$ and $(S_b^j)^{DISC}$ are the bubble volume fractions predicted by the simulation and discrete formulation respectively. In figure 5.6 we plot the relationship between $\hat{t}$ and N for $\epsilon = 10^{-4}$. It is clear that increasing N results in a later time $\hat{t}$ at which the discrete system breaks down. The line of best fit through the data points for $N = 10^2, 10^3, 10^4, 10^5$ gives the scaling $\hat{t} \sim N^{1/4}$. Thus we may conclude that the discrete formulation for the bubble size distribution (5.10)–(5.14) holds only for times $t \lesssim N^{1/4}$. To model later time predictions more ac-

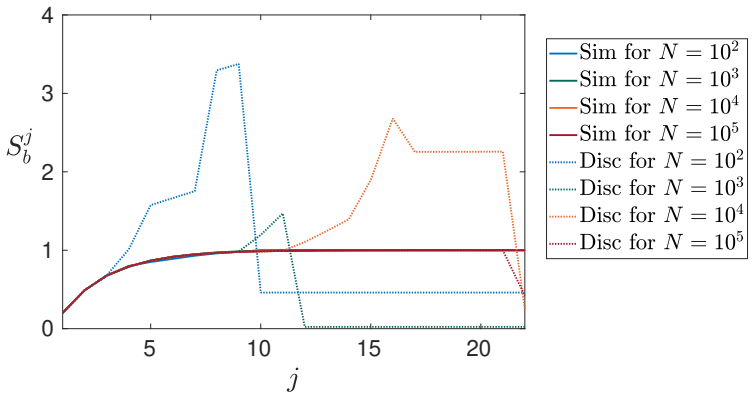


Figure 5.5: Convergence of the discrete formulation to the Monte Carlo simulation of growth dynamics for S_b^j with $N_t = 22$, $p = 0$ and varying size discretisation N.

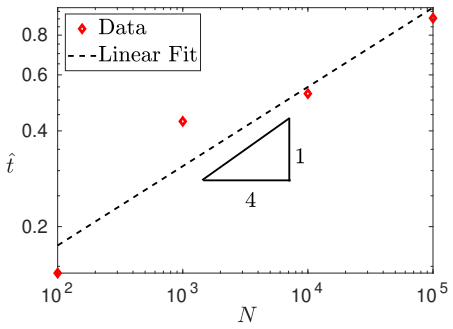


Figure 5.6: Relationship between the size domain discretisation and the limit of the discrete formulation shown through a log-log plot of the number of points N to the time $\hat{t}$.

curately, one must increase the number of points in the size discretisation, or include the more complex multi-coalescence mechanics.

Reducing the system to a deterministic model with $p = 0$ shows that, even in the simplest case, Monte Carlo simulations are essential for capturing the complexity of bubble growth and coalescence. It is not so straightforward to independently examine the effect of increasing N in the case $p \neq 0$ because p is proportional to N. Therefore increasing N consequently decreases the probability of nucleation p, and we need to correspondingly increase the time domain N_t to capture the domain-filling dynamics. This results in the Monte Carlo simulations becoming extremely slow and expensive. We therefore extend the conclusion of the $p = 0$ case, and assume the dependency on N to carry through to the $p \neq 0$ case.

5.4 Continuous limit

The accuracy of the model is dependent on taking an increasing number of points, so it seems sensible to consider a continuum model. We will consider the continuum limit of Δx, $\Delta t \to 0$. In order to convert the discrete formulation we define continuous size and time variables, x and t respectively, and a continuous rate of growth v and nucleation rate γ:

$$x = i\Delta x, \quad t = j\Delta t, \quad v = \frac{\Delta x}{\Delta t}, \quad \gamma = \frac{p}{\Delta x \Delta t}. \tag{5.16}$$

As before, the length of the domain is $L = N\Delta x$ and the time domain is $T = N_t \Delta t$. Note that, as we have chosen a constant probability p for all times, we have a constant rate of nucleation γ. We now use (5.16) to derive continuum equations for the hole and bubble populations.

5.4.1 Holes

We define the continuous hole density by

$$h(x,t)\,\Delta x = H_i^j. \tag{5.17}$$

We can then proceed to the continuum limit of (5.5) and (5.8) using (5.16) and (5.17), which gives

$$h_t - 2vh_x = -\gamma x h + 2\gamma \int_x^L h(y,t)\,\mathrm{d}y, \quad n_h = \int_0^L h\,\mathrm{d}x. \tag{5.18}$$

This is identical to the model (5.1a) from Ben-Naim and Krapivsky [1996], with the exceptions being that the upper limit of the integral is L, and we now have an arbitrary rate of growth v (Ben-Naim and Krapivsky [1996] took $v = \frac{1}{2}$). The total number of unoccupied sites is S_h^j in (5.6), and thus in the continuum limit the hole volume fraction is

$$\alpha_h = \frac{1}{L}\int_0^L xh\,\mathrm{d}x. \tag{5.19}$$

Whilst we have periodicity in the physical space, our domain of interest is the size domain $x \in [0, L]$. The characteristics of (5.18) are $x = s - 2vt$, and we therefore require a boundary condition for the holes of size $x = L$. The required boundary condition comes from the continuum limit of (5.9):

$$h = 0 \quad \text{at} \quad x = L. \tag{5.20}$$

The continuous limit of the initial condition in (5.4) corresponding to one occupied site is

$$h(x,0)\,\Delta x = \begin{cases} 1, & \text{if } x = L, \\ 0, & \text{if } x < L. \end{cases} \tag{5.21}$$

This may be formulated as the left-sided delta function:

$$h(x,0) = \delta_-(L-x), \tag{5.22}$$

defined such that $\delta_-(L-x) = 0$ for $x < L$, and $\int_0^L \delta_-(L-x)\,\mathrm{d}x = 1$.

5.4.2 Bubbles

Analogous to the hole density, the continuous bubble density is defined by

$$b(x,t)\,\Delta x = B_i^j. \tag{5.23}$$

Using this in (5.10) leads to

$$b_t + 2vb_x = \frac{2vh(0,t)}{n_h^2}\left[\int_0^x b(y,t)b(x-y,t)\,\mathrm{d}y - 2n_h b\right], \tag{5.24}$$

which reproduces equation (5.1b), without the delta-function term and, as in (5.18), with an arbitrary rate of growth v. The delta function is really a manifestation of the nucleation rate for b. Specifically, (5.10) does not apply for $i = 1, 2$, for which the relevant prescription is (5.12)–(5.13), the continuum limit of which (where we use that $B_1^j + B_2^j = 2b(0,t)\Delta x$) is the nucleation rate

$$b(0,t) = \frac{\gamma}{2v}\int_0^L xh\,\mathrm{d}x. \tag{5.25}$$

Note that in the continuum limit this nucleation rate acts as a boundary condition for bubbles of size $x = 0$. This is appropriate as the characteristics of (5.24) are $x = s + 2vt$.

The initial condition for $b(x,t)$ in (5.4) becomes

$$b(x,0)\,\Delta x = \begin{cases} 1, & \text{if } x = 0, \\ 0, & \text{if } x > 0, \end{cases} \tag{5.26}$$

which we write as a right-sided delta function $\delta_+(x)$ defined to be zero for $x > 0$ and such that $\int_0^L \delta_+(x)\,\mathrm{d}x = 1$:

$$b(x,0) = \delta_+(x). \tag{5.27}$$

The associated total number of bubbles and bubble volume fraction from (5.5) and (5.7) are given by

$$n_b = \int_0^L b \, \mathrm{d}x, \quad \alpha_b = \frac{1}{L} \int_0^L xb \, \mathrm{d}x. \tag{5.28}$$

The continuum equations for the holes (5.18) and bubbles (5.24) were derived from the discrete formulations (5.8) and (5.10) respectively. The solutions of the two formulations should therefore match exactly. The convergence of the numerical solution for the continuum equations to the analogous discrete formulation is presented in Appendix A.

5.5 Dimensionless model

For further analysis, we nondimensionalise the system of equations (5.18), (5.20), (5.22) for the holes and (5.24), (5.25), (5.27) for the bubbles.

5.5.1 Holes

For the hole equations (5.18) and (5.19), we scale the variables as

$$t \sim \frac{1}{\sqrt{2\gamma v}}, \quad x \sim \left(\frac{2v}{\gamma}\right)^{1/2}, \tag{5.29}$$

and defining the following dimensionless quantities:

$$f = \left(\frac{2v}{\gamma L}\right) h, \quad \mathcal{L} = L \left(\frac{\gamma}{2v}\right)^{1/2}, \quad n_f = \frac{n_h}{\mathcal{L}}, \quad \alpha_f = \alpha_h; \tag{5.30}$$

it follows that the dimensionless versions of (5.18) and (5.19) are

$$f_t - f_x = -xf + 2 \int_x^{\mathcal{L}} f(y,t) \, \mathrm{d}y, \quad n_f = \int_0^{\mathcal{L}} f \, \mathrm{d}x, \tag{5.31}$$

$$\alpha_f = \int_0^{\mathcal{L}} xf \, \mathrm{d}x. \tag{5.32}$$

Rescaling the boundary condition (5.20) gives

$$f = 0 \ \text{ at } \ x = \mathcal{L}. \tag{5.33}$$

Note that the initial condition (5.22) becomes (using $|a|\delta(ax) = \delta(x)$)

$$f(x,0) = \frac{1}{\mathcal{L}} \delta_-(\mathcal{L} - x). \tag{5.34}$$

5.5.2 Bubbles

We make the equations for b dimensionless by employing the nondimensionalisation (5.29)–(5.30) along with

$$g = \left(\frac{2v}{\gamma L}\right) b, \quad n_g = \frac{n_b}{\mathcal{L}}, \quad \alpha_g = \alpha_b. \tag{5.35}$$

Using this in (5.24) leads to

$$g_t + g_x = \frac{f(0,t)}{n_f^2}\left[\int_0^x g(y,t)g(x-y,t)\,\mathrm{d}y - 2n_f g\right]. \tag{5.36}$$

The dimensionless total number of bubbles and bubble volume fraction from (5.28) are given by

$$n_g = \int_0^{\mathcal{L}} g\,\mathrm{d}x, \quad \alpha_g = \int_0^{\mathcal{L}} xg\,\mathrm{d}x. \tag{5.37}$$

The boundary condition (5.25) becomes

$$g(0,t) = \int_0^{\mathcal{L}} xf\,\mathrm{d}x, \tag{5.38}$$

and the initial condition (5.27) becomes

$$g(x,0) = \frac{1}{\mathcal{L}}\delta_+(x). \tag{5.39}$$

Note that in scaling (5.18) and (5.24) the only parameter that remains is the dimensionless domain length $\mathcal{L}$.

5.5.3 Continuum model for the infinite domain

We can compare our continuum model in the finite domain to the model presented in Ben-Naim and Krapivsky [1996] in the infinite domain by taking the limit $\mathcal{L} \to \infty$. For the hole size distribution, for the infinite domain $0 \le x < \infty$, we can set $\mathcal{L} = \infty$ in the integrals in (5.31). Note, however, that the characteristics for f in (5.31) ($x = s - t$) propagate information into the system from the boundary condition at $x = \mathcal{L}$. We solve this issue by fixing $\mathcal{L}$ finite but such that $\mathcal{L} \gg 1$ and defining $f \equiv 0$ for $x > \mathcal{L}$. This is consistent with (5.31), and the boundary condition (5.33) is automatically satisfied.

The initial condition for the holes (5.34) is, however, less easily dealt with. To take $f = 0$ everywhere initially is not satisfactory as this disagrees with assuming the infinite domain $0 \le x < \infty$ in (5.34) which gives

$$\int_0^\infty f(x,0)\,\mathrm{d}x = 0, \quad \int_0^\infty xf(x,0)\,\mathrm{d}x = 1, \tag{5.40}$$

which is precisely (5.3) from Ben-Naim and Krapivsky [1996]. This corresponds to no holes ($n_f = 0$) from (5.31) initially, but also to the domain being filled by a hole ($\alpha_f = 1$) from (5.32). Whilst this is not an intuitive initial condition for the hole population, Ben-Naim and Krapivsky [1996] argue that this initial condition corresponds to no bubbles being present initially. Thus if we relax our previous definition of a hole existing only between two bubbles to a hole being any space unoccupied by bubbles, the initial condition (5.40) is justifiable.

For the bubble size distribution g in (5.36), the characteristics ($x = s + t$) move to the right in the (x, t) plane. The location of the right boundary condition at $\mathcal{L}$ is therefore inconsequential for the bubble equation (5.36). The bubble equation depends on the hole population so, providing we specify $f = g = 0$ for $x > \mathcal{L}$ as discussed above, we can simply set the upper bound of the integrals (5.37) and (5.38) to be $\mathcal{L} = \infty$. Note that this gives $g \to 0$ for $x \to \infty$. For the initial condition in (5.39) we can take

$$g(x, 0) = 0 \quad \text{for all} \quad x \in [0, \infty). \tag{5.41}$$

5.6 Conservation of volume

On a ring it is clear that the number of bubbles equals the number of holes until one of the populations fills the entire domain. It is also evident that the total number of sites remains constant, and thus that the total length of holes and bubbles combined is constant. However, we saw in Section 5.3.3 that the discrete formulation fails to capture the required conservation laws. Therefore, taking the continuum limit of the discrete system (5.8) and (5.10) will result in a continuum model with the same issues.

In the continuum limit, we can however ensure that conservation of volume holds by explicitly accounting for it through reformulating the equations. In this section, we examine how we might do this.

5.6.1 Conservation in the finite domain

The hole density is governed by (5.31) subject to the boundary condition (5.33) and initial condition (5.34). The bubble density is governed by (5.36) with boundary condition (5.38) and initial condition (5.39). In the finite domain we defined the total hole number, n_f, in (5.31) and hole volume fraction, α_f, in (5.32). Similarly the total bubble number, n_g, and bubble volume fraction, α_g, are given by (5.37). Conservation

requires

$$\alpha_f + \alpha_g = 1, \tag{5.42a}$$

$$n_g = n_f. \tag{5.42b}$$

Integration of (5.31) and (5.36) yield the following set of equations:

$$\dot{n}_f = -f_0 + \alpha_f, \tag{5.43a}$$

$$\dot{n}_g = g_0 - g_{\mathcal{L}} + \frac{f_0}{n_f^2}\left[\int_0^{\mathcal{L}}\int_0^x g(y,t)g(x-y,t)\,\mathrm{d}y\,\mathrm{d}x - 2n_f n_g\right], \tag{5.43b}$$

$$\dot{\alpha}_f = -n_f, \tag{5.43c}$$

$$\dot{\alpha}_g = n_g - \mathcal{L}g_{\mathcal{L}} + \frac{f_0}{n_f^2}\left[\int_0^{\mathcal{L}}\int_0^x x\,g(y,t)g(x-y,t)\,\mathrm{d}y\,\mathrm{d}x - 2n_f\alpha_g\right], \tag{5.43d}$$

where the overdot denotes differentiation with respect to time, $g_0 = g(0,t)$ (note we have, for now, not assumed the boundary condition (5.38)) and $g_{\mathcal{L}} = g(\mathcal{L},t)$. From (5.42a) we must have $\dot{\alpha}_f + \dot{\alpha}_g = 0$, and from (5.42b) we require $\dot{n}_f = \dot{n}_g$. It is clear from (5.43) that we need to do further work to ensure that the conservation laws hold. We proceed with two approaches; firstly, we consider amending the boundary condition (5.38) by solving for the appropriate g_0 in (5.43b) that ensures (5.42) holds. Secondly, we follow the approach followed by Ben-Naim and Krapivsky [1996] for the infinite domain and assume the rate of coalescence to be an unknown function of time; we then solve for functions that govern the rate of coalescence and enforce (5.42).

5.6.1.1 Amended boundary condition

In this case, we do not assume the boundary condition (5.38) for $g(0,t)$, and instead derive the boundary condition for $g(0,t)$ by enforcing the consistency conditions.

The summation of (5.43c) and (5.43d) gives an expression for the boundary value $g_{\mathcal{L}} = g(\mathcal{L},t)$:

$$g_{\mathcal{L}} = \frac{1}{\mathcal{L}}\left[(n_g - n_f) + \frac{f_0}{n_f^2}\left(\int_0^{\mathcal{L}}\int_0^x xg(y,t)g(x-y,t)\,\mathrm{d}y\,\mathrm{d}x - 2n_f\alpha_g\right)\right]. \tag{5.44}$$

Using (5.44), we can reduce (5.43d) to

$$\dot{\alpha}_g = n_f, \tag{5.45}$$

so (5.42a) is satisfied. The condition (5.42b) is, as stated above, consistent with $\dot{n}_f = \dot{n}_g$. Equating (5.43a) to (5.43b) yields an expression for the boundary condition g_0:

$$g_0 = g_{\mathcal{L}} - f_0 + \alpha_f - \frac{f_0}{n_f^2}\left(\int_0^{\mathcal{L}}\int_0^x g(y,t)g(x-y,t)\,\mathrm{d}y\,\mathrm{d}x - 2n_f n_g\right). \tag{5.46}$$

Equation (5.46) should therefore update (5.38) as the appropriate boundary condition that conserves total volume and ensures the total number of bubbles equals the total number of holes.

Note that g_0 in (5.46) depends on the value $g_{\mathcal{L}}$ from (5.44). Information is being propagated along characteristics ($x = s + t$) from $x = 0$ to $x = \mathcal{L}$, so this is conceptually dubious as well as physically counter-intuitive. Furthermore, it cannot be guaranteed that the enforced expression for $g_{\mathcal{L}}$ provides a physically realistic value: for example, it may well give g_0, $g_{\mathcal{L}} < 0$. We thus conclude that this is not the appropriate method to use to ensure conservation of volume.

5.6.1.2 Amended rate of coalescence

The rate of coalescence in (5.36) was derived from the probability that there exists a sufficiently small hole between two bubbles in (5.11). This probability was taken to be an *averaged probability* over the whole domain, in the sense that the probability of one hole being sufficiently small was independent to that of any other hole. However, this already assumes an infinite domain where the probability of coalescence is independent of the volume fraction of bubbles. One could rewrite (5.11) to capture the dependence of coalescence on the finite population of holes in the discrete system. We will instead consider the analogous problem in the continuum setting and derive the appropriate coalescence source and sink prefactors. To do this, we rewrite (5.36) with an unknown rate of coalescence:

$$g_t + g_x = a_1(t) \int_0^x g(y,t)g(x-y,t)\,\mathrm{d}y - 2a_2(t)g, \tag{5.47}$$

where $a_1(t)$ and $a_2(t)$ are functions that govern the coalescence-driven source and sink terms. From the discrete formulation, we previously derived (5.36) with $a_1(t) = f_0/n_f^2$ and $a_2(t) = f_0/n_f$ from the discrete probabilities (5.11). We now relax the assumption of the form of $a_1(t)$ and $a_2(t)$ and treat them as unknown functions. We use (5.42) and (5.43), and keep the boundary condition g_0 from (5.38) in order to derive appropriate forms for $a_1(t)$ and $a_2(t)$ which ensure (5.42) holds; this gives

$$a_1(t) = \frac{\mathcal{L}g_{\mathcal{L}} + \dfrac{\alpha_g}{n_g}(f_0 - g_{\mathcal{L}}) - (n_g - n_f)}{\displaystyle\int_0^{\mathcal{L}} \left(x - \frac{\alpha_g}{n_g}\right) \int_0^x g(y,t)g(x-y,t)\,\mathrm{d}y\,\mathrm{d}x}, \tag{5.48a}$$

$$a_2(t) = \frac{1}{n_g}\left[f_0 - g_{\mathcal{L}} + a_1(t)\int_0^{\mathcal{L}}\int_0^x g(y,t)g(x-y,t)\,\mathrm{d}y\,\mathrm{d}x\right]. \tag{5.48b}$$

The forms of these coalescence rate terms are not physically intuitive; note that a_1 and a_2 may well be negative. However, replacing equation (5.36) for the bubble

distribution by (5.47) with (5.48a)–(5.48b) ensures conservation of volume for the system of holes and bubbles, so we persevere and use them in our model. We note that the equation for the holes (5.31) remains unchanged except for setting $\mathcal{L} \to \infty$ in the integrals.

We now derive the corresponding consistency conditions for the infinite domain. We expect both methods studied for the finite domain to collapse to the same conservation laws in the infinite domain.

5.6.2 Conservation in the infinite domain

We can compare the analysis on the finite domain with that in the limit $\mathcal{L} \gg 1$ in the infinite domain $0 \leq x < \infty$. For the infinite domain, the integral term in (5.43d) gives

$$\int_0^\infty \int_0^x x g(y,t) g(x-y,t)\, \mathrm{d}y\, \mathrm{d}x = 2\alpha_g n_g, \tag{5.49}$$

provided $g(x,t)$ decays sufficiently fast as $x \to \infty$. Furthermore, the integral term in g_0 (5.43b) can be written

$$\int_0^\infty \int_0^x g(y,t) g(x-y,t)\, \mathrm{d}y\, \mathrm{d}x = n_g^2, \tag{5.50}$$

if we assume the same decay condition for $g(x,t)$ as we did for (5.49). Thus in the infinite domain, (5.43) gives

$$\dot{n}_f = -f_0 + \alpha_f, \tag{5.51a}$$

$$\dot{n}_g = g_0 + \frac{f_0}{n_f^2}\left(n_g^2 - 2 n_f n_g\right), \tag{5.51b}$$

$$\dot{\alpha}_f = -n_f, \tag{5.51c}$$

$$\dot{\alpha}_g = n_g + \frac{2 f_0 \alpha_g (n_g - n_f)}{n_f^2}. \tag{5.51d}$$

In fact, (5.51) can be derived directly by taking derivatives of (5.31) and (5.36) and using the relevant continuous versions of hole and bubble number in the infinite domain:

$$n_f = \int_0^\infty f\, \mathrm{d}x, \quad n_g = \int_0^\infty g\, \mathrm{d}x, \tag{5.52}$$

and the hole and bubble fractional occupancy:

$$\alpha_f = \int_0^\infty x f\, \mathrm{d}x, \quad \alpha_g = \int_0^\infty x g\, \mathrm{d}x. \tag{5.53}$$

Through the amended-boundary-condition approach, we found that in the finite domain the boundary condition g_0 in (5.46) retains various integrals which do not

vanish. However, we see that (5.46) reduces to the previously derived boundary condition (5.38) in the infinite limit. Recall that in the infinite domain, we assumed $g \to 0$ as $x \to \infty$. Using (5.49) in (5.44) we find that

$$g_{\mathcal{L}} = \frac{1}{\mathcal{L}} \left[(n_g - n_f) \left(1 + \frac{2 f_0 \alpha_g}{n_f^2} \right) \right], \tag{5.54}$$

therefore, given that $n_f = n_g$, we do in fact have $g \to 0$ for $\mathcal{L} \gg 1$. Similarly, using (5.50) and $g_{\mathcal{L}} = 0$ in g_0 (5.46) with $\mathcal{L} \gg 1$, we find

$$g_0 = -f_0 + \alpha_f - \frac{f_0}{n_f^2} \left(n_g^2 - 2 n_f n_g \right). \tag{5.55}$$

From (5.51c)–(5.51d) we see that $\alpha_f + \alpha_g$ is constant if $n_f = n_g$, and that $\dot{n}_f = \dot{n}_g$ providing (5.55) holds. Note that if $n_f = n_g$ then from (5.55) $g_0 = \alpha_f$, which is identical to the boundary condition (5.38) on $x = 0$.

Our second approach of amending the rate of coalescence in the bubble equation (5.47) produced functions $a_1(t)$ and $a_2(t)$ for conservation in the finite domain in (5.48). Taking $\mathcal{L} \gg 1$ in (5.48a) and (5.48b) reproduces the averaged probability functions $a_1(t) = f_0/n_f^2$ and $a_2(t) = f_0/n_f$ that were derived from the discrete probabilities (5.11). Thus both methods of ensuring conservation in the finite domain reproduce the same system of equations in the infinite domain.

We conclude that the continuum model for the hole (5.31) and bubble (5.36) size distributions naturally conserves space for the infinite domain. Therefore, in the model presented by Ben-Naim and Krapivsky [1996], it is imperative that the limit $\mathcal{L} \gg 1$ is assumed as, without amending the system of equations derived from first principles, the conservation laws fail for the finite domain.

5.7 Finite domain solution

As discussed above, to accurately model the finite domain, we must consider an amended model. We assume the amended rates of coalescence, and take the full system of equations for the finite domain to be

$$f_t - f_x = -xf + 2 \int_x^{\mathcal{L}} f(y,t)\, \mathrm{d}y, \tag{5.56a}$$

$$g_t + g_x = a_1(t) \int_0^x g(y,t) g(x-y,t)\, \mathrm{d}y - 2 a_2(t) g, \tag{5.56b}$$

with a_1 and a_2 from (5.48a) and (5.48b) respectively, and boundary conditions

$$f(\mathcal{L},t) = 0, \tag{5.57a}$$

$$g(0,t) = \alpha_f, \tag{5.57b}$$

with initial conditions

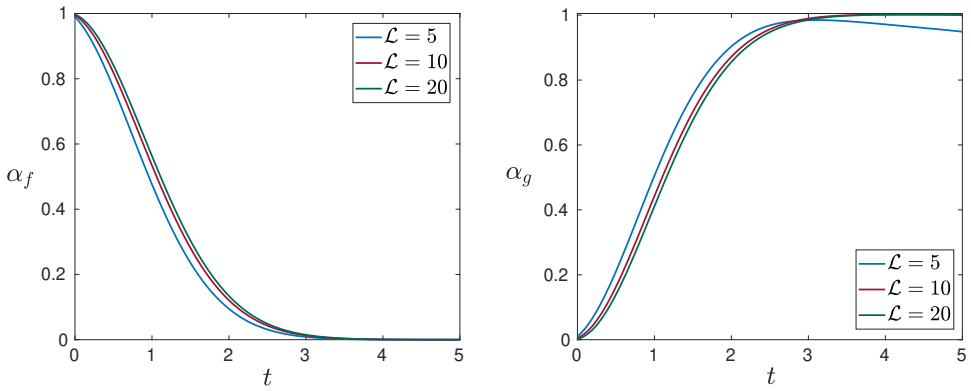
$$f(x,0) = \frac{1}{\mathcal{L}}\delta_+(\mathcal{L}-x), \tag{5.58a}$$

$$g(x,0) = \frac{1}{\mathcal{L}}\delta_+(x). \tag{5.58b}$$

Analytical solutions for the model equations are not easily found and so we seek numerical solutions for the system.

We solve the system (5.56)–(5.58) using finite differences in MATLAB. The spatial discretisation of the equations (5.56a) and (5.56b) is guided by the discrete formulation from which the continuum equations were originally derived, as discussed in Appendix A.

Recall that $\mathcal{L}$ is the only parameter in the dimensionless system. We present the numerical results for varying values of $\mathcal{L}$ in figure 5.7. We see that as we increase $\mathcal{L}$ we approach the solution we expect: the bubble volume fraction α_g converges to unity in finite time, which physically corresponds to the domain being filled by a single bubble. In Section 5.3.3 we found that the discrete model required the domain to be sufficiently large to accurately match the simulation results. This result is mirrored here, as the prediction from the continuum model depends on $\mathcal{L}$ being sufficiently large. Note that by re-deriving the appropriate rates of coalescence a_1 and a_2 we have dampened the noticeable (and unphysical) increase to above unity in the bubble volume fraction as seen in figure 5.5.



(a) Holes volume fraction. **(b)** Bubbles volume fraction.

Figure 5.7: Numerical solution to the finite domain system (5.56)–(5.58) for varying values of domain length $\mathcal{L}$ with $\Delta x = 0.05$, $\Delta t = 0.001$ and $T = 5$.

5.8 The limit $\mathcal{L} \gg 1$

We now wish to consider the limit $\mathcal{L} \gg 1$ in (5.31)–(5.34) for the hole size distribution, and in (5.36)–(5.39) for the bubble size distribution.

5.8.1 Solution for the hole size distribution

For the hole population, we seek the solution of (5.31) on the infinite domain $0 \leq x < \infty$, subject to the initial condition (5.34), and define $f \equiv 0$ for $x > \mathcal{L}$. The system of equations to solve is

$$f_t - f_x = -xf + 2\int_x^\infty f(y,t)\,\mathrm{d}y, \tag{5.59a}$$

$$f(x,0) = \frac{1}{\mathcal{L}}\delta(x-\mathcal{L}). \tag{5.59b}$$

We define the Laplace transform of f as

$$\phi(x,s) = \int_0^\infty f(x,t)e^{-st}\,\mathrm{d}t. \tag{5.60}$$

Taking the Laplace transform of (5.59a) gives

$$\Phi'' - (x+s)\Phi' - 2\Phi = \frac{1}{\mathcal{L}}\delta(x-\mathcal{L}), \tag{5.61}$$

where

$$\Phi(x,s) = \int_x^\infty \phi(y,s)\,\mathrm{d}y, \tag{5.62}$$

and the prime notation is used for differentiation with respect to x. From the definition of $f(x,t)$ for $x > \mathcal{L}$ we have $\Phi(x,t) \equiv 0$ for $x > \mathcal{L}$. Note that Φ is a Green's function for the homogeneous differential equation.

The solutions to (5.61) can be found by defining Ψ such that

$$\Phi = \Psi(\xi)\, e^{\frac{1}{4}\xi^2}, \quad \xi = x + s, \tag{5.63}$$

where Ψ satisfies

$$\Psi'' - (\tfrac{1}{4}\xi^2 + \tfrac{3}{2})\Psi = \frac{1}{\mathcal{L}}e^{-\frac{1}{4}\xi^2}\delta[\xi - (s+\mathcal{L})]. \tag{5.64}$$

Given that $\Psi \equiv 0$ for $x > \mathcal{L}$, we need to solve

$$\Psi'' - (\tfrac{1}{4}\xi^2 + \tfrac{3}{2})\Psi = 0, \tag{5.65}$$

in $0 < \xi < \mathcal{L} + s$, with the following boundary conditions

$$\Psi = 0, \quad \Psi' = -\frac{1}{\mathcal{L}}e^{-\frac{1}{4}(\mathcal{L}+s)^2} \text{ on } \xi = \mathcal{L} + s. \tag{5.66}$$

The solutions of (5.65) are parabolic cylinder functions written, for example by Abramowitz and Stegun (1964), as $U(\frac{3}{2},\xi)$ and $V(\frac{3}{2},\xi)$, with the following asymptotic behaviours in the limit $\xi \to \infty$ (corresponding to the large-x limit from (5.63)):

$$U \sim \frac{1}{\xi^2} e^{-\frac{1}{4}\xi^2}, \quad V \sim \sqrt{\frac{2}{\pi}}\, \xi\, e^{\frac{1}{4}\xi^2}. \tag{5.67}$$

The required solution is therefore a linear combination of U and V:

$$\Psi = AU + BV, \tag{5.68}$$

where A and B are constants whose values are found by using the asymptotic expressions (5.67) and applying the boundary conditions (5.66):

$$A \approx 1 + \frac{s}{\mathcal{L}}, \quad B \approx -\sqrt{\frac{\pi}{2}} \frac{e^{-\frac{1}{2}(\mathcal{L}+s)^2}}{\mathcal{L}(\mathcal{L}+s)^2}. \tag{5.69}$$

Note that (5.68)–(5.69) hold for finite $\mathcal{L}$. For $\mathcal{L} \gg 1$ we find the solution to leading order for Φ from (5.63) using (5.67)–(5.69) (ignoring the term in B in (5.68)):

$$\Phi \approx U(\xi) e^{\frac{1}{4}\xi^2}. \tag{5.70}$$

Recall that Φ is the Laplace transform of the integral of $f(x,t)$:

$$\Phi(x,s) = \int_0^\infty e^{-st} \left(\int_x^\infty f(y,t)\, \mathrm{d}y \right) \mathrm{d}t, \tag{5.71}$$

the inverse Laplace transform of Φ is therefore

$$F(x,t) \coloneqq \int_x^\infty f(y,t)\, \mathrm{d}y = \frac{1}{2\pi i} \int_{\gamma-i\infty}^{\gamma+i\infty} \Phi(x,s) e^{st}\, \mathrm{d}s, \tag{5.72}$$

where $\gamma > 0$ parametrises the line of integration such that all the singularities of Φ are to the left of the line. Using (5.70) this becomes

$$F(x,t) = \frac{1}{2\pi i} \int_{\gamma-i\infty}^{\gamma+i\infty} e^{\frac{1}{4}(x+s)^2} U(x+s) e^{st}\, \mathrm{d}s = e^{-xt} \frac{1}{2\pi i} \int_{\gamma'-i\infty}^{\gamma'+i\infty} e^{\frac{1}{4}\xi^2} U(\xi) e^{\xi t}\, \mathrm{d}\xi, \tag{5.73}$$

for some suitable γ and γ'. Thus F is e^{-xt} times the inverse transform of $U(\xi)e^{\frac{1}{4}\xi^2}$. Now, by equation (19.5.3) from Abramowitz and Stegun [1964], $U(\xi)e^{\frac{1}{4}\xi^2}$ is the Laplace transform of $te^{-\frac{1}{2}t^2}$. Therefore

$$F = te^{-xt-\frac{1}{2}t^2}, \tag{5.74}$$

and from (5.72) we have

$$f = t^2 e^{-xt-\frac{1}{2}t^2}. \tag{5.75}$$

This reproduces the solution of Ben-Naim and Krapivsky [1996], but shows how the infinite domain relates to the finite-$\mathcal{L}$ system.

5.8.2 Solution to the bubble size distribution

We can also solve for the bubble size distribution g. Assuming (5.75) for the hole size distribution f in the limit $\mathcal{L} \gg 1$, we have

$$n_f = te^{-\frac{1}{2}t^2}, \quad \alpha_f = e^{-\frac{1}{2}t^2}, \tag{5.76}$$

for the total number of holes (5.31) and the hole volume fraction (5.32). The equation for the bubble size distribution (5.36) is

$$g_t + g_x + 2tg = e^{\frac{1}{2}t^2} g * g, \tag{5.77}$$

where $g * g$ is the Laplace convolution:

$$g * g = \int_0^x g(y,t)g(x-y,t)\,\mathrm{d}y. \tag{5.78}$$

We define the Laplace transform of g in x as

$$G(s,t) = \int_0^\infty g(x,t)e^{-sx}\,\mathrm{d}x. \tag{5.79}$$

Taking the Laplace transform of (5.77) and assuming that $g \to 0$ as $x \to \infty$ yields the Riccati equation

$$G_t + (s+2t)G - e^{\frac{1}{2}t^2}G^2 = e^{-\frac{1}{2}t^2}. \tag{5.80}$$

We define the function $W(s,t)$ by writing

$$G = e^{-\frac{1}{2}t^2}W(s,t). \tag{5.81}$$

Substituting (5.81) into (5.80) gives the following equation for W:

$$W_t + (s+t)W - W^2 = 1. \tag{5.82}$$

We then define the following transformation for W (motivated by a similar functional form assumed by Ben-Naim and Krapivsky [1996]):

$$W(\eta) = \eta - \frac{w'(\eta)}{w(\eta)}, \quad \eta = s + t; \tag{5.83}$$

this yields the following equation for $w(\eta)$: $w'' = \eta w'$. The solution of this leads to

$$W(\eta) = \eta - \frac{e^{\frac{1}{2}\eta^2}}{\displaystyle\int_c^\eta e^{\frac{1}{2}\xi^2}\,\mathrm{d}\xi}, \tag{5.84}$$

where c is a constant of integration found using the Laplace transform of the initial condition $g(x,0)$ in (5.41): $G(s,0)=0$. Applying this initial condition and substituting (5.84) into (5.81), we can then solve for $G(s,t)$:

$$G = e^{-\frac{1}{2}t^2}W(s,t) = e^{-\frac{1}{2}t^2}\left[(s+t) - \frac{s\,e^{\frac{1}{2}(s+t)^2}}{s\displaystyle\int_s^{(s+t)} e^{\frac{1}{2}\xi^2}\,\mathrm{d}\xi + e^{\frac{1}{2}s^2}}\right]. \tag{5.85}$$

We consider the asymptotic solution for the large-time limit of $W(s,t)$ in (5.85). For large time we can write

$$W \sim \frac{1}{(s+t)} + \frac{2}{(s+t)^2} - \frac{5}{(s+t)^5} + \ldots, \qquad \text{as} \quad t \to \infty; \tag{5.86}$$

we can take the inverse Laplace transform of this expansion for W and use this in (5.85) for the inverse Laplace transform of G in (5.79) to give the large-time limit for the bubble size distribution g:

$$g \sim e^{-xt-\frac{1}{2}t^2}. \tag{5.87}$$

Note that for the large-time limit the *a priori* assumption of a suitably well-behaved $g(x,t)$ in Section 5.6.2 was therefore reasonable.

5.9 Summary

In this chapter, we have studied a model (5.1)–(5.2), originally presented by Ben-Naim and Krapivsky [1996], for deterministic growth and nucleation in one dimension. We re-derived the model from first principles with a discrete formulation in a finite domain. Comparison of the discrete model to a Monte Carlo simulation of the system highlighted limitations of the model; specifically the model is only accurate in a dilute system where there are not significant numbers of bubbles. This is understood to be related to the occurrence of coalescence between more than two bubbles which the model does not account for. Therefore increasing the number of points in the spatial discretisation (which corresponds to a dilute system) increased the length of time over which the model was accurate.

We then derived the corresponding continuous system from the discrete formulation; this continuum model was similar to that of Ben-Naim and Krapivsky [1996], with minor differences only in the way the boundary condition at $x=0$ was formulated and the domain; we derived equations for bubbles and holes whose domain is finite.

Every point in the system is associated with either a hole or a bubble; thus the total volume of the system must be conserved. This led to a discussion of conservation of volume in the finite-domain system. We found that the finite-domain system did not conserve volume, and required physically non-intuitive amendments. The infinite domain equations, analogous to those presented by Ben-Naim and Krapivsky [1996], did naturally conserve volume. However, we are interested in how this modelling approach may be applied to study the flow regime transition between bubbly and slug flow through a pipe. In such an application, the bubble and hole sizes will certainly be constrained by the finite domain, and thus we need to understand how to ensure conservation of volume in a finite-domain system.

Whilst the finite-domain equations (5.56)–(5.58) were not analytically tractable, we were able to make analytical progress for the simpler infinite domain equations (5.59) and (5.77). Moving forward, we want to build on this modelling approach to study bubble interactions in the bubbly-to-slug transition. In such a system, bubbles will not be growing and nucleating deterministically. They will be being moved around by the velocity field of the liquid domain. Moreover, the shape of the bubbles becomes relevant for bubble coalescence and fragmentation. In Chapter 6, we will consider how to include shape in the formulation of a model of coalescence and fragmentation. This will then be used in Chapter 7 to derive a model for the distribution of bubbles comparable to that studied in this chapter.

Chapter 6

Coalescence and fragmentation in higher dimensions

In this chapter we begin to develop a theoretical description of the bubbly-to-slug regime transition. We introduce a discretised system of equations describing the evolution of a bubble population. The motivation for this chapter is to provide preliminary work for a kinetic-theory-based macroscale model of an evolving bubble distribution. We seek the relevant variables and control parameters required to study such a system.

6.1 Introduction

We now return to the original motivation for this part of the thesis: modelling the bubble dynamics (of coalescence and fragmentation) in the bubbly-to-slug flow regime transition. Our aim is to model an evolving bubble distribution in a continuous liquid phase. Modelling the bubbles is complicated by the fact that the mass is concentrated within the liquid phase; thus the liquid dynamics are the driving force that move the bubbles around.

In this chapter we present a theoretical description of bubbles in a liquid. Importantly we account for the shape of the bubbles as we believe shape to be an important variable in the bubbly-to-slug transition. We develop an appropriate characterisation of a single bubble that allows us to track its position, shape and velocity. We then extend this framework to a system of bubbles and incorporate inter-bubble interactions. The bubbly-to-slug flow regime transition is driven by fragmentation — when a single bubble breaks up into two or more — and coalescence: where multiple bubbles merge to form one bigger bubble. There is substantial research looking at the dynam-

ics of single bubble interactions, and we briefly introduce the mechanisms governing fragmentation and coalescence here.

The fragmentation (also known as break-up) of a single bubble occurs when the hydrodynamic forces surrounding the bubble overcome the surface tension of the bubble boundary, thus causing an instability of the surface [Clift et al., 2005]. An imbalance between the external forces, acting to deform the bubble, and counteracting surface stresses therefore provides the break-up mechanism [Liao and Lucas, 2009]. The processes that cause break-up can be categorised as being due to viscous shear forces, turbulent flow fields, resonance and interfacial instability [Wang et al., 2005; Clift et al., 2005; Liao and Lucas, 2009; Sa, 2017]. The shape of the bubble is important for fragmentation as the liquid needs to squeeze and deform the bubble in such a way that pinch-off of a secondary daughter bubble is possible.

The opposite of fragmentation is coalescence, which occurs when two or more bubbles collide in such a way as to become one single bubble. When modelling coalescence, one considers the *collision frequency* and *coalescence efficiency* [Wang et al., 2005]. The collision frequency is contingent on the sizes, shapes, velocities and density of the bubbles present in the system [Prince and Blanch, 1990; Lehr and Mewes, 2001]. The coalescence efficiency corresponds to the proportion of bubble collisions that lead to coalescence. This efficiency is given as a function of two time scales; the time required for coalescence τ_1, and the time the two bubbles are in contact τ_2 [Prince and Blanch, 1990; Luo and Svendsen, 1996]. It is evident that $\tau_1 \leq \tau_2$ for coalescence to occur.

In this chapter, we consider fragmentation and coalescence driven by the liquid surrounding the bubble. The fragmentation criterion is prescribed in terms of shape evolution, and coalescence is governed by the collision frequency. We derive a system of equations for an evolving bubble distribution, and simulate the model to visualise the bubble population predictions. This chapter provides the preliminary work necessary for the development of the appropriate framework to be used in a statistical model which will be addressed in Chapter 7.

6.2 Single bubble characterisation

In this section, we consider the classification of a single bubble to understand how many variables we must keep to effectively describe the bubble dynamics. The surface of a bubble, at time t, is described by the surface function $r = \hat{R}(\theta, \chi, t)$ in terms of the spherical polar angle $\theta \in [0, \pi]$ and the azimuthal angle $\chi \in [0, 2\pi]$. For a sufficiently convex bubble, the surface function $\hat{R}$ can be written as an infinite series

of spherical harmonics. We will immediately limit our consideration to azimuthally symmetric bubbles, so that we can write the surface function in terms of the Legendre polynomials P_n:

$$\hat{R} = \sum_{k=0}^{\infty} a_{2k}(t) P_{2k}(\cos\theta). \tag{6.1}$$

This provides an infinite-dimensional shape vector $\boldsymbol{\sigma}_\infty = (a_0,\, a_2,\, a_4,\, \dots)$. To reduce this to a finite-dimensional shape vector we truncate (6.1) to two terms:

$$\hat{R} = a_0 + a_2 P_2(\cos\theta). \tag{6.2}$$

The truncated surface function (6.2) is sufficient to describe the shape evolution from one extreme of a vertical 'peanut' through to a sphere and then to the other extreme of a horizontal 'pinched-torus'; see figure 6.1.

The surface function (6.2) is therefore an appropriate description of the bubble shapes that satisfy our symmetry assumptions. We define new shape variables by

$$\hat{\xi} = a_0 + a_2, \quad \hat{\eta} = a_0 - \tfrac{1}{2} a_2. \tag{6.3}$$

The finite-dimensional shape vector is therefore given by $\boldsymbol{\sigma} = (\xi,\, \eta)$. Note that $\xi = 0$ corresponds to a vertical 'figure-of-eight', $\eta = 0$ to a horizontal 'figure-of-eight' and $\xi = \eta$ to a sphere; see figure 6.1. The truncated surface function (6.2) now becomes

$$\hat{R} = \hat{\xi}\cos^2\theta + \hat{\eta}\sin^2\theta. \tag{6.4}$$

The associated volume of the bubble is given by:

$$\hat{V} = \frac{4\pi}{3}\int_0^{\pi/2} \hat{R}^3 \sin\theta \,\mathrm{d}\theta. \tag{6.5}$$

Using the surface function $\hat{R}$ from (6.4) this becomes

$$\hat{V} = \frac{4\pi}{105}\left(5\hat{\xi}^3 + 6\hat{\xi}^2\hat{\eta} + 8\hat{\xi}\hat{\eta}^2 + 16\hat{\eta}^3\right). \tag{6.6}$$

In this chapter, we consider a system of bubbles translating along a horizontal axis and allow for horizontal break-up. It therefore makes sense to rotate the bubbles ninety degrees such that $(\hat{\xi}, \hat{\eta}) \mapsto (\eta, \xi)$, with $\eta = a_0 + a_2$ as the horizontal length and $\xi = a_0 - \frac{1}{2}a_2$ as the vertical length. The surface function is now given by

$$R = \eta\cos^2\theta + \xi\sin^2\theta; \tag{6.7}$$

we present the resulting bubble shapes at $\eta = 0$, $\xi = \eta$ and $\xi = 0$ in figure 6.2. From (6.5) the associated volume is

$$V = \frac{4\pi}{105}\left(5\eta^3 + 6\eta^2\xi + 8\eta\xi^2 + 16\xi^3\right). \tag{6.8}$$

Thus, to capture shape and position it is sufficient to track $\{X, \eta, \xi\}$, where X is position of the bubble centre; see figure 6.3.

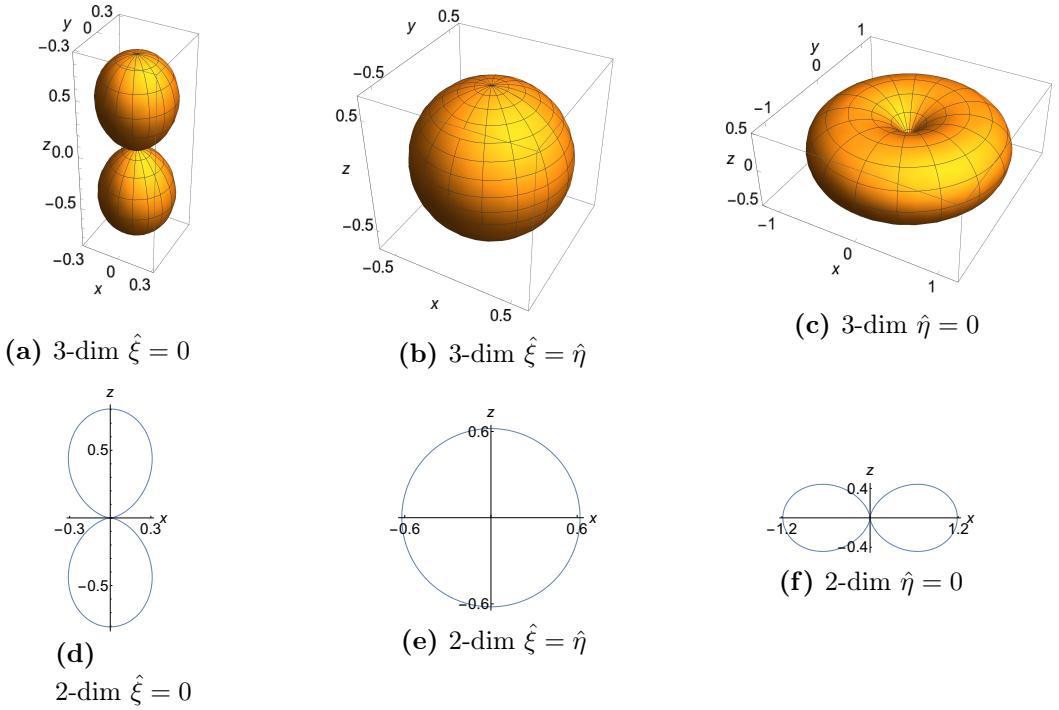


Figure 6.1: Bubble shapes described by the finite-dimensional surface function (6.4) for varying $(\hat{\xi}, \hat{\eta})$ with $\hat{V} = 1$ in figures 6.1a–6.1c with corresponding slices through the (x, z)-plane at $y = 0$ in figures 6.1d–6.1f.

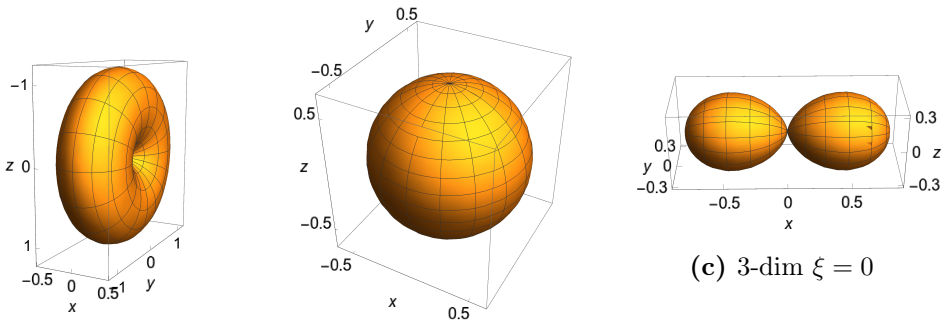
6.3 Bubble evolution

The evolution of the shape will be driven by the difference between the end-point velocities corresponding to the 'stretching' and 'shrinking' of the bubble. Moreover the bubble centre governs the translation of the bubble and this is also determined by the end-point velocities. In this section we discuss how to evolve a bubble's shape and position, but firstly and importantly we consider conservation of the bubble volume.

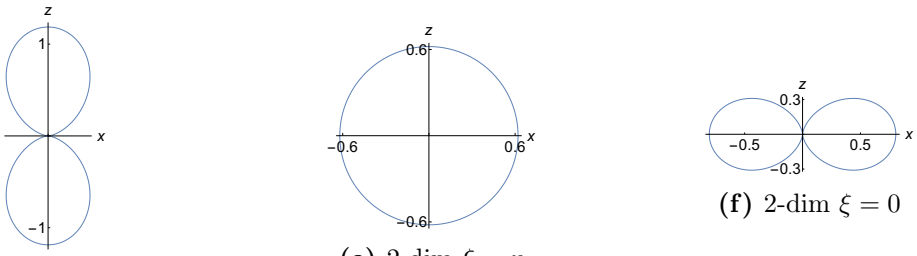
6.3.1 Volume conservation

The volume of the bubble is given in (6.8) and the relationship between the volume V and shape variables ξ and η is shown in figure 6.4. As the bubble shape evolves, conservation of volume is ensured by $\dot{V} = 0$, where the overdot notation represents the time derivative. Using (6.8), $\dot{V} = 0$ gives an expression for $\dot{\xi}$:

$$\dot{\xi} = -\left(\frac{15\eta^2 + 12\eta\xi + 8\xi^2}{6\eta^2 + 16\eta\xi + 48\xi^2}\right)\dot{\eta}. \tag{6.9}$$



(a) 3-dim $\eta = 0$ **(b)** 3-dim $\xi = \eta$ **(c)** 3-dim $\xi = 0$



(d) 2-dim $\eta = 0$ **(e)** 2-dim $\xi = \eta$ **(f)** 2-dim $\xi = 0$

Figure 6.2: Bubble shapes described by the finite-dimensional surface function (6.7) for varying (η, ξ) with $V = 1$ in figures 6.2a–6.2c with corresponding slices through the (x, z)-plane at $y = 0$ in figures 6.2d–6.2f.

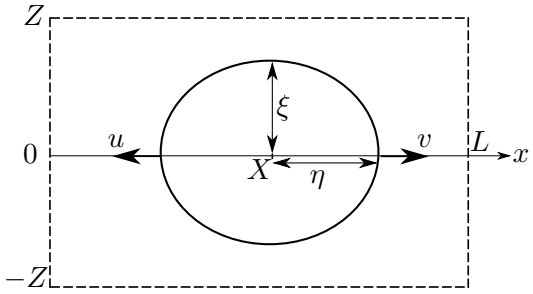


Figure 6.3: Schematic of a single bubble in a one-dimensional domain defined by (X, η, ξ).

We therefore only need prescribe $\dot{X}$ and $\dot{\eta}$ to fully describe the evolution of the bubble. Note that each variable is a function of time only: $(X(t), \eta(t), \xi(t))$.

6.3.2 Model equations

It is clear that in a system of gas bubbles in a continuous liquid domain the mass in the system is predominantly in the liquid phase. Thus the gas bubbles will be moved around by the liquid and consequently the evolution of the bubble population is driven by the liquid dynamics. We expect a turbulent liquid flow and we therefore

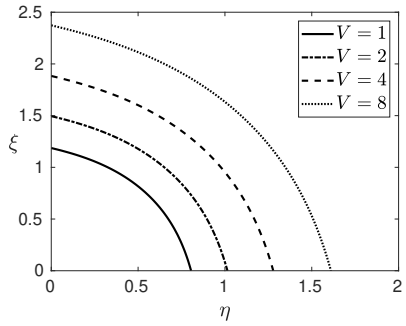


Figure 6.4: Contour plot for the volume of the bubble as a function of ξ and η in (6.8).

prescribe a random Fourier series for the velocity field along the horizontal axis that governs the translation and shape evolution of the bubbles. The velocity field is given by:

$$V(x,t) = \sum_{m,n} a_{mn} \cos(mx)\cos(nt), \tag{6.10}$$

for constants a_{mn}, where x denotes the horizontal axis and t time. We choose the constants a_{mn} to be decreasing and randomly sampled from a uniform distribution between $[-A, A]$ for constant A, and we take $m, n \in [1, 5]$. Translation and shape evolution are governed by the velocity at both ends of the bubble. From (6.10) we can prescribe velocities at the left and right end-points of the bubble, denoted u and v respectively (see figure 6.3):

$$u(t) = V(X - \eta, t), \tag{6.11a}$$

$$v(t) = V(X + \eta, t). \tag{6.11b}$$

Given u, v above, the complete system of equations for the evolution of a single bubble characterised by the variables (X, η, ξ) is:

$$\dot{X} = \frac{1}{2}(v + u), \tag{6.12a}$$

$$\dot{\eta} = \begin{cases} \frac{1}{2}(v-u), & \text{for} \quad \eta > \epsilon, \\ \max\left[0, \frac{1}{2}(v-u)\right], & \text{for} \quad \eta \leq \epsilon, \end{cases} \tag{6.12b}$$

$$\dot{\xi} = \dot{\xi}(\eta, \xi, \dot{\eta}). \tag{6.12c}$$

Note that we have introduced a discontinuous function in the $\dot{\eta}$ equation; this is to avoid the situation when $\eta < 0$ where the bubble evolves through itself to the unphysical shape of two perpendicular peanut shapes. Thus we evolve the shape through $\dot{\eta}$ until $\eta \leq \epsilon$ for some constant $\epsilon > 0$, we then set $\dot{\eta} = 0$ until the end-point velocities are stretching the bubble horizontally such that $\dot{\eta} > 0$.

The system of equations (6.11)–(6.12) is easily extended to a system of any arbitrary number of bubbles. We consider N bubbles aligned along the horizontal axis and indexed $i = 1 \ldots, N$ (for an integer N). That is, the first bubble, indexed $i = 1$, is adjacent to the left wall at $x = 0$ and the last N^{th} bubble is adjacent to the right wall at $x = L$.

Analogous to the single bubble system, the volume of each bubble is conserved by $\dot{V}_i = 0$ where V_i is the volume of the i^{th} bubble given by (6.8). As before, volume conservation provides an equation for the vertical velocity $\dot{\xi}_i$ from (6.9). The system of equations for the i^{th} bubble is

$$
\begin{aligned}
u_i &= V(X_i - \eta_i, t), && \text{(6.13a)}\\
v_i &= V(X_i + \eta_i, t), && \text{(6.13b)}\\
\dot{X}_i &= \frac{1}{2}(v_i + u_i), && \text{(6.13c)}\\
\dot{\eta}_i &= \begin{cases} \frac{1}{2}(v_i - u_i), & \text{for} \quad \eta_i > \epsilon, \\ \max\left[0, \frac{1}{2}(v_i - u_i)\right], & \text{for} \quad \eta_i \leq \epsilon, \end{cases} && \text{(6.13d)}\\
\dot{\xi}_i &= \dot{\xi}(\eta_i, \xi_i, \dot{\eta}_i). && \text{(6.13e)}
\end{aligned}
$$

where the subscript i denotes the i^{th} bubble. Thus for N bubbles, at each time step, we need to solve $3N$ ordinary differential equations.

6.4 Bubble interactions

In an evolving system of bubbles, we need to think about interactions which may result in a changing number of bubbles. We consider a system of bubbles that is governed by equations (6.13) until 'an event' occurs, in which case we reset the variables appropriately and then continue solving (6.13). More specifically the events that may occur are: coalescence of neighbouring bubbles, fragmentation of any bubble and wall collisions of either end bubble. We consider each of these possible events and their effect on the system in turn.

6.4.1 Coalescence

Coalescence occurs when two or more bubbles merge to become one larger bubble. The process requires the bubbles to be in contact for a certain amount of time to allow the liquid film between them to drain [Wang et al., 2005]. It is clear that, at the very least, the necessary criterion for coalescence between two bubbles is $X_i + \eta_i = X_{i+1} - \eta_{i+1}$ where coalescence occurs along the axis; see figure 6.5. We make the

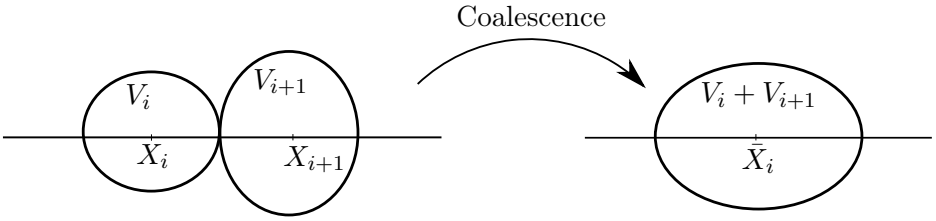


Figure 6.5: Schematic of coalescence between the i^{th} and $(i+1)^{th}$ bubbles forming the i^{th} bubble.

simplifying assumption that as soon as two bubbles meet, they coalesce. It is necessary to consider situations where coalescence does not occur along the axis. This can happen when the widest part of either coalescing bubble is not along the axis with $\xi > \eta$. Coalescence therefore occurs at the point of meeting. We can account for this by specifying the coalescence criterion to be

$$X_i + \max(\eta_i, \xi_i) = X_{i+1} - \max(\eta_{i+1}, \xi_{i+1}). \tag{6.14}$$

When two bubbles coalesce we lose a bubble from the system, and need to define variables for the new bubble. To conserve total volume, it is clear that the volume of the new bubble must be the sum of the volumes of the two coalescing bubbles: $\bar{V}_i = V_i + V_{i+1}$, where the bar notation is used for the new variables. The midpoint of the new bubble is prescribed to be: $\bar{X}_i = \frac{1}{2}(X_i + X_{i+1})$. For the shape of the new bubble we assume surface tension effects to be sufficient such that coalescence immediately results in a spherical bubble. The shape variables are therefore given by $\bar{\eta}_i = \bar{\xi}_i = (3\bar{V}_i/4\pi)^{1/3}$.

6.4.2 Fragmentation

We assume fragmentation to be governed by shape evolution; break up occurs when a single bubble is stretched from either end resulting in a horizontal peanut-shape at $\eta_i = 0$ (see figure 6.2c).

Recall that, by (6.13d), we do not allow the bubble shape to evolve past $\eta = 0$ where in three dimensions the bubble is a vertical pinched-torus. For this shape it is not natural to consider vertical pinch-off resulting from a pinched-torus (see figure 6.2a). We therefore account only for horizontal pinch-off.

Fragmentation is the inverse of coalescence: a single bubble breaks up to produce two new daughter bubbles (therefore introducing an additional bubble to the system). We need to prescribe the variables for the two new bubbles. We assume that

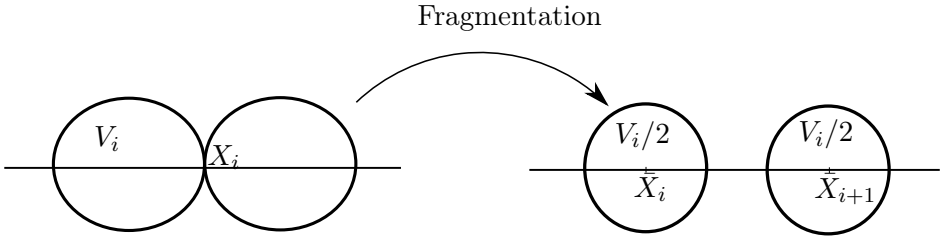


Figure 6.6: Schematic of the i^{th} bubble fragmenting from horizontal pinch-off creating daughter i^{th} and $(i+1)^{th}$ bubbles.

fragmentation will produce two equally sized bubbles, meaning a bubble of volume V_i will produce two daughter bubbles both of volume $\bar{V}_i = \bar{V}_{i+1} = V_i/2$; see figure 6.6.

It is clear that to avoid immediate coalescence we need to assume $\bar{X}_i + \bar{\eta}_i \neq \bar{X}_{i+1} + \bar{\eta}_{i+1}$. We therefore separate the daughters bubbles slightly by taking $\bar{X}_i = X_i - \eta_i/2 - \epsilon$ on the left, and $\bar{X}_{i+1} = X_i + \eta_i/2 + \epsilon$ on the right for some $\epsilon > 0$. This takes the centres of the new bubbles to be the centre of the respective halves of the fragmenting bubble shifted apart by ϵ. The remaining variables are prescribed under the assumption that both daughter bubbles are of equal volume and both spherical: $\bar{\eta}_i = \bar{\xi}_i = (3\bar{V}_i/4\pi)^{1/3}$.

6.4.3 Wall effects

We need to consider end effects to the left of the first bubble and to the right of the last bubble. Clearly, the first bubble hits the left wall when $X_1 - \eta_1 = 0$, and the last (N^{th}) bubble hits the right wall when $X_N + \eta_N = L$; see figure 6.3 for the $N = 1$ case. However, as with coalescence, we need to extend our consideration to bubbles such that $\xi > \eta$. We therefore prescribe the criterion for a left-wall hit to be $X_1 - \max(\eta_1, \xi_1) = 0$; and $X_N + \max(\eta_N, \xi_N) = L$ on the right.

As with coalescence and fragmentation we require further assumptions on the resulting position and velocity of the bubbles should they hit the wall. There are various ways to do this. We could treat the wall as an infinitely large bubble with zero velocity. However, we do not want to coalesce the bubble with the wall as this would result in a loss of volume. Ideally, therefore, we would somehow bounce the bubble off the wall.

For the left wall we will assume that if $X_1 - \max(\eta_1, \xi_1) = 0$, then we reset the position of the bubble (keeping the shape variables (η_1, ξ_1) fixed):

$$X_1 \to X_1 + \max(\eta_1, \xi_1), \tag{6.15}$$

the analogous assumption holds for X_N at the right wall. We are essentially shifting the bubble away from the wall. Physically this approximation to a 'wall-bounce' is

reasonable.

6.5 Stochastic simulation

We now develop an approach for solving the system presented above in (6.13). We use explicit time-stepping to evolve the solution variables $(X_i,\, \eta_i,\, \xi_i)$ for $i = 1, \ldots, N$. The basic outline for setting up the simulation is to solve the system until an *event* occurs or until a stopping criterion is reached. We label an event to be either coalescence, fragmentation or a bubble wall-bounce as discussed in Sections 6.4.1, 6.4.2 and 6.4.3 respectively. The two possible stopping criteria comprise either reaching the prescribed end time T or the prescribed maximum number of events K.

When initialising the system, we prescribe the total volume of bubbles V (which remains constant throughout the simulation) and the initial number of bubbles N. We sample random positions for the bubbles (ensuring no overlap) and random sizes for each bubble (such that the sum is V) whilst keeping the shape of all the bubbles to be initially spherical. Moreover, as discussed above, we sample a_{mn} from a uniform distribution between $[-A, A]$ for constant A. The algorithm is described here:

1. Initialise: N bubbles; V total volume; domain parameters $(L,\, Z)$; initial conditions (X_i, η_i, ξ_i) for $i = 1, \ldots, N$; sample values a_{mn}; the maximum number of events K; the end time T; the event count $k = 0$.

2. Solve the system (6.13) until an event occurs, or a stopping criterion is reached. If an event occurs then set $k \to k + 1$, reset the system variables and restart the solver.

   - Coalescence occurs between i^{th} and $(i{+}1)^{th}$ bubbles when $X_i{+}\max(\eta_i, \xi_i) = X_{i+1} - \max(\eta_{i+1}, \xi_{i+1})$. We reduce the total number of bubbles by one $(N \to N - 1)$, introduce the variables $(\bar{X}_i,\, \bar{\eta}_i, \bar{\xi}_i)$ for the new i^{th} bubble as described in Section 6.4.1, and re-index the bubbles to the right of the $(i + 1)^{th}$ bubbles: $(X_k,\, \eta_k,\, \xi_k) \to (X_{k-1},\, \eta_{k-1},\, \xi_{k-1})$ for $k > i + 1$.
   - Fragmentation of the i^{th} bubble occurs when $\eta_i = 0$. We increase the number of bubbles by one $(N \to N{+}1)$, introduce the variables $(\bar{X}_i,\, \bar{\eta}_i, \bar{\xi}_i)$ and $(\bar{X}_{i+1},\, \bar{\eta}_{i+1}, \bar{\xi}_{i+1})$ for the new i^{th} and $(i + 1)^{th}$ bubbles as described in Section 6.4.2, and re-index the bubbles to the right of the i^{th} bubble: $(X_k,\, \eta_k,\, \xi_k) \to (X_{k+1},\, \eta_{k+1},\, \xi_{k+1})$ for $k > i$.
   - Where the first bubble hits the left wall with $X_1 - \max(\eta_1,\, \xi_1) = 0$, or the N^{th} bubble hit the right wall with $X_N + \max(\eta_N,\, \xi_N) = L$ reset the

variables for the first or last bubble only as described in Section 6.4.3.

3. Terminate the simulation when $k = K$ or $t = T$.

4. Output: (X_i, η_i, ξ_i) for $i = 1, \ldots, N_k$ for every time point, where N_k denotes the number of bubbles after the k^{th} event and the corresponding distribution of bubble volumes after each event.

Each simulation produces an evolving bubble distribution at every time step for a given set of initial conditions where the variables of interest are the distribution of individual bubble volumes and the total number of bubbles in the system. Note that, for each run, the volume distribution will remain constant between events.

Ideally we want our results to be independent of the initial conditions. We therefore introduce randomness to the initial conditions for the individual volume and position of the bubbles (whilst setting all bubbles to be spherical initially and ensuring that there is no overlap), and the horizontal velocity field. With randomness, we re-run the simulation N_{sim} times to produce a Monte Carlo simulation by averaging across the runs (where a single run is associated to a given set of initial conditions).

Parameter	Value
Z	5 mm
K	200
T	5 s
ϵ	10^{-3} mm
Δt	10^{-2}
A	2
N_{sim}	100

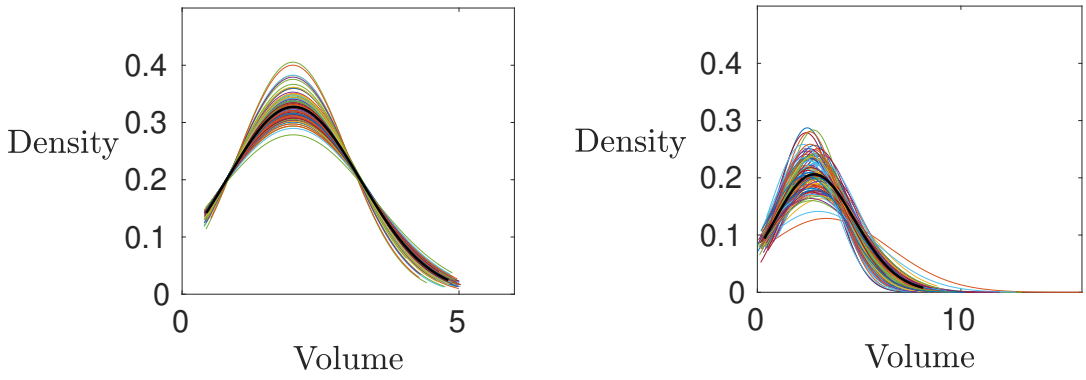
Table 6.1: List of parameters used in the simulation; Z is the vertical height of the domain; K the maximum number of events; T the end time; ϵ is the value used in the resetting of variables for fragmentation; Δt denotes the step size in the time discretisation; A provides the bounds for the randomly sampled coefficients in the prescribed velocity field; and N_{sim} the number of simulations.

6.5.1 Results

There are two principal parameters to investigate when simulating the system; the initial number of bubbles and the total volume of bubbles; the latter of which remains

constant over time. To visualise the results of the stochastic simulation we average the results over all the runs. We study how the number of bubbles changes with time, and assess how the volume of individual bubbles evolves over time using a probability density function of volume. Another method for visualising the changing volumes of bubbles is the use of histograms to show the number of bubbles in a prescribed 'volume bin' scaled by the total number of bubbles, thus providing a probability measure for the volume of individual bubbles. For the histogram, we choose to have three volume bins of equal size between volume 0 and $V^* \equiv 5V/N$; this upper bound is advised by the largest individual volume amongst all runs.

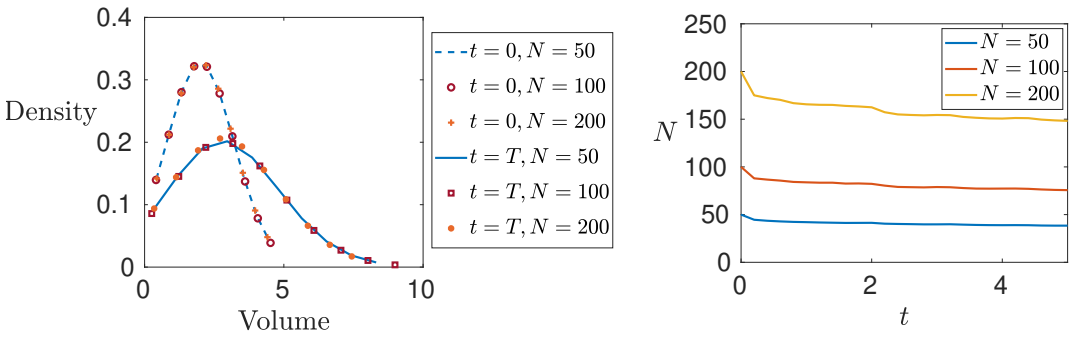
To assess the performance of the average we present the probability density function of volume for $t = 0$ and $t = T$ with $N = 50$, $V = 100$ mm^3 and $L = 250$ mm and the parameters given in table 6.1 in figure 6.7. We see that the average represents the general trend amongst the volume distributions well for both the starting time $t = 0$ and the end time $t = T$. The general behaviour sees the volume distribution shift from predominantly smaller bubbles at $t = 0$ (in figure 6.7a) to larger bubbles at $t = T$ (in figure 6.7b). For the remainder of this section we will present averaged results for the system of bubbles using the parameters given in table 6.1.



(a) $t = 0$ **(b)** $t = T$

Figure 6.7: Performance of averaging process shown through the probability density function of volume for $t = 0$ and $t = T$. The $N_{sim} = 100$ runs are plotted with the average shown in black for $N = 50$, $V = 100$ mm^3 and $L = 250$ mm.

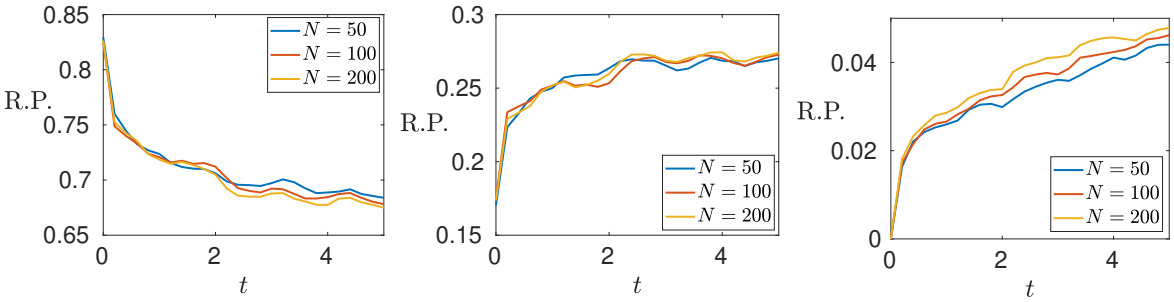
To assess the robustness of the system we examine the scalability of the system. We do this by varying the number of bubbles N in the system, and prescribe the length L and total volume V to be proportional to N. We note the analogy with spatial discretisation, where convergence of a solution is a function of the spatial step size. In figure 6.8, we show the averaged results for $N = 50$, 100, 200 with $V = 2N$



(a) Volume probability density function. **(b)** Number of bubbles.

Figure 6.8: Scalability of the system visualised through the volume probability density function of number of bubbles for $N = 50$, 100, 200 with $V = 2N$ mm^3 and $L = 5N$ mm.

and $L = 5N$. Thus we are keeping the initial bubble distribution at $t = 0$ and the volume of the bins the same between setups. The initial and final volume probability density functions match well for the values of N tested; see figure 6.8a. Moreover for all setups the total number of bubbles decreases, with the most significant decrease occurring for the largest N; see figure 6.8b.



(a) $V_i < \frac{1}{3}V^*$ **(b)** $\frac{1}{3}V^* < V_i < \frac{2}{3}V^*$ **(c)** $V_i > \frac{2}{3}V^*$

Figure 6.9: Scalability of the system visualised through the relative probability (R. P.) for individual bubbles (of volume V_i mm^3) to be in one of three bins for $N = 50$, 100, 200 with $V = 2N$ mm^3 and $L = 5N$ mm. Values for the bin edges given in mm^3.

We can further explore the scalability of the system by looking at the histogram results in figure 6.9. There is a consistent trend of a decrease of smaller bubbles for all values of N tested (see figure 6.9a), and a corresponding increase in larger bubbles in figures 6.9b and 6.9c. These results are in line with the reduced total number of bubbles seen in figure 6.8b, and together suggest that coalescence dominates. Importantly, these results predict consistent trends in each volume bin for all values of N tested, therefore supporting the robustness of the system.

We now consider the effect of varying the number of bubbles in the system whilst keeping all other parameters fixed. Note that the initial conditions between setups will vary as we have a different number of bubbles contributing to a fixed total bubble volume V on a fixed domain length L. The simulation results for varying $N = 50, 100, 200$ are shown in figures 6.10 and 6.11. We first see that for $N = 50$, the lowest value of N tested, the number of bubbles remains almost constant; whereas for the largest value of $N = 200$ there is a significant decrease in bubbles (see figure 6.10).

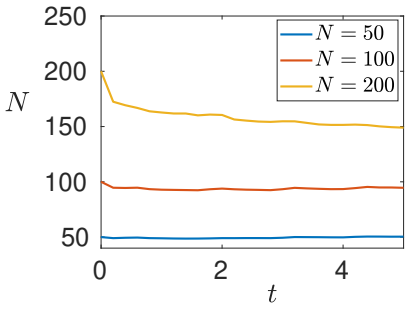
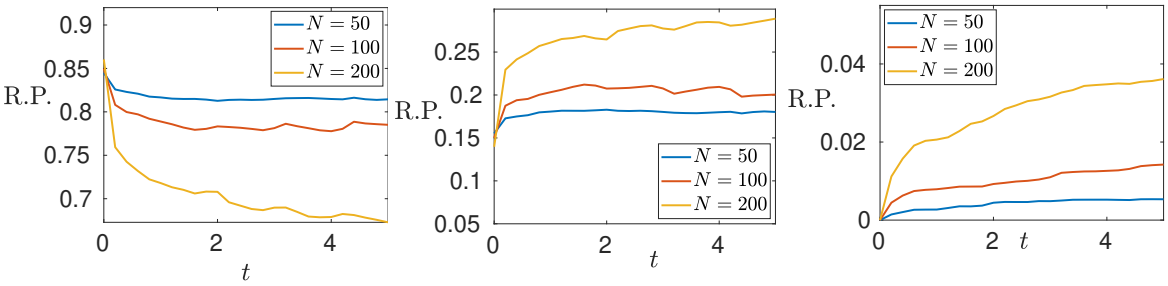


Figure 6.10: Number of bubbles as a function of time for $N = 50, 100, 200$ with $V = 500$ mm^3 and $L = 1000$ mm.



(a) $V_i < \frac{1}{3}V^*$ **(b)** $\frac{1}{3}V^* < V_i < \frac{2}{3}V^*$ **(c)** $V_i > \frac{2}{3}V^*$

Figure 6.11: Relative probabilities (R. P.) for individual bubbles (of volume V_i mm^3) to be in one of three bins for $N = 50, 100, 200$ with $V = 500$ mm^3 and $L = 1000$ mm. Values for the bin edges given in mm^3.

This is consistent with the results from the histograms in figure 6.11. We see that in the first small-volume-bin there is a consistent decrease of bubbles for all values of N tested; see figure 6.11a. The decrease for $N = 50$ happens at early times and the number of bubbles in the small-volume-bin then seems to reach a steady state. For larger N at $N = 200$ the decreasing number of bubbles in the small-volume-bin is

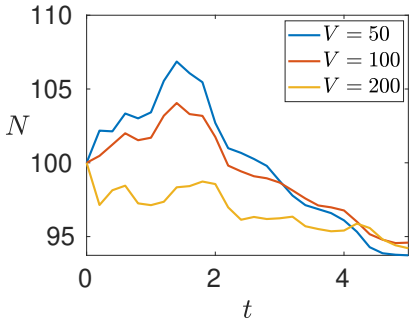
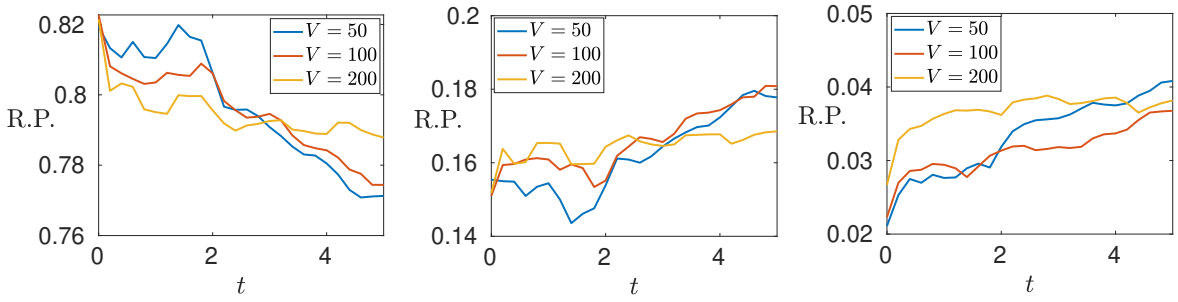


Figure 6.12: Number of bubbles as a function of time for $V = 50$, 100, 200 mm^3 with $N = 100$ and $L = 1000$ mm.

much more obvious and persistent throughout time. There is a corresponding increase in bubbles in both the medium-volume and large-volume bins with a higher relative probability of being in the medium-volume bin (compare figures 6.11b and 6.11c). These results suggest that coalescence is dominant in all setups, and that there are more coalescence events for larger N. It is clear that for an increased number of bubbles the likelihood of bubbles meeting and coalescing will increase.

The second principal parameter to explore is the total volume of bubbles; we therefore now look at the effects of changing V whilst keeping all other parameters fixed; see figures 6.12 and 6.13. Note that the results appear noisier than those in figures 6.10 and 6.11 due to the depth of the vertical axis shown. We first note that for smaller total volumes with $V = 50$, 100 mm^3 the total number of bubbles N increases in early times before decreasing at later times; see figure 6.12. This represents dominating fragmentation at early times, followed by dominating coalescence. For the largest value of V tested, $V = 200$ mm^3 we do not have an initial increase in N and there is a consistent decrease in number of bubbles.

We can explore this further using the histogram results in figure 6.13. Initially we can see a decrease in bubbles in the first bin in figure 6.13a and a corresponding increase in bubbles in the large-volume bin in 6.13c for all values of V tested. This suggests that at very early times small bubbles coalesce. This is followed by a decrease in bubbles in the medium-volume-bin in figure 6.13b with a corresponding increase in small bubbles suggesting that 'medium-sized' bubbles have broken up into smaller bubbles. After this fragmentation, there is a consistent decrease in smaller bubbles in the first bin and a corresponding increase in both the medium-volume and the large-volume bins; suggesting that coalescence is again the dominant process.



(a) $V_i < \frac{1}{3}V^*$ **(b)** $\frac{1}{3}V^* < V_i < \frac{2}{3}V^*$ **(c)** $V_i > \frac{2}{3}V^*$

Figure 6.13: Relative probabilities (R. P.) for individual bubbles (of volume V_i mm^3) to be in one of three bins for $V = 50$, 100, 200 mm^3 with $N = 100$ and $L = 1000$ mm. Values for the bin edges given in mm^3.

6.6 Summary

In this chapter we studied a system of bubbles moving in a one-dimensional domain. We began by thinking about how to characterise a bubble population by position, velocity and shape. Through consideration of the flow around a single bubble we described the shape of a bubble using two parameters $\{\eta, \xi\}$. To track position in space we account for the midpoint of the bubble X. Thus we found that three is the minimum number of variables required to track the position and the shape of a bubble and we consequently defined the variable space to be (X, η, ξ).

We considered a system of N bubbles with each i^{th} bubble classified by the corresponding variables (X_i, η_i, ξ_i). Each bubble was evolved by sampling the velocities at the horizontal end-points $\{u, v\}$ from a specified random Fourier series for the velocity field along the horizontal axis. From conservation of volume we were able to express the vertical velocity $\dot{\xi}$ in terms of the variables $(\xi, \eta, \dot{\eta})$. Through evolving the system of bubbles, the following bubble interactions would occur: coalescence, fragmentation and the end bubbles hitting the wall. We considered each of these events in turn and discussed how to reset the system variables at such an occurrence (for example, at coalescence we lose a bubble and need to prescribe the variables of the new bubble).

We developed a stochastic simulation for the evolution of a system of bubbles (governed by the equations of motion (6.13)) in MATLAB to demonstrate how one might utilise this general approach. The algorithm process was discussed in Section 6.5, and we considered a Monte Carlo simulation by introducing randomness to the initial conditions. Finally we presented results for the probability distribution of bubble volumes in Section 6.5.1. We looked at the effect of changing the initial

number of bubbles and the total bubble volume in the system. For all the parameter values tested, our results suggested that coalescence was the dominant process. More precisely, our study showed that for an increased initial number of bubbles there were more coalescence events. Furthermore, for a larger total bubble volume in the system early-time fragmentation dynamics were dampened giving way to the dominating coalescence.

Our aim in this part of the thesis is to develop models of evolving bubble distributions motivated by studying the bubbly-to-slug flow regime transition. The approach in this chapter produced a large system of equations to solve, and we now build on the preliminary framework discussed here and consider a statistical model in Chapter 7.

Chapter 7

Two-phase flow regime transition

In this chapter we utilise kinetic theory to derive a master equation governing the evolution of a bubble distribution. We account for coalescence and fragmentation of bubbles and examine the appropriate conservation laws.

7.1 Introduction

The aim of Part II of this thesis is to model the bubble dynamics in the bubbly-to-slug flow regime. In Chapter 6 we introduced a discretised system of equations for a system of bubbles moving in a one-dimensional domain. The purpose of this was to understand what variables we need to describe the position, shape and velocity of each bubble. However, when the number of bubbles becomes large, the deterministic model becomes expensive and intractable. We therefore now turn to kinetic theory to model probabilistic macroscale quantities. More precisely, we will derive a master equation for a bubble population.

Our approach will be based on the derivation of the Boltzmann equation, which is used to describe the evolution of the velocity distribution of colliding rigid particles. In Section 7.2 we introduce the Boltzmann equation for a distribution of (uniformly sized and shaped) particles. In particular, we discuss the derivation of the collision integral.

In Section 7.3 we apply the approach used for the Boltzmann equation to derive a model for a distribution of bubbles dependent on additional variables: position, velocity, shape and rate of change of shape. The corresponding evolution equation for the bubble distribution generalises the Boltzmann equation to allow for the description of bubble shape evolution, coalescence and fragmentation. We discuss coalescence and

fragmentation dynamics in Sections 7.4 and 7.5 respectively. The final generalised master equation for a bubble distribution is presented in Section 7.6. The model involves complex integral terms, and — as a sanity check — we examine conservation of mass, momentum and energy in the system in Section 7.7.

7.2 Boltzmann equation

The Boltzmann equation describes the behaviour of fluids in terms of the motion of their constituent molecules. The molecules are considered as identical rigid bodies that collide and bounce off each other (i.e. no coalescence). The quantity of interest is a velocity distribution function $f(\mathbf{r}, \mathbf{v}, t)$, where $f(\mathbf{r}, \mathbf{v}, t)\,\mathrm{d}\mathbf{r}\,\mathrm{d}\mathbf{v}$ is the expected number of particles at time t within the six-dimensional hypervolume element $\mathrm{d}\mathbf{r}\,\mathrm{d}\mathbf{v}$ centred at position $\mathbf{r}$ and velocity $\mathbf{v}$. The Boltzmann equation takes the conservation form

$$f_t + \boldsymbol{\nabla}_{\mathbf{r}} \cdot (f\mathbf{v}) + \boldsymbol{\nabla}_{\mathbf{v}} \cdot (f\mathbf{a}) = c, \tag{7.1}$$

where $\mathbf{a} = \dot{\mathbf{v}}$ is the particle acceleration (the overdot denotes the material time derivative) and c is the collision integral which corresponds to the changes in $f(\mathbf{r}, \mathbf{v}, t)$ due to collisions between particles. There are associated sink and source terms in the collision integral, denoted c_- and c_+ respectively, so we can write c as

$$c = c_+ - c_-. \tag{7.2}$$

The collision integrals require some thought regarding the configuration space that actually contributes to collision. In this section we consider the collision criteria between two particles. We then use this to derive the appropriate sink and source terms. In this section our main reference is Fowler [2017].

7.2.1 Collision criteria

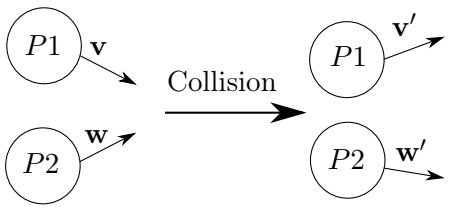


Figure 7.1: Particles with velocities $\mathbf{v}$ and $\mathbf{w}$ colliding and bouncing off with velocities $\mathbf{v}'$ and $\mathbf{w}'$.

Consider the collision between two particles $P1$ and $P2$, with respective velocities $\mathbf{v}$ and $\mathbf{w}$, that results in the particles bouncing off with respective velocities $\mathbf{v}'$ and

$\mathbf{w}'$; see figure 7.1. We denote the relative velocity of $P2$ with respect to $P1$ before collision by $\mathbf{V} = \mathbf{w} - \mathbf{v}$. If $\mathbf{k}$ is the unit vector along the line from the centre of $P2$ to the centre of $P1$ at the point of contact, then collision requires $\mathbf{V} \cdot \mathbf{k} = |\mathbf{V}| \cos\theta > 0$, where θ is the angle between $\mathbf{V}$ and $\mathbf{k}$. This is because for any angle $\theta > \pi/2$ the particles will be moving away from each other; see figure 7.2.

We can derive a relationship between the incoming velocities ($\mathbf{v}$, $\mathbf{w}$) and the outgoing velocities ($\mathbf{v}'$, $\mathbf{w}'$). To do this, we first observe that conservation of momentum gives

$$\mathbf{v} + \mathbf{w} = \mathbf{v}' + \mathbf{w}'. \tag{7.3}$$

Next, we note that at collision the normal component of the relative velocity $\mathbf{V}$ is reversed, and the tangential component remains the same (think of a ball hitting a surface). The vector $\mathbf{k}$ is the normal vector to the surface of $P1$ at the point of contact, thus the normal component of $\mathbf{V}$ is $(\mathbf{V}\cdot\mathbf{k})\mathbf{k}$ and the corresponding tangential component is $\mathbf{V}-(\mathbf{V}\cdot\mathbf{k})\mathbf{k}$. The relative velocity of $P2$ with respect to $P1$ after collision is $\mathbf{V}' = \mathbf{w}' - \mathbf{v}'$. So we can relate the relative velocities before and after collision by

$$\mathbf{V} \cdot \mathbf{k} = -\mathbf{V}' \cdot \mathbf{k}, \tag{7.4a}$$

$$\mathbf{V} - (\mathbf{V} \cdot \mathbf{k})\mathbf{k} = \mathbf{V}' - (\mathbf{V}' \cdot \mathbf{k})\mathbf{k}. \tag{7.4b}$$

Rearranging (7.3) for $\mathbf{v}$ and $\mathbf{w}$ in turn, and substituting them into $\mathbf{V} - (\mathbf{V} \cdot \mathbf{k})\mathbf{k} = \mathbf{V}' + (\mathbf{V} \cdot \mathbf{k})\mathbf{k}$ from (7.4) gives the following expressions for $\mathbf{v}'$ and $\mathbf{w}'$ in terms of $\mathbf{v}$ and $\mathbf{w}$:

$$\mathbf{v}' = \mathbf{v} + (\mathbf{V} \cdot \mathbf{k})\mathbf{k}, \tag{7.5a}$$

$$\mathbf{w}' = \mathbf{w} - (\mathbf{V} \cdot \mathbf{k})\mathbf{k}. \tag{7.5b}$$

Importantly this mapping is linear and invertible, which we will come back to in Section 7.2.3. We now derive the collision sink term in (7.2).

7.2.2 Collision sink

To account for the number of particles with velocity $\mathbf{v}$ lost due to collision with other particles, we seek to isolate the configuration space that actually contributes to collisions. Consider again a particle $P1$ at position $\mathbf{r}$ with velocity $\mathbf{v}$; of which there are $f(\mathbf{r}, \mathbf{v}, t)\,\mathrm{d}\mathbf{r}\,\mathrm{d}\mathbf{v}$. As discussed above, a particle $P2$ moving at velocity $\mathbf{w}$ will collide with $P1$ if the relative velocity $\mathbf{V}$ is such that $\mathbf{V} \cdot \mathbf{k} > 0$. The number of particles $P2$ colliding with $P1$ is $f(\mathbf{r} - l\mathbf{k}, \mathbf{w}, t)\,\mathrm{d}V_{cyl}\,\mathrm{d}\mathbf{w}$ where, as shown in figure 7.2, $\mathrm{d}V_{cyl}$ is the relevant volume of configuration space that contributes to collisions and l is the distance between the two centres.

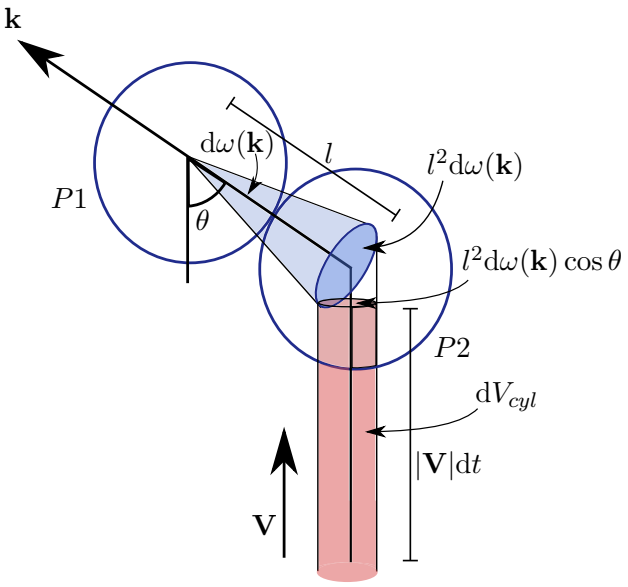


Figure 7.2: Schematic of the collisional configuration space between particles $P1$ and $P2$ where $\mathbf{V}$ is the velocity of $P2$ relative to $P1$.

To find an expression for $\mathrm{d}V_{cyl}$ we consider the solid angle $\mathrm{d}\omega(\mathbf{k})$ in the direction of $\mathbf{k}$. At the point of contact, this solid angle spans an area of $l^2\mathrm{d}\omega(\mathbf{k})$ on the particle $P2$, which gives the cross-section of the cylinder $\mathrm{d}V_{cyl}$ to be $l^2\mathrm{d}\omega(\mathbf{k})\cos\theta$. Thus the volume of the cylinder is $\mathrm{d}V_{cyl} = |\mathbf{V}|\,\mathrm{d}t\,l^2\,\mathrm{d}\omega(\mathbf{k})\cos\theta$. Recall that $\mathbf{V}\cdot\mathbf{k} = |\mathbf{V}|\cos\theta$, so in fact we have

$$\mathrm{d}V_{cyl} = l^2(\mathbf{V}\cdot\mathbf{k})\,\mathrm{d}\omega(\mathbf{k})\,\mathrm{d}t. \tag{7.6}$$

If we assume the displacement of centres $(-l\mathbf{k})$ and the conical volume at the top of the cylinder (see figure 7.2) to be negligible, then the number of particles at $(\mathbf{r},\mathbf{v})$ being lost due to collision is

$$f(\mathbf{r},\mathbf{v},t)f(\mathbf{r},\mathbf{w},t)\,\mathrm{d}\mathbf{r}\,\mathrm{d}\mathbf{v}\,\mathrm{d}\mathbf{w}\,\mathrm{d}\Omega\,\mathrm{d}t, \tag{7.7}$$

where we have introduced the collisional configuration space Ω and corresponding element $\mathrm{d}\Omega$ defined by

$$\Omega = \{\mathbf{k}\,|\mathbf{V}\cdot\mathbf{k} > 0\}, \tag{7.8a}$$

$$\mathrm{d}\Omega = l^2(\mathbf{V}\cdot\mathbf{k})\,\mathrm{d}\omega(\mathbf{k}). \tag{7.8b}$$

Integration of (7.7) over $\mathbf{r}$, $\mathbf{v}$ and t gives the rate of loss of particles at $(\mathbf{r},\mathbf{v},t)$ due to collision:

$$c_- = \int_U\int_\Omega f(\mathbf{r},\mathbf{v},t)f(\mathbf{r},\mathbf{w},t)\,\mathrm{d}\mathbf{w}\,\mathrm{d}\Omega, \tag{7.9}$$

where U is the velocity space. Next, we consider the corresponding source term.

7.2.3 Collision source term

We now want the number of particles with velocity $\mathbf{v}$ created due to the collision between any two particles with velocities $\mathbf{v}'$ and $\mathbf{w}'$. We start by simply swapping the variables in the collision shown in figure 7.1, or equivalently reversing the arrows. We consequently consider particles $P1$ and $P2$ with velocities $\mathbf{v}'$ and $\mathbf{w}'$ colliding and bouncing off with new velocities $\mathbf{v}$ and $\mathbf{w}$. The number of particles introduced to the system with velocity $\mathbf{v}$ due to collision is

$$f(\mathbf{r}, \mathbf{v}', t) f(\mathbf{r}, \mathbf{w}', t)\, \mathrm{d}\mathbf{r}\, \mathrm{d}\mathbf{v}'\, \mathrm{d}\mathbf{w}'\, \mathrm{d}\Omega'\, \mathrm{d}t. \tag{7.10}$$

This is simply (7.7) where we have swapped ($\mathbf{v}$, $\mathbf{w}$) with ($\mathbf{v}'$, $\mathbf{w}'$). The geometry is the same, so to work out $\mathrm{d}\Omega'$ we use figure (7.2) and reverse the arrows. From (7.8) we have $\Omega' = \{\mathbf{k}' \,|\mathbf{V}' \cdot \mathbf{k}' > 0\}$ and $\mathrm{d}\Omega' = l^2(\mathbf{V}' \cdot \mathbf{k}')\, \mathrm{d}\omega(\mathbf{k}')$, where $\mathbf{V}' = \mathbf{w}' - \mathbf{v}'$ is now the relative velocity before collision and $\mathbf{k}'$ is the unit vector along the line from centre of $P1$ to the centre of $P2$ at the point of contact. The relative velocity after collision is now $\mathbf{V}$, and from (7.4a) we have $\mathbf{V} \cdot \mathbf{k}' = -\mathbf{V}' \cdot \mathbf{k}' < 0$. We seek a source term in the same configuration space as the sink term, and noting that $\mathbf{k}' = -\mathbf{k}$ we have $\mathbf{V} \cdot \mathbf{k} > 0$. Thus we have $\Omega' = \Omega$ and $\mathrm{d}\Omega' = \mathrm{d}\Omega$ as defined in (7.8).

Finally, we consider mapping the volume element $\mathrm{d}\mathbf{v}'\, \mathrm{d}\mathbf{w}'$ to $\mathrm{d}\mathbf{v}\, \mathrm{d}\mathbf{w}$ under the transformation given in (7.5). This mapping is given by $\mathrm{d}\mathbf{v}'\, \mathrm{d}\mathbf{w}' = |\mathcal{J}|\, \mathrm{d}\mathbf{v}\, \mathrm{d}\mathbf{w}$ where $|\mathcal{J}|$ is the Jacobian of the transformation, which is the determinant of the following block matrix:

$$|\mathcal{J}| = \left| \frac{\partial(\mathbf{v}', \mathbf{w}')}{\partial(\mathbf{v}, \mathbf{w})} \right| = \left| \begin{pmatrix} I - K & K \\ K & I - K \end{pmatrix} \right|, \tag{7.11}$$

where I is the three-by-three identity matrix and K is the matrix defined by the elements of the vector $\mathbf{k}$: $K_{ij} = k_i k_j$. The determinant of the block matrix (7.11) is $|\mathcal{J}| = 1$. Thus, from (7.10), the number of particles with velocity $\mathbf{v}$ introduced by collisions can be written as

$$f(\mathbf{r}, \mathbf{v} + (\mathbf{V} \cdot \mathbf{k})\mathbf{k}, t) f(\mathbf{r}, \mathbf{w} - (\mathbf{V} \cdot \mathbf{k})\mathbf{k}, t)\, \mathrm{d}\mathbf{r}\, \mathrm{d}\mathbf{v}\, \mathrm{d}\mathbf{w}\, \mathrm{d}\Omega\, \mathrm{d}t. \tag{7.12}$$

Integration over $\mathbf{r}$, $\mathbf{v}$ and t gives the rate of increase of particles at $(\mathbf{r}, \mathbf{v}, t)$ due to collision:

$$c_+ = \int_U \int_\Omega f(\mathbf{r}, \mathbf{v} + (\mathbf{V} \cdot \mathbf{k})\mathbf{k}, t) f(\mathbf{r}, \mathbf{w} - (\mathbf{V} \cdot \mathbf{k})\mathbf{k}, t)\, \mathrm{d}\mathbf{w}\, \mathrm{d}\Omega. \tag{7.13}$$

The collision integral (7.2) using (7.9) and (7.13) is then written as

$$c = \int_U \int_\Omega [f(\mathbf{r}, \mathbf{v} + (\mathbf{V} \cdot \mathbf{k})\mathbf{k}, t) f(\mathbf{r}, \mathbf{w} - (\mathbf{V} \cdot \mathbf{k})\mathbf{k}, t) - f(\mathbf{r}, \mathbf{v}, t) f(\mathbf{r}, \mathbf{w}, t)]\, d\Omega\, d\mathbf{w}, \tag{7.14}$$

and the Boltzmann equation is (7.1) with (7.14). The evolution equation we seek for the bubble number density will mirror this form. We now turn to the task in hand: adapting the derivation of the Boltzmann equation for the application to bubbles.

7.3 Modelling the bubble distribution

We want to develop a model for an evolving bubble distribution. If we consider bubbles to be particles within a fluid, then we can derive a model similar to the Boltzmann equation. Bubbles are clearly not rigid: there is a shape evolution. Moreover, bubbles coalesce and fragment, so we need to adapt the derivation of the Boltzmann equation to account for this. There have been several studies that rely on the theory discussed above for bubble distributions [Wang et al., 2012, 2005; Ishii et al., 2002; Yao and Morel, 2004; Shen and Hibiki, 2018; Sun et al., 2004]. We will detail three such studies: Navarro-Valenti et al. [1991], Kalkach-Navarro et al. [1994] and Hibiki and Ishii [2000] in order to motivate the work presented in this chapter.

Navarro-Valenti et al. [1991] modelled a bubble size distribution function $f(V, \mathbf{r}, t)$ for bubbles of volume V and position $\mathbf{r}$. Note that the model was independent of any bubble acceleration and only spherical bubbles were considered. The evolution of the bubble population was driven by break-up (which is equivalent to fragmentation) and coalescence dynamics:

$$f_t + \boldsymbol{\nabla}_{\mathbf{r}} \cdot (f\mathbf{v}) \;=\; c + b, \tag{7.15}$$

where c and b correspond to coalescence and break-up respectively. The coalescence and break-up terms were both assumed to comprise integrals for the sink and source terms:

$$\begin{aligned} c \;&=\; \tfrac{1}{2}\int_0^V C(U, V-U) f(U, \mathbf{r}, t) f(V-U, \mathbf{r}, t)\,\mathrm{d}U \\ &\qquad - \int_0^\infty C(U, V) f(U, \mathbf{r}, t) f(V, \mathbf{r}, t)\,\mathrm{d}U, \end{aligned} \tag{7.16a}$$

$$b \;=\; \int_V^\infty B(U, V) f(U, \mathbf{r}, t)\,\mathrm{d}U - \int_0^V B(V, U) f(V, \mathbf{r}, t)\,\mathrm{d}U, \tag{7.16b}$$

where $C(U, V)$ is the rate of coalescence of bubbles of volume U with bubbles of volume V. Similarly $B(U, V)$ is the rate of break-up of bubbles of volume U that form bubbles of volume V. The first term on the right-hand side of (7.16a) gives the rate of coalescence of smaller bubbles forming a bubble of volume V, the factor of $\frac{1}{2}$ is because two bubbles merge to produce a single coalesced bubble. The second term on the right-hand side of (7.16a) gives the corresponding rate of loss due to bubbles

of volume V coalescing with any other bubble. Similarly, in (7.16b) the source term corresponds to the rate of break-up of bubbles of volume bigger than V, thereby producing a bubble of volume V. The corresponding loss term in (7.16b) governs the break-up of a bubble of volume V producing daughter bubbles with smaller volumes.

Navarro-Valenti et al. [1991] assumed the rate of coalescence $C(U, V)$ between two bubbles to be proportional to the sum of the two volumes. The break-up rate $B(U, V)$ was derived from the assumption that bubbles greater than a prescribed volume broke in half at constant rate. Numerical simulation of the steady state solution showed a sharp increase in the volume of the bubbles and a decrease in the number of bubbles, when the gas volume fraction was approximately $\alpha = 0.3$. This agrees with findings from previous experimental studies by Hibiki and Ishii [1999], and previous mechanistic models developed by Taitel et al. [1980], that suggest at this volume fraction the flow undergoes a transition from bubbly to slug flow.

Kalkach-Navarro et al. [1994] further developed this approach to analyse the bubbly-to-slug flow regime transition. The same master equation (7.15) was used but the coalescence and break-up rates $C(U, V)$ and $B(U, V)$ were adapted. The authors made the assumption of negligible break-up for individual bubbles. This motivated the study of bubble clusters, the break-up of which was included in their model. The rate of coalescence was derived from the probability that a bubble was in a specified position in the domain. The rate of break-up of a cluster of volume V into a pair of bubbles or clusters of sizes V_1 and V_2 (such that $V_1 + V_2 = V$) was assumed to follow a parabolic function, symmetric around $\frac{1}{2}V$. To analyse how bubbly flow transitions to slug flow, a general two-fluid model for bubbly flow was coupled to conservation equations for the gas volume fraction and bubble number density; both quantities are derived from moments of the bubble size distributions $f(V, \mathbf{r}, t)$. Linear stability analysis of the extended two-fluid model suggested that an increase in the volume fraction of bubble clusters will lead to an instability of the system and an assumed flow regime transition. Empirical studies were used to advise the values of gas volume fraction that identified the different regimes.

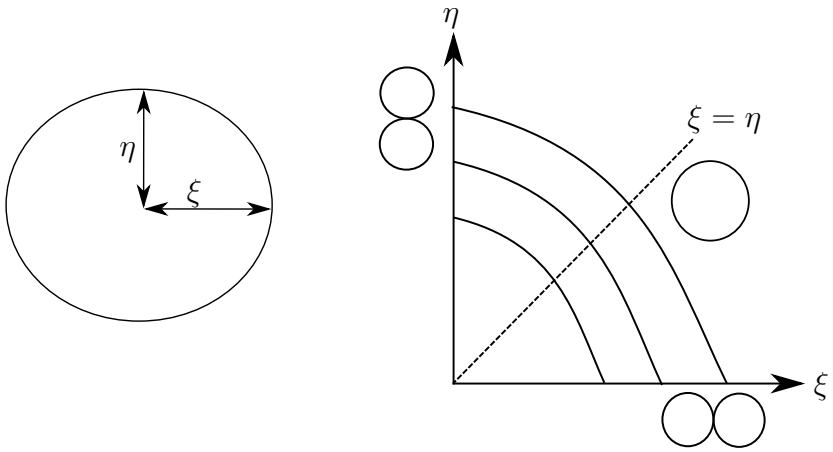
The spherical assumption made by Navarro-Valenti et al. [1991] and Kalkach-Navarro et al. [1994] will break down in the transition from bubbly to slug flow, where bubbles coalesce to form bullet-shaped slugs. This obervation motivated work by Hibiki and Ishii [2000] to extend the approach discussed above to two groups of bubbles; spherical and distorted bubbles, and slug and cap bubbles. The authors considered two bubble size distributions, one for each group, again dependent only on volume and position. Coalescence and break-up were accounted for between groups, which led to numerous possible outcomes and scenarios. Moments of the two master

equations were used to derive evolution equations for the average interfacial area of each bubble group. The interfacial area equations were coupled with a two-fluid model to study the interfacial area at the transition from bubbly to slug flow. Wang et al. [2012] used the findings from Hibiki and Ishii [2000] to develop a flow-chart based on the system variables that predicts the particular flow regime for a given system.

The work by Navarro-Valenti et al. [1991] and Kalkach-Navarro et al. [1994] showed that kinetic theory can be a useful tool for examining the bubbly-to-slug flow regime transition, and Hibiki and Ishii [2000] highlighted the importance of accounting for the variable shape of the bubbles. We will build on these previous studies to use kinetic theory to derive a model for a bubble distribution that additionally accounts for the acceleration and shape evolution of bubbles.

7.3.1 Bubble shape

We believe it to be necessary to include bubble shape (as opposed to just volume) in order to describe bubble fragmentation, which we associate with bubble pinch-off. In Chapter 6 we described the bubble surface function by means of an infinite series of spherical harmonics in (6.1). Assuming the bubbles to be azimuthally symmetric, we can describe the shape by a truncated Legendre series as in (6.2). It is clear that two terms is the minimum requirement to describe shape (a single component describes the volume). Thus we conclude the appropriate shape vector to be $\boldsymbol{\sigma} = (\xi, \eta)$ in (6.3). The (horizontal) semi-major axis of the bubbles is described by ξ and the (vertical) semi-minor axis by η; see figure 7.3a.



(a) Schematic of a bubble shape described by ξ and η.

(b) Schematic of the volume contour plot with the bubble shapes shown.

Figure 7.3: Bubble shape and volume as a function of ξ and η.

In terms of ξ and η, the bubble volume is

$$V = \frac{4\pi}{105}\left(5\xi^3 + 6\xi^2\eta + 8\xi\eta^2 + 16\eta^3\right) \tag{7.17}$$

(this was also given in (6.6)). The contours of V are shown schematically in figure 7.3b. We see that there are three notable values of V corresponding to: the value ξ_M where $\eta = 0$ corresponding to a horizontal pinched-torus in three dimensions, the value ξ_S when the bubble is spherical where $\xi = \eta$ and the value η_M at vertical pinch-off where $\xi = 0$ and the bubble shape is a three-dimensional vertical peanut-shape; these are given by

$$V = \frac{4\pi}{21}\xi_M^3, \quad V = \frac{4\pi}{3}\xi_S^3, \quad V = \frac{64\pi}{105}\eta_M^3. \tag{7.18}$$

7.3.2 Formulating the master equation

We now begin formulating an equation describing the evolution of the bubble shape and size. In the sense of stochastic processes, this equation will be an evolution equation for the bubble number density defined in terms of position $\mathbf{r}$, velocity $\mathbf{v}$, shape $\boldsymbol{\sigma}$ and the rate of change of shape which we will call *transformation* $\mathbf{s} = \dot{\boldsymbol{\sigma}}$. The bubble number density is therefore $g(\mathbf{r}, \mathbf{v}, \boldsymbol{\sigma}, \mathbf{s}, t)$ where at time t

$$g(\mathbf{r}, \mathbf{v}, \boldsymbol{\sigma}, \mathbf{s}, t)\,\mathrm{d}\mathbf{r}\,\mathrm{d}\mathbf{v}\,\mathrm{d}\boldsymbol{\sigma}\,\mathrm{d}\mathbf{s} \tag{7.19}$$

is the expected number of bubbles in the ten-dimensional hypervolume element $\mathrm{d}\mathbf{r}\,\mathrm{d}\mathbf{v}\,\mathrm{d}\boldsymbol{\sigma}\,\mathrm{d}\mathbf{s}$ at the point $(\mathbf{r}, \mathbf{v}, \boldsymbol{\sigma}, \mathbf{s})$ in configuration space. We highlight the difference in configuration space to that considered in Chapter 6; the position and velocity space ($\mathbf{r}$, $\mathbf{v}$) accounted for here relates to that of the bubble centre, not to either end-point of the bubble.

An evolution equation for the bubble number density analogous to (7.1) is then

$$g_t + \boldsymbol{\nabla}_{\mathbf{r}}.(g\mathbf{v}) + \boldsymbol{\nabla}_{\mathbf{v}}.(g\mathbf{a}) + \boldsymbol{\nabla}_{\boldsymbol{\sigma}}.(g\mathbf{s}) + \boldsymbol{\nabla}_{\mathbf{s}}.(g\mathbf{q}) = c(\mathbf{r}, \mathbf{v}, \boldsymbol{\sigma}, \mathbf{s}, t) + b(\mathbf{r}, \mathbf{v}, \boldsymbol{\sigma}, \mathbf{s}, t), \tag{7.20}$$

where $\mathbf{a} = \dot{\mathbf{v}}$ is the acceleration, $\mathbf{q} = \dot{\mathbf{s}}$ is the rate of change of $\mathbf{s}$, which we will call the *adaptation*, c is the coalescence term and b is the fragmentation term. We need to prescribe forms for $\mathbf{a}$, $\mathbf{q}$, c and b.

We aim for the simplest description possible, and to this end we restrict our attention to a single space dimension. Note, however, that although we consider a one-dimensional translational domain, by keeping the shape parameters ξ and η we are able to describe the full three-dimensional bubble shape. If we define the space variable to be x, the velocity to be v, the shape vector to be (ξ, η), the transformation

to be (s, w) (i.e. $\dot{\xi} = s$, $\dot{\eta} = w$), and the adaptation to be (q, r) (i.e. $\dot{s} = q$, $\dot{w} = r$), then (7.20) takes the form

$$g_t + (gv)_x + (ga)_v + (gs)_\xi + (gw)_\eta + (gq)_s + (gr)_w = c + b, \tag{7.21}$$

where c and b are function of $(x, v, \xi, \eta, s, w, t)$.

We will assume that bubbles conserve volume as they deform (this is appropriate for an incompressible gas). From $\dot{V} = 0$ in (7.17), we can therefore define w by $V_\xi s + V_\eta w = 0$, so w is not an independent coordinate of the phase space. The configuration space vector is denoted $\mathbf{\Omega} = (v, \xi, \eta, s)$, so that we have $g = g(x, \mathbf{\Omega}, t)$; we will eventually be interested in distributions which are independent of spatial position and time. It is clear that it may be easier to define the shape variables to be ξ, the radial extent, and V, the bubble volume. We will come back to this in due course, but for the moment retain ξ and η as the shape variables. We now consider the contributions to (7.21) due to coalescence and fragmentation.

7.4 Coalescence

In this section we first discuss the collisional configuration space (analogous to Section 7.2). We then prescribe the appropriate coalescence rules for the configuration of the new coalesced bubble. We use the collision criteria and new bubble configuration to prescribe the sink and source terms governed by coalescence.

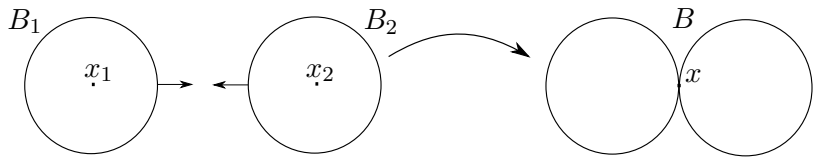


Figure 7.4: Coalescence of bubbles.

7.4.1 Coalescence criteria

As indicated in figure 7.4, coalescence occurs when two neighbouring bubbles collide. Although drawn as spheres, they are in general given by $r = R(\xi, \eta)$ in (6.4). The position and velocity of the bubble on the left ($B1$) are x_1 and v_1, and those of the right hand bubble ($B2$) are x_2 and v_2. In the specific case $x_1 < x_2$, for coalescence we must have $x_2 = x_1 + \xi_1 + \xi_2$. The velocity of the right end-point of $B1$ is $(v_1 + s_1)$, and the velocity of the left end-point of $B2$ is $(v_2 - s_2)$. So for coalescence to occur

we also need $v_1 - v_2 + (s_1 + s_2) > 0$, and in a time interval $\mathrm{d}t$, the number density of coalescing bubbles at $\mathbf{\Omega}_1$ is

$$g(x_1, \mathbf{\Omega}_1, t) g(x_1 + \xi_1 + \xi_2, \mathbf{\Omega}_2, t)[v_1 - v_2 + (s_1 + s_2)]_+ \,\mathrm{d}x \,\mathrm{d}\mathbf{\Omega}_1 \,\mathrm{d}\mathbf{\Omega}_2 \,\mathrm{d}t. \tag{7.22}$$

On the other hand, if $B1$ is to the right of $B2$ with $x_1 > x_2$, coalescence occurs if $x_2 = x_1 - \xi_1 - \xi_2$ and $v_2 - v_1 + (s_1 + s_2) > 0$, so in a time interval $\mathrm{d}t$, the number density of coalescing bubbles at $\mathbf{\Omega}_1$ will be

$$g(x_1, \mathbf{\Omega}_1, t) g(x_1 - \xi_1 - \xi_2, \mathbf{\Omega}_2, t)[-v_1 + v_2 + (s_1 + s_2)]_+ \,\mathrm{d}x \,\mathrm{d}\mathbf{\Omega}_1 \,\mathrm{d}\mathbf{\Omega}_2 \,\mathrm{d}t. \tag{7.23}$$

We can combine the two cases in (7.22) and (7.23) to write the total number density of coalescing bubbles at $\mathbf{\Omega}_1$:

$$\begin{aligned} g(x_1, \mathbf{\Omega}_1, t) \,[&g(x_1 + \xi_1 + \xi_2, \mathbf{\Omega}_2, t)[v_1 - v_2 + (s_1 + s_2)]_+ \\ &+ g(x_1 - \xi_1 - \xi_2, \mathbf{\Omega}_2, t)[-v_1 + v_2 + (s_1 + s_2)]_+] \,\mathrm{d}x \,\mathrm{d}\mathbf{\Omega}_1 \,\mathrm{d}\mathbf{\Omega}_2 \,\mathrm{d}t. \end{aligned} \tag{7.24}$$

7.4.2 Criteria for the coalesced bubble

We need to decide on a rule as to what shape and velocity the newly coalesced bubbles take. Ideally this comes from conservation of mass, momentum and energy. Mass is conserved if we suppose that bubble volume is conserved. For the coalescence of bubbles $B1$ and $B2$ (of volume V_1 and V_2), the new bubble at configuration $\mathbf{\Omega} = (v, \xi, \eta, s)$ has volume V such that

$$V = V_1 + V_2. \tag{7.25}$$

We seek to conserve the momentum and energy for gas bubbles in a continuous liquid phase. Consider for a moment the Euler equations for an incompressible liquid in a (continuous) volume V_C containing (dispersed) gas bubbles of volume V_D:

$$\frac{\mathrm{d}\mathbf{u}}{\mathrm{d}t} = -\frac{\boldsymbol{\nabla} p}{\rho}, \tag{7.26a}$$

$$\boldsymbol{\nabla} \cdot \mathbf{u} = 0, \tag{7.26b}$$

where $\mathbf{u}$, p and ρ are the velocity, pressure and density of the liquid respectively, and $\mathrm{d}/\mathrm{d}t$ is the material time derivative. We assume ρ to be a constant for the incompressible liquid phase. If the gas density is much less than the liquid density, the mass is predominantly concentrated in the liquid phase. The gaseous bubbles are therefore moved around by the liquid, and it is reasonable to assume the pressure inside each bubble to be constant. At the interface from (2.39) we have $p_g - p_l = 2\gamma\kappa$,

where p_g is the pressure inside the bubble, p_l is the liquid pressure on the bubble surface, γ is surface tension and κ is the mean curvature. Thus ignoring surface tension effects, the liquid pressure p will be constant on the bubble surface. From (7.26a) the rate of change of momentum in the liquid ($\rho\mathbf{u}$) is conserved:

$$\frac{\mathrm{d}}{\mathrm{d}t}\int_{V_C}\rho\mathbf{u}\,\mathrm{d}V = -\int_{V_C}\boldsymbol{\nabla}p\,\mathrm{d}V = \int_{\partial V_D}p\mathbf{n}\,\mathrm{d}S = 0. \tag{7.27}$$

Similarly, the kinetic energy ($\frac{1}{2}\rho u^2$ where $u = |\mathbf{u}|$) is conserved:

$$\frac{\mathrm{d}}{\mathrm{d}t}\int_{V_C}\tfrac{1}{2}\rho u^2\,\mathrm{d}V = 0. \tag{7.28}$$

We now consider the inverse system with (dispersed) liquid droplets of volume V_D in a continuous gas phase of volume V_C. The density in the liquid droplets will still be significantly larger than the gas phase so we can again take the pressure in the gas phase to be constant. The same analysis holds and in this case the droplet momentum $\mathbf{M}$ and energy E are constant:

$$\int_{V_D}\rho\mathbf{u}\,\mathrm{d}V = \mathbf{M}, \quad \int_{V_D}\tfrac{1}{2}\rho u^2\,\mathrm{d}V = E. \tag{7.29}$$

We need to assign coalescence rules that are consistent with the conservation rules for momentum and energy. So — although it is not clear that this analysis adapts to a system of a dispersed gas phase in a continuous liquid phase where the mass is concentrated — we use the approach discussed above to identify the bubble momentum with the quantity Vv. For the energy, we consider the sum of a mean kinetic energy (per unit mass) $\frac{1}{2}Vv^2$ and an 'internal' energy associated with the bubble transformation $\frac{1}{2}Vs^2$. The energy measure is therefore $\frac{1}{2}V(v^2+s^2)$.

To conserve mass, momentum and energy defined above, we prescribe the following coalescence rules for bubbles at x_1 and x_2 of configuration $\boldsymbol{\Omega}_1$ and $\boldsymbol{\Omega}_2$ in forming a bubble at x of configuration $\boldsymbol{\Omega}$:

$$\begin{aligned}
x &= x_1 \pm \xi_1 \quad (= x_2 \mp \xi_2), && \text{(7.30a)}\\
V &= V_1 + V_2, && \text{(7.30b)}\\
\xi &= \xi_M(V), && \text{(7.30c)}\\
\eta &= 0, && \text{(7.30d)}\\
Vv &= V_1v_1 + V_2v_2, && \text{(7.30e)}\\
\tfrac{1}{2}V(v^2+s^2) &= \tfrac{1}{2}V_1(v_1^2+s_1^2) + \tfrac{1}{2}V_2(v_2^2+s_2^2). && \text{(7.30f)}
\end{aligned}$$

The momentum and energy rules, (7.30e) and (7.30f) respectively, can be simplified by defining

$$\phi = \frac{V_1}{V}, \tag{7.31}$$

which gives $(1-\phi) = V_2/V$. The velocity of the coalesced bubble from (7.30e) can then be written as

$$v = \phi v_1 + (1-\phi)v_2. \tag{7.32}$$

We can rearrange (7.30f) to rewrite the transformation s of the coalesced bubble as

$$s^2 = \phi(v_1^2 + s_1^2) + (1-\phi)(v_2^2 + s_2^2) - v^2. \tag{7.33}$$

Using the velocity (7.32) in (7.33) above, we get

$$\begin{aligned} s^2 &= \phi v_1^2 + (1-\phi)v_2^2 - [\phi v_1 + (1-\phi)v_2]^2 + \phi s_1^2 + (1-\phi)s_2^2 \\ &= \phi(1-\phi)(v_1 - v_2)^2 + \phi s_1^2 + (1-\phi)s_2^2. \end{aligned} \tag{7.34}$$

In (7.30c)–(7.30d) we have assumed the shape of the coalesced bubble to be a horizontal figure-of-eight (which represents a pinched-torus in three dimensions as shown in figure 6.1c). This is described by $(\xi, \eta) = (\xi_M(V), 0)$ where ξ_M is defined in (7.18); see figure 7.3b. When $\xi = \xi_M$ we require that $\dot{\xi} = s < 0$, and we will in fact assume that $s < 0$ everywhere which corresponds to bubbles being compressed horizontally only. This assumption supposes that when two bubbles coalesce, they continue to deform until they split when $\xi = 0$ (this is associated to a vertical peanut-shape in three dimensions) as described in figure 7.5. Using this assumption, we circumvent the issue of multiple solutions for the new transformation s in (7.34), as well as avoiding an unphysical pinch-off resulting from a horizontal pinched-torus.

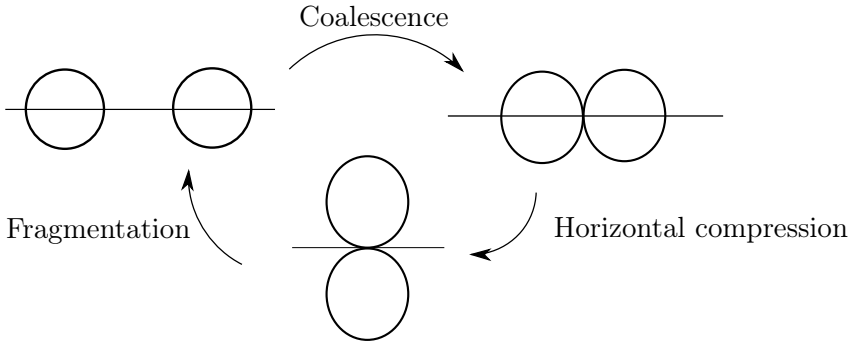


Figure 7.5: Schematic for the evolution of bubbles with $s < 0$.

7.4.3 Coalescence terms

Analogous to the collision integral in the Boltzmann equation (7.1), the coalescence of bubbles contributes a sink and a source term to the right-hand side of (7.21). Thus as in (7.2) we write $c = c_+ - c_-$ for the coalescence term in (7.21). Note that by

assuming $s < 0$, the source term for coalescence must therefore be supplied as a flux at the boundary $\eta = 0$ of the domain; see figure 7.6. So, in fact, the coalescence term on the right-hand side of (7.21) only involves the sink term (7.38): $c = -c_-$.

The coalescence sink term corresponds to the loss of bubbles at $(x, \mathbf{\Omega})$ due to coalescence with any other bubble at the appropriate point $(x', \mathbf{\Omega}')$ in configuration space. From (7.24), the number of bubbles lost from $(x, \mathbf{\Omega})$ is

$$\begin{aligned} c_- \,\mathrm{d}x\,\mathrm{d}\mathbf{\Omega}\,\mathrm{d}t &= g(x,\mathbf{\Omega},t)\,[g(x+\xi+\xi',\mathbf{\Omega}',t)[v-v'+(s+s')]_+ \\ &\quad + g(x-\xi-\xi',\mathbf{\Omega}',t)[-v+v'+(s+s')]_+]\;\mathrm{d}x\,\mathrm{d}\mathbf{\Omega}\,\mathrm{d}\mathbf{\Omega}'\,\mathrm{d}t. \quad (7.35) \end{aligned}$$

Integration gives the following coalescence sink term:

$$\begin{aligned} c_- &= \int_U \big\{g(x+\xi+\xi',\mathbf{\Omega}',t)[(v-v')+(s+s')]_+ \\ &\quad + g(x-\xi-\xi',\mathbf{\Omega}',t)[-(v-v')+(s+s')]_+\big\}\;\mathrm{d}\mathbf{\Omega}'\;g(x,\mathbf{\Omega},t), \quad (7.36) \end{aligned}$$

where the space U is defined by

$$U = \{v, s \in \mathbb{R},\ \xi, \eta \in [0, \infty)\}. \quad (7.37)$$

We want a bubble distribution independent of spatial position and time; we therefore suppress the dependence on x and t in (7.36) which gives

$$c_- = \int_U g(\mathbf{\Omega}')K(\mathbf{\Omega},\mathbf{\Omega}')\,\mathrm{d}\mathbf{\Omega}'\;g(\mathbf{\Omega}), \quad (7.38)$$

where we have introduced the (symmetric) coalescence kernel

$$K(\mathbf{\Omega},\mathbf{\Omega}') = [|v-v'|+(s+s')]_+. \quad (7.39)$$

We will assume (x,t)-independence henceforth, and therefore consider the bubble distribution as a function of the configuration space $\mathbf{\Omega}$ only.

The coalescence sink term (7.38) represents the rate of loss of bubbles at state $\mathbf{\Omega}$. It is evident that in coalescence we lose two bubbles but immediately gain one. We now derive the corresponding source term which emerges at $\eta = 0$, i.e. at the point $(v, 0, \xi_M, S)$, as opposed to the arbitrary point $\mathbf{\Omega}$. The flux at $\eta = 0$ is $g\dot{\eta}|_{\eta=0} = gw|_{\eta=0}$. Recall that since $V(\xi,\eta)$ is constant, we have $w = -V_\xi s/V_\eta$. From (7.17) we find that at $\eta = 0$ we have $V_\xi = \frac{5}{2}V_\eta$. The flux of bubbles in at $\eta = 0$ is therefore $-\frac{5}{2}sg|_{\eta=0}$. Integrating over v, ξ and s, we get the total rate of increase of bubbles per unit volume per unit time:

$$-\tfrac{5}{2}\int_0^\infty\!\!\int_{\mathbb{R}^2} g|_{\eta=0}s\,\mathrm{d}v\,\mathrm{d}s\,\mathrm{d}\xi. \quad (7.40)$$

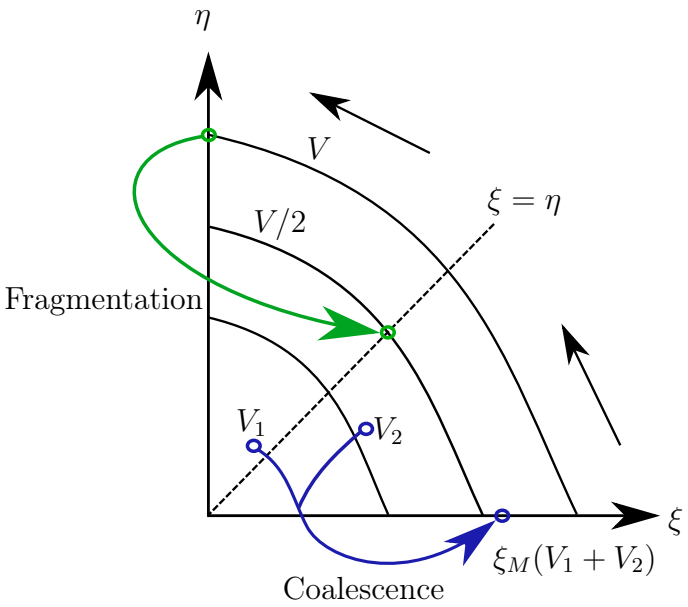


Figure 7.6: Coalescence and fragmentation on the $V(\xi, \eta)$ domain with $s < 0$. Coalescence occurs when two bubbles of volumes V_1 and V_2 collide, and the resultant bubble is re-introduced at $(\xi, \eta) = (\xi_M, 0)$; fragmentation occurs when $\xi = 0$ (vertical splitting) and the two resultant spherical bubbles are re-introduced to the domain with volume $V/2$.

The flux in at $\eta = 0$ clearly balances the flux out which corresponds to two bubbles coalescing. The coalescence sink term (7.38) gives the loss of bubbles at $\mathbf{\Omega}$. If we integrate (7.38) over U, we get the total rate of loss of bubbles per unit volume per unit time due to coalescence. As previously stated, this total loss must balance the flux into the domain at $\eta = 0$ given by (7.40). So the coalescence-source boundary condition must be

$$-\tfrac{5}{2}\int_0^\infty\!\!\int_{\mathbb{R}^2} g|_{\eta=0} s \,\mathrm{d}v \,\mathrm{d}s \,\mathrm{d}\xi = \tfrac{1}{2}\int_U\!\!\int_U g(\mathbf{\Omega}_1) g(\mathbf{\Omega}_2) K(\mathbf{\Omega}_1, \mathbf{\Omega}_2) \,\mathrm{d}\mathbf{\Omega}_1 \,\mathrm{d}\mathbf{\Omega}_2, \tag{7.41}$$

where the factor of $\frac{1}{2}$ on the right-hand side is due to the coalescence of two bubbles producing a single coalesced bubble.

At the moment, the double integral on the right of (7.41) is expressed in terms of arbitrary pairs of points $\mathbf{\Omega}_1$ and $\mathbf{\Omega}_2$. We need to rewrite it in terms of the variables that satisfy the three conservation laws in (7.30b), (7.30e) and (7.30f) which are written in terms of volume V. We therefore introduce a change of the shape variables from (ξ, η) to (ξ, V), where $V = V(\xi, \eta)$, under the transformation

$$\mathbf{\Omega} = (v, \xi, \eta, s) \quad \rightarrow \quad \mathbf{\Sigma} = (v, \xi, V, s). \tag{7.42}$$

The Jacobian of the transformation is the determinant of the following four-by-four

matrix:

$$|J| = \left|\frac{\partial \mathbf{\Sigma}}{\partial \mathbf{\Omega}}\right| = \left|\begin{pmatrix} 1 & 0 & 0 & 0 \\ 0 & 1 & 0 & 0 \\ 0 & V_\xi & V_\eta & 0 \\ 0 & 0 & 0 & 1 \end{pmatrix}\right| = V_\eta. \tag{7.43}$$

The bubble density in the new coordinate system $G(\mathbf{\Sigma})$ is thus defined to be

$$g = GV_\eta. \tag{7.44}$$

The conservation equation (7.21) is now written in the form

$$G_t + (Gv)_x + (Ga)_v + (Gs)_\xi + (Gq)_s + (Gr)_w = B - C, \tag{7.45}$$

where the transformed fragmentation and coalescence terms are defined, respectively, by

$$b = V_\eta B, \quad c = V_\eta C. \tag{7.46}$$

The coalescence term from (7.38), with $c = -c_-$, becomes

$$C = -\int_W G(\mathbf{\Sigma}'))K(\mathbf{\Sigma}, \mathbf{\Sigma}')\,\mathrm{d}\mathbf{\Sigma}'\; G(\mathbf{\Sigma}), \tag{7.47}$$

where

$$W = \{v, s \in \mathbb{R}, \xi \in [0, \xi_M(V)], V \in [0, \infty)\}. \tag{7.48}$$

Note that as the velocity and transformation space (v, s) is unchanged by the transformation (7.42), the coalescence kernel K defined in (7.39) also remains unchanged.

Returning to the coalescence-driven boundary condition, we apply the transformation (7.42) to the left-hand side of (7.41) corresponding to the flux in at $\eta = 0$ to get

$$-\tfrac{5}{2}\int_0^\infty\!\!\int_{\mathbb{R}^2} V_\eta|_{\eta=0} G|_{\xi=\xi_M(V)} s\,\mathrm{d}v\,\mathrm{d}s\,\mathrm{d}\xi = -\int_0^\infty\!\!\int_{\mathbb{R}^2} G|_{\xi=\xi_M(V)} s\,\mathrm{d}v\,\mathrm{d}s\,\mathrm{d}V, \tag{7.49}$$

since on $\eta = 0$ we have $dV = V_\xi\, d\xi$ and $V_\xi = \frac{5}{2}V_\eta$. The right-hand side of (7.41) is transformed to give

$$\tfrac{1}{2}\int_W\!\int_W G(\mathbf{\Sigma}_1)G(\mathbf{\Sigma}_2)K(\mathbf{\Sigma}_1, \mathbf{\Sigma}_2)\,\mathrm{d}\mathbf{\Sigma}_1\,\mathrm{d}\mathbf{\Sigma}_2. \tag{7.50}$$

Thus the transformed boundary condition (7.41) is

$$-\int_0^\infty\!\!\int_{\mathbb{R}^2} G|_{\xi=\xi_M(V)} s\,\mathrm{d}v\,\mathrm{d}s\,\mathrm{d}V = \tfrac{1}{2}\int_W\!\int_W G(\mathbf{\Sigma}_1)G(\mathbf{\Sigma}_2)K(\mathbf{\Sigma}_1, \mathbf{\Sigma}_2)\,\mathrm{d}\mathbf{\Sigma}_1\,\mathrm{d}\mathbf{\Sigma}_2. \tag{7.51}$$

In order to write (7.51) in pointwise form for the flux (i.e. by removing the triple integral from the left-hand side), we rewrite (7.50) as a double integral involving V, v and s that satisfy the conservation laws in (7.30b), (7.30e) and (7.30f). In order to do this, we change variables in the integral (7.50) as follows:

$$V_1, V_2 \;\to\; V, V_2, \tag{7.52a}$$

$$v_1, v_2 \;\to\; v, v_2, \tag{7.52b}$$

$$s_1, s_2 \;\to\; s, s_2, \tag{7.52c}$$

where V, v and s are as defined in (7.30b), (7.32) and (7.34) respectively. More precisely, (7.52), with additionally $\xi = \xi_1$, $\xi_2 = \xi_2$, is a transformation from $(\boldsymbol{\Sigma}_1, \boldsymbol{\Sigma}_2)$ to $(\boldsymbol{\Sigma}, \boldsymbol{\Sigma}_2)$. The Jacobian of the transformation is the determinant of the eight-by-eight matrix which can be written as a four-by-four block matrix:

$$|\mathcal{J}| = \left| \frac{\partial(\boldsymbol{\Sigma}, \boldsymbol{\Sigma}_2)}{\partial(\boldsymbol{\Sigma}_1, \boldsymbol{\Sigma}_2)} \right| = \left| \begin{pmatrix} A & O \\ C & I \end{pmatrix} \right|, \tag{7.53}$$

where I and O are, respectively, the four-by-four identity and zero matrices. Thus the determinant $|\mathcal{J}|$ is equal to the determinant of A where A can itself be expressed as a four-by-four block matrix:

$$A = \begin{pmatrix} I & O \\ O & \hat{A} \end{pmatrix}, \quad \text{with} \quad \hat{A} = \begin{pmatrix} \phi & 0 \\ \phi(1-\phi)(v_1 - v_2)/s & \phi s_1/s \end{pmatrix}, \tag{7.54}$$

where I and O now denote, respectively, the two-by-two identity and zero matrices. The matrix $\hat{A}$ is derived using the definitions of v and s from (7.32) and (7.34) together with the assumption that $s_1, s < 0$. Thus the Jacobian of the transformation is

$$|\mathcal{J}| = |A| = \frac{\phi^2 s_1}{s}. \tag{7.55}$$

We use the transformation (7.52) to rewrite a double integral of some function $f(\boldsymbol{\Sigma}_1, \boldsymbol{\Sigma}_2)$ over $(\boldsymbol{\Sigma}_1, \boldsymbol{\Sigma}_2)$-space (like that in (7.50)) as follows:

$$\int_W \int_W f(\boldsymbol{\Sigma}_1, \boldsymbol{\Sigma}_2)\, d\boldsymbol{\Sigma}_1\, d\boldsymbol{\Sigma}_2 = \int_0^\infty \int_{\mathbb{R}^2} \int_0^{\xi_M(V)} \int_W f(\boldsymbol{\Sigma}, \boldsymbol{\Sigma}_2) |\mathcal{J}|^{-1}\, \mathrm{d}\xi\, \mathrm{d}v\, \mathrm{d}s\, \mathrm{d}V\, \mathrm{d}\boldsymbol{\Sigma}_2, \tag{7.56}$$

where (v, V, s) correspond to the elements of configuration space for the new bubble formed by coalescence that satisfy the conservation laws (7.30b), (7.32) and (7.34).

Applying the change of variables (7.52) to (7.50) gives

$$\tfrac{1}{2} \int_0^\infty \int_{\mathbb{R}^2} \int_0^{\xi_M(V)} \int_W G(\boldsymbol{\Sigma}) G(\boldsymbol{\Sigma}_2) K(\boldsymbol{\Sigma}, \boldsymbol{\Sigma}_2) \left(\frac{V^2 s}{V_1^2 s_1} \right) \mathrm{d}\xi\, \mathrm{d}v\, \mathrm{d}s\, \mathrm{d}V\, d\boldsymbol{\Sigma}_2, \tag{7.57}$$

where $V_1 = V - V_2$ from (7.30b). Using this in the coalescence-driven boundary condition (7.51) and differentiating with respect to v, s and V, we can now write the (transformed) pointwise form of the boundary condition as

$$G|_{\xi=\xi_M(V)} = -\tfrac{1}{2}\int_0^{\xi_M(V)} \int_W G(\mathbf{\Sigma})G(\mathbf{\Sigma}_2)K(\mathbf{\Sigma},\mathbf{\Sigma}_2)\left(\frac{V^2}{V_1^2 s_1}\right) \mathrm{d}\xi\,\mathrm{d}\mathbf{\Sigma}_2. \tag{7.58}$$

This provides the boundary condition which is to be applied on $\xi = \xi_M(V)$ (or equivalently $\eta = 0$). Note that in writing (7.58) we have cancelled a factor s from each side.

In the master equation (7.45) defined in terms of the configuration space $\mathbf{\Sigma}$, the coalescence sink term C is given by (7.47), which is associated with the loss of bubbles due to coalescence. The corresponding coalescence-driven source term is manifested as a boundary condition on $\xi = \xi_M(V)$ from (7.58). We next turn our attention to the fragmentation term B in (7.45).

7.5 Fragmentation

We now revert to our original configuration space $\mathbf{\Omega}$, as it is simpler to initially formulate the fragmentation dynamics in terms of the shape variables (ξ, η). We then assume the transformation (7.42) to express the fragmentation terms in the master equation (7.45) in the configuration space $\mathbf{\Sigma}$ in terms of volume.

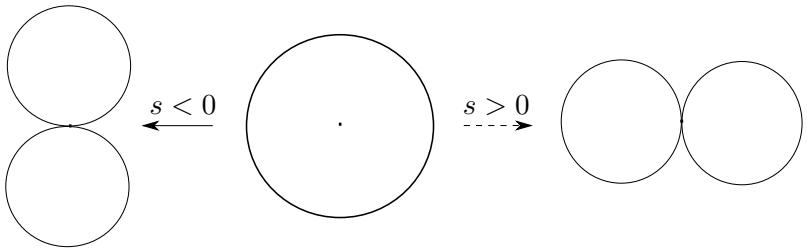


Figure 7.7: Fragmentation of bubbles: to the left, vertical pinch-off occurs when $\xi = 0$. If $s > 0$ a bubble heads to a horizontal pinched-torus with $\eta = 0$. We only consider vertical pinch-off with $s < 0$.

7.5.1 Fragmentation criteria

A bubble evolving with $\dot{\xi} = s < 0$ heads to vertical pinch-off, and one with $\dot{\xi} = s > 0$ heads to a horizontal pinched-torus; see figure 7.7. As discussed above, we assume $s < 0$ and consider fragmentation to occur at $\xi = 0$; see figure 7.6. In the same way that the coalescence term in the master equation was initially assumed to have a sink

and source term, the fragmentation term in (7.21) can be written as the sum of a sink and source term: $b = b_+ - b_-$.

7.5.2 Criteria for the daughter bubbles

We assume that fragmentation of a bubble results in two new spherical bubbles of equal volume $\frac{1}{2}V$ (thus conserving mass), as indicated in figure 7.6. We also endeavour to conserve the momentum and energy as defined in (7.30e) and (7.30f). This is easily achieved if the two daughter bubbles have the same values of v and s.

7.5.3 Fragmentation terms

Let us first consider the fragmentation sink term. As discussed above, we assume that bubbles fragment at $\xi = 0$, thus the sink term is represented as a flux on the boundary $\xi = 0$ (analogous to the $\eta = 0$ boundary condition from the coalescence source term). The flux out at vertical pinch-off is $-g\dot{\xi}|_{\xi=0} = -gs|_{\xi=0}$. Note that, as $s < 0$, the characteristics in the shape space (ξ, η) leave $\eta = 0$ (where the coalescence-driven boundary condition (7.58) is prescribed) and travel towards $\xi = 0$; see figure 7.6. The flux at $\xi = 0$, and consequently the fragmentation sink term, is therefore determined from the solution of the master equation (7.21).

For the corresponding fragmentation source term, note that the bubble flux leaving the domain at $\xi = 0$ is re-introduced as a source term in the equation, so the master equation becomes non-local. Consequently, the fragmentation source term cannot be supplied as a boundary condition and needs to be given as part of the master equation: i.e. $b = b_+$ in (7.21). We therefore need to prescribe how the two daughter bubbles are re-introduced to the configuration space. The inflow of daughter bubbles exactly balances the flux out at $\xi = 0$, as shown in figure 7.6.

We can consider the relationship between the fragmenting bubble and the daughter bubbles. At vertical pinch-off the volume of the fragmenting bubble can be written as $\hat{V} = \frac{64\pi}{105}\hat{\eta}^3$. Fragmentation results in two spherical daughter bubbles each with volume $V = \frac{4\pi}{3}\eta^3$. Thus the bubbles fragmenting at the point $(v, 0, \hat{\eta}, s)$ are re-introduced into the domain at the point (v, η, η, s). As we know the shapes of both the fragmenting and the new daughter bubbles, we can use conservation of volume $\hat{V} = 2V$ to find that $\hat{\eta} = k\eta$ with $k = \frac{1}{2}(35)^{1/3} \approx 1.64$. The number of fragmenting bubbles at $\xi = 0$ can then be written as:

$$-sg(v, 0, \hat{\eta}, s)\,\mathrm{d}v\,\mathrm{d}\hat{\eta}\,\mathrm{d}s = -ksg(v, 0, k\eta, s)\,\mathrm{d}v\,\mathrm{d}\eta\,\mathrm{d}s. \tag{7.59}$$

Note that (7.59) is positive because $s < 0$. The fragmentation-driven rate of increase

of bubbles per unit volume per unit time to the point (v, ξ, η, s) is therefore found by integrating (7.59) over v, η and s:

$$b = -2ksg(v, 0, k\eta, s)\delta(\xi - \eta), \tag{7.60}$$

where the factor of 2 corresponds to two bubbles being formed from the fragmentation of a single bubble, and the delta function ensures the formation of spherical bubbles.

To be consistent with the coalescence dynamics, we now transform the fragmentation source term (7.60) to the coordinate $\mathbf{\Sigma}$ defined by (7.42). To do this, recall that from (7.44) we have $g = V_\eta G$. If we momentarily suppress the dependence on v and s, which are not altered by the transformation, we can write this as

$$g(\xi, \eta) = V_\eta(\xi, \eta)\, G[\xi, V(\xi, \eta)]. \tag{7.61}$$

Direct substitution from (ξ, η) to $(k\xi, k\eta)$ gives

$$g(k\xi, k\eta) = \frac{1}{k} V_\eta(k\xi, k\eta)\, G[k\xi, V(k\xi, k\eta)]. \tag{7.62}$$

If we take k, as introduced above, to be the constant such that $V(k\xi, k\eta) = 2V(\eta, \xi)$ then we find

$$g(k\xi, k\eta) = \frac{2}{k} V_\eta(\xi, \eta)\, G(k\xi, 2V(\xi, \eta)). \tag{7.63}$$

Finally, using (7.63) in the transformation of (7.60) from $\mathbf{\Omega}$ to $\mathbf{\Sigma}$ we derive the fragmentation source term to be

$$B = -4G(v, 0, 2V, s)s\, \delta[\xi - \xi_S(V)]. \tag{7.64}$$

7.6 The master equation for a bubble distribution

Using the coalescence and fragmentation terms given by (7.47) and (7.64) respectively, the master equation (7.45) for G takes the form

$$\begin{aligned} G_t + (Gv)_x + (Ga)_v + (Gs)_\xi + (Gq)_s + (Gr)_w \;\; = \\ -4G(v, 0, 2V, s)s\, \delta[\xi - \xi_S(V)] - \int_W G(\mathbf{\Sigma}')K(\mathbf{\Sigma}, \mathbf{\Sigma}')\, d\mathbf{\Sigma}'\; G(\mathbf{\Sigma}), \end{aligned} \tag{7.65}$$

and this is subject to the boundary condition (7.58) on $\xi = \xi_M(V)$. The system (7.65) is defined in a four-dimensional phase space $\mathbf{\Sigma} = (v, \xi, V, s)$, and it remains to find suitable prescriptions for the acceleration a and the adaptation (q, r).

To assess the reliability of what we have derived, we check for consistency of the units in the equation (7.65). The quantity $G\,\mathrm{d}x\,\mathrm{d}\mathbf{\Sigma}$ is dimensionless, as G is defined

to be the number of bubbles per unit volume per unit of each element of phase space. Thus the units of G are $[G] = \mathrm{s}^2\ \mathrm{m}^{-7}$, where we use the square bracket notation to describe units. The units of the left-hand side of (7.65) are $[G][t]^{-1} = \mathrm{s}\ \mathrm{m}^{-7}$. In the fragmentation term on the right-hand side of (7.65) we note that $[\delta] = \mathrm{m}^{-1}$ because $[\int \delta(\xi)\,\mathrm{d}\xi] = 1$. Thus the units of the fragmentation term are $[G][s][\delta] = \mathrm{s}\ \mathrm{m}^{-7}$. Finally, in the coalescence term on the right-hand side it is clear that $[G\,\mathrm{d}\mathbf{\Sigma}] = \mathrm{m}^{-1}$ and $[K] = \mathrm{m}\ \mathrm{s}^{-1}$; so the coalescence term has units $[G\,\mathrm{d}\mathbf{\Sigma}][K][G] = \mathrm{s}\ \mathrm{m}^{-7}$. We therefore have consistency across the units in the master equation. We now examine the relevant conservation laws.

7.7 Conserved quantities

We need to check that conservation of the appropriate quantities holds. A quantity ψ is conserved if:

$$\frac{\mathrm{d}}{\mathrm{d}t}\int_W \psi G\,\mathrm{d}\mathbf{\Sigma} = 0. \tag{7.66}$$

For simplicity, we again suppose G is independent of x and take $a = q = r = 0$ so that (7.65) reduces to:

$$G_t + (Gs)_\xi = -4\,G(v,0,2V,s)s\,\delta[\xi - \xi_S(V)] - \int_W G(\mathbf{\Sigma}')K(\mathbf{\Sigma},\mathbf{\Sigma}')\,d\mathbf{\Sigma}'\ G(\mathbf{\Sigma}). \tag{7.67}$$

We now check that (7.66) holds for mass, momentum and energy.

7.7.1 Conservation of volume

We first check for conservation of volume where the conserved quantity is $\psi = V$. Multiplying (7.67) by V and integrating we find

$$\frac{\mathrm{d}}{\mathrm{d}t}\int_W VG\,d\mathbf{\Sigma} = -I_1 + I_2 + I_3 - I_4, \tag{7.68}$$

where I_1 and I_2 correspond to the ξ boundary terms:

$$I_1 = \int_0^\infty\!\!\int_{\mathbb{R}^2} VG\Big|_{\xi=\xi_M(V)} s\,\mathrm{d}v\,\mathrm{d}s\,\mathrm{d}V, \tag{7.69a}$$

$$I_2 = \int_0^\infty\!\!\int_{\mathbb{R}^2} VG(v,0,V,s)s\,\mathrm{d}v\,\mathrm{d}s\,\mathrm{d}V, \tag{7.69b}$$

and I_3 and I_4 to the fragmentation and coalescence terms:

$$I_3 = -4\int_W VG(v,0,2V,s)s\,\delta[\xi - \xi_S(V)]\,\mathrm{d}\mathbf{\Sigma}, \tag{7.70a}$$

$$I_4 = \int_W\!\int_W VG(\mathbf{\Sigma})G(\mathbf{\Sigma}')K(\mathbf{\Sigma},\mathbf{\Sigma}')\,\mathrm{d}\mathbf{\Sigma}'\,\mathrm{d}\mathbf{\Sigma}. \tag{7.70b}$$

From (7.68) we need to prove that $-I_1 + I_2 + I_3 - I_4 = 0$.

First we note that I_3 can be written as

$$I_3 = -4 \int_0^\infty \int_{\mathbb{R}^2} VG(v, 0, 2V, s) s \, \mathrm{d}v \, \mathrm{d}s \, \mathrm{d}V. \tag{7.71}$$

Changing variables in I_3 above to $\tilde{V} = 2V$ we see that $I_3 = -I_2$.

Next we use the boundary condition (7.58) to rewrite I_1 as

$$I_1 = -\int_0^\infty \int_{\mathbb{R}^2} \int_0^{\xi_M(V)} \int_W \tfrac{1}{2} VG(\mathbf{\Sigma}) G(\mathbf{\Sigma}_2) K(\mathbf{\Sigma}, \mathbf{\Sigma}_2) \left(\frac{V^2 s}{V_1^2 s_1} \right) \mathrm{d}\xi \, \mathrm{d}v \, \mathrm{d}s \, \mathrm{d}V \, \mathrm{d}\mathbf{\Sigma}_2. \tag{7.72}$$

Now we transform the variables of integration $(\mathbf{\Sigma}, \mathbf{\Sigma}_2)$ back to $(\mathbf{\Sigma}_1, \mathbf{\Sigma}_2)$ by inverting the transformation (7.52) (which maps $(V_1,\, v_1,\, s_1)$ to $(V,\, v,\, s)$ as defined in (7.30)). This inversion is possible as the Jacobian (7.53) is non-zero. Using (7.56) we can write (7.72) as

$$I_1 = -\int_W \int_W \tfrac{1}{2}(V_1 + V_2) G(\mathbf{\Sigma}_1) G(\mathbf{\Sigma}_2) K(\mathbf{\Sigma}_1, \mathbf{\Sigma}_2) \, \mathrm{d}\mathbf{\Sigma}_1 \, \mathrm{d}\mathbf{\Sigma}_2. \tag{7.73}$$

The coalescence kernel $K(\mathbf{\Sigma}_1, \mathbf{\Sigma}_2)$ defined in (7.39) is symmetric, and so the integrand of (7.73) is symmetric, and I_1 becomes

$$I_1 = -\int_W \int_W V_1 G(\mathbf{\Sigma}_1) G(\mathbf{\Sigma}_2) K(\mathbf{\Sigma}_1, \mathbf{\Sigma}_2) \, \mathrm{d}\mathbf{\Sigma}_1 \, \mathrm{d}\mathbf{\Sigma}_2. \tag{7.74}$$

Relabelling the integration variables $(\mathbf{\Sigma}_1, \mathbf{\Sigma}_2) \to (\mathbf{\Sigma}, \mathbf{\Sigma}')$ in (7.74) we see that $I_1 = -I_4$. Thus (7.67) does in fact conserve volume.

7.7.2 Conservation of momentum

Next we need to check for conservation of momentum where the conserved quantity is now $\psi = Vv$. Multiplying (7.67) by Vv and integrating we find

$$\frac{\mathrm{d}}{\mathrm{d}t} \int_W Vv \, G \, d\mathbf{\Sigma} = -I_a + I_b + I_c - I_d, \tag{7.75}$$

where I_a and I_b (analogous to I_1 and I_2 above) correspond to the ξ-boundary terms:

$$I_a = \int_0^\infty \int_{\mathbb{R}^2} Vv \, G \Big|_{\xi = \xi_M(V)} s \, \mathrm{d}v \, \mathrm{d}s \, \mathrm{d}V, \tag{7.76a}$$

$$I_b = \int_0^\infty \int_{\mathbb{R}^2} Vv \, G(v, 0, V, s) s \, \mathrm{d}v \, \mathrm{d}s \, \mathrm{d}V, \tag{7.76b}$$

and I_c and I_d (analogous to I_3 and I_4) to the fragmentation and coalescence terms:

$$I_c = -4 \int_W Vv \, G(v, 0, 2V, s) s \, \delta(\xi - \xi_S(V)) \, \mathrm{d}\mathbf{\Sigma}, \tag{7.77a}$$

$$I_d = \int_W \int_W Vv \, G(\mathbf{\Sigma}) G(\mathbf{\Sigma}') K(\mathbf{\Sigma}, \mathbf{\Sigma}') \, \mathrm{d}\mathbf{\Sigma}' \, \mathrm{d}\mathbf{\Sigma}. \tag{7.77b}$$

As with volume conservation, our aim is to prove that $-I_a + I_b + I_c - I_d = 0$.

The method is analogous, and we first note that I_c can be written as

$$I_c = -4 \int_0^\infty \int_{\mathbb{R}^2} V v \, G(v, 0, 2V, s) s \, \mathrm{d}v \, \mathrm{d}s \, \mathrm{d}V. \tag{7.78}$$

The same change of variables $\tilde{V} = 2V$ in I_c gives $I_c = -I_b$.

The boundary condition (7.58) at $\xi = \xi_M(V)$ is used in I_a to give

$$I_a = -\int_0^\infty \int_{\mathbb{R}^2} \int_0^{\xi_M(V)} \int_W \tfrac{1}{2} V v \, G(\mathbf{\Sigma}) G(\mathbf{\Sigma}_2) K(\mathbf{\Sigma}, \mathbf{\Sigma}_2) \left(\frac{V^2 s}{V_1^2 s_1} \right) \mathrm{d}\xi \, \mathrm{d}v \, \mathrm{d}s \, \mathrm{d}V \, \mathrm{d}\mathbf{\Sigma}_2. \tag{7.79}$$

We again invert the transformation (7.52) and map $(\mathbf{\Sigma}, \mathbf{\Sigma}_2)$ back to $(\mathbf{\Sigma}_1, \mathbf{\Sigma}_2)$; we then utilise the symmetry of the integrand to re-write (7.79) as

$$I_a = -\int_W \int_W V_1 v_1 \, G(\mathbf{\Sigma}_1) G(\mathbf{\Sigma}_2) K(\mathbf{\Sigma}_1, \mathbf{\Sigma}_2) \, \mathrm{d}\mathbf{\Sigma}_1 \, \mathrm{d}\mathbf{\Sigma}_2. \tag{7.80}$$

Relabelling the integration variables in I_a gives $I_a = -I_d$, and we conclude that (7.67) is momentum conserving.

7.7.3 Conservation of energy

Finally we check for conservation of energy where the conserved quantity is $\psi = \frac{1}{2} V(v^2 + s^2)$. The method is exactly the same as that used for mass and momentum conservation. For completeness, we briefly summarise the steps. Multiplying (7.67) by $\frac{1}{2} V(v^2 + s^2)$ and integrating we find

$$\frac{\mathrm{d}}{\mathrm{d}t} \int_W \tfrac{1}{2} V(v^2 + s^2) \, G \, d\mathbf{\Sigma} = -I_A + I_B + I_C - I_D, \tag{7.81}$$

where

$$I_A = \int_0^\infty \int_{\mathbb{R}^2} \tfrac{1}{2} V(v^2 + s^2) \, G \Big|_{\xi = \xi_M(V)} s \, \mathrm{d}v \, \mathrm{d}s \, \mathrm{d}V, \tag{7.82a}$$

$$I_B = \int_0^\infty \int_{\mathbb{R}^2} \tfrac{1}{2} V(v^2 + s^2) \, G(v, 0, V, s) s \, \mathrm{d}v \, \mathrm{d}s \, \mathrm{d}V, \tag{7.82b}$$

$$I_C = -4 \int_W \tfrac{1}{2} V(v^2 + s^2) G(v, 0, 2V, s) s \, \delta(\xi - \xi_S(V)) \, \mathrm{d}\mathbf{\Sigma}, \tag{7.82c}$$

$$I_D = \int_W \int_W \frac{1}{2} V(v^2 + s^2) G(\mathbf{\Sigma}) G(\mathbf{\Sigma}') K(\mathbf{\Sigma}, \mathbf{\Sigma}') \, \mathrm{d}\mathbf{\Sigma}' \, \mathrm{d}\mathbf{\Sigma}. \tag{7.82d}$$

As with the conservation of volume and momentum, our aim is to prove that $-I_A + I_B + I_C - I_D = 0$.

We first note that I_C can be written as

$$I_C = -4\int_0^\infty\!\!\int_{\mathbb{R}^2} \tfrac{1}{2}V(v^2+s^2)\,G(v,0,2V,s)s\,\mathrm{d}v\,\mathrm{d}s\,\mathrm{d}V. \tag{7.83}$$

The change of variables $\tilde{V} = 2V$ in I_C gives $I_C = -I_B$.

The integral I_A is re-written using the boundary condition (7.58):

$$I_A = -\int_0^\infty\!\!\int_{\mathbb{R}^2}\!\!\int_0^{\xi_M(V)}\!\!\int_W \tfrac{1}{4}V(v^2+s^2)\,G(\mathbf{\Sigma})G(\mathbf{\Sigma}_2)K(\mathbf{\Sigma},\mathbf{\Sigma}_2)\left(\frac{V^2 s}{V_1^2 s_1}\right)\mathrm{d}\xi\,\mathrm{d}v\,\mathrm{d}s\,\mathrm{d}V\,\mathrm{d}\mathbf{\Sigma}_2. \tag{7.84}$$

Inverting the transformation (7.52) from $(\mathbf{\Sigma},\mathbf{\Sigma}_2)$ back to $(\mathbf{\Sigma}_1,\mathbf{\Sigma}_2)$, together with the symmetry of the integrand, gives

$$I_A = -\int_W\!\!\int_W \tfrac{1}{2}V_1(v_1^2+s_1^2)\,G(\mathbf{\Sigma}_1)G(\mathbf{\Sigma}_2)K(\mathbf{\Sigma}_1,\mathbf{\Sigma}_2)\,\mathrm{d}\mathbf{\Sigma}_1\,\mathrm{d}\mathbf{\Sigma}_2. \tag{7.85}$$

Again, a simple relabelling of integration variables gives $I_A = -I_D$, and thus it is evident that conservation of energy for (7.67) holds.

Proof of conservation of mass, momentum and energy relied on the derived coalescence and fragmentation terms. More precisely the coalescence-driven boundary source term on $\xi = \xi_M(V)$ was derived to exactly balance the coalescence-source integral on the right-hand side of the conservation equation (7.67). Similarly the fragmentation sink term on the boundary $\xi = 0$ exactly balanced the fragmentation-source integral term. We therefore do not expect any additional conserved quantities, aside from linear combination of mass, momentum and energy.

7.8 Summary

In this chapter we have derived a master equation for the evolution of a bubble distribution that is defined on the four-dimensional configuration space $\mathbf{\Sigma} = (v,\, \xi,\, V,\, s)$. The space classifies the velocity, shape, volume and transformation (rate of change of shape) of the bubble population. We accounted for the coalescence and fragmentation of bubbles, and for each process we discussed the appropriate criteria for such an occurrence and where the newly coalesced and fragmented bubbles should appear in configuration space.

The result of this chapter is a rather involved master equation (7.65) which required a few validity checks. Firstly we considered the units of the equation, which we concluded to be consistent. The second sanity check was to ensure that the appropriate conservation laws hold. We proved that conservation of mass, momentum

and energy is ensured by the master equation with the relevant boundary conditions (for the simplified system with $a = 0$, $q = 0$, $r = 0$ and x-independence). The conservation laws relied on the fact that the coalescence source term was supplied to the system as a boundary condition, and that the fragmentation sink term was observed to be an outflow flux.

We can compare the model derived in this chapter to the previous work in this field. An earlier model introduced by Kalkach-Navarro et al. [1994] was concerned with the same bubble dynamics in a configuration space defined by position and volume. Their governing equations given by (7.15) and (7.16) are analogous to the model presented here in (7.65), in that the derivation relies on the evolution of a bubble distribution, which is driven by coalescence and fragmentation. In particular, the coalescence sink terms (7.16a) and (7.47) are of a similar form. However, the coalescence source term, which appears in the master equation from Kalkach-Navarro et al. [1994] as an integral term (given in (7.16a)), appears in our model as a boundary condition in shape space. Similarly the fragmentation terms (7.16b) do not appear as integral terms in our master equation. This is because we have included shape variables in our configuration space and thus the fragmentation sink emerged as an outflow flux, and the source term as a point-source contribution in the master equation. However there is a clear similarity in the basic structure of the master equation derived in this chapter with that presented by Kalkach-Navarro et al. [1994].

Hibiki and Ishii [2000] modelled populations of bubbles specified by a finite number of 'shape classes'. We have developed this idea further and introduced continuous shape variables (ξ, η) that allow us to track the smooth evolution of the bubble shapes. Although we increase the dimensionality of the configuration space by introducing new variables, we also reduce the complexity in the model by Hibiki and Ishii [2000] which considered all the possible outcomes and perturbations for bubbles within the two groups with regards to coalescence and fragmentation criteria.

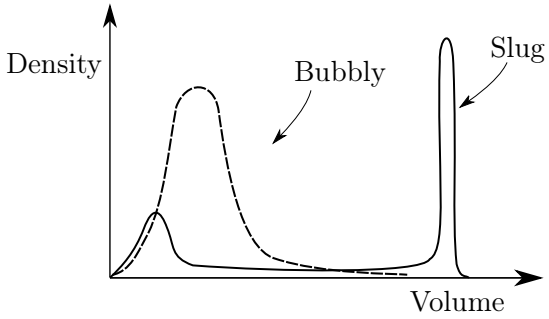
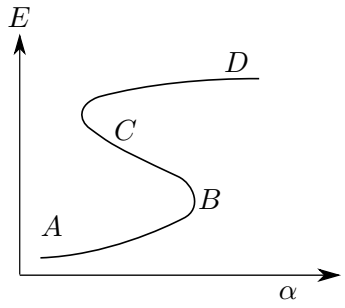


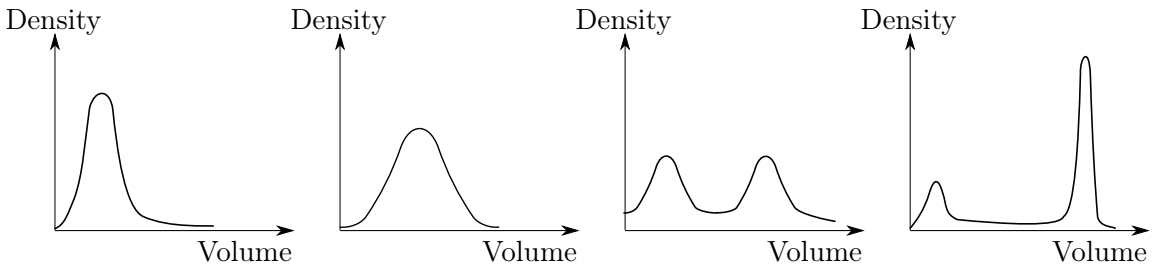
Figure 7.8: Hypothesised schematic of bubbly and slug flow regimes as probability density functions of volume.

Having derived the appropriate master equation that ensures conservation of mass, momentum and energy, the next step is to look and see what we might be able to do with it — be it analytically or numerically. Analysis of the model will enable the prediction of bubble volume distributions that may be visualised as probability distribution functions of volume (similar to those discussed in Chapter 6). We predict that this may be used to identify different flow regimes and advise as to their stability. We hypothesise bubble volume probability distributions for bubbly flow and slug flow similar to those shown schematically in figure 7.8. A bubbly flow comprises uniformly-sized bubbles; and a slug flow consists of large bubbles with smaller bubbles trailing in the wake of the larger ones. Where we have presented a schematic in volume-space, one could similarly study the probability distribution function in shape-space; but this seems of less relevance.

Moreover, supposing we find two solutions for volume distribution (one corresponding to bubbly flow and the other to slug flow) we would hope to use this model to study the stability of the solutions. Key parameters will include the gas volume fraction $\alpha = \int_W VG \, \mathrm{d}\boldsymbol{\Sigma}$ and total energy in the system $E = \int_W \frac{1}{2} V(v^2 + s^2) G \, \mathrm{d}\boldsymbol{\Sigma}$. We believe that analysis of the sensitivity of the model solutions will provide understanding as to why and where the transition between bubbly and slug flow occurs.



(a) Bifurcation diagram.



(b) A **(c)** B **(d)** C **(e)** D

Figure 7.9: Hypothesised schematic of a bifurcation diagram in bubble volume–energy space with schematics of the expected probably density functions of volume.

One technique that may be useful is bifurcation analysis of these parameters. We present a schematic for a possible bifurcation diagram involving hysteresis in (α, E)-space in figure 7.9a. In the schematic we hypothesise that for a given energy there exists region A representing the values of α for which only bubbly flow can exist; the corresponding probability density function of volume is shown in figure 7.9b. The critical point B in (α, E)-space depicts the limit of a stable bubbly flow; a schematic for which is given in figure 7.9c. In region C, described in figure 7.9d, we hypothesise a range of α for which unstable 'transitioning' solutions exist. Finally in region D we suggest that the slug flow solution is the only stable solution present; the associated probability density function of volume is shown in figure 7.9e. This discussion and the schematics in figures 7.8 and 7.9 suggest how we might use the model derived in this chapter to analyse the bubbly-to-slug flow regime transition.

An alternative possibility is that there is an exchange of stability through a transcritical bifurcation, or even through a Hopf bifurcation, since one can interpret slug flow as a finite amplitude periodic travelling wave, and a similar idea has been expressed by Pauchon and Banerjee [1986]. We discuss additional possible avenues and more specific methods for analysis which provide future work in Chapter 8.

Chapter 8

Conclusions

For detailed summaries of the work presented in each chapter, we refer the reader to the concluding parts of each chapter. Here we present a brief overview and discuss possible avenues for future work.

This thesis is concerned with the two-phase liquid–gas flow through pipes. The motivation for this study was originally proposed by our industrial partner, PDS, who are interested in gaining a better understanding of the fluid dynamics through a producing oil well. The initial focus — of flow through an oil well — followed directly from this motivation. The study of two-phase pipe flow highlighted interesting problems in bubble dynamics and regime transitions. The work in this thesis was therefore presented in two parts. In Part I we modelled the two-phase flow in oil wells, and in Part II we thought about how to model the bubbly-to-slug flow regime transition.

8.1 Part I

In the first part of the thesis we modelled a vertical oil well operating under natural lift; meaning the liquid and gas mixture was driven upwards due to a pressure gradient between the reservoir at the bottom of the well and the well-head pressure on the surface. We considered a system in which the fluid at the bottom of the well was at sufficiently high pressure (higher than the bubble point) that all the gaseous hydrocarbons were in solution. The pressure decreased as the fluid mixture moved up the well and, when the bubble-point pressure was reached, the exsolution of the dissolved gaseous components began.

We assumed a one-dimensional domain along the axis of the well, and derived the governing equations from conservation of mass of the liquid phase, the total gas phase and the dissolved gas in the liquid; and conservation of momentum of both

phases. Scaling of the equations suggested that for our application it was appropriate to assume an isothermal flow with a single velocity and pressure for both phases; thus we analysed a homogeneous model.

In Chapter 3 we studied the homogeneous model in two parameter regions; in the first we took the gas–liquid density ratio to be small and the initial concentration of dissolved gas to be of order one. In the second, the initial concentration of dissolved gas was assumed to be proportional to the small density ratio. We found that, in the first parameter region, the model predicts an unexpected rapid transition from liquid to a highly gaseous foam at the bubble-point pressure. In the second parameter region, we found that, we were able to control the rate of exsolution and see a substantial two-phase region in the pipe. Importantly in Chapter 3, we found that the model conclusions for a compressible–incompressible liquid–gas system were identical to those of an incompressible–incompressible liquid–gas system. However, we were concerned with the validity of our conclusions as we noted that in practice there are oil wells producing gas and liquid mixtures from reservoirs that do not necessarily have a small initial dissolved gas concentration.

In Chapter 4, therefore, we examined rate-limiting non-equilibrium dynamics for the nucleation and bubble growth dynamics in the two-phase model introduced in Chapter 3. We found that bubble growth driven by the diffusion of the dissolved gas through the liquid was not by itself a significant rate-limiting mechanism. Thus we examined the initial nucleation of bubbles together with the diffusive growth. We found that for certain parameters — namely where the rate of mass transfer was order one — the inclusion of the non-equilibrium dynamics proved to be suitably rate-limiting. We say "suitably" as for a large rate of mass transfer the non-equilibrium dynamics were so rate-limiting that the gas exsolution was almost totally suppressed. Thus we concluded Part I of the thesis with the result that it is important to include nucleation and growth kinetics when modelling the flow in oil wells.

Note that in the models presented in Chapters 3 and 4 we have an increasing gas volume fraction. At the bubble-point pressure bubbles are nucleated and we initially expect a bubbly flow. However, as bubbles grow and further bubbles nucleate, the gas volume fraction will become sufficiently large that the flow will undergo a regime transition from bubbly to slug flow. In slug flow, dynamics that we had thus far neglected (e.g. the slip between phases) become important. Future work for this part of the thesis could include the examination of the effect of coalescence dynamics and the bubbly-to-slug flow regime transition, which will be important for the system in which the initial concentration of dissolved gas is comparable to the small gas–liquid density ratio.

8.2 Part II

The importance of the bubbly-to-slug flow regime transition is evident, and this motivates the work in the second part of the thesis. In Part II, we thought about how we might model the particular flow regime transition. The governing dynamics can be reduced to bubble coalescence and fragmentation. Thus we were concerned with modelling bubbles. To do this we turned to stochastic processes where the variable of interest was a bubble distribution function.

In our pursuit of a stochastic model for bubble populations, we spent Chapter 5 examining a simple model that is, in some respects, similar to the bubble model we sought. We took the simple model first introduced by Ben-Naim and Krapivsky [1996] for two arbitrary populations of islands and holes, and applied it to populations of bubbles and inter-bubble liquid holes. The governing processes considered were nucleation, growth and coalescence of bubbles. This preliminary work provided an initial understanding of how to model evolving populations in a stochastic framework. In the bubbly-to-slug regime transition, fragmentation dynamics are important. Thus future work could be concerned with how to include fragmentation (e.g. nucleation of holes in the bubbles) which will yield a more relevant model.

In Chapter 6 we considered what the appropriate way to classify a system of bubbles might be; the aim was to develop the minimum configuration space that accounts for shape, position and velocity space. We concluded that to track the shape of an azimuthally symmetric bubble the minimum number of variables is two: the horizontal and vertical axes. We looked at how to include coalescence and fragmentation dynamics in a deterministic model for a system of bubbles. We then incorporated the model equations within a stochastic simulation of an evolving bubble distribution by introducing randomness to the initial conditions and through prescribing a random-Fourier series for the velocity field.

Future work for Chapter 6 could include further exploration on the imposed velocity field. In our results, we found that coalescence appeared to be the dominant process. In a bubble distribution, a small number of large bubbles may well be interpreted as slug flow; and a large number of smaller bubbles could be interpreted as a bubbly flow. Therefore derivation of the appropriate velocity fields that result in either flow regime would provide more understanding to the flow necessary for the different flow regimes. Furthermore, we visualised the results of the simulation using histograms to display the distribution of bubble volumes. This naturally leads to the consideration of the appropriate number of volume bins for the system. Future work could also include investigation of the sensitivity of the results to the number of bins considered.

The preliminary work in Chapters 5 and 6 provided the basis for the work in Chapter 7 where we derived a master equation for a bubble distribution defined in a four-dimensional configuration space. Careful derivation of the appropriate coalescence and fragmentation terms ensured conservation of mass, momentum and energy. There is clearly plenty of potential for future work arising from this part of the thesis, and there are several possible ways to proceed.

Previous work by Kalkach-Navarro et al. [1994] and Hibiki and Ishii [2000] would advise coupling the master equation to a two-fluid model like that discussed in Chapter 3. This requires consideration of the appropriate prescription for the acceleration and adaptation terms. Moreover, Hibiki and Ishii [2000] noted the importance of capturing the bullet-shaped bubbles in slug flow. Therefore further work could include extending the current definition of the shape variables to capture additional bubble shapes.

Importantly the principal focus will be to analyse the master equation by itself. Ideally, we will look for two steady state solutions: one which corresponds to small uniformly shaped bubbles (i.e. bubbly flow) and one which corresponds to larger bubbles (i.e. slug flow); see figure 7.8. A useful tool to check such a solution (be it numerical of analytical) would be to compare the predicted bubble distribution to a stochastic simulation of the same system (similar to that developed in Chapter 6). Once we have confirmed the existence of two solutions, we will look to examine the stability and to see whether we might be able to drive one stable solution to another. Such an instability would be interpreted as the transition between regimes.

Appendix A

Comparison between discrete and continuum models

In this appendix we compare the numerical solutions of the discrete formulation for the evolution of bubbles and holes derived in Section 5.3 to the continuum analogue given in Section 5.4. The continuum equations for the holes (5.18) and bubbles (5.24) were derived from the discrete equations (5.8) and (5.10) respectively. The solutions of the two formulations should therefore match exactly. It is clear that we can choose a discretisation of the continuum equations that exactly reproduces the discrete formulation. However, initial attempts to numerically solve the continuum model utilising a 'naive' spatial discretisation of the equations resulted in stability and convergence issues. We will illustrate these issues in this appendix.

We first consider the system of holes, which is decoupled from the bubble equations. The continuum model is given by (5.18). To examine the spatial discretisation, we define the time-dependent hole size distribution: $h_i(t) = h(i\Delta x, t)$. The naive finite-difference spatial discretisation is given by

$$\frac{\mathrm{d}h_i}{\mathrm{d}t} = 2v\left(\frac{h_{i+1} - h_i}{\Delta x}\right) - \gamma x_i h_i + 2\gamma \sum_{k=i}^{N} h_k \, \Delta x, \tag{A.1}$$

for $i = 1, \ldots, N$, with v and γ defined in (5.16). To be consistent with the discrete formulation, we numerically solve (A.1) with explicit time-stepping.

When one considers the numerical stability of a simple finite-difference scheme, one turns to the Courant–Friedrichs–Lewy (CFL) number: $C = v\Delta x/\Delta t$. The condition for stability reduces to choosing the CFL number sufficiently small, and for an explicit time-stepping one typically finds that stability holds providing $C \leq 1$. From the definition of $v = \Delta x/\Delta t$ in (5.16) we find that the CFL number for (A.1) is $C = 1$, and we do not have any flexibility in this. Whilst this should be sufficient to

ensure stability, we find that, in practice, it is not. We therefore go back to the discrete formulation derived from first principles to re-assess the choice of spatial discretisation.

Consider the analogous spatial discretisation corresponding to the discrete formulation given in (5.8). We write this in terms of the variable $H_i(t) = H_i^t$:

$$\frac{\mathrm{d}H_i}{\mathrm{d}t} = 2v\left(\frac{H_{i+2} - H_i}{2\Delta x}\right) - \gamma x_i H_{i+2} + 2\gamma \sum_{k=i+3}^{N} H_k\,\Delta x. \tag{A.2}$$

There are a few subtle differences between (A.1) and (A.2). The first we see in the finite-difference discretisation of the spatial derivative. In (A.1) we use a one-step method, but in (A.2) we have two-step difference. For stability, we need to adopt the two-step difference for the derivative. Moreover, we find that the stability of the numerical scheme is also dependent on keeping the second term on the right-hand side which corresponds to the sink term due to nucleation. The summation term in (A.1) does not effect the stability. We therefore present our updated 'naive' discretisation of the continuum equations:

$$\frac{\mathrm{d}h_i}{\mathrm{d}t} = 2v\left(\frac{h_{i+2} - h_i}{2\Delta x}\right) - \gamma x_i h_{i+2} + 2\gamma \sum_{k=i}^{N} h_k\,\Delta x. \tag{A.3}$$

Having stabilised the numerical solution to the continuum model, we can compare the results from (A.3) to the corresponding solution of the discrete formulation in (A.2). We supply the same boundary condition (5.20) and initial condition (5.22). The only difference between (A.2) and (A.3) is the discretisation of the integral, i.e. the summation term. In (A.3) we account for three additional terms: $\Delta x(h_i + h_{i+1} + h_{i+2})$. If we define an error measure assessing the difference between the two solutions, we therefore expect the difference between them to converge to zero at a rate Δx. To assess convergence, we consider the difference between the two hole volume fractions:

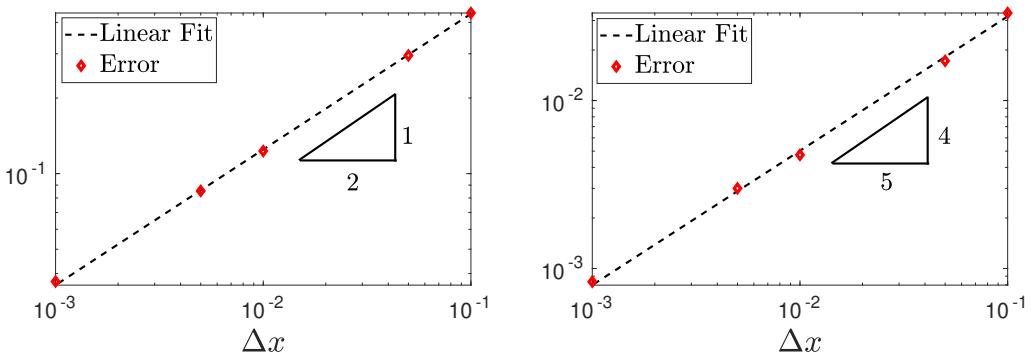
$$\alpha_h(t) = \sum_i h_i(t), \tag{A.4a}$$

$$\alpha_H(t) = \sum_i H_i(t). \tag{A.4b}$$

We define the error measure to be the infinity norm of the difference:

$$e_h = \|\alpha_H - \alpha_h\|_\infty. \tag{A.5}$$

The infinity norm simply gives the maximum absolute value between the two solutions. We show the relationship between e_h and Δx in figure Ii. The rate of convergence is approximately $\Delta x^{1/2}$, not the expected Δx. We will discuss the results following the analogous analysis for the bubble population.



(i) Hole volume fraction. **(ii)** Bubble volume fraction.

Figure I: Log-log plot showing the convergence of the difference between continuous formulation to discrete formulation for the volume fractions of holes and bubbles with varying Δx and $\Delta t = 10^{-3}$, $L = 5$, $T = 1.2$.

For the bubble distribution $b_i(t) = b(i\Delta x, t)$, we consider the solution to the continuum equation (5.24). Again, we find that the two-step finite-difference discretisation of the derivative is required for stability. The spatial discretisation of the equation (5.24) is

$$\frac{\mathrm{d}b_i}{\mathrm{d}t} = -2v\left(\frac{b_{i+2} - b_i}{\Delta x}\right) - \frac{4vh_1}{n_h}b_{i-2} + \frac{2vh_1}{n_h^2}\sum_{k=1}^{i} b_k b_{i-k}\Delta x. \tag{A.6}$$

We compare the numerical solution to (A.6) to that of the discrete system (5.10) written in terms of $B_i(t) = B_i^t$:

$$\begin{aligned}\frac{\mathrm{d}B_i}{\mathrm{d}t} &= -2v\left(\frac{B_{i+2} - B_i}{\Delta x}\right) - \frac{2v(H_1 + H_2)}{N_h}B_{i-2} \\ &\quad + \frac{vH_1}{N_h^2}\sum_{k=1}^{i-4} B_k B_{i-k-3}\Delta x + \frac{vH_2}{N_h^2}\sum_{k=1}^{i-5} B_k B_{i-k-4}\Delta x.\end{aligned} \tag{A.7}$$

We supply the same boundary condition (5.27) and initial condition (5.25), and adopt explicit time-stepping for both systems. The principal difference is the integral discretisation, so as above we expect the two solutions to converge at rate Δx. As for the hole population, we consider the bubble volume fraction from each discretisation:

$$\alpha_b(t) = \sum_i b_i(t), \tag{A.8a}$$

$$\alpha_B(t) = \sum_i B_i(t). \tag{A.8b}$$

We define the error measure to be the infinity norm of the difference:

$$e_b = \|\alpha_B - \alpha_b\|_\infty. \tag{A.9}$$

Recall that the bubble population depends on the hole population; to isolate the study of the spatial discretisation, we therefore solve both bubble systems (A.6) and (A.7) with the hole population corresponding to (A.2).

The convergence of α_b to α_B as a function of Δx is shown in figure Iii. The rate of convergence of the error is $\Delta x^{4/5}$ which, although is not what we expect, is closer to Δx than the $\Delta x^{1/2}$ convergence of the hole population.

There is clearly further work to be done to better understand the convergence and stability issues of the continuum equations for both the system of holes (5.18) and the system of bubbles (5.24). We do note, however, that the need for the spatial discretisation to be advised from first principles is intuitive as the spatial derivatives in (5.18) and (5.24) are derived from the growth of bubbles in both directions along the one-dimensional domain; the bubbles are growing by two at each time step. Thus, the spatial derivative should be a two-step discretisation.

The stability and convergence of the numerics was not a focus of this thesis, but we presented the discussion in this appendix for completeness, and to highlight the evident issues. For a robust understanding, further work could therefore include a more detailed analysis of the numerical scheme.

Bibliography

M. Abramowitz and I. A. Stegun. *Handbook of Mathematical Functions: with Formulas, Graphs, and Mathematical Tables*, volume 55. Courier Corporation, 1964.

E. M. Al-Safran and J. P. Brill. *Applied Multiphase Flow in Pipes and Flow Assurance - Oil and Gas Production*. Society of Petroleum Engineers Richardson, 2017.

C. J. Aldridge and A. C. Fowler. Stability and instability in evaporating two-phase flows. *Surveys on Mathematics for Industry*, 6:75–107, 1996.

P. A. Allen and J. R. Allen. *Basin Analysis: Principles and Application to Petroleum Play Assessment*. John Wiley & Sons, 2013.

A. M. Ansari, N. D. Sylvester, O. Shoham, and J. P. Brill. A comprehensive mechanistic model for upward two-phase flow in wellbores. In *SPE Annual Technical Conference and Exhibition*. Society of Petroleum Engineers, 1990.

G. K. Batchelor. *An Introduction to Fluid Dynamics*. Cambridge University Press, 1967.

D. H. Beggs and J. P. Brill. A study of two-phase flow in inclined pipes. *Journal of Petroleum Technology*, 25(5):607–617, 1973.

E. Ben-Naim and P. L. Krapivsky. Nucleation and growth in one dimension. *Physical Review E*, 54(4):3562–3568, 1996.

E. Ben-Naim, J. B. Knight, E. R. Nowak, H. M. Jaeger, and S. R. Nagel. Slow relaxation in granular compaction. *Physica D: Nonlinear Phenomena*, 123(1–4): 380–385, 1998.

K. H. Bendiksen, D. Maines, R. Moe, and S. Nuland. The dynamic two-fluid model OLGA: Theory and application. *SPE Production Engineering*, 6(2):171–180, 1991.

R. B. Bird, W. E. Stewart, and E. N. Lightfoot. *Transport Phenomena*. Princeton University Press, 2014.

J. M. Bradley, A. Hopkinson, and D. A. King. A molecular beam study of ammonia adsorption on Pt{100}. *Surface Science*, 371(2–3):255–263, 1997.

C. E. Brennen. *Fundamentals of Multiphase Flow*. Cambridge University Press, 2005.

Y. A. Buyevich and I. N. Shchelchkova. Flow of dense suspensions. *Progress in Aerospace Sciences*, 18:121–150, 1979.

E. Caglioti, V. Loreto, H. J. Herrmann, and M. Nicodemi. A "Tetris-like" model for the compaction of dry granular media. *Physical Review Letters*, 79(8):1575–1578, 1997.

O. Cazarez, D. Montoya, A. G. Vital, and A. C. Bannwart. Modeling of three-phase heavy oil–water–gas bubbly flow in upward vertical pipes. *International Journal of Multiphase Flow*, 36(6):439–448, 2010.

O. Cazarez-Candia and M. A. Vásquez-Cruz. Prediction of pressure, temperature, and velocity distribution of two-phase flow in oil wells. *Journal of Petroleum Science and Engineering*, 46(3):195–208, 2005.

Z. Chen. *Reservoir Simulation: Mathematical Techniques in Oil Recovery*, volume 77. SIAM, 2007.

N. I. Christensen and W. D. Mooney. Seismic velocity structure and composition of the continental crust: A global view. *Journal of Geophysical Research: Solid Earth*, 100(B7):9761–9788, 1995.

R. Clift, J. Grace, and M. Weber. *Bubbles, Drops, and Particles*. Courier Corporation, 2005.

B. H. Dale. *Production Optimization Using NODAL Analysis*. Oil and Gas Consultants International Publications, 1991.

J. H. Davies. Global map of solid earth surface heat flow. *Geochemistry, Geophysics, Geosystems*, 14(10):4608–4622, 2013.

T. N. Dinh, R. R. Nourgaliev, and T. G. Theofanous. Understanding the ill-posed two-fluid model. In *Proceedings of the 10th International Topical Meeting on Nuclear Reactor Thermal-Hydraulics*, 2003.

D. A. Drew. Mathematical modeling of two-phase flow. Technical report, DTIC Document, 1982.

D. A. Drew and R. T. Lahey. Application of general constitutive principles to the derivation of multidimensional two-phase flow equations. *International Journal of Multiphase Flow*, 5(4):243–264, 1979.

D. A. Drew and S. L. Passman. *Theory of Multicomponent Fluids*, volume 135. Springer Science & Business Media, 2006.

D. A. Drew and R. T. Wood. Overview and taxonomy of models and methods. In *Proceedings of 1st International Workshop on Two-phase Flow Fundamentals*, 1985.

J. M. Duley, A. C. Fowler, I. R. Moyles, and S. B. G. O'Brien. On the Keller–Rubinow model for Liesegang ring formation. *Proceedings of the Royal Society A: Mathematical, Physical and Engineering Sciences*, 473(2205):20170128, 2017.

H. Duns Jr and N. C. J. Ros. Vertical flow of gas and liquid mixtures in wells. In *6th World Petroleum Congress*. World Petroleum Congress, 1963.

M. J. Economides. *Petroleum Production Systems*. Upper Saddle River, 2013.

J. W. Evans. Random and cooperative sequential adsorption. *Reviews of Modern Physics*, 65(4):1281–1329, 1993.

A. C. Fowler. Linear and non-linear stability of heat exchangers. *IMA Journal of Applied Mathematics*, 22(3):361–382, 1978.

A. C. Fowler. *Mathematical Geoscience*, volume 36. Springer Science & Business Media, 2011.

A. C. Fowler. Notes of statistical mechanics, *University of Oxford*, 2017.

A. C. Fowler and M. Robinson. Counter-current convection in a volcanic conduit. *Journal of Volcanology and Geothermal Research*, 356:141–162, 2018.

C. M. R. Fowler. *The solid earth: an introduction to global geophysics*. Cambridge University Press, 1990.

H. Ghorbani, D. A. Wood, J. Moghadasi, A. Choubineh, P. Abdizadeh, and N. Mohamadian. Predicting liquid flow-rate performance through wellhead chokes with genetic and solver optimizers: an oil field case study. *Journal of Petroleum Exploration and Production Technology*, 9(2):1355–1373, 2019.

M. Golan and C. H. Whitson. *Well Performance*. Prentice Hall PTR, 2nd revised edition, 1991.

G. W. Govier and K. Aziz. *The Flow of Complex Mixtures in Pipes*. Society of Petroleum Engineers, 2008.

B. Guo, W. C. Lyons, and Ghalambor. *Petroleum Production Engineering, a Computer-Assisted Approach*. Gulf Professional Publishing, 2011.

B. Guo, K. Sun, and A. Ghalambor. *Well Productivity Handbook*. Elsevier, 2014.

A. R. Hagedorn and K. E. Brown. Experimental study of pressure gradients occurring during continuous two-phase flow in small-diameter vertical conduits. *Journal of Petroleum Technology*, 17(4):475–484, 1965.

T. Hantschel and A. I. Kauerauf. *Fundamentals of Basin and Petroleum Systems Modeling*. Springer Science & Business Media, 2009.

R. B. Hargraves. *Physics of Magmatic Processes*. Princeton University Press, 2014.

J. Herrick, S. Jun, J. Bechhoefer, and A. Bensimon. Kinetic model of DNA replication in eukaryotic organisms. *Journal of Molecular Biology*, 320(4):741–750, 2002.

T. Hibiki and M. Ishii. Experimental study on interfacial area transport in bubbly two-phase flows. *International Journal of Heat and Mass Transfer*, 42(16):3019–3035, 1999.

T. Hibiki and M. Ishii. Two-group interfacial area transport equations at bubbly-to-slug flow transition. *Nuclear Engineering and Design*, 202(1):39–76, 2000.

M. Ishii and T. Hibiki. *Thermo-fluid Dynamics of Two-Phase Flow*. Springer Science & Business Media, 2010.

M. Ishii and K. Mishima. Two-fluid model and hydrodynamic constitutive relations. *Nuclear Engineering and Design*, 82(2):107–126, 1984.

M. Ishii, S. Kim, and J. Uhle. Interfacial area transport equation: model development and benchmark experiments. *International Journal of Heat and Mass Transfer*, 45 (15):3111–3123, 2002.

A. Iske and T. Randen. *Mathematical Methods and Modelling in Hydrocarbon Exploration and Production*, volume 7. Springer, 2006.

M. F. Jerez-Carrizales, J. E. Jaramillo, and D. Fuentes. Simulation of the two-phase flow in a wellbore using two-fluid model. In *11th World Congress on Computational Mechanics*, 2014.

A. V. Jones and A. Prosperetti. On the suitability of first-order differential models for two-phase flow prediction. *International Journal of Multiphase Flow*, 11(2): 133–148, 1985.

S. Kalkach-Navarro, R. T. Lahey Jr, and D. A. Drew. Analysis of the bubbly/slug flow regime transition. *Nuclear Engineering and Design*, 151(1):15–39, 1994.

P. L. Krapivsky. Kinetics of random sequential parking on a line. *Journal of Statistical Physics*, 69(1–2):135–150, 1992.

F. Lehr and D. Mewes. A transport equation for the interfacial area density applied to bubble columns. *Chemical Engineering Science*, 56(3):1159–1166, 2001.

A. C. Levi and M. Kotrla. Theory and simulation of crystal growth. *Journal of Physics: Condensed Matter*, 9(2):299–344, 1997.

Y. Liao and D. Lucas. A literature review of theoretical models for drop and bubble breakup in turbulent dispersions. *Chemical Engineering Science*, 64(15):3389–3406, 2009.

I. M. Lifshitz and V. V. Slyozov. The kinetics of precipitation from supersaturated solid solutions. *Journal of Physics and Chemistry of Solids*, 19(1–2):35–50, 1961.

S. Livescu, L. J. Durlofsky, K. Aziz, and J. C. Ginestra. A fully-coupled thermal multiphase wellbore flow model for use in reservoir simulation. *Journal of Petroleum Science and Engineering*, 71(3):138–146, 2010.

H. Luo and H. Svendsen. Modeling and simulation of binary approach by energy conservation analysis. *Chemical Engineering Communications*, 145(1):145–153, 1996.

R. W. Lyczkowski, D. Gidaspow, C. W. Solbrig, and E. D. Hughes. Characteristics and stability analyses of transient one-dimensional two-phase flow equations and their finite difference approximations. *Nuclear Science and Engineering*, 66(3): 378–396, 1978.

R. F. Meyer and E. D. Attanasi. Heavy oil and natural bitumen-strategic petroleum resources. Technical report, United States Geological Survey, 2003.

K. Mishima and M. Ishii. Flow regime transition criteria for upward two-phase flow in vertical tubes. *International Journal of Heat and Mass Transfer*, 27(5):723–737, 1984.

A. Muggeridge, A. Cockin, K. Webb, H. Frampton, I. Collins, T. Moulds, and P. Salino. Recovery rates, enhanced oil recovery and technological limits. *Philosophical Transactions of The Royal Society A*, 372, 2014.

S. Navarro-Valenti, A. Clausse, D. A. Drew, and R. T. Lahey Jr. A contribution to the mathematical modeling of bubbly/slug flow regime transition. *Chemical Engineering Communications*, 102(1):69–85, 1991.

C. Pauchon and S. Banerjee. Interphase momentum interaction effects in the averaged multifield model: Part I: Void propagation in bubbly flows. *International Journal of Multiphase Flow*, 12(4):559–573, 1986.

F. H. Poettman and P. G. Carpenter. The multiphase flow of gas, oil, and water through vertical flow strings with application to the design of gas-lift installations. In *Drilling and Production Practice*. American Petroleum Institute, 1952.

M. Prince and H. Blanch. Bubble coalescence and break-up in air-sparged bubble columns. *AIChE Journal*, 36(10):1485–1499, 1990.

J. J. Ramsden. Puzzles and paradoxes in protein adsorption. *Chemical Society Reviews*, 24(1):73–78, 1995.

J. D. Ramshaw and J. A. Trapp. Characteristics, stability, and short-wavelength phenomena in two-phase flow equation systems. *Nuclear Science and Engineering*, 66(1):93–102, 1978.

M. R. Riaza. *Characterization and Properties of Petroleum Fractions*. ASTM International, 2005.

G. J. Rodgers and J. A. N. Filipe. Exact results for surface deposition with precursor layer diffusion. *Journal of Physics A: Mathematical and General*, 30(10):3449–3461, 1997.

S. Sa. Flow-induced breakup of drops and bubbles. *arXiv preprint arXiv:1701.06157*, 2017.

Schlumberger. OLGA Dynamic Multiphase Flow Simulator. 2016.

G. T. Schuster. Notes on the basics of seismic imaging, *King Abdullah University of Science and Technology*, 2010.

X. Shen and T. Hibiki. Bubble coalescence and breakup model evaluation and development for two-phase bubbly flows. *International Journal of Multiphase Flow*, 109:131–149, 2018.

M. Shippen and W. J. Bailey. Steady-state multiphase flow past, present, and future, with a perspective on flow assurance. *Energy & Fuels*, 26(7):4145–4157, 2012.

O. Shoham. *Mechanistic Modeling of Gas-Liquid Two-Phase Flow in Pipes*. Society of Petroleum Engineers Richardson, 2006.

H. B. Stewart. Stability of two-phase flow calculation using two-fluid models. *Journal of Computational Physics*, 33(2):259–270, 1979.

J. H. Stuhmiller. The influence of interfacial pressure forces on the character of two-phase flow model equations. *International Journal of Multiphase Flow*, 3(6): 551–560, 1977.

X. Sun, S. Kim, M. Ishii, and S. G. Beus. Modeling of bubble coalescence and disintegration in confined upward two-phase flow. *Nuclear Engineering and Design*, 230(1–3):3–26, 2004.

Y. Taitel and A. E. Dukler. A model for predicting flow regime transitions in horizontal and near horizontal gas-liquid flow. *AIChE Journal*, 22(1):47–55, 1976.

Y. Taitel, D. Bornea, and A. E. Dukler. Modelling flow pattern transitions for steady upward gas-liquid flow in vertical tubes. *AIChE Journal*, 26(3):345–354, 1980.

G. Tarjus, P. Schaaf, and J. Talbot. Generalized random sequential adsorption. *The Journal of Chemical Physics*, 93(11):8352–8360, 1990.

A. V. Teran, A. Bill, and R. B. Bergmann. Time-evolution of grain size distributions in random nucleation and growth crystallization processes. *Physical Review B*, 81 (7):075319, 2010.

R. E. Terry. Enhanced oil recovery. *Encyclopedia of Physical Science and Technology*, 18:503–518, 2001.

A. K. Tharanivasan, C. Yang, and Y. Gu. Measurements of molecular diffusion coefficients of carbon dioxide, methane, and propane in heavy oil under reservoir conditions. *Energy & fuels*, 20(6):2509–2517, 2006.

D. L. Turcotte, H. Ockendon, J. R. Ockendon, and S. J. Cowley. A mathematical model of vulcanian eruptions. *Geophysical Journal International*, 103(1):211–217, 1990.

E. Van Den Bark and O. D. Thomas. Ekofisk: first of the giant oil fields in western europe. *AAPG Bulletin*, 65(11):2341–2363, 1981.

M. Vazquez and H. D. Beggs. Correlations for fluid physical property prediction. In *SPE Annual Fall Technical Conference and Exhibition*. Society of Petroleum Engineers, 1977.

G. B. Wallis. *One-dimensional Two-Phase Flow*. McGraw-Hill, 1969.

T. Wang, J. Wang, and Y. Jin. Population balance model for gas–liquid flows: Influence of bubble coalescence and breakup models. *Industrial & Engineering Chemistry Research*, 44(19):7540–7549, 2005.

X. Wang, X. Sun, B. Doup, and H. Zhao. Dynamic modeling strategy for flow regime transition in gas-liquid two-phase flows. *The Journal of Computational Multiphase Flows*, 4(4):387–397, 2012.

B. Widom. Random sequential addition of hard spheres to a volume. *The Journal of Chemical Physics*, 44(10):3888–3894, 1966.

W. Yao and C. Morel. Volumetric interfacial area prediction in upward bubbly two-phase flow. *International Journal of Heat and Mass Transfer*, 47(2):307–328, 2004.

N. Zuber and J. A. Findlay. Average volumetric concentration in two-phase flow systems. *Journal of Heat Transfer*, 87(4):453–468, 1965.